

1

²A SEARCH FOR LONG-LIVED, CHARGED, SUPERSYMMETRIC PARTICLES
³USING IONIZATION WITH THE ATLAS DETECTOR

⁴BRADLEY AXEN

5



6

September 2016 – Version 0.58

⁸ Bradley Axen: *A Search for Long-Lived, Charged, Supersymmetric Particles using*
⁹ *Ionization with the ATLAS Detector*, Subtitle, © September 2016

¹⁰ The dissertation of Bradley Axen, titled *A Search for Long-Lived, Charged, Super-*
¹¹ *symmetric Particles using Ionization with the ATLAS Detector*, is approved:

¹² _____
¹³ Chair _____ Date

¹⁴ _____
¹⁵ _____ Date

¹⁶ _____
¹⁷ _____ Date

¹⁸ University of California, Berkeley

19

Usually a quotation.

20

Dedicated to.

₂₁ ABSTRACT

₂₂ How to write a good abstract:

₂₃ <https://plg.uwaterloo.ca/~migod/research/beck00PSLA.html>

24 PUBLICATIONS

25 Some ideas and figures have appeared previously in the following publications:

26

27 Put your publications from the thesis here. The packages `multibib` or `bibtopic`
28 etc. can be used to handle multiple different bibliographies in your document.

30 ACKNOWLEDGEMENTS

31 Put your acknowledgements here.

32

33 And potentially a second round.

34

35 CONTENTS

36	I	INTRODUCTION	1
37	1	INTRODUCTION	2
38	II	THEORETICAL CONTEXT	4
39	2	STANDARD MODEL	5
40	2.1	Action and the Lagrangian	5
41	2.2	Gauge Invariance and Forces	6
42	2.2.1	$SU(2) \times U(1)$ and the Electroweak Force	8
43	2.2.2	$SU(3)$ and the Strong Force	8
44	2.3	Noether's Theorem, Charges, and Matter	8
45	2.3.1	Quarks	9
46	2.3.2	Leptons	10
47	2.3.3	Chirality	10
48	2.4	Higgs Mechanism and Mass	11
49	2.5	Phenomenology	12
50	2.5.1	Electroweak Physics	12
51	2.5.2	Strong Physics	13
52	2.5.3	Proton-Proton Collisions	13
53	2.6	Limitations	14
54	2.6.1	Theoretical Concerns	14
55	2.6.2	Cosmological Observations	16
56	3	SUPERSYMMETRY	18
57	3.1	Structure	18
58	3.1.1	Simplified Models	20
59	3.2	Motivation	20
60	3.3	Long-Lived Particles	22
61	III	EXPERIMENTAL STRUCTURE AND RECONSTRUCTION	24
62	4	THE LARGE HADRON COLLIDER	25
63	4.1	Injection Chain	26
64	4.2	Design	27
65	4.2.1	Layout	27
66	4.2.2	Magnets	28
67	4.2.3	RF Cavities	29
68	4.2.4	Beam	31
69	4.3	Luminosity Parameters	31
70	4.4	Delivered Luminosity	32
71	5	THE ATLAS DETECTOR	35
72	5.1	Coordinate System	37
73	5.2	Magnetic Field	38
74	5.3	Inner Detector	40

75	5.3.1	Pixel Detector	43
76	5.3.2	Semiconductor Tracker	45
77	5.3.3	Transition Radiation Tracker	48
78	5.4	Calorimetry	49
79	5.4.1	Electromagnetic Calorimeter	50
80	5.4.2	Hadronic Calorimeters	51
81	5.5	Muon Spectrometer	53
82	5.5.1	Monitored Drift Tube	55
83	5.5.2	Resistive Plate Chamber	56
84	5.5.3	Cathode Strip Chamber	56
85	5.5.4	Thin Gap Chamber	57
86	5.6	Trigger	58
87	6	EVENT RECONSTRUCTION	62
88	6.1	Charged Particles	62
89	6.1.1	Pixel Neural Network	64
90	6.1.2	Pixel dE/dx	65
91	6.1.3	Vertex Reconstruction	66
92	6.2	Electrons and Photons	66
93	6.2.1	Photon Identification	68
94	6.2.2	Electron Identification	68
95	6.3	Muons	68
96	6.3.1	Muon Identification	69
97	6.4	Jets	69
98	6.4.1	Topological Clustering	69
99	6.4.2	Jet Algorithms	71
100	6.4.3	Jet Energy Scale	71
101	6.5	Missing Transverse Energy	72
102	IV	CALORIMETER RESPONSE	75
103	7	RESPONSE MEASUREMENT WITH SINGLE HADRONS	76
104	7.1	Dataset and Simulation	77
105	7.1.1	Data Samples	77
106	7.1.2	Simulated Samples	77
107	7.1.3	Event Selection	77
108	7.2	Inclusive Hadron Response	78
109	7.2.1	E/p Distribution	78
110	7.2.2	Zero Fraction	79
111	7.2.3	Neutral Background Subtraction	81
112	7.2.4	Corrected Response	82
113	7.2.5	Additional Studies	84
114	7.3	Identified Particle Response	87
115	7.3.1	Decay Reconstruction	88
116	7.3.2	Identified Response	89
117	7.3.3	Additional Species in Simulation	91
118	7.4	Summary	91
119	8	JET ENERGY RESPONSE AND UNCERTAINTY	93

120	8.1	Motivation	93
121	8.2	Uncertainty Estimate	93
122	8.3	Summary	96
123	V	SEARCH FOR LONG-LIVED PARTICLES	99
124	9	LONG-LIVED PARTICLES IN ATLAS	100
125	9.1	Event Topology	100
126	9.1.1	Detector Interactions	101
127	9.1.2	Lifetime Dependence	102
128	9.2	Simulation	105
129	10	EVENT SELECTION	107
130	10.1	Trigger	108
131	10.2	Kinematics and Isolation	109
132	10.3	Particle Species Rejection	113
133	10.4	Ionization	116
134	10.4.1	Mass Estimation	117
135	10.5	Efficiency	118
136	11	BACKGROUND ESTIMATION	121
137	11.1	Background Sources	121
138	11.2	Prediction Method	122
139	11.3	Validation	123
140	11.3.1	Closure in Simulation	123
141	11.3.2	Validation Region in Data	124
142	12	SYSTEMATIC UNCERTAINTIES AND RESULTS	126
143	13	SYSTEMATIC UNCERTAINTIES AND RESULTS	127
144	13.1	Systematic Uncertainties	127
145	13.1.1	Background Estimate	127
146	13.1.2	Signal Yield	128
147	13.2	Final Yields	134
148	13.3	Cross Sectional Limits	135
149	13.4	Mass Limits	137
150	13.5	Context for Long-Lived Searches	139
151	VI	CONCLUSIONS	142
152	14	SUMMARY AND OUTLOOK	143
153	14.1	Summary	143
154	14.2	Outlook	143
155	VII	APPENDIX	144
156	A	INELASTIC CROSS SECTION	145
157	B	EXPANDED R-HADRON YIELDS AND LIMITS	146
158		BIBLIOGRAPHY	152

159 LIST OF FIGURES

160	Figure 1	A Feynman diagram representing the interaction of the A field with a generic fermion, f	8
161			
162	Figure 2	The particle content of the Standard Model (SM)	10
163	Figure 3	The Feynman diagrams representing the decays of the W and Z bosons to fermions. Here f indicates a generic fermion, \bar{f} its antiparticle, and f' the partner of that fermion in the same generation.	13
164			
165			
166			
167	Figure 4	The parton distribution functions (PDFs) for proton- proton collisions at $Q^2 = 10 \text{ GeV}^2$ and $Q^2 = 10^4$ GeV^2 . Each shows the fraction of particles which carry a fraction x of the total proton energy at the specified scale [1].	14
168			
169			
170			
171			
172	Figure 5	An approximation of the running of the coupling con- stants in the SM up to the Planck scale [unification_plot].	15
173			
174	Figure 6	The distribution of velocities of stars as a function of the radius from the center of the galaxy. The contribu- tions to the velocity from the various components of matter in the galaxy are shown [2].	16
175			
176			
177			
178	Figure 7	An approximation of the running of the coupling con- stants in the SM up to the Planck scale [unification_plot].	21
179			
180	Figure 8	The decay of a gluino to quarks and an Lightest Su- persymmetric Particle (LSP), which precedes through a squark.	22
181			
182			
183	Figure 9	The four collision points and corresponding experi- ments of the Large Hadron Collider (LHC). The image includes the location of the nearby city of Geneva as well as the border of France and Switzerland.	26
184			
185			
186			
187	Figure 10	The cumulative luminosity over time delivered to the A Toroidal LHC ApparatuS (ATLAS) experiment from high energy proton-proton collisions since 2011. The energies of the collisions are listed for each of the data- taking periods.	27
188			
189			
190			
191			
192	Figure 11	The accelerator complex that builds up to the full de- sign energies at the LHC . The protons are passed in order to Linac 2, the PSB , the PS , the SPS and then the LHC	28
193			
194			
195			
196	Figure 12	A schematic of the layout of the LHC , not to scale. The arched and straight sections are illustrated at the bot- tom of the schematic, and all four crossing sites are indicated with their respective experiments.	29
197			
198			
199			

200	Figure 13	A cross section of the the cryodipole magnets which bend the flight path of protons around the circumference of the LHC. The diagram includes both the superconducting coils which produce the magnetic field and the structural elements which keep the magnets precisely aligned.	30
201			
202			
203			
204			
205			
206	Figure 14	The arrangement of four radiofrequency (RF) cavities within a cryomodule.	30
207			
208	Figure 15	The cumulative luminosity versus time delivered to ATLAS (green), recorded by ATLAS (yellow), and certified to be good quality data (blue) during stable beams for pp collisions at 13 TeV in 2015.	33
209			
210			
211			
212	Figure 16	The luminosity-weighted distribution of the mean number of interactions per crossing for the 2015 pp collision data at 13 TeV.	34
213			
214			
215	Figure 17	A cut-away schematic of the layout of the ATLAS detector. Each of the major subsystems is indicated.	36
216			
217	Figure 18	A cross-sectional slice of the ATLAS experiment which illustrates how the various SM particles interact with the detector systems.	36
218			
219			
220	Figure 19	The layout of the four superconducting magnets in the ATLAS detector.	39
221			
222	Figure 20	The arrangement of the subdetectors of the ATLAS inner detector. Each of the subdetectors is labeled in the cut-away view of the system.	41
223			
224			
225	Figure 21	A quarter section of the ATLAS inner detector which shows the layout of each of the subdetectors in detail. The lower panel shows an enlarged view of the pixel detector. Example trajectories for a particle with $\eta = 1.0, 1.5, 2.0, 2.5$ are shown. The Insertible B-Layer (IBL), which was added after the original detector commissioning, is not shown.	41
226			
227			
228			
229			
230			
231			
232	Figure 22	A computer generated three-dimensional view of the inner detector along the line of the beam axis. The subdetectors and their positions are labeled.	42
233			
234			
235	Figure 23	An alternative computer generated three-dimensional view of the inner detector transverse to the beam axis. The subdetectors and their positions are labeled.	42
236			
237			
238	Figure 24	The integrated radiation lengths traversed by a straight track at the exit of the ID envelope, including the services and thermal enclosures. The distribution is shown as a function of $ \eta $ and averaged over ϕ . The breakdown indicates the contributions of individual subdetectors, including services in their active volume.	43
239			
240			
241			
242			
243			
244	Figure 25	A cut away image of the outer three layers of the pixel detector.	46
245			

246	Figure 26	An image of the insertion of the IBL into the current pixel detector.	46
247			
248	Figure 27	A three-dimensional computer-generated image of the geometry of the IBL with a view (a) mostly transverse to the beam pipe (b) mostly parallel to the beam pipe.	47
249			
250	Figure 28	An expanded view of the geometry of the silicon microstrip (SCT) double layers in the barrel region.	48
251			49
252	Figure 29		
253	Figure 30	The depth of (a) the electromagnetic barrel calorimeter in radiation lengths and (b) all calorimeters in interaction lengths as a function of pseudorapidity.	50
254			
255	Figure 31	A schematic of the liquid argon (LAr) calorimeter in the barrel region, highlighting the accordion structure.	51
256			
257	Figure 32	A schematic of a hadronic tile module which shows the alternating layers of steel and plastic scintillator.	52
258			
259	Figure 33	The segmentation in depth and η of the tile-calorimeter modules in the central (left) and extended (right) barrels.	53
260			
261	Figure 34	A cut-away diagram of the muon systems on ATLAS	54
262			
263	Figure 35	A quarter view of the muon spectrometer which highlights the layout of each of the detecting elements. The BOL, BML, BIL, EOL, EML, and EIL are all Monitored Drift Tube (MDT) elements, where the acronyms encode their positions.	54
264			
265	Figure 36	A schematic of the cross-section of the muon spectrometer in the barrel region.	55
266			
267	Figure 37	A schematic of a single MDT chamber, which shows the multilayers of drift tubes as well as the alignment system.	56
268			
269	Figure 38	A schematic of the Cathode Strip Chamber (CSC) end-cap, showing the overlapping arrangement of the eight large and eight small chambers.	57
270			
271	Figure 39	A schematic of the Thin Gap Chamber (TGC) doublet and triplet layers.	58
272			
273	Figure 40	The L1 Trigger rate broken down into the types of triggers as a function of the luminosity block for the 2015 data collection period.	60
274			
275	Figure 41	The HLT Trigger rate broken down into the types of triggers as a function of the luminosity block for the 2015 data collection period.	61
276			
277	Figure 42	An illustration of the perigee representation of track parameters for an example track. The charge is not directly shown, but is indicated by the direction of curvature of the track [20].	63
278			
279			
280			
281			
282			
283			
284			
285			
286			
287			
288			

289	Figure 43	The x and y locations of the hits generated in a simulated $t\bar{t}$ event in the inner detector. The hits which belong to tracks formed using the inside-out algorithm are highlighted in red, while the hits which belong to tracks formed using the outside-in algorithm are circled in black.	64
290			
291			
292			
293			
294			
295	Figure 44	Examples of the clusters formed in a single layer of the pixel detector for (a) a single isolated particle, (b) two nearly-overlapping particles, and (c) a particle which emits a δ -ray [21].	65
296			
297			
298			
299	Figure 45	The total, fractional jet energy scale (JES) uncertainties estimated for 2015 data as a function of jet p_T	73
300			
301	Figure 46	The E/p distribution and ratio of simulation to data for isolated tracks with (a) $ \eta < 0.6$ and $1.2 < p/\text{GeV} < 1.8$ and (b) $ \eta < 0.6$ and $2.2 < p/\text{GeV} < 2.8$	79
302			
303			
304	Figure 47	The fraction of tracks as a function (a, b) of momentum, (c, d) of interaction lengths with $E \leq 0$ for tracks with positive (on the left) and negative (on the right) charge.	80
305			
306			
307			
308	Figure 48	An illustration (a) of the geometry of energy deposits in the calorimeter. The red energy deposits come from the charged particle targeted for measurement, while the blue energy deposits are from nearby neutral particles and must be subtracted. The same diagram (b) for the neutral-background selection, described in Section 7.2.3.	81
309			
310			
311			
312			
313			
314			
315	Figure 49	$\langle E/p \rangle_{\text{BG}}$ as a function of the track momentum for tracks with (a) $ \eta < 0.6$, (b) $0.6 < \eta < 1.1$, and as a function of the track pseudorapidity for tracks with (c) $1.2 < p/\text{GeV} < 1.8$, (d) $1.8 < p/\text{GeV} < 2.2$	82
316			
317			
318			
319	Figure 50	$\langle E/p \rangle_{\text{COR}}$ as a function of track momentum, for tracks with (a) $ \eta < 0.6$, (b) $0.6 < \eta < 1.1$, (c) $1.8 < \eta < 1.9$, and (d) $1.9 < \eta < 2.3$	83
320			
321			
322	Figure 51	$\langle E/p \rangle_{\text{COR}}$ calculated using LCW-calibrated topological clusters as a function of track momentum for tracks with (a) zero or more associated topological clusters or (b) one or more associated topological clusters.	84
323			
324			
325			
326	Figure 52	Comparison of the $\langle E/p \rangle_{\text{COR}}$ for tracks with (a) less than and (b) greater than 20 hits in the TRT.	85
327			
328	Figure 53	Comparison of the $\langle E/p \rangle_{\text{COR}}$ for (a) positive and (b) negative tracks as a function of track momentum for tracks with $ \eta < 0.6$	86
329			
330			
331	Figure 54	Comparison of the E/p distributions for (a) positive and (b) negative tracks with $0.8 < p/\text{GeV} < 1.2$ and $ \eta < 0.6$, in simulation with the FTFP_BERT and QGSP_BERT physics lists.	86
332			
333			
334			

335	Figure 55	Comparison of the response of the hadronic calorimeter as a function of track momentum (a) at the EM-scale and (b) after the LCW calibration.	87
336			
337			
338	Figure 56	Comparison of the response of the EM calorimeter as a function of track momentum (a) at the EM-scale and (b) with the LCW calibration.	87
339			
340			
341	Figure 57	The reconstructed mass peaks of (a) K_S^0 , (b) Λ , and (c) $\bar{\Lambda}$ candidates.	88
342			
343	Figure 58	The E/p distribution for isolated (a) π^+ , (b) π^- , (c) proton, and (d) anti-proton tracks.	89
344			
345	Figure 59	The fraction of tracks with $E \leq 0$ for identified (a) π^+ and π^- , and (b) proton and anti-proton tracks	90
346			
347	Figure 60	The difference in $\langle E/p \rangle$ between (a) π^+ and π^- (b) p and π^+ , and (c) \bar{p} and π^-	91
348			
349	Figure 61	$\langle E/p \rangle_{\text{COR}}$ as a function of track momentum for (a) π^+ tracks and (b) π^- tracks.	92
350			
351	Figure 62	The ratio of the calorimeter response to single particles of various species to the calorimeter response to π^+ with the physics list FTFP_BERT.	92
352			
353			
354	Figure 63	The spectra of true particles inside anti- k_t , $R = 0.4$ jets with (a) $90 < p_T/\text{GeV} < 100$, (b) $400 < p_T/\text{GeV} < 500$, and (c) $1800 < p_T/\text{GeV} < 2300$	94
355			
356			
357	Figure 64	The JES response uncertainty contributions, as well as the total JES uncertainty, as a function of jet p_T for (a) $ \eta < 0.6$ and (b) $0.6 < \eta < 1.1$	97
358			
359			
360	Figure 65	The correlations between bins of average reconstructed jet momentum as a function of jet p_T and $ \eta $ for jets in the central region of the detector.	98
361			
362			
363	Figure 66	A schematic diagram of an R-Hadron event with a lifetime around 0.01 ns. The diagram includes one charged R-Hadron (solid blue), one neutral R-Hadron (dashed blue), LSPs (dashed green) and charged hadrons (solid orange). The pixel detector, calorimeters, and muon system are illustrated but not to scale.	102
364			
365			
366			
367			
368			
369	Figure 67	A schematic diagram of an R-Hadron event with a lifetime around 4 ns. The diagram includes one charged R-Hadron (solid blue), one neutral R-Hadron (dashed blue), LSPs (dashed green) and a charged hadron (solid orange). The pixel detector, calorimeters, and muon system are illustrated but not to scale.	103
370			
371			
372			
373			
374			
375	Figure 68	A schematic diagram of an R-Hadron event with a lifetime around 5 ns. The diagram includes one charged R-Hadron (solid blue), one neutral R-Hadron (dashed blue), LSPs (dashed green) and charged hadrons (solid orange). The pixel detector, calorimeters, and muon system are illustrated but not to scale.	104
376			
377			
378			
379			
380			

381	Figure 69	A schematic diagram of an R-Hadron event with a life-time around 20 ns. The diagram includes one charged R-Hadron (solid blue), one neutral R-Hadron (dashed blue), LSPs (dashed green) and charged hadrons (solid orange). The pixel detector, calorimeters, and muon system are illustrated but not to scale.	104
382			
383			
384			
385			
386			
387	Figure 70	A schematic diagram of an R-Hadron event with a life-time around 20 ns. The diagram includes one charged R-Hadron (solid blue) and one neutral R-Hadron (dashed blue). The pixel detector, calorimeters, and muon system are illustrated but not to scale.	105
388			
389			
390			
391			
392	Figure 71	The distribution of (a) E_T^{miss} and (b) Calorimeter E_T^{miss} for simulated signal events before the trigger requirement.	108
393			
394			
395	Figure 72	The distribution of E_T^{miss} for data and simulated signal events, after the trigger requirement.	110
396			
397	Figure 73	The trigger efficiency for the HLT_xe70 trigger requirement as a function of (a) E_T^{miss} and (b) Calorimeter E_T^{miss} for simulated signal events.	111
398			
399			
400	Figure 74	The dependence of dE/dx on N_{split} in data after basic track hit requirements have been applied.	112
401			
402	Figure 75	The distribution of dE/dx with various selections applied in data and simulated signal events.	112
403			
404	Figure 76	The distribution of track momentum for data and simulated signal events, after previous selection requirements have been applied.	113
405			
406			
407	Figure 77	The distribution of M_T for data and simulated signal events, after previous selection requirements have been applied.	114
408			
409			
410	Figure 78	The distribution of summed tracked momentum within a cone of $\Delta R < 0.25$ around the candidate track for data and simulated signal events, after previous selection requirements have been applied.	115
411			
412			
413			
414	Figure 79	The normalized, two-dimensional distribution of E/p and f_{EM} for simulated (a) $Z \rightarrow ee$, (b) $Z \rightarrow \tau\tau$, (c) 1200 GeV Stable R-Hadron events, and (d) 1200 GeV, 10 ns R-Hadron events.	116
415			
416			
417			
418	Figure 80	Two-dimensional distribution of dE/dx versus charge signed momentum (qp) for minimum-bias tracks. The fitted distributions of the most probable values for pions, kaons and protons are superimposed.	117
419			
420			
421			
422	Figure 81	The distribution of mass estimated using dE/dx for simulated stable R-Hadrons with masses between 1000 and 1600 GeV.	118
423			
424			

425	Figure 82	The acceptance \times efficiency as a function of R-Hadron (a) mass and (b) lifetime. (a) shows all of the combinations of mass and lifetime considered in this search, and (b) highlights the lifetime dependence for 1000 GeV and 1600 GeV R-Hadrons.	120
426			
427			
428			
429			
430	Figure 83	The distribution of (a) dE/dx and (b) momentum for tracks in data and simulated signal after requiring the event level selection and the track selection on p_T , hits, and N_{split} . Each sub-figure shows the normalized distributions for tracks classified as hadrons, electrons, and muons in data and R-Hadrons in the simulated signal.	122
431			
432			
433			
434			
435			
436			
437	Figure 84	The distribution of $M_{dE/dx}$ (a) before and (b) after the ionization requirement for tracks in simulated W boson decays and for the randomly generated background estimate.	124
438			
439			
440			
441	Figure 85	The distribution of $M_{dE/dx}$ (a) before and (b) after the ionization requirement for tracks in the validation region and for the randomly generated background estimate.	125
442			
443			
444			
445	Figure 86	The trigger efficiency for the HLT_xe70 trigger requirement as a function of Calorimeter E_T^{miss} for simulated data events with a W boson selection. Simulated signal events and simulated W boson events are also included.	130
446			
447			
448			
449			
450	Figure 87	The efficiency of the muon veto for R-hadrons of two different masses, as a function of $\frac{1}{\beta}$ for simulated R-Hadron tracks.	132
451			
452			
453	Figure 88	The average reconstructed MDT β distribution for $Z \rightarrow \mu\mu$ events in which one of the muons is reconstructed as a slow muon, for both data and simulation. A gaussian fit is superimposed.	133
454			
455			
456			
457	Figure 89	The observed mass distribution of events in data and the generated background distribution in (a) the stable and (b) the metastable signal region. A few example simulated signal distributions are superimposed.	134
458			
459			
460			
461	Figure 90	The observed and expected cross section limits as a function of mass for the stable simulated signal. The predicted cross section values for the corresponding signals are included.	137
462			
463			
464			
465	Figure 91	The observed and expected cross section limits as a function of mass for each generated lifetime. The predicted cross section values for the corresponding signals are included.	138
466			
467			
468			

- 469 Figure 92 The excluded range of masses as a function of gluino
470 lifetime. The expected lower limit (LL), with its exper-
471 imental $\pm 1\sigma$ band, is given with respect to the nominal
472 theoretical cross-section. The observed 95% LL ob-
473 tained at $\sqrt{s} = 8$ TeV [82] is also shown for comparison.¹⁴⁰
474 Figure 93 The constraints on the gluino mass as a function of
475 lifetime for a split-supersymmetry model with the gluino
476 R-Hadrons decaying into a gluon or light quarks and
477 a neutralino with mass of 100 GeV. The solid lines in-
478 dicate the observed limits, while the dashed lines in-
479 dicate the expected limits. The area below the curves
480 is excluded. The dots represent results for which the
481 particle is assumed to be prompt or stable.¹⁴¹

482 LIST OF TABLES

483 Table 1	The particles in the SM and their corresponding super-partners in the Minimal Supersymmetric Model (MSSM).	19
484		
485 Table 2	The design parameters of the LHC beam that determines the energy of collisions and the luminosity, for both the injection of protons and at the nominal circulation.	32
486		
487		
488		
489 Table 3	The performance goals for each of the subsystems of the ATLAS detector. The $ \eta $ coverage specifies the range where the subsystem needs to be able to provide measurements with the specified resolution. The resolutions include a p_T or E dependence that is added in quadrature with a p_T/E independent piece.	37
490		
491		
492		
493		
494		
495 Table 4	A summary of the parameters of each of the three magnet systems on ATLAS	39
496		
497 Table 5	A summary of the parameters of the inner detector and each of the subdetectors [12].	44
498		
499 Table 6	A summary of the expected performance of the combined inner detector [16]. Included are the reconstruction efficiencies for multiple particle types as well as the momentum and impact parameter (IP) resolution for various momenta.	45
500		
501		
502		
503		
504 Table 7	The trigger menu for the 2015 data collection with $L = 5 \times 10^{33} \text{ cm}^{-2} \text{ s}^{-1}$. Both the L1 and high level trigger (HLT) selection requirements and their trigger rates are shown measured at the specified luminosity are shown. The typical offline selections represent a typical set of offline requirements imposed after the trigger in an analysis.	59
505		
506		
507		
508		
509		
510		
511 Table 8	The dominant sources of corrections and systematic uncertainties in the JES estimation technique, including typical values for the correcting shift (Δ) and the associated uncertainty (σ).	95
512		
513		
514		
515 Table 9	The expected number of events at each level of the selection for metastable 1600 GeV, 10 ns R-Hadrons, along with the number of events observed in data, for 3.2 fb^{-1} . The simulated yields are shown with statistical uncertainties only. The total efficiency \times acceptance is also shown for the signal.	119
516		
517		
518		
519		
520		

521	Table 10	A summary of the sources of systematic uncertainty for the data-driven background in the signal region. If the uncertainty depends on the mass, the maximum values are reported.	127
522			
523			
524			
525	Table 11	A summary of the sources of systematic uncertainty for the simulated signal yield. The uncertainty depends on the mass and lifetime, and the maximum negative and positive values are reported in the table.	129
526			
527			
528			
529	Table 12	Example of the contributing systematic variations to the total systematic for the E_T^{miss} Scale, as measured in a 1200 GeV, Stable R-Hadron signal sample.	131
530			
531			
532	Table 13	The estimated number of background events and the number of observed events in data for the specified selection regions prior to the requirement on mass. The background estimates show statistical and systematic uncertainties.	134
533			
534			
535			
536			
537	Table 14	The left and right extremum of the mass window for each generated mass point with a 10 ns lifetime.	135
538			
539	Table 15	The left and right extremum of the mass window used for each generated stable mass point.	135
540			
541	Table 16	The expected number of signal events, the expected number of background events, and the observed number of events in data with their respective statistical errors within the respective mass window for each generated stable mass point	136
542			
543			
544			
545			
546	Table 17	The expected number of signal events, the expected number of background events, and the observed number of events in data with their respective statistical errors within the respective mass window for each generated mass point with a lifetime of 10 ns.	136
547			
548			
549			
550			
551	Table 18	The observed and expected 95% CL lower limit on mass for gluino R-Hadrons for each considered lifetime.	139
552			
553	Table 19	The left and right extremum of the mass window for each generated mass point with a 50 ns lifetime.	146
554			
555	Table 20	The left and right extremum of the mass window for each generated mass point with a 30 ns lifetime.	146
556			
557	Table 21	The left and right extremum of the mass window for each generated mass point with a 10 ns lifetime.	147
558			
559	Table 22	The left and right extremum of the mass window used for each generated mass point with a lifetime of 3 ns.	147
560			
561	Table 23	The left and right extremum of the mass window used for each mass point with a lifetime of 1 ns.	147
562			
563	Table 24	The left and right extremum of the mass window for each generated mass point with a lifetime of 0.4 ns.	148
564			
565	Table 25	The left and right extremum of the mass window used for each generated stable mass point.	148
566			

567	Table 26	The expected number of signal events, the expected number of background events, and the observed number of events in data with their respective statistical errors within the respective mass window for each generated mass point with a lifetime of 50 ns.	148
568			
569			
570			
571			
572	Table 27	The expected number of signal events, the expected number of background events, and the observed number of events in data with their respective statistical errors within the respective mass window for each generated mass point with a lifetime of 30 ns.	149
573			
574			
575			
576			
577	Table 28	The expected number of signal events, the expected number of background events, and the observed number of events in data with their respective statistical errors within the respective mass window for each generated mass point with a lifetime of 10 ns.	149
578			
579			
580			
581			
582	Table 29	The expected number of signal events, the expected number of background events, and the observed number of events in data with their respective statistical errors within the respective mass window for each generated mass point with a lifetime of 3 ns.	150
583			
584			
585			
586			
587	Table 30	The expected number of signal events, the expected number of background events, and the observed number of events in data with their respective statistical errors within the respective mass window for each generated mass point with a lifetime of 1 ns.	150
588			
589			
590			
591			
592	Table 31	The expected number of signal events, the expected number of background events, and the observed number of events in data with their respective statistical errors within the respective mass window for each generated mass point with a lifetime of p4 ns.	151
593			
594			
595			
596			
597	Table 32	The expected number of signal events, the expected number of background events, and the observed number of events in data with their respective statistical errors within the respective mass window for each generated stable mass point	151
598			
599			
600			
601			

602 LISTINGS

603 ACRONYMS

- 604 SM Standard Model
605 CERN European Organization for Nuclear Research
606 SUSY Supersymmetry
607 MSSM Minimal Supersymmetric Model
608 cMSSM Constrained MSSM
609 pMSSM Phenomenological MSSM
610 LSP Lightest Supersymmetric Particle
611 LHC Large Hadron Collider
612 ATLAS A Toroidal LHC ApparatuS
613 CMS Compact Muon Solenoid
614 ALICE A Large Ion Collider Experiment
615 LHCb Large Hadron Collider beauty experiment
616 LEP the Large Electron Positron collider
617 PS Proton Synchrotron
618 PSB Proton Synchrotron Booster
619 SPS Super Proton Synchrotron
620 SCT silicon microstrip
621 TRT Transition Radiation Tracker
622 LAr liquid argon
623 EM electromagnetic
624 RPC Resistive Plate Chamber
625 TGC Thin Gap Chamber
626 MDT Monitored Drift Tube
627 CSC Cathode Strip Chamber
628 ToT time over threshold
629 RoI Region of Interest

- 630 LCW local cluster weighted
631 MIP minimally ionizing particle
632 IP impact parameter
633 EPJC European Physical Journal C
634 JES jet energy scale
635 LLP Long-Lived Particle
636 CR Control Region
637 NLO next-to-leading order
638 NLL next-to-leading logarithmic
639 PDF parton distribution function
640 ISR initial state radiation
641 RMS root mean square
642 IBL Insertible B-Layer
643 CP Combined Performance
644 MDT Monitored Drift Tube
645 RF radiofrequency
646 HLT high level trigger
647 QCD quantum chromodynamics
648 BSM beyond the Standard Model

649

PART I

650

INTRODUCTION

651

You can put some informational part preamble text here.

652

653 INTRODUCTION

654 As of 2012, with the discovery of the Higgs boson, the **SM** provides a complete
655 and validated description of the interactions of fundamental particles. It de-
656 scribes a remarkable range of phenomena given its simple foundation, and has
657 been successful in explaining high energy physics in all experiments yet per-
658 formed. However, it is clear that the picture is incomplete: without a descrip-
659 tion of gravity or an explanation for dark matter, an extension is necessary to
660 describe new physics at higher energies. These deficiencies motivate a wide
661 range of experiments that search for new physics. The **LHC** provides the high-
662 est energy approach, seeking to discover unobserved particles or interactions in
663 high energy proton collisions.

664 The experiments at the **LHC** have searched for a wide range of new phenomena
665 in the years since collisions began in 2010. A major focus of these searches has
666 been on Supersymmetry (**SUSY**), an extension to the **SM** which has the potential
667 to ameliorate many of its shortfalls. None of the searches have found evidence of
668 new physics, and between them they have begun to rule out a number of models
669 that would predict new particles at the TeV scale. This motivates searches for
670 more exotic signals that may have been missed, using analysis techniques that
671 provide additional reach for the more specific cases.

672 This dissertation presents a search for Long-Lived Particles (**LLPs**) using the
673 13 TeV collisions collected during 2015 at the **LHC**. Charged **LLPs** are predicted
674 to exist in a subset of **SUSY** models, and have dramatically different detector sig-
675 natures than both **SM** processes and other **SUSY** models. This search focuses on
676 isolating that unique signature using ionization in the ATLAS detector.

677 Part **II** provides the theoretical context and motivation for a search for new
678 physics in high energy collisions. Chapter **2** outlines the basic framework of the
679 **SM** and describes its particles and interactions. It also discusses the limitations
680 of the **SM** that motivate the existence of new physics. Chapter **3** discusses on
681 possible solution to the shortcomings of the **SM**, the theory of Supersymmetry,
682 and the ways that it can generate **LLP**.

683 Part **III** discusses the structure of the accelerator complex that provides col-
684 lisions as well as the experiment that measures them. Chapter **4** summarizes
685 the design and performance of the **LHC** and the features of the proton-proton
686 collisions it produces. Chapter **5** then discusses the components of the ATLAS
687 detector and how they can be used to measure the particles produced in **LHC** col-
688 lisions. The part concludes with a description of the algorithms used to recon-
689 struct physics particles and processes from the electronic signals in the detector
690 in Chapter **6**.

691 Part **IV** presents a measurement of calorimeter response, an important compo-
692 nent of event reconstruction used in many physics analyses. Chapter **7** describes
693 a direct, in situ measurement of calorimeter response using isolated hadrons, and

694 investigates the modeling of that response in simulation. Chapter 8 uses those
695 measurements to construct a correction for the energy for jets in simulation, the
696 JES, and to estimate an uncertainty for that correction.

697 Part V details the search for LLPs. It begins with a discussion of the simulation
698 of LLPs in ATLAS, focusing on the detector signatures and how they vary with
699 the properties of those particles in Chapter 9. Then Chapter 10 discusses the
700 strategy of the search and the requirements used to select LLPs and to reject SM
701 backgrounds. Chapter 11 explains a method for predicting the background from
702 SM processes, and shows a validation of the technique. Chapter 12 describes the
703 systematic uncertainties on both the selection efficiency for signal events and
704 the background method. The results of the search are presented in Chapter 13.

705

PART II

706

THEORETICAL CONTEXT

707

You can put some informational part preamble text here.

708

709 STANDARD MODEL

710 The SM of particle physics seeks to explain the symmetries and interactions of
 711 fundamental particles. The SM provides predictions in particle physics for in-
 712 teractions up to the Planck scale (10^{15} – 10^{19} GeV). It has been tested by several
 713 generations of experiments and has been remarkably successful; no significant
 714 deviations from its predictions have been found.

715 The theory itself is a quantum field theory grown from an underlying sym-
 716 metry, $SU(3) \times SU(2) \times U(1)$, that generates all of the interactions consistent
 717 with experimental observations. These interactions are referred to as the Strong,
 718 Weak, and Electromagnetic forces. Each postulated symmetry necessitates the
 719 existence of an associated conserved charge, which appear as properties of the
 720 observed particles in nature.

721 Although this model has been very predictive, the theory is incomplete; for
 722 example, it is not able to describe gravity or astronomically observed dark mat-
 723 ter. These limitations suggest a need for an extension or new theory to describe
 724 physics at higher energies.

725 2.1 ACTION AND THE LAGRANGIAN

Originally, both action and the Lagrangian were constructed for an integral reformulation of the laws of classical mechanics, which is a purely mathematical step: any differential equation can be re-expressed in terms of an integral equation. The Lagrangian, \mathcal{L} , is classically given by the difference of kinetic energy and potential energy. The Lagrangian is defined this way so that the action, \mathcal{S} , given by

$$\mathcal{S}[\mathbf{q}(t)] = \int_{t_1}^{t_2} \mathcal{L}(\mathbf{q}, \dot{\mathbf{q}}, t) dt \quad (1)$$

726 returns the classical equations of motion when one requires it to be stationary
 727 in the path, $\mathbf{q}(t)$. This formulation of classical mechanics is extremely useful in
 728 calculations, and generalizes beautifully to cover all types of physics.

729 In particular, with the development of quantum mechanics in the twentieth
 730 century, the concepts of action and the Lagrangian were found to generalize to
 731 more complicated physics for which the classical laws do not hold. Quantum
 732 mechanics and quantum field theory can be constructed from the action, using
 733 the path integral formulation, by assuming that a particle undergoes all possible
 734 paths $\mathbf{q}(t)$ with an imaginary phase given by $e^{i\mathcal{S}[\mathbf{q}(t)]/\hbar}$. This reduces to classical
 735 mechanics in the limit as \hbar goes to zero, as all paths for which the action is not
 736 stationary interfere with each other so as to cancel their contributions. Because
 737 the wavefunction of a particle can be completely determined through the action

738 and the action depends only on the Lagrangian, the Lagrangian itself is sufficient
 739 to describe the physics governing the particle.

740 So, in both classical and quantum mechanics, the Lagrangian of a system con-
 741 tains everything there is to know about the system, apart from initial conditions.
 742 Thus, the most natural way to express that a system has a certain symmetry is to
 743 require that the Lagrangian is invariant under a corresponding symmetry trans-
 744 formation. This makes the Lagrangian the central piece of the discussion of
 745 gauge invariance; the mathematical representation of gauge invariance is that a
 746 gauge transformation on the appropriate components of the Lagrangian returns
 747 an identical Lagrangian. That is,

$$\mathcal{L}(\psi, D^\mu) = \mathcal{L}(U\psi, D'^\mu) \quad (2)$$

748 where ψ is the wavefunction and D^μ is the covariant derivative, both of which
 749 transform under a symmetry operation. There are a number of immediate and
 750 surprisingly powerful consequences of requiring that the Lagrangian is invariant
 751 under a symmetry operation.

752 2.2 GAUGE INVARIANCE AND FORCES

753 The simplest possible relativistic, quantum Lagrangian is the free Dirac Lagrangian,
 754 which describes a relativistic fermion in a vacuum.

$$\mathcal{L} = i\bar{\psi}\not{d}\psi - m\bar{\psi}\psi \quad (3)$$

755 A fermion denotes a particle with spin-1/2, and the kinematic term is chosen to
 756 correctly describe the free propagation of a fermionic particle with mass m . This
 757 equation is clearly invariant under a global $U(1)$ transformation, that is chang-
 758 ing ψ by a complex phase has no effect. The derivative operator commutes with
 759 a constant phase factor, and wherever ψ appears its complex conjugate also ap-
 760 pears so as to cancel out the change of phase. However, the Lagrangian as written
 761 is not invariant under the local $U(1)$ symmetry postulated for the [SM](#), which can
 762 be written as $U = e^{i\alpha(x)}$. The piece of the Lagrangian involving a derivative will
 763 return an extra term that will break the invariance of the Lagrangian under this
 764 transformation:

$$\begin{aligned} \mathcal{L}' &= i(\bar{\psi}U^\dagger)\not{d}(U\psi) - m(\bar{\psi}U^\dagger)(U\psi) \\ &= i(\bar{\psi}U^\dagger)U(\not{d} - \gamma^\mu\partial_\mu\alpha(x))\psi - m(\bar{\psi}U^\dagger)(U\psi) \\ &= i\bar{\psi}\not{d}\psi - m\bar{\psi}\psi - i\gamma^\mu\partial_\mu\alpha(x)\bar{\psi}\psi \\ &= \mathcal{L} - i\gamma^\mu\partial_\mu\alpha(x)\bar{\psi}\psi \\ &\neq \mathcal{L} \end{aligned}$$

765 So, in order to enforce the required symmetry, the typical approach is to con-
 766 struct a covariant derivative, that is to add a term to the derivative operator

so that the unwanted term in \mathcal{L}' is exactly canceled. A generic form for such a derivative is given by

$$D^\mu = \partial^\mu - iqA^\mu$$

where at this point A^μ is an arbitrary field that transforms under the $U(1)$ operator and q is a scaling factor. Adding this component to the above Lagrangian gives

$$\mathcal{L}' = i(\bar{\psi}U^\dagger)U(\not{d} - \gamma^\mu\partial_\mu\alpha(x) - iq\gamma^\mu A'_\mu)\psi - m(\bar{\psi}U^\dagger)(U\psi) \quad (4)$$

$$\mathcal{L}' = \mathcal{L} + \gamma^\mu(-i\partial_\mu\alpha(x) - iqA'_\mu + iqA_\mu)\bar{\psi}\psi \quad (5)$$

and because the transformation of A^μ is unspecified, $\mathcal{L} = \mathcal{L}'$ whenever

$$A'_\mu = A_\mu - \frac{1}{q}\partial_\mu\alpha(x)$$

The above procedure demonstrated that beginning with the Lagrangian for a free fermion and imposing a local $U(1)$ symmetry required the existence of a vector field A^μ , and specified its transformation under the $U(1)$ gauge group. The additional term in the derivative can be expanded to form a completely separate term in the Lagrangian,

$$\mathcal{L} = i\bar{\psi}\not{d}\psi - m\bar{\psi}\psi - (q\bar{\psi}\gamma^\mu\psi)A^\mu \quad (6)$$

and in this form it is clear that the A^μ term has the exact form of the electromagnetic interaction. That is, this is the Lagrangian which reproduces the relativistic form of Maxwell's equations for a particle interacting with an electromagnetic field. It is natural to also introduce a term to the Lagrangian at this point to describe the free propagation of the vector A field, where the propagation of a vector field has the form of

$$-\frac{1}{16\pi}F^{\mu\nu}F_{\mu\nu} \quad \text{with} \quad F_{\mu\nu} = \partial_\mu A_\nu - \partial_\nu A_\mu \quad (7)$$

This then also describes the electromagnetic interactions in a vacuum and the propagation of a photon. The photon is an example of a gauge boson, a spin-0 particle required to exist by a gauge symmetry of the Lagrangian and one that corresponds to a force. In summary, requiring the $U(1)$ symmetry was enough to recover all of electromagnetism and to predict the existence of a photon in the SM.

The interaction term that was placed into the Lagrangian by this procedure can be conveniently summarized with Feynman diagrams, which diagrammatically represent a transition from an initial state to a final state. All diagrams that start with the same initial state and end with the same final state must be considered, but more complicated diagrams can be built by linking together the simplest versions. A diagram that corresponds to the above term, $(q\bar{\psi}\gamma^\mu\psi)A^\mu$, is shown in Figure 1, for an interaction with a generic fermion.

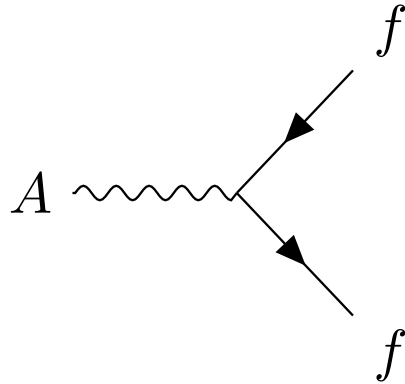


Figure 1: A Feynman diagram representing the interaction of the A field with a generic fermion, f .

797 2.2.1 $SU(2) \times U(1)$ AND THE ELECTROWEAK FORCE

798 The full picture of the electroweak section of the SM is more complicated than the
 799 simplified explanation of the electromagnetic piece described above. In practice,
 800 it is necessary to consider the entire $SU(2) \times U(1)$ symmetry together, but the
 801 procedure is the same. Enforcing the symmetry on the Lagrangian requires the
 802 introduction of a covariant derivative, this time with four total distinct terms,
 803 one for each of the generators of $SU(2) \times U(1)$. The result is a series of terms
 804 in the Lagrangian which describe the interaction of a fermion with four vector
 805 fields, the W_1 , W_2 , W_3 , and B fields. These fields can mix in the quantum sense,
 806 and linear combinations form the W^+ , W^- , Z , and A fields that are considered
 807 actual particles in the SM¹.

808 2.2.2 $SU(3)$ AND THE STRONG FORCE

809 The same procedure can be applied starting with the $SU(3)$ symmetry require-
 810 ment, where eight additional fields must be introduced, one for each of the gen-
 811 erators of $SU(3)$. The resulting Lagrangian describes quantum chromodynam-
 812 ics (QCD) and predicts the existence of eight gauge bosons known collectively as
 813 gluons.

814 2.3 NOETHER'S THEOREM, CHARGES, AND MATTER

815 Another direct consequence of the symmetries stipulated in the SM are a series
 816 of conserved quantities, Noether charges, named after the mathematician and
 817 physicist Emmy Noether. The charges arise as a direct consequence of Noether's
 818 theorem, which can be informally stated as

¹ These states are the actual particles because they are mass eigenstates, but the full explanation of this will have to wait for the discussion of the Higgs mechanism.

819 *For every symmetry of the Lagrangian, there exists a corresponding phys-
820 ical quantity whose value is conserved in time.*

821 Or, stated another way, symmetries of the Lagrangian mathematically require
822 the conservation of specific quantities taken from the Lagrangian. This rela-
823 tionship can also be thought of as operating in the other direction, the exist-
824 ence of a conserved charge can be shown to generate the symmetry in the La-
825 grangian. This theorem is actually quite striking in a somewhat unexpected re-
826 lation between simple geometric symmetries and physically observable conser-
827 vation laws. For example, the theorem connects the translation invariance of
828 the Lagrangian in space to the conservation of momentum and the translation
829 invariance in time to the conservation of energy.

830 In the context of the SM, the required symmetries of $U(1) \times SU(2) \times SU(3)$
831 correspond to the charges that are considered properties of all elementary par-
832 ticles. The most familiar of these properties is the electric charge, Q , which is
833 one of the conserved quantities of $SU(2) \times U(1)$. The remaining pieces of
834 $SU(2) \times U(1)$ correspond to weak isospin, T and T_3 , where T has only non-
835 negative values and T_3 can be positive and negative. The $SU(3)$ symmetry is
836 generated by the three colors of QCD, red, green, and blue, each with a corre-
837 sponding opposite color, anti-red, anti-green, and anti-blue.

838 The matter in the observable universe consists of a collection of particles which
839 carry these charges, in addition to spin and mass. The particles typically thought
840 of as matter are all fermions: particles with spin-1/2. All of the fermions belong
841 to one of two groups, quarks and leptons, and one of three generations. Each
842 of the generations have similar properties but significantly different masses; the
843 particles in consecutive generations have increasing mass. Quarks are distin-
844 guished from leptons in that they carry color charge, in addition to electric charge
845 and weak isospin. The particles in the SM are summarized in Figure 2, and the
846 matter particles are the twelve types of fermions displayed on the left side of the
847 graphic.

848 2.3.1 QUARKS

849 The three generations of quarks each have a particle with electric charge +2/3
850 and one with charge -1/3. They are referred to us up and down, charm and
851 strange, and top and bottom respectively, and these are referred to as the quark
852 flavors. Although Figure 2 only shows these six flavors, there is a unique particle
853 for each combination of the three colors and flavor. And each quark has an anti-
854 particle with the opposite electric and color charge values.

855 However, individual quarks are never observed in nature, but instead form
856 color-neutral bound states. One way to form a color neutral combination is a
857 bound state of three quarks with three different color charges, called a baryon.
858 Baryons are the most common type of quark configuration in conventional mat-
859 ter, and include protons and neutrons. The other common configuration is a
860 bound state of a quark and an anti-quark, called a meson, where the two quarks
861 have the same type but opposite colors. The conservation of the various charges
862 carried by quarks, along with the requirement that quarks appear in color-neutral

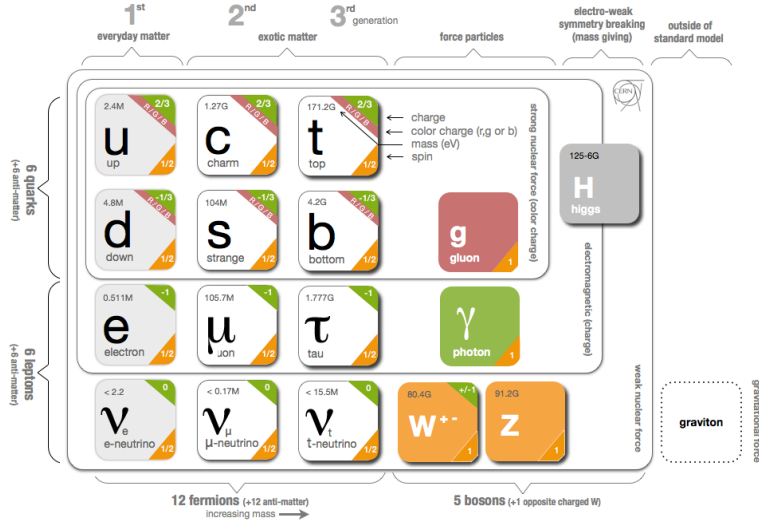


Figure 2: The particle content of the SM.

863 states, result in the observed conservation of baryon number, B , where baryons
 864 have $B = 1$ and mesons have $B = 0$.

865 2.3.2 LEPTONS

866 The remaining fermions, the leptons, do not carry color charge. Each generation
 867 contains an electrically charged lepton, the electron, muon, and tau, and an elec-
 868 trically neutral lepton called a neutrino. For the charged leptons, the flavors are
 869 mass eigenstates, with the masses listed in Figure 2. The flavors of the neutrinos,
 870 on the other hand, are not mass eigenstates: they propagate in mass eigenstates
 871 and so can oscillate between different flavors. The absolute masses of the neu-
 872 trinos are not currently known, but the phenomenon of oscillations shows that
 873 they have three different mass values. Although there is no direct conservation
 874 law resulting from the symmetries of the SM Lagrangian, no interactions have
 875 been observed which alter lepton number, L , the difference in the number of lep-
 876 tons and anti-leptons.

877 2.3.3 CHIRALITY

878 All of the fermions described above have two possible values of the magnitude
 879 of weak isospin, T , either 0 or $1/2$. The fermions with $T = 0$ are called right-
 880 handed, while those with $T = 1/2$ are called left-handed. For left-handed fermions,
 881 each of the quark and lepton generations have one particle with $T_3 = -1/2$ and
 882 one with $T_3 = +1/2$. The neutrinos have $T_3 = +1/2$, while the charged leptons
 883 have $T_3 = -1/2$. Similarly, the positively charged quarks have $T_3 = +1/2$ and the
 884 negatively charged quarks have $T_3 = -1/2$. Because the right-handed neutrinos
 885 would have no charge of any type, it is not clear if they exist at all.

886 2.4 HIGGS MECHANISM AND MASS

887 The description of the electroweak forces above left out an important part of the
 888 observed nature of the electroweak force. Many physical experiments observed
 889 phenomena corresponding to the interaction of the weak bosons that were best
 890 explained if they had significant masses. A large mass for the W and Z bosons
 891 would explain the relative weakness of their interactions compared to the elec-
 892 tromagnetic field. The Lagrangian's discussed above did not include a mass term
 893 for the gauge bosons, and in fact such a term would not be allowed by the require-
 894 ment of gauge invariance. This was a significant problem for the **SM**, and the
 895 symmetry of the electroweak sector would have to be broken in order to allow
 896 for non zero masses for some of the gauge bosons.

897 One mechanism to allow for this spontaneous symmetry breaking is the Higgs
 898 mechanism, which posits the existence of an additional scalar field. It begins
 899 with a $SU(2) \times U(1)$ invariant Lagrangian of the form

$$\mathcal{L} = |D_\mu \phi|^2 - \frac{1}{2}\mu^2\phi^+\phi - \frac{1}{4}\lambda(\phi^+\phi)^2 \quad (8)$$

900 where ϕ is the new scalar field and, importantly, μ^2 is negative. This leads to a
 901 minimum value of the field at a non-zero value of ϕ , specifically where

$$\langle \phi \rangle = \frac{1}{\sqrt{2}} \begin{pmatrix} 0 \\ v \end{pmatrix} \quad \text{with} \quad v = \frac{2\mu^2}{\lambda} \quad (9)$$

902 Expanding the original Lagrangian about its expectation value,

$$\langle \phi \rangle = \frac{1}{\sqrt{2}} \begin{pmatrix} 0 \\ v + H \end{pmatrix} \quad (10)$$

903 gives potential terms in the Lagrangian like

$$\mathcal{L}_H = -\frac{1}{2}m_H^2 H^2 - \sqrt{\frac{\lambda}{2}}m_H H^3 - \frac{1}{4}\lambda H^4 \quad (11)$$

904 where $m_H = \sqrt{2}\mu$. The form of this Lagrangian shows that the non-zero ex-
 905 pectation value of the ϕ field has introduced a massive scalar field H with self
 906 interaction terms. It has an additional important consequence on the description
 907 of the gauge bosons, through the expansion of the term involving the covariant
 908 derivative:

$$|D_\mu \phi|^2 \supset \frac{1}{8} (g^2(W_{1\mu}W_1^\mu + W_{2\mu}W_2^\mu) + (g'B_\mu - gW_3\mu)^2) \quad (12)$$

909 where the W_i and B fields are the original $SU(2) \times U(1)$ gauge fields men-
 910 tioned previously. The above equation can be rearranged using linear combina-
 911 tions of the fields to from mass terms for the gauge bosons, and the mass eigen-
 912 states are exactly the W^\pm , Z , and A fields. Only the A field, corresponding to

913 the photon, results in a zero mass, and the remaining three fields acquire masses.
 914 Because the originally introduced Lagrangian, written in terms of ϕ , was clearly
 915 gauge invariant, this resulting configuration must also be gauge invariant.

916 This is the Higgs mechanism, where the introduction of a gauge invariant
 917 scalar field with a non-zero expectation value can generate masses for the gauge
 918 bosons without violating the underlying symmetries. The particle that is asso-
 919 ciated with the perturbations of this field, H , is called the Higgs boson, and is
 920 said to generate the masses of the remaining bosons. The resulting masses are
 921 listed in Figure 2. Because this mechanism was so successful in describing the
 922 observed properties of the W and Z bosons, it has been considered part of the
 923 SM for decades, although the actual Higgs boson was only recently observed in
 924 2012, confirming the theory.

925 The Higgs mechanism is also responsible for generating the masses of the
 926 fermions. The original mass terms that were listed in the Lagrangian for fermions
 927 are replaced with Yukawa coupling terms, which introduce interactions between
 928 the ϕ field and the fermions. Like with the gauge bosons, the non-zero expec-
 929 tation value of the field yields mass terms, and the expansion about that value
 930 introduces interaction terms between the fermions and the Higgs boson. The
 931 masses are different between each fermion because each has a different Yukawa
 932 coupling, which results in the masses listed in Figure 2.

933 2.5 PHENOMENOLOGY

934 The SM Lagrangian described above contains all of the information necessary
 935 to describe particle physics through the path integral formulation. However, a
 936 tremendous amount of complexity emerges from that description because of the
 937 diverse allowed interactions between the ensemble of particles in the SM. A qual-
 938 itative understanding of the phenomenology produced by those interactions is
 939 immensely helpful in understanding the analysis of particle physics.

940 2.5.1 ELECTROWEAK PHYSICS

941 The masses of the W and Z bosons result in significantly different processes
 942 for the weak fields than the electromagnetic field, despite their interactions be-
 943 ing similar before symmetry breaking. The massless photon is stable, and can
 944 propagate in a vacuum, resulting in the familiar long range interactions of elec-
 945 tromagnetism. The W and Z bosons, however, are unstable, as they have large
 946 enough masses to decay to fermions, such as the decays shown in Figure 3. For
 947 this reason, photons can be observed directly, while the other bosons are suffi-
 948 ciently short-lived that they can only be measured from their decay products.

949 Because the W and Z bosons interact with both quarks and leptons, they are
 950 responsible for the production of leptons in proton-proton collisions. Z bosons
 951 produce pairs of opposite sign, same flavor leptons. W bosons, on the other hand,
 952 produce a single lepton and the corresponding neutrino.

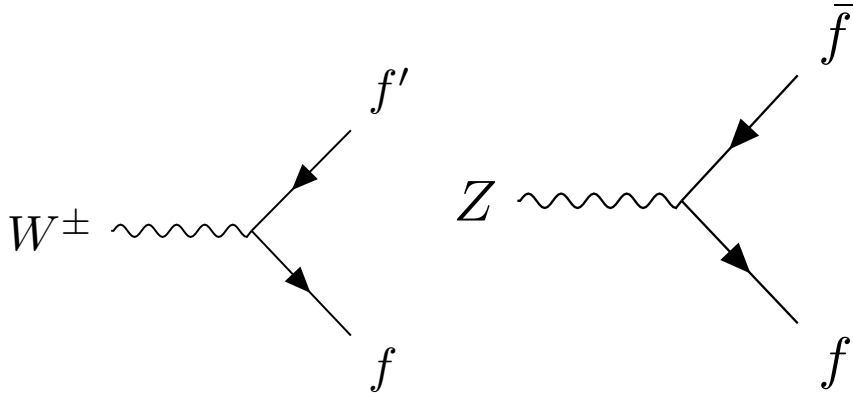


Figure 3: The Feynman diagrams representing the decays of the W and Z bosons to fermions. Here f indicates a generic fermion, \bar{f} its antiparticle, and f' the partner of that fermion in the same generation.

953 2.5.2 STRONG PHYSICS

954 The phenomenology of the strong sector differs significantly from the weak sec-
 955 tor because the gluons are massless but color charged. Because of this, gluons
 956 can interact with each other, and contributions from multiple gluon interactions
 957 lead to a significant growth in the strength of the field at low energies. The depen-
 958 dence of the field strength on the energy scale is described by renormalization,
 959 and in [QCD](#) the coupling is only small at high energies. Above around the GeV
 960 scale, the interactions of quarks become perturbative, similar to the electroweak
 961 fields; this phenomenon is known as asymptotic freedom.

962 At lower energies, however, the strength of the strong interaction is so signif-
 963 icant that the interactions of color-charged particles create additional particles
 964 until they form neutral bound-states. This process is known as hadronization,
 965 and explains why no quarks are observed isolated in nature: they all form bound
 966 states of hadrons like protons, neutrons, and pions. The hadronization process
 967 can produce a significant number of particles, so that a single energetic quark
 968 recoiling against another quark can generate a cascade of dozens of hadrons.
 969 Because of the initial boost of such an energetic configuration, the resulting
 970 hadrons are collimated, and conical spray of particles often referred to as a jet.

971 2.5.3 PROTON-PROTON COLLISIONS

972 Proton-proton collisions are a convenient way to generate high energy interac-
 973 tions to probe the [SM](#) and to search for new physics. At the energies that will be
 974 discussed in this analysis, the substructure of the protons is very important to the
 975 description of the resulting interactions. At lowest order, protons are composed
 976 of two up quarks and one down quark, but this description is incomplete. The
 977 actual bound state includes a chaotic sea of additional quarks and gluons, each of
 978 which carries a variable fraction of the proton's energy. When a proton-proton

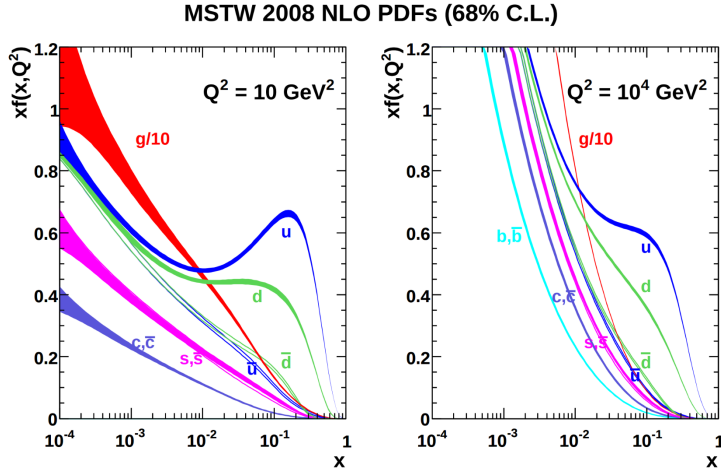


Figure 4: The PDFs for proton-proton collisions at $Q^2 = 10 \text{ GeV}^2$ and $Q^2 = 10^4 \text{ GeV}^2$. Each shows the fraction of particles which carry a fraction x of the total proton energy at the specified scale [1].

979 collision takes place, it is these constituents that interact with each other, resulting
 980 in a highly variable collision energy even when the proton-proton energy is
 981 consistent.

982 The fraction of the energy carried by each constituent varies moment to moment,
 983 but can be modelled probabilistically by PDFs. These are difficult to predict
 984 theoretically, as the QCD calculations are extremely complex, and instead
 985 are measured in hard-scattering experiments. They are usually represented by
 986 how often a given type of particle carries a fraction x of the total proton energy.
 987 Those fraction change significantly with the scale of the interaction; the PDFs of
 988 proton-proton collisions at both $Q^2 = 10 \text{ GeV}^2$ and $Q^2 = 10^4 \text{ GeV}^2$ are shown
 989 in Figure 4.

990 2.6 LIMITATIONS

991 Despite the great success of the relatively simple SM in describing such a broad
 992 range of emergent phenomena, it is clear that the picture it presents of the interactions
 993 of fundamental particles is incomplete. The SM contains concerning
 994 coincidences that suggest a more ordered underlying substructure that is not ex-
 995 pressed in the current form. It also fails to explain a number of cosmological
 996 measurements of the nature of matter in the universe. These limitations suggest
 997 the need for new, beyond the Standard Model (BSM) physics that would provide
 998 a more complete description at higher energies.

999 2.6.1 THEORETICAL CONCERNs

1000 There have been no successful integrations of the SM's description of the elec-
 1001 troweak and strong forces with the description of gravity, and it is still unclear
 1002 how to account for the effects of gravity at the Planck scale of approximately

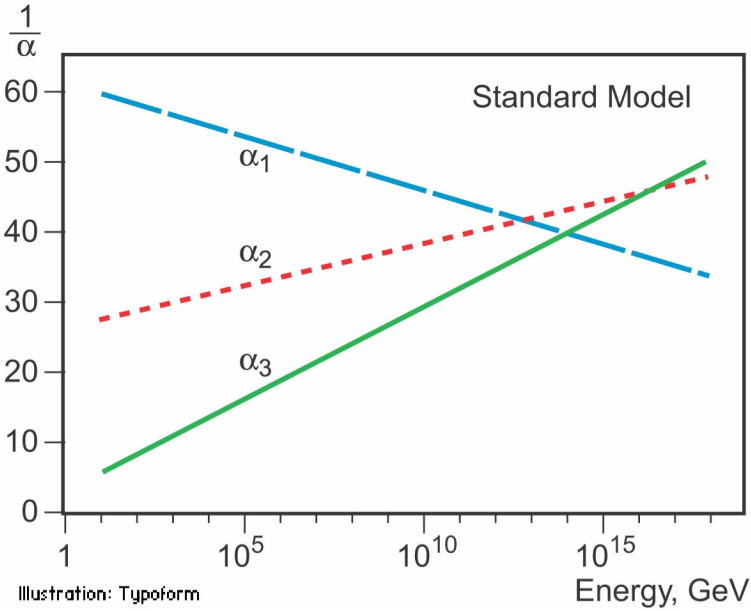


Figure 5: An approximation of the running of the coupling constants in the SM up to the Planck scale [unification_plot].

1003 10^{19} GeV, where it can no longer be ignored. The Planck scale is an important
 1004 cutoff for the SM, as it is clear that the SM must break down somewhere between
 1005 the current highest energy tests of the SM, around 1 TeV, and the Planck scale.

1006 One example of this is the Higgs mass, which is determined in the SM by a
 1007 sum of its bare mass and the interactions in the vacuum with all massive parti-
 1008 cles. As their must be new physics at the Planck scale to describe gravity, some
 1009 of those corrections would include contributions at a scale seventeen orders of
 1010 magnitude above the mass of the Higgs. Either the bare mass of the Higgs boson
 1011 precisely cancels those contributions to leave a remainder seventeen orders of
 1012 magnitudes smaller, or a new theory exists at a lower scale the shields the Higgs
 1013 mass from those terms. A theory where such a unlikely cancellation of free pa-
 1014 rameters occurs is called fine-tuned, and one that is free from such cancellations
 1015 is called natural. Theories where the mass of the Higgs is natural are usually pre-
 1016 ferred, as the suggest an underlying, coherent structure. The enormous differ-
 1017 ence in scales between the weak scale (including the Higgs mass), and the Planck
 1018 scale, is often referred to as the hierarchy problem.

1019 There is also a compelling argument that the $SU(3) \times SU(2) \times U(1)$ gauge
 1020 structure of the SM might originate from a single, unified gauge theory. For ex-
 1021 ample, it is possible to represent that gauge structure as a $SU(5)$ gauge group
 1022 with only a few inconsistencies with the current implementation. This unifica-
 1023 tion is suggested by the scaling of the coupling constants for each of the forces
 1024 under renormalization; they come close to converging to a single value at higher
 1025 energies, as seen in Figure 5. An additional correction to the scaling of the cou-
 1026 pling constants from new physics above the TeV scale could cause them to merge
 1027 into a single value at high energies.

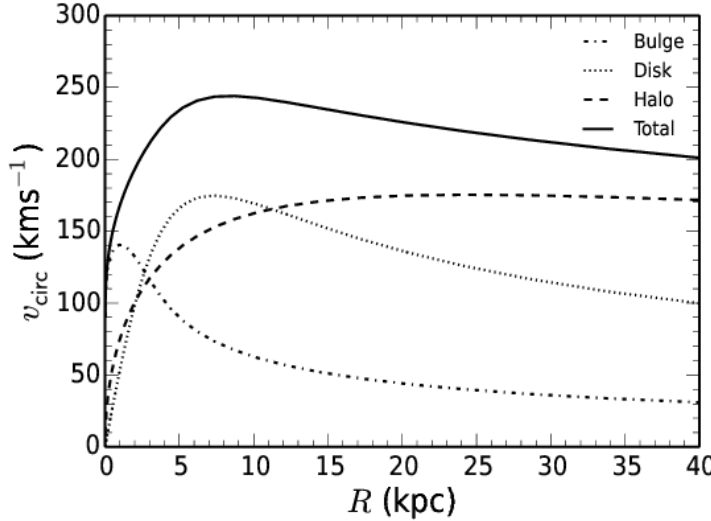


Figure 6: The distribution of velocities of stars as a function of the radius from the center of the galaxy. The contributions to the velocity from the various components of matter in the galaxy are shown [2].

1028 2.6.2 COSMOLOGICAL OBSERVATIONS

1029 The SM contains a symmetry in the description of matter and antimatter that is
 1030 not reflected in cosmological observations. The process of the standard model
 1031 create or remove matter and antimatter in equal amounts, so a universe that be-
 1032 gins with an equal quantity of each should result in a universe with an approxi-
 1033 mate balance of matter and antimatter. However, cosmological observations of
 1034 the relative amount of each type clearly show that the directly observable mass
 1035 of the universe is overwhelmingly made of matter. As this difference is largely
 1036 a difference in the generation of baryons and anti-baryons, this discrepancy is
 1037 often referred to as the baryogenesis problem.

1038 A number of astrophysical observations of large scale gravitational interac-
 1039 tions suggest the presence of a significant amount of non-luminous matter that
 1040 interacts with the normal matter only gravitationally. The first evidence of this
 1041 came from the observation of galactic rotation curves, the velocities of stars as
 1042 a function of the radius from the center of a galaxy. These can be directly pre-
 1043 dicted from the amount of matter contained within the sphere up to the radius
 1044 of the star. An estimate based only on the luminous matter in the galaxies would
 1045 predict a dependence that falls off with the radius, but the observed curves show
 1046 a mostly constant distribution of velocities [2], as seen in Figure 6. The higher
 1047 velocities than predicted by the luminous matter can be explained by a halo of
 1048 dark matter that extends significantly outside the galactic disk.

1049 This dark matter accounts for a majority of the matter in the universe, and is
 1050 incompatible with the matter particles predicted by the SM. Many observations
 1051 support its existence, but there have been no direct detections of a particle which
 1052 could account for the large quantity of gravitationally interacting dark matter.
 1053 The SM would have to require a significant extension to include the particles

1054 needed to explain dark matter and the processes needed to explain the observed
1055 matter-antimatter asymmetry.

1056

1057 SUPERSYMMETRY

1058 The theory of [SUSY](#) presents an extension to the [SM](#) that solves a number of the
 1059 outstanding issues. It is based on another proposed symmetry, one which intro-
 1060 duces an equality between the fermionic particles and proposed bosonic part-
 1061 ners. The symmetry is defined by extending spacetime into a superspace, which
 1062 includes one dimension that describes a particle's spin: a transformation in this
 1063 space moves a fermion with spin-1/2 to a boson with spin-0 or vice-versa. Re-
 1064quiring the [SM](#) to be symmetrical under these transformations requires the ex-
 1065istence of a bosonic partner for every current matter fermion in the [SM](#) and a
 1066 fermionic partner for every boson. The partners are called superparticles (spar-
 1067 ticles), where quarks partner with squarks and leptons partner with sleptons, and
 1068 each boson has a fermionic partner called a gaugino, such as the wino for the W
 1069 boson. The superpartners, in the original form of the theory, should be identical
 1070 to the original particle in every way except for spin; that is they would have the
 1071 same quantum charges and the same mass.

1072 However, the simplest version of the theory, where the symmetry is unbro-
 1073 ken, is incompatible with current observations of physics in a number of sys-
 1074 tems. The most striking example comes from the electron, as the superpartner
 1075 of an electron would introduce a stable, negatively charged, and bosonic parti-
 1076 cle. Such a particle would drastically alter atomic properties by providing a way
 1077 to create atoms without the valence structure of electrons that results from the
 1078 Pauli exclusion principle for fermions. Various high energy physics measure-
 1079 ments have also confirmed the spin of the W and Z bosons, for example, and
 1080 a fermionic gaugino has never been produced at those masses. The solution to
 1081 this incompatibility with observation is to conjecture that the symmetry exists
 1082 but is spontaneously broken, where the masses of the supersymmetric particles
 1083 are significantly larger than those of the current [SM](#) particles. Like the sponta-
 1084 neous symmetry breaking of the electroweak system, this symmetry breaking
 1085 can be accomplished by introducing an additional Higgs mechanism.

1086 3.1 STRUCTURE

1087 There are a number of ways to model the particulars of [SUSY](#), but many of the
 1088 resulting phenomena are similar, and a discussion of an example is sufficient
 1089 to describe the structure and results of the theory. The [MSSM](#) is one example of
 1090 a complete description that includes the necessary symmetry breaking to result
 1091 in the different masses between particles and sparticles [3]. It is called minimal
 1092 because it is designed to use the simplest possible extension to the [SM](#) that incor-
 1093 portaes [SUSY](#). However even a minimal version includes a remarkable number of
 1094 free parameters, over 100, and the [MSSM](#) is often further constrained to include

Sector	Particles	Sparticles
Baryonic Matter	(u, d)	(\tilde{u}, \tilde{d})
	(c, s)	(\tilde{c}, \tilde{s})
	(t, b)	(\tilde{t}, \tilde{b})
Leptonic Matter	(ν_e, e)	$(\tilde{\nu}_e, \tilde{e})$
	(ν_μ, μ)	$(\tilde{\nu}_m u, \tilde{\mu})$
	(ν_τ, τ)	$(\tilde{\nu}_\tau, \tilde{\tau})$
Higgs	(H_u^+, H_u^0)	$(\tilde{H}_u^+, \tilde{H}_u^0)$
	(H_d^0, H_d^-)	$(\tilde{H}_d^0, \tilde{H}_d^-)$
Strong	g	\tilde{g}
Electroweak	(W^\pm, W^0)	$(\tilde{W}^\pm, \tilde{W}^0)$
	B^0	\tilde{B}^0

Table 1: The particles in the **SM** and their corresponding superpartners in the **MSSM**.

1095 fewer parameters in models such as the Phenomenological MSSM (**pMSSM**) and
 1096 the Constrained MSSM (**cMSSM**) [4].

1097 The theory includes a sparticle partner for every standard model particle, which
 1098 are listed in Table 1. To then provide the different masses for those sparticles, the
 1099 **MSSM** introduces a second Higgs interaction. The resulting scalar field, along
 1100 with the original Higgs field, generates five total particles, h^0 , the original Higgs
 1101 boson, A^0 , H^0 , and H^\pm , where the last two are electrically charged. These Higgs
 1102 bosons can mix with the supersymmetric gauginos to form a series of mass eigen-
 1103 states. These are usually referred to by the order of their masses, where the neu-
 1104 tral gauginos (neutralinos) are labelled $\tilde{\chi}_1^0, \tilde{\chi}_2^0, \tilde{\chi}_3^0$, and $\tilde{\chi}_4^0$. The charged gauginos
 1105 (charginos) are similarly labelled $\tilde{\chi}_1^\pm$ and $\tilde{\chi}_2^\pm$. Table 1, lists the gauginos which are
 1106 direct partners of the original gauge bosons in the **SM** rather than these resulting
 1107 mass eigenstates.

1108 In addition to the new particle content, the **MSSM** introduces new interactions
 1109 for the gauge bosons and gauginos. All interaction terms are added to the La-
 1110 grangian which describe the interaction of a gauge boson or gaugino with a par-
 1111 ticle or sparticle with the appropriate charge. Such terms include a few interac-
 1112 tions which would violate the observed $B - L$ symmetry that prevents proton
 1113 decay. Either the couplings on these terms must be fine-tuned to match the ex-
 1114 perimental limits on those decays, or an additional symmetry must be imposed
 1115 to exclude the terms. The **MSSM** and several other **SUSY** models choose to intro-
 1116 duce a new symmetry known as R-parity. Sparticles are R-parity odd while **SM**
 1117 particles are R-parity even. And by requiring that each term in the supersymmet-
 1118 ric Lagrangian conserves R-parity, it is enforced that sparticles are produced in
 1119 pairs.

1120 The conservation of R-parity removes the $B - L$ violating terms naturally
 1121 from the Lagrangian. The remaining terms include all of the interactions of the
 1122 **SM** where two of the particles are replaced with their **SUSY** partners, so that R-
 1123 parity is conserved in the interactions. This also has an important significance

in making the LSP, the $\tilde{\chi}_1^0$, stable, as it cannot decay to only SM particles without violating the conservation of R-parity. The heavier sparticles then decay in chains, emitting an SM particle in each step, and leave behind the LSP at the end of the chain.

3.1.1 SIMPLIFIED MODELS

The MSSM is just one example of a large suite of SUSY models with similar results. Each of those models can have hundreds of individual parameters that ultimately determine the masses and interactions of the supersymmetric particles. To avoid this complexity in making experimental measurements, the analyses of high energy collisions often rely on simplified models. These models focus on a single process predicted by a theory, and the observable parameters such as the mass of the particles and their lifetimes are controlled directly, rather than tuning the hundreds of underlying parameters. This allows straightforward simulation of a specific event topology with control over the parameters that most directly influence the experimental signatures.

Experimental analyses use these models to search for new physics and to set limits on the production rates for a given type of process with working points of a few observable parameters. As one example, a simplified model may specify pair production of gluinos where the free parameters are the mass of the gluino and the types and masses of the particles it can decay into. The small number of parameters allows the phase space to be searched in a grid by simulating events with a few examples for the parameters and interpolating between them. The resulting analysis can set cross sectional limits as a function of the simplified parameters, and this allows for an easy interpretation of the result in a number of SUSY models.

3.2 MOTIVATION

SUSY models, including The MSSM, ameliorate many of the issues in the SM discussed in Section 2.6. SUSY is particularly well motivated as a natural extension to the SM because the simple underlying assumption solves three major, seemingly unrelated concerns. And these benefits all require that at least some of the sparticles exist near the TeV scale, within the reach of modern collider experiments.

The first, a solution to the hierarchy problem, comes as a direct consequence of the introduction of massive superpartners for each SM particle. The contributions to the Higgs mass from the much higher energy Planck scale come from a series of loop diagrams in the SM, where each massive SM particle has a loop contribution. The introduction of superpartners generates a series of corresponding diagrams for correction to the Higgs mass, with opposite sign contributions because the superpartners have different spins. Those opposite sign contributions cancel the correction terms at high energies, leaving behind a correction to the Higgs mass that is at the same scale as the masses of the superpartners. If the

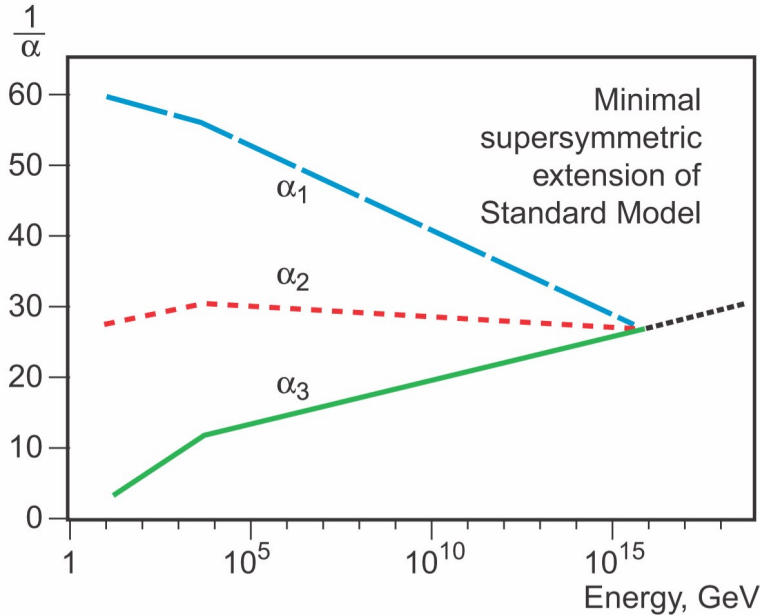


Figure 7: An approximation of the running of the coupling constants in the [SM](#) up to the Planck scale [[unification_plot](#)].

superpartners exist at the TeV scale, then the Higgs mass of 125 GeV can be explained without significant fine-tuning, and the theory becomes natural.

[SUSY](#) also has the potential to precisely enable the unification of the coupling constants at high energy. Without supersymmetric contributions, the coupling constants come close to a single value near the Planck scale suggesting an underlying trend, as shown in Figure 5, but they do not exactly merge. With the addition of the [MSSM](#), they join almost exactly at a single point, enabling a unification into a single gauge theory at high energy, as shown in Figure 7. This precise unification, like the naturalness argument, also requires that the masses of the superpartners be near the TeV scale.

The presence of R-parity in a [SUSY](#) model also provides an explanation for dark matter. The [LSP](#), as discussed in Section 3.1, is a massive, neutral, and stable particle as long as R-parity is conserved. In the early universe, when the energy density was extremely high, [LSPs](#) could be spontaneously produced just as often as other particles like photons, and would result in a thermal equilibrium. Then, as the universe cooled, the average energy would be too low to create additional [LSPs](#), and they would be left behind and only interact with the remaining matter gravitationally, a process called freeze out. Since those particles are stable, they would remain indefinitely. With the existence of an [LSP](#) at around the TeV scale, this process can explain the observed amount of dark matter in the universe.

Together, this variety of solutions to existing problems provides strong theoretical support for the existence of [SUSY](#) near the TeV scale. The [LHC](#) is the first collider experiment to be able to probe into TeV scale interactions, making it an exciting time to look for this extension to the [SM](#). A range of models have begun to be excluded with masses above 1 TeV [5], leading to a motivation to explore a

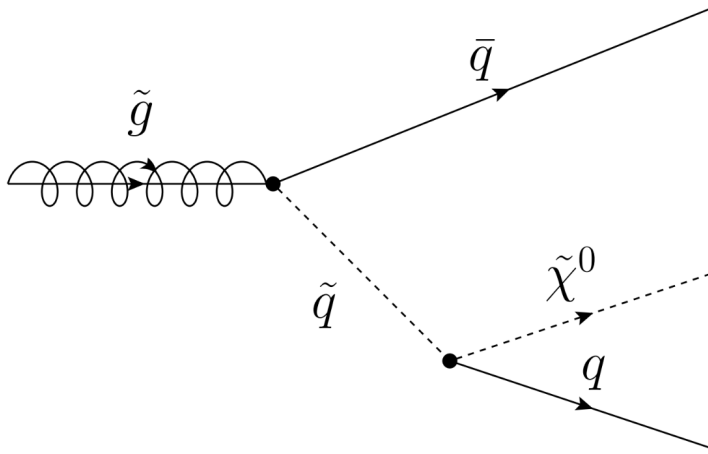


Figure 8: The decay of a gluino to quarks and an [LSP](#), which precedes through a squark.

1190 wider variety of models with phenomena that may have been missed by the most
 1191 direct search strategies.

1192 3.3 LONG-LIVED PARTICLES

1193 Some proposed [SUSY](#) models can produce [LLPs](#) other than just the [LSP](#). The most
 1194 direct search strategies for [SUSY](#) often assume that the various non-stable sparcles decay promptly, rather than propogating through some fraction of the de-
 1195 tector. Although the processes involved are very similar, the long-lifetime of
 1196 the produced particles can lead to very different experimental signatures, and
 1197 often require separate dedicated searches. It is important to design and execute
 1198 search strategies for [LLPs](#) in order to completely cover possible production of
 1199 new physics.
 1200

1201 There are a several ways to generate long lifetimes for the massive [SUSY](#) par-
 1202 ticles, depending on the specific model. In examples like Spread Supersymme-
 1203 try [6] and Split Supersymmetry [7, 8], the introduction of a split between two
 1204 mass scales supresses the decay of gluinos. In these and similar models, the
 1205 squarks are much heavier than the gluino, and the gluino must decay through
 1206 the production of a virtual squark, as shown in the diagram of Figure 8. The
 1207 large mass of the squarks in the split models suppresses the decay rate, and can
 1208 result in lifetimes of the order of 1 ns [6].

1209 Nearly degenerate particles is another mechanism that results in long life-
 1210 times, again by supressing decay rates. When a particle must decay to another
 1211 particle with nearly the same mass, the phase space factor in the decay results in
 1212 a low decay rate. For example, a neutron has a lifetime of roughly fifteen min-
 1213 utes because its mass is so close to the proton. Models which result in a nearly
 1214 degenerate chargino and [LSP](#) provide a long-lived chargino as well.

1215 Again, because of the wide variety of models which can produce [LLPs](#) and the
 1216 large number of parameters which determine their masses and lifetimes, the anal-
 1217 ysis presented here focuses on simplified models rather than assuming any par-

1218 ticular underlying theory. The models directly specify the decay mode of the
1219 LLPs as well as their masses and lifetimes, using a grid of values. The results of
1220 searches using these simplified models can be interpreted over a very wide range
1221 of models that predict LLPs, even including non-supersymmetric extensions to
1222 the SM.

1223

PART III

1224

EXPERIMENTAL STRUCTURE AND RECONSTRUCTION

1225

You can put some informational part preamble text here.

1226

1227 THE LARGE HADRON COLLIDER

1228 The LHC, a two-ring superconducting hadron accelerator, provides high energy
1229 proton-proton collisions for several large experiments at European Organiza-
1230 tion for Nuclear Research (CERN) in Geneva, Switzerland [9, 10]. It is the largest,
1231 highest-luminosity, and highest-energy proton collider ever built, and was con-
1232 structed by a collaboration of more than 10,000 scientists from the more than
1233 100 countries that contribute to CERN. The original design of the LHC focused on
1234 providing collision energies of up to 14 TeV and generating enough collisions to
1235 reveal physics beyond the SM which is predicted to exist at higher energy scales.

1236 The LHC was installed in an existing 27 km tunnel at CERN which was orig-
1237 inally designed to house the Large Electron Positron collider (LEP) [11]. This
1238 allows the collider to use existing accelerators at the same complex to provide
1239 the initial acceleration of protons up to 450 GeV before injecting into LHC. The
1240 injected hadrons are accelerated up to as much as 14 TeV while being focused
1241 into two beams traveling in opposite directions. During this process the protons
1242 circulate around the tunnel millions of times, while the beams are intermittently
1243 crossed at the four locations of the experiments to provide collisions. These col-
1244 lision points correspond to the four major LHC experiments: ATLAS, Compact
1245 Muon Solenoid (CMS), Large Hadron Collider beauty experiment (LHCb), and
1246 A Large Ion Collider Experiment (ALICE), and Figure 9 shows the layout of the
1247 experiments both on the surface and below. ATLAS and CMS are both general
1248 purpose, high-luminosity detectors which search for a wide range of new types
1249 of physics [12, 13]. LHCb studies the interactions of b-hadrons to explore the
1250 asymmetry between matter and antimatter [14]. ALICE focuses on the collisions
1251 of lead ions, which the LHC also provides, in order to study the properties of
1252 quark-gluon plasma [15].

1253 During the first five years of continued operation, after the LHC turned on in
1254 2010, the LHC has provided four major data collecting periods. In 2010 the LHC
1255 generated collisions at several energies, starting at 900 GeV. It increased the
1256 energy from 900 GeV to 2.76 TeV and then subsequently to 7 TeV, with a peak
1257 luminosity of $2 \times 10^{32} \text{ cm}^{-2}\text{s}^{-1}$, and a total delivered luminosity of 50 pb^{-1} .
1258 The next run, during 2011, continued the operation at 7 TeV and provided an
1259 additional 5 fb^{-1} with a peak luminosity of $4 \times 10^{33} \text{ cm}^{-2}\text{s}^{-1}$. The energy was
1260 then increased to 8 TeV for the data collection during 2012, which provided 23 fb^{-1}
1261 with a peak luminosity of $7.7 \times 10^{33} \text{ cm}^{-2}\text{s}^{-1}$. After the first long shutdown
1262 for 2013 and 2014, the LHC resumed operation and increased the energy to 13
1263 TeV in 2015, where it delivered 4.2 fb^{-1} with a peak luminosity of $5.5 \times 10^{33} \text{ cm}^{-2}\text{s}^{-1}$.
1264 The LHC is currently providing additional 13 TeV collisions in 2016 with higher
1265 luminosities than during any previous data collection periods. These running
1266 periods are summarized in Figure 10, which shows the total delivered

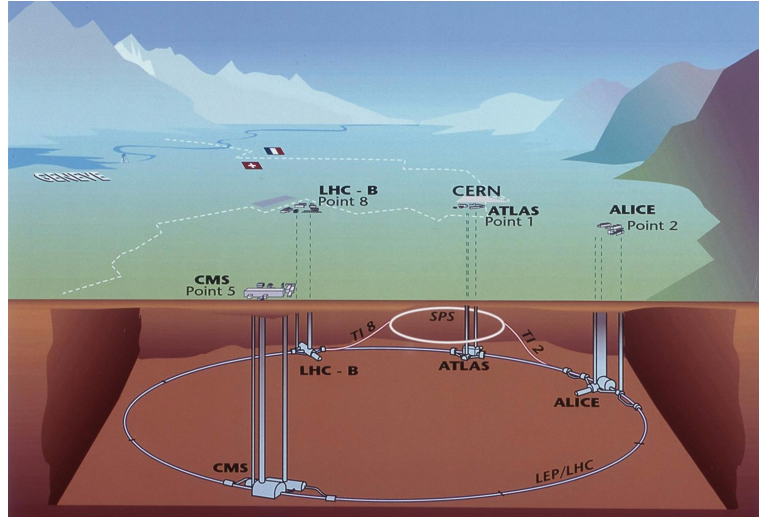


Figure 9: The four collision points and corresponding experiments of the [LHC](#). The image includes the location of the nearby city of Geneva as well as the border of France and Switzerland.

luminosity over time for the [ATLAS](#) experiment during each of the four years of data collection since 2011.

4.1 INJECTION CHAIN

The [LHC](#) takes advantage of the presence of previously built accelerators at [CERN](#) to work up to the target energy in consecutive stages. The series of accelerators that feed into the [LHC](#) are known collectively as the injection chain, and together with the [LHC](#) form the accelerator complex. The full complex is illustrated in Figure 11, which details the complex series required to reach collisions of 13 or 14 TeV.

Protons at the [LHC](#) begin as hydrogen atoms in the Linac 2, a linear accelerator which replaced Linac 1 as the primary proton accelerator at [CERN](#) in 1978. In Linac 2, the hydrogen atoms are stripped of their electrons by a strong magnetic field, and the resulting protons are accelerated up to 50 MeV by cylindrical conductors charged by radio frequency cavities. The protons are then transferred to the Proton Synchrotron Booster ([PSB](#)), which uses a stack of four synchrotron rings to accelerate the protons up to 1.4 GeV. Then the protons are injected into the Proton Synchrotron ([PS](#)) which again uses synchrotron rings to bring the energy up to 25 GeV. The intermediate step between Linac 2 and the [PS](#) is not directly necessary, as the [PS](#) can accelerate protons starting from as low as 50 MeV. The inclusion of the [PSB](#) allows the [PS](#) to accept a higher intensity of injection and so increases the deliverable luminosity in the [LHC](#). The penultimate stage of acceleration is provided by the Super Proton Synchrotron ([SPS](#)), a large synchrotron with a 7 km circumference that was commissioned at [CERN](#) in 1976. During this step the protons increase in energy to 450 GeV, after which they can be directly injected into the [LHC](#).

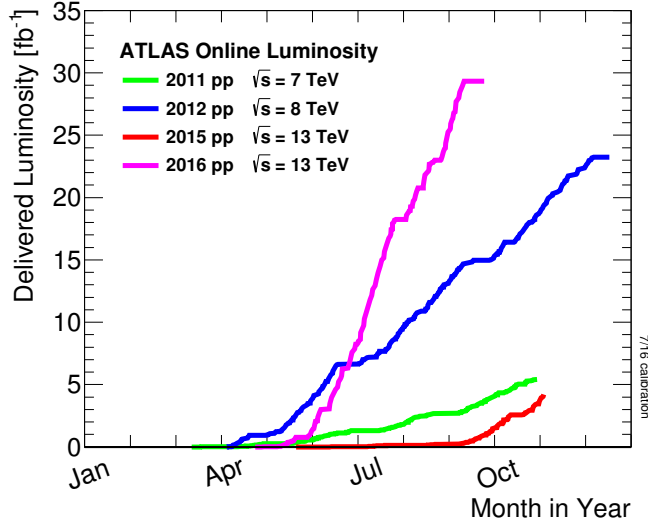


Figure 10: The cumulative luminosity over time delivered to the [ATLAS](#) experiment from high energy proton-proton collisions since 2011. The energies of the collisions are listed for each of the data-taking periods.

1292 The final step is the [LHC](#) itself, which receives protons from the [SPS](#) into two
 1293 separate beam pipes which circulate in opposite directions. The filling process
 1294 at this steps takes approximately 4 minutes, and the subsequent acceleration to
 1295 the final energy (6.5 TeV during 2015 and up to 7 TeV by design) takes approxi-
 1296 mately half an hour. At this point the protons circulate around the circumference
 1297 tens of thousands of times a second and continue for up to two hours.

1298 4.2 DESIGN

1299 4.2.1 LAYOUT

1300 Many of the aspects of the [LHC](#) design are driven by the use of the existing [LEP](#)
 1301 tunnel. This tunnel slopes gradually, with a 1.4% decline, with 90% of its length
 1302 built into molasse rock which is particularly well suited to the application. The
 1303 circumference is composed of eight 2987 meter arcs and eight 528 meter straight
 1304 sections which connect them; this configuration is illustrated in Figure 12. The
 1305 tunnel diameter is 3.7 m throughout its length.

The design energy is directly limited by the size of this tunnel, with its radius of curvature of 2804 m. A significant magnetic field is required to curve the protons around that radius of curvature; the relationship is given by

$$p \simeq 0.3BR \quad (13)$$

1306 where p is the momentum of the particle in GeV, B is the magnetic field in Tesla,
 1307 and R is the radius of curvature in meters. From the target design energy of
 1308 14 TeV, or 7 TeV of momentum for protons in each beam, the required mag-
 1309 netic field is 8.33 Tesla. This is too large a field strength to be practical with
 1310 iron electromagnets, because of the enormous power required and the resulting

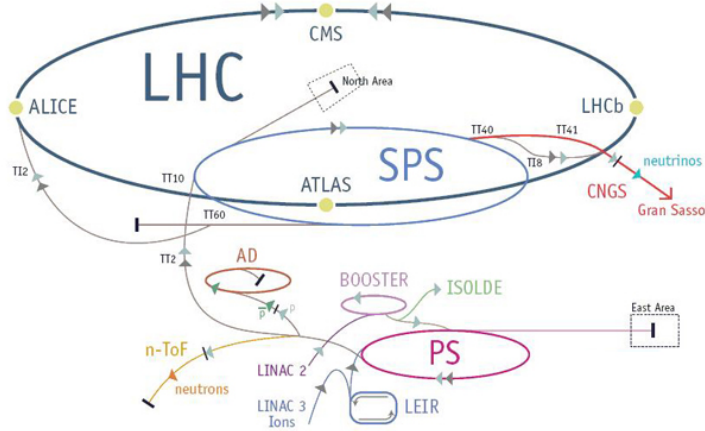


Figure 11: The accelerator complex that builds up to the full design energies at the LHC. The protons are passed in order to Linac 2, the PSB, the PS, the SPS and then the LHC.

1311 requirements for cooling. Because of these constraints, the LHC uses superconducting
 1312 magnets which can maintain that field strength with significantly less power consumption.
 1313

1314 4.2.2 MAGNETS

1315 The magnets chosen were Niobium and Titanium (NbTi) which allow for field
 1316 strengths as high as 10 Tesla when cooled down to 1.9 K. Reaching the target
 1317 temperature of 1.9 K for all of the magnets requires superfluid helium and a large
 1318 cryogenic system along the entire length of the tunnel. During normal operation,
 1319 the LHC uses 120 tonnes of helium within the magnets, and the entire system is
 1320 cooled by eight cryogenic helium refrigerators. The temperature increase that
 1321 occurs during transit from the refrigerator along the beam necessitates that the
 1322 refrigerators cool the helium down to 1.8 K. Any significant increase above this
 1323 temperature range can remove the superconductive properties of the magnets,
 1324 which in turn generates drastically larger heat losses from the current within the
 1325 magnets and causes a rapid rise in temperature called a quench.

1326 There are approximately 8000 superconducting magnets distributed around
 1327 the LHC. The 1232 bending magnets, which keep the protons curving along the
 1328 length of the beam, are twin bore cryodipoles, which allow both proton beams
 1329 to be accommodated by one magnet and all of the associated cooling structure.
 1330 Figure 13 shows the cross section of the design for these dipoles. The magnets
 1331 are very large, 16.5 m long with a diameter of 0.57 meters and a total weight of 28
 1332 tonnes. They are slightly curved, with an angle of 5.1 mrad, in order to carefully
 1333 match the beam path. The twin bore accommodates both magnets inside the
 1334 two 5 cm diameter holes which are surrounded by the superconducting coils.
 1335 The coils require 12 kA of current in order to produce the required magnetic
 1336 field. These coils are comprised of NbTi cable wound in two layers; the wire in

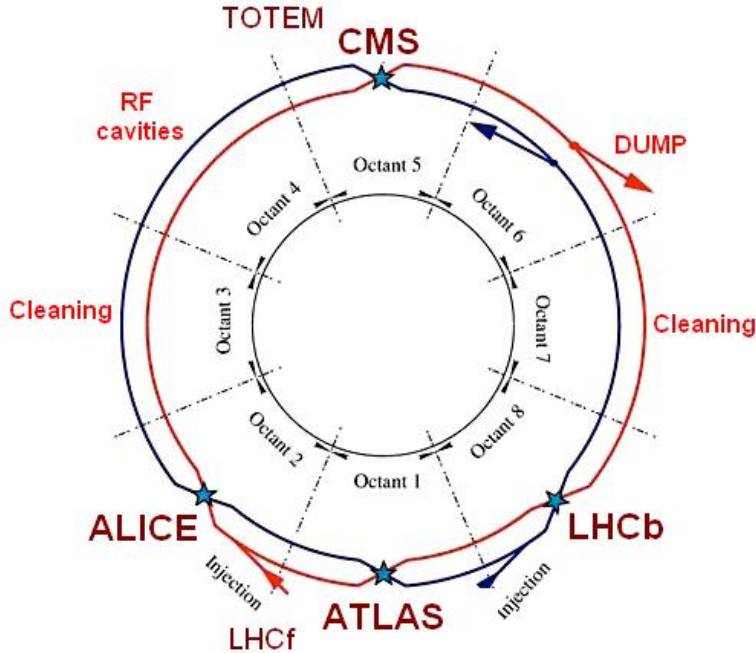


Figure 12: A schematic of the layout of the LHC, not to scale. The arched and straight sections are illustrated at the bottom of the schematic, and all four crossing sites are indicated with their respective experiments.

1337 the inner layer has a diameter of 1.065 mm while the wire in the outer layer has
 1338 a diameter of 0.825 mm.

1339 The large currents in the wires, along with the magnetic field produced, result
 1340 in forces on the magnets which would tend to push them apart with over 10,000
 1341 Newtons per meter. Constraining the magnets requires a significant amount of
 1342 structure including non-magnetic stainless steel collars. Both the presence of
 1343 these electromagnetic forces and the varying thermal contraction coefficient of
 1344 the pieces of the magnet produce significant forces on the cold mass structure.
 1345 The cold mass is carefully engineered to so that these stresses do not significantly
 1346 alter the magnetic field shape, which must be maintained between magnets to a
 1347 precision of approximately 10^{-4} for successful operation.

1348 The remaining 6800 magnets are a variety of quadrupole, sextapole, octopole,
 1349 and single bore dipole magnets. These are used to damp oscillations, correct
 1350 beam trajectories, focus the beams during circulation, and to squeeze the beams
 1351 before collisions.

1352 4.2.3 RF CAVITIES

1353 Sixteen RF cavities produce the actual acceleration of the proton beam up to the
 1354 design energy. These RF cavities are tuned to operate at 400 MHz, and are pow-
 1355 ered by high-powered electron beams modulated at the same frequency, called
 1356 klystrons. The resonance within the cavity with the oscillating electric field
 1357 establishes a voltage differential of 2 MV per cavity. The sixteen cavities are
 1358 split between the two beams, so combined the cavities provide 16 MV per beam,

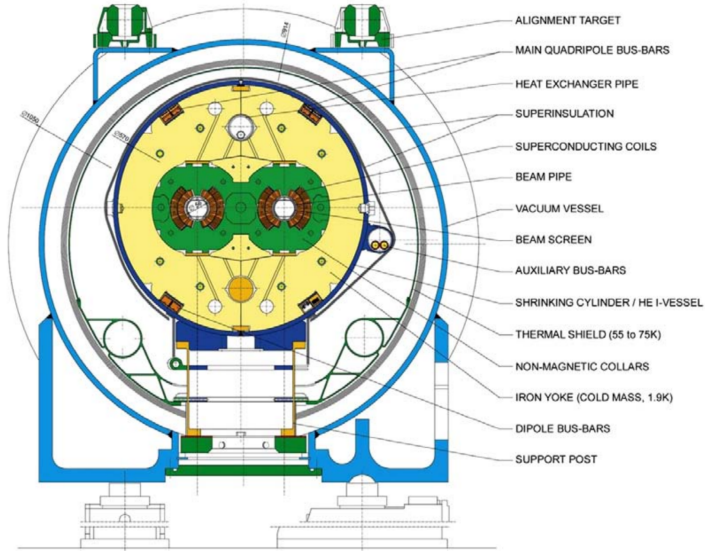


Figure 13: A cross section of the the cryodipole magnets which bend the flight path of protons around the circumference of the LHC. The diagram includes both the superconducting coils which produce the magnetic field and the structural elements which keep the magnets precisely aligned.

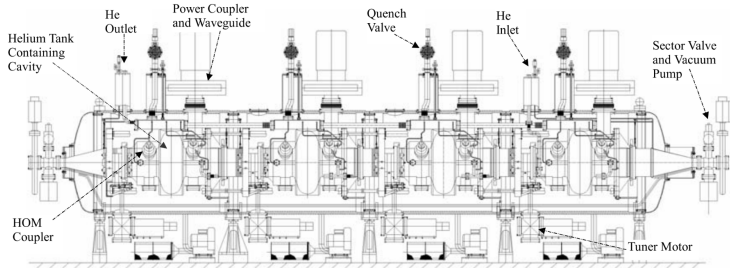


Figure 14: The arrangement of four RF cavities within a cryomodule.

1359 which accelerate the protons on each consecutive pass through the cavity. This
 1360 acceleration is also necessary during circulation even after the target energy has
 1361 been reach in order to compensate for losses from synchrotron radiation.

1362 The cavities are arranged in cryomodules which contain four cavities, with
 1363 two cryomodules per beam; this arrangement is illustrated in Figure 14. These
 1364 cryomodules are necessary to maintain the superconducting state of the cavities,
 1365 which are also constructed from niobium. The RF cavities use niobium along
 1366 with copper to allow for low power losses in the superconductors. The copper
 1367 provides a reduced susceptibility to quenching, as it rapidly conducts away heat
 1368 generated by imperfections in the niobium, as well as natural shielding from the
 1369 earth's magnetic field which can interfere with the RF system.

1370 The nature of the radio frequency oscillations tends to group protons together
 1371 into buckets. A proton traveling exactly in phase with the RF oscillations will not
 1372 be displaced at all during a single circulation, and those slightly ahead or behind
 1373 of that phase will slightly decelerate or accelerate, respectively. This produces

1374 separate clusters of protons which arrive in phase to the cavities every 2.5 ns,
 1375 corresponding to the 400 MHz frequency.

1376 4.2.4 BEAM

1377 The beams of protons circulate within 54 km of 5 cm diameter beam pipe. This
 1378 entire structure is kept under vacuum at 1.9 K to prevent interactions between
 1379 the beam pipe and the magnets as well as to prevent any interactions between the
 1380 circulating protons and gas in the pipe. The vacuum within the pipe establishes
 1381 a pressure as low as 10^{-9} mbar before the protons are introduced.

1382 Because of the very high energies of the circulating protons, synchrotron ra-
 1383 diation is not negligible in the bending regions. The protons are expected to
 1384 radiate 3.9 kW per beam at 14 TeV, with 0.22 W/m, which is enough power to
 1385 heat the liquid helium and cause a quench were it absorbed by the magnets. To
 1386 prevent this, a copper screen is placed within the vacuum tube that absorb the
 1387 emitted photons. This screen is kept between 5 and 20 K by the liquid helium
 1388 cooling system.

1389 4.3 LUMINOSITY PARAMETERS

In addition to the high energy of the collisions, the rate of collisions is extremely important to enabling the discovery of new physics. Many measurements and searches require a large number of events in order to be able to make statistically significant conclusions. The rate of collisions is measured using luminosity, the number of collisions per unit time and unit cross section for the proton-proton collisions. From the beam parameters, luminosity is given by

$$\mathcal{L} = \frac{N_b^2 n_b f_{rev} \gamma}{4\pi \epsilon_n \beta^*} F \quad (14)$$

1390 where N_b is the number of protons per bunch, n_b is the number of bunches per
 1391 beam, f_{rev} is the frequency of revolution, γ is the Lorentz factor for the protons
 1392 at the circulating energy, ϵ_n is the emittance, β^* is the amplitude function at the
 1393 collision point, and F is a geometric factor that accounts for the crossing angle of
 1394 the beams at the collision point. The emittance measures the average spread of
 1395 particles in both position and momentum space, while the amplitude function
 1396 is a beam parameter which measures how much the beam has been squeezed.
 1397 Together ϵ_n and β^* give the size of the beam in the transverse direction, $\sigma =$
 1398 $\sqrt{\epsilon \beta^*}$. β changes over the length of the beam as the accessory magnets shape the
 1399 distribution of protons, but only the value at the point of collisions, β^* , affects
 1400 the luminosity.

1401 The luminosity is maximized to the extent possible by tuning the parameters
 1402 in Equation 14. A number of these are constrained by the design decisions. The
 1403 revolution frequency is determined entirely by the length of the tunnel, as the
 1404 protons travel at very close to the speed of light. The geometric factor F is de-
 1405 termined by the crossing angle of the beams at the collision points, again a com-

Parameter	Unit	Injection	Nominal
Beam Energy	TeV	0.450	7
Peak Instantaneous Luminosity	$\text{cm}^{-2}\text{s}^{-1}$	-	10^{34}
Bunch Spacing	ns	25	25
Number of Filled Bunches	-	2808	2808
Normalized Transverse Emittance	μm	3.75	3.75
Frequency	MHz	400.789	400.790
RF Voltage/Beam	MV	8	16
Stored Energy	MJ	-	362
Magnetic Field	T	0.54	8.33
Operating Temperature	K	1.9	1.9

Table 2: The design parameters of the [LHC](#) beam that determines the energy of collisions and the luminosity, for both the injection of protons and at the nominal circulation.

1406 ponent of the tunnel design; this angle is already very small at $285 \mu\text{rad}$, which
 1407 helps to maximize the geometric factor.

1408 The major pieces that can be adjusted are the number of protons per bunch,
 1409 N_b , the number of bunches in the beam, n_b , and the amplitude function β . In-
 1410 creasing either N_b or n_b increases the amount of energy stored in the beam,
 1411 which presents a danger if control of the beam is lost. At design specifications,
 1412 the beam stores 362 MJ, which is enough energy to damage the detectors or ac-
 1413 celerator if the beam were to wander out of the beam pipe. So, the luminosity
 1414 is primarily controlled at the [LHC](#) by adjusting β^* , where lowering β^* increases
 1415 the luminosity. β^* is tuned to provide the various values of luminosity used at
 1416 the [LHC](#) which can be raised to as much as 10^{34} .

1417 The nominal bunch structure consists of 3654 bunches, each holding 10^{11} pro-
 1418 tons, which cross a collision point in 25 ns. These are further subdivided into the
 1419 buckets mentioned in Section 4.2.3 by the clustering properties of the [RF](#) cavities.
 1420 The bunches are further grouped into trains of 72 bunches which are separated
 1421 by a gap which would otherwise hold 12 bunches. At nominal operation 2808
 1422 of the bunches will actually be filled with protons, while the remainder are left
 1423 empty to form an abort gap that can be used in case the beam needs to be dumped.

1424 The various beam parameters are summarized in Table 2 for the designed op-
 1425 eration. In practice, the beam has operated at lower energies and lower luminosi-
 1426 ties than the design values for the majority of its lifetime, but the [LHC](#) has begun
 1427 to operate at full design values during Run 2.

1428 4.4 DELIVERED LUMINOSITY

During the data collection of 2015, the [LHC](#) operated at luminosities as large as
 $5 \times 10^{33} \text{ cm}^{-2}\text{s}^{-1}$. It is convenient to refer to the integrated luminosity, the inte-

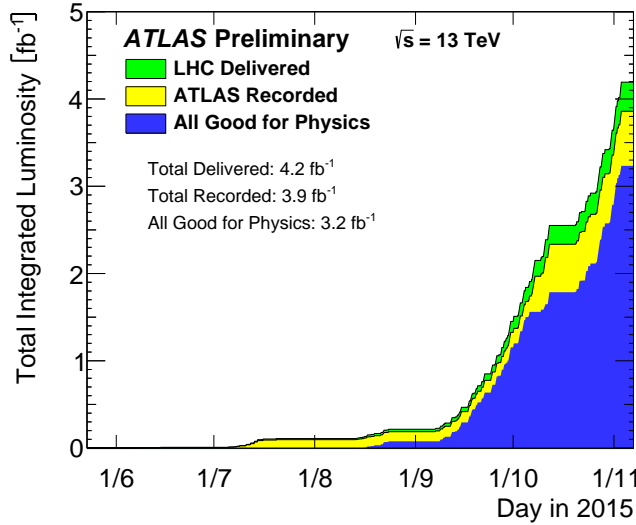


Figure 15: The cumulative luminosity versus time delivered to ATLAS (green), recorded by ATLAS (yellow), and certified to be good quality data (blue) during stable beams for pp collisions at 13 TeV in 2015.

gral of the instantaneous luminosity, which corresponds directly to the number of delivered events for a given process.

$$N = \sigma \times \int \mathcal{L}(t) dt$$

where σ is the cross section for the process of interest. The integrated luminosity over time is shown in Figure 15. This includes the luminosity delivered by the LHC as well as the luminosity that was recorded by ATLAS. ATLAS only records collisions when the LHC reports that the beam conditions are stable, so some of the delivered luminosity is not recorded. The figure also includes the amount of luminosity marked as good for physics, which includes additional requirements on the operation of the detector during data collection that are necessary for precise measurements.

Because the beam circulates and collides bunches of protons, it is possible for a single crossing to produce multiple proton-proton collisions. As the instantaneous luminosity is increased, the average number of collisions generated per bunch crossing increases. An event refers to the entire collection of interactions during a single bunch crossing, while interactions refer to the individual proton-proton collisions. The additional interactions produced during each bunch crossing are referred to as pileup, which can be more precisely defined quantified using the average number of additional proton-proton interactions per crossing, often denoted μ . Figure 16 shows the luminosity-weighted distribution of the mean number of interactions for events collected in 2015. The presence of as many as twenty interactions in a single collision provides a significant challenge in reconstructing events and isolating the targeted physical processes.

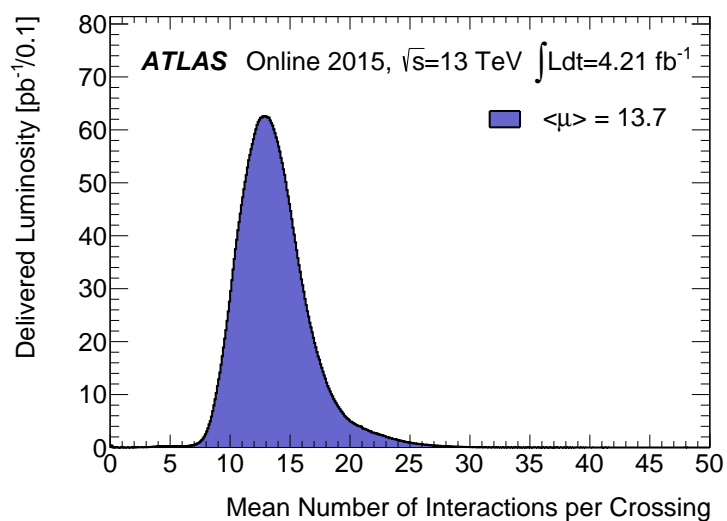


Figure 16: The luminosity-weighted distribution of the mean number of interactions per crossing for the 2015 pp collision data at 13 TeV.

1450

1451 THE ATLAS DETECTOR

1452 The four major LHC experiments at CERN seek to use the never before matched
 1453 energies and luminosities of the new collider to explore the boundaries of par-
 1454 ticle physics and to gain insight into the fundamental forces of nature. Two of
 1455 these experiments, ATLAS and CMS, are general purpose detectors that seek to
 1456 measure a variety of processes in the up to 13 TeV proton-proton collisions that
 1457 occur as much as 800 million times per second at the LHC at the design lumi-
 1458 nosity of $10^{34} \text{ cm}^{-2}\text{s}^{-1}$. ATLAS employs a hermetic detector design, one which
 1459 encloses the particle collisions as completely as possible with detecting elements,
 1460 that allows it to study a wide range of physics from SM and Higgs measurements
 1461 to searches for new physics in models like SUSY [12].

1462 Accommodating this wide variety of goals is a challenge for the design of the
 1463 detector. The wide range of energies involved requires high measurement pre-
 1464 cision over several orders of magnitude, and the numerous physics processes
 1465 require an ability to measure a variety of particle types. At the time of the con-
 1466 struction of ATLAS, the Higgs boson had yet to be discovered, but the diphoton
 1467 decay mode was (correctly) expected to be important and necessitated a high
 1468 resolution photon measurement. The potential for decays of new heavy gauge
 1469 bosons, W' and Z' , required a similarly high momentum resolution for leptons
 1470 with momentum up to several TeV. Hadronic decay modes of several possible
 1471 new high energy particles could result in very energetic jets, again up to several
 1472 TeV, and reconstructing the decay resonances would again require good energy
 1473 resolution. Several models, such as SUSY or Extra Dimensions, predict the exis-
 1474 tence of particles which would not interact with traditional detecting elements.
 1475 However these particles can still be observed in a hermetic detector by accurately
 1476 measuring the remaining event constituents to observe an imbalance in energy
 1477 called missing energy or E_T^{miss} . Measuring E_T^{miss} implicitly requires a good res-
 1478 olution on all SM particles that can be produced. And at the lower end of the
 1479 energy spectrum, precision SM measurements would require good resolution of
 1480 a variety of particle types at energies as low as a few GeV, so the design needs to
 1481 accommodate roughly three orders of magnitude.

1482 This broad spectrum of measurements requires a variety of detector systems
 1483 working together to form a cohesive picture of each collision. Two large mag-
 1484 net systems produce magnetic fields that provide a curvature to the propaga-
 1485 tion of charged particles and allows for precision momentum measurements by
 1486 other systems. The inner detector uses a combination of tracking technologies
 1487 to reconstruct particle trajectories and vertices for charged particles. A variety
 1488 of calorimeters measure the energies of hadrons, electrons, and photons over a
 1489 large solid angle. A large muon spectrometer identifies muons and uses the sec-
 1490 ond magnet system to provide an independent measurement of their momentum

1491 from the inner detector and improve the resolution. The layout of all of these
 1492 systems is shown in Figure 17.

1493 The performance goals needed to achieve the various targeted measurements
 1494 and searches discussed above can be summarized as resolution and coverage re-
 1495 quirements on each of these systems. Those requirements are listed in Table 3.

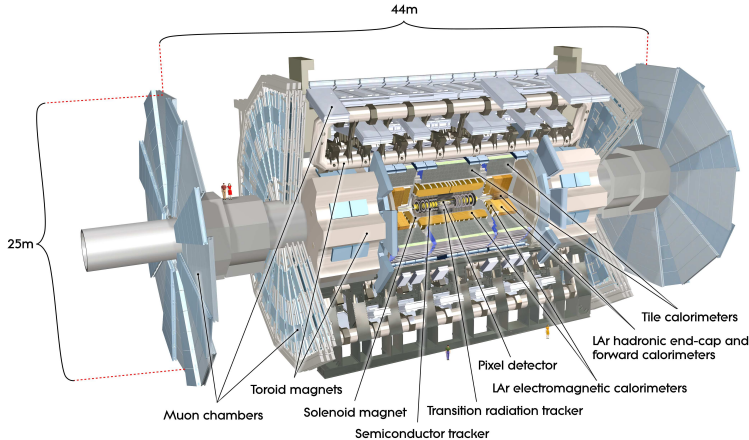


Figure 17: A cut-away schematic of the layout of the [ATLAS](#) detector. Each of the major subsystems is indicated.

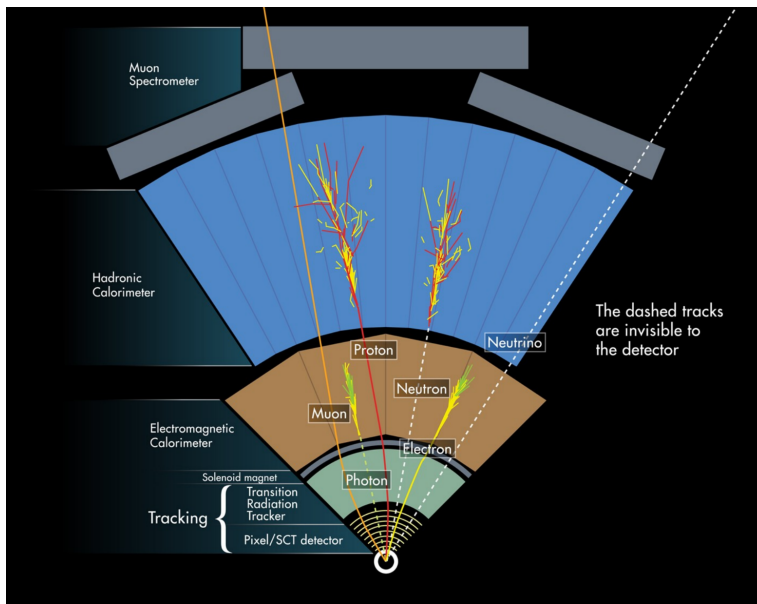


Figure 18: A cross-sectional slice of the [ATLAS](#) experiment which illustrates how the various SM particles interact with the detector systems.

1496 Incorporating these various pieces into a single detector is a significant tech-
 1497 nical challenge. The resulting detector has a diameter of 22 m, is 46 m long,
 1498 and weighs 7,000 tons; it is the largest volume particle detector ever constructed.
 1499 The various detector elements need to be constructed and assembled with pre-
 1500 cision as low as micrometers. These systems all need to function well even after
 1501 exposure to the significant radiation dose from the collisions. Designing, con-

Detector Component	Required Resolution	$ \eta $ Coverage	
		Measurement	Trigger
Tracking	$\sigma_{p_T}/p_T = 0.05\% p_T + 1\%$	2.5	-
EM Calorimetry	$\sigma_E/E = 10\%/\sqrt{E} + 0.7\%$	3.2	2.5
Hadronic Calorimetry			
Barrel and Endcap	$\sigma_E/E = 50\%/\sqrt{E} + 3\%$	3.2	3.2
Forward	$\sigma_E/E = 100\%/\sqrt{E} + 10\%$	3.1 – 4.9	3.1 – 4.9
Muon Spectrometer	$\sigma_{p_T}/p_T = 10\% \text{ at } p_T = 1 \text{ TeV}$	2.7	2.4

Table 3: The performance goals for each of the subsystems of the [ATLAS](#) detector. The $|\eta|$ coverage specifies the range where the subsystem needs to be able to provide measurements with the specified resolution. The resolutions include a p_T or E dependence that is added in quadrature with a p_T/E independent piece.

1502 structing, and installing the detector took the combined effort of more than 3000
 1503 scientists from 38 countries over almost two decades.

1504 5.1 COORDINATE SYSTEM

1505 The coordinate system defined for the [ATLAS](#) detector is used throughout all of
 1506 the sections of this thesis. The system begins with the choice of a z axis along
 1507 the beamline. The positive z side of the detector is commonly referred to
 1508 as the A -side, and the negative z side is referred to as the C -side. The $x - y$
 1509 plane is then the plane transverse to the beam direction, with the x direction
 1510 defined as pointing from the interaction point to the center of the [LHC](#) ring and
 1511 the y direction defined as pointing upwards. The nominal interaction point is
 1512 the origin of this system.

1513 It is more convenient in practice to use a cylindrical coordinate system; this
 1514 choice of coordinate system reflects the cylindrical symmetry of the [ATLAS](#) de-
 1515 tector. The distance from the beamline is the radius, r' , and the angle from the
 1516 z -axis is θ . The azimuthal angle uses the usual definition, with ϕ running around
 1517 the z -axis and $\phi = 0$ corresponding to the x -axis. Many aspects of the detector
 1518 are independent of the this coordinate to first order. The θ direction is typically
 1519 specified using rapidity or pseudorapidity, where rapidity is defined as

$$y = \frac{1}{2} \ln \frac{E + p_z}{E - p_z} \quad (15)$$

1520 Rapidity is particularly useful to indicate the component along the z direction
 1521 because differences in rapidity are invariant to boosts along the z -direction. A
 1522 similar quantity which depends only the θ is pseudorapidity,

$$\eta = -\ln \tan \frac{\theta}{2} \quad (16)$$

1523 which is the same as rapidity when the particle is massless and in the limit where
 1524 the energy is much larger than the particle's mass. It is often useful to refer to
 1525 differences in solid angle using the pseudorapidity and the azimuthal angle:

$$\Delta R = \sqrt{\Delta\phi^2 + \Delta\eta^2} \quad (17)$$

1526 The pseudorapidity is also invariant to boosts along the z -axis for high mo-
 1527 mentum particles, and is preferable to rapidity because it does not depend on
 1528 the specific choice of particle. Pseudorapidity is also preferable to θ because par-
 1529 ticle production is roughly uniform in equal-width intervals of η up to about
 1530 $\eta = 5.0$. A particle traveling along the beampipe has $\eta = \text{inf}$ and a particle
 1531 traveling perpendicular to the beampipe has $\eta = 0$. The extent of the tracker,
 1532 $|\eta| < 2.5$, corresponds to approximately $0.05\pi < \theta[\text{rad}] < 0.95\pi$ and the
 1533 extent of the calorimeters, $|\eta| < 4.9$ corresponds to approximately $0.005\pi <$
 1534 $\theta[\text{rad}] < 0.995\pi$. Many detector components are broken into multiple subsys-
 1535 tems to provide coverage at greater $|\eta|$. The lower $|\eta|$ region is referred to as the
 1536 barrel, typically with $|\eta| \lesssim 2$, and the greater $|\eta|$ region is often referred to as the
 1537 endcap.

1538 The initial energy and momentum of a proton-proton collision along the z di-
 1539 rection is unknown in hadron colliders because different energies and momenta
 1540 can be carried by the partons. Along the transverse plane, however, the vector
 1541 sum of momentum will be zero. For this reason, many physical quantities are
 1542 quantified in terms of their projection onto the transverse plan, such as p_T or
 1543 E_T . In addition, p_T alone determines the amount of curvature in the magnetic
 1544 field, and can be measured independently by measuring the curvature of a parti-
 1545 cle's propagation.

1546 5.2 MAGNETIC FIELD

1547 The magnet system used in [ATLAS](#) is designed to provide a substantial magnetic
 1548 field in the two regions where the trajectory of particles is measured, the inner
 1549 detector and the muon spectrometer. The magnetic field provides a curvature to
 1550 the trajectory of charged particles and allows the precision tracking elements to
 1551 make high resolutions measurements of p_T . To provide a magnetic field in these
 1552 regions, [ATLAS](#) uses a hybrid system with four separate, superconducting mag-
 1553 nets. A single solenoid provides a 2 T axial, uniform magnetic field for the inner
 1554 detector, while a barrel toroid and two endcap toroids produce a non-uniform
 1555 magnetic field of 0.5 and 1 T, respectively, for the muon detectors. This geom-
 1556 etry is illustrated in Figure 19, and the parameters of the three magnet systems
 1557 are summarized in Table 4.

1558 The central solenoid uses a single-layer coil with a current of 7.730 kA to gen-
 1559 erate the 2 T axial field at the center of the magnet. The single-layer coil design
 1560 enables a minimal amount of material to be used in the solenoid's construction,
 1561 which is important because the solenoid is placed between the inner detector
 1562 and the calorimeters. At normal incidence the magnet has only 0.66 radiation
 1563 lengths worth of material, where one radiation length is the mean distance over

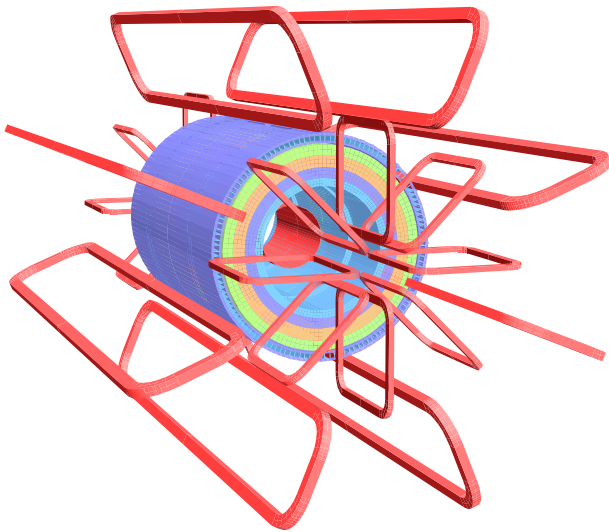


Figure 19: The layout of the four superconducting magnets in the [ATLAS](#) detector.

Parameter	Unit	Solenoid	Barrel Toroid	Endcap Toroids
Inner Diameter	m	2.4	9.4	1.7
Outer Diameter	m	2.6	20.1	10.7
Axial Length	m	5.3	25.3	5.0
Weight	tons	5.7	830	239
Conductor Size	mm ²	30×4.25	57×12	41×4.25
Peak Field	T	2.6	3.9	4.1
Heat Load	W	130	990	330
Current	kA	7.7	20.5	20.0
Stored Energy	MJ	38	1080	206

Table 4: A summary of the parameters of each of the three magnet systems on [ATLAS](#).

which a high-energy electron loses all but $1/e$ of its energy through material interactions [5]. The coil is made of a high-strength aluminum stabilized NbTi superconductor which was optimized to achieve a high field with minimal thickness. The axial magnetic field produced by the solenoid bends charged particles in the ϕ direction, following a circular path with a radius specified by Maxwell's equations (see Equation 13).

The barrel toroid consists of eight coils which generate a 0.5 T magnetic field, on average, in the cylindrical region around the calorimeters with an approximately 20 kA current. The coils are separated only by air to reduce the scattering of muons as they propagate through the region. The coils are made of an aluminum stabilized NbTiCu superconductor and each is separately housed in a vacuum and cold chamber. This magnetic configuration produces a field in the ϕ and so curves muons traversing the volume primarily in the η direction.

The endcap toroids follow a similar design to the barrel toroid and produce a 1.0 T magnetic field, on average. Each has eight separate NbTiCu coils, and in this case all eight are housed within a single cold mass. This extra structure is necessary to withstand the Lorentz forces exerted by the magnets. These magnets are rotated 22.5% relative to the barrel toroid to provide a uniform field in the transition between the two systems. The endcap toroids also produce a field in the ϕ direction and curve muons primarily in the η direction.

5.3 INNER DETECTOR

The ATLAS inner detector provides excellent momentum resolution as well as accurate primary and secondary vertex measurements through robust pattern recognition that identifies tracks left by charged particles. These tracks fulfill a number of important roles in the ATLAS measurement system: they measure the momentum of charged particles including electrons and muons, they can identify electrons or photon conversions, they assign various particles and jets to different vertices, and they provide a correction to E_T^{miss} measurements from low energy particles. The system has to be accurate enough to separate tracks from dozens of vertices, to resolve each vertex individually, and to measure the p_T of very high momentum tracks which curve very little even in the large magnetic field. This is accomplished by several independent layers of tracking systems. Closest to the interaction point is the very high granularity Pixel detector, including the newly added Insertible B-Layer, which is followed by the SCT layers. These silicon subdetectors both use discrete space-points to reconstruct track patterns. The final layer, the Transition Radiation Tracker (TRT), uses many layers of straw tube elements interleaved with transition radiation material to provide continuous tracking. The arrangement of these subdetectors is shown in Figure 20. To provide the desired hermetic coverage, the subdetectors are divided into barrel and endcap geometries. Figure 21 shows the layout of the subdetectors in more detail, and illustrates how tracks at various pseudorapidities can traverse the subdetectors; tracks with $\eta > 1.1$ begin to traverse the endcap subdetectors rather than those in the barrel, and tracks with $\eta > 1.7$ use primar-

ily endcap elements. The IBL was not present during the original commissioning of the inner detector and is not shown in this figure.

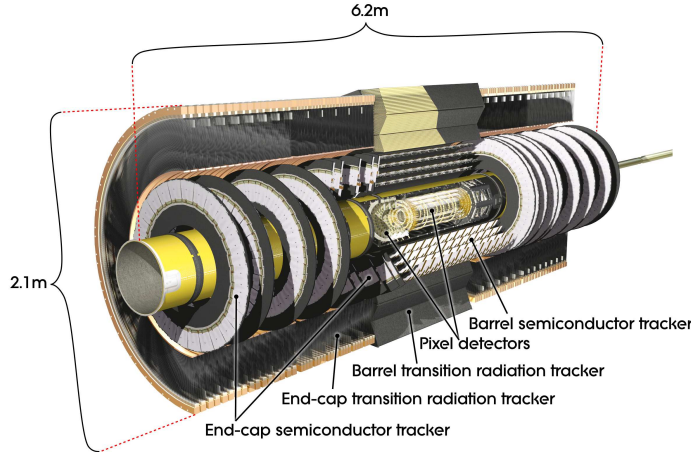


Figure 20: The arrangement of the subdetectors of the ATLAS inner detector. Each of the subdetectors is labeled in the cut-away view of the system.

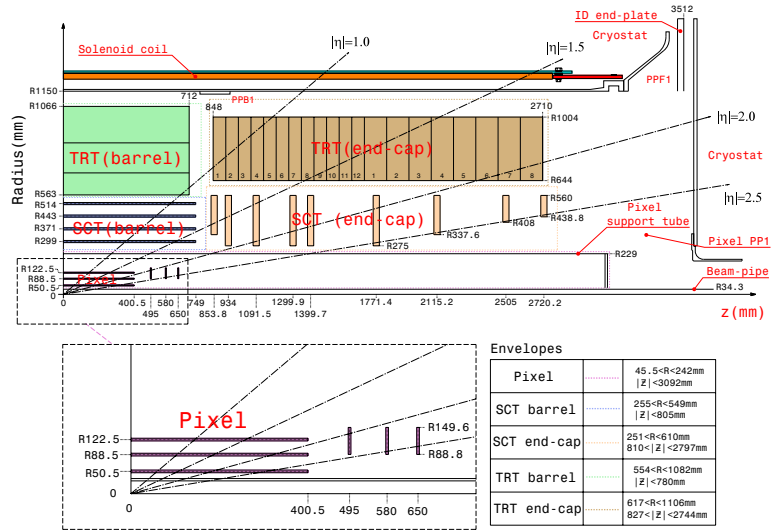


Figure 21: A quarter section of the ATLAS inner detector which shows the layout of each of the subdetectors in detail. The lower panel shows an enlarged view of the pixel detector. Example trajectories for a particle with $\eta = 1.0, 1.5, 2.0, 2.5$ are shown. The IBL, which was added after the original detector commissioning, is not shown.

Figure 22 shows a computer generated three-dimensional view of the inner detector along the beam axis, which emphasizes the straw tube structure of the TRT as well as the overlapping geometry of the SCT. This figure also includes the IBL, which was added during the long shutdown and provides an additional measurement layer in the Pixel detector as of the beginning of Run 2. Figure 23 shows an alternative computer generated three-dimensional view transverse to the beam axis which emphasizes the endcap structures of the SCT and TRT.

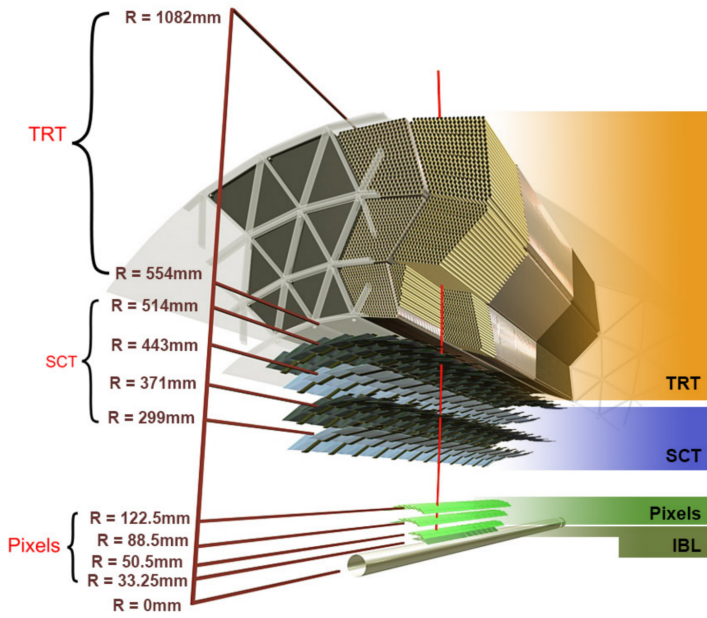


Figure 22: A computer generated three-dimensional view of the inner detector along the line of the beam axis. The subdetectors and their positions are labeled.

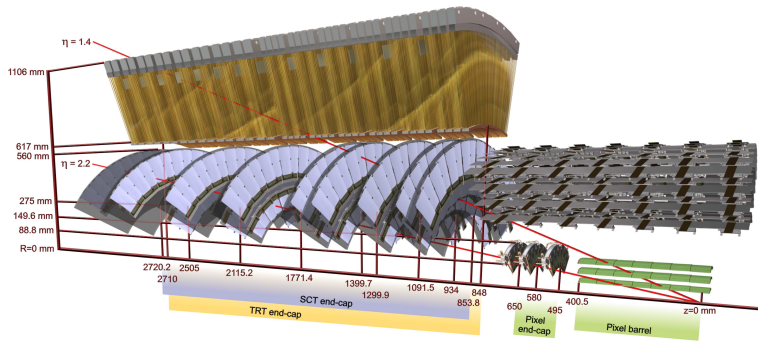


Figure 23: An alternative computer generated three-dimensional view of the inner detector transverse to the beam axis. The subdetectors and their positions are labeled.

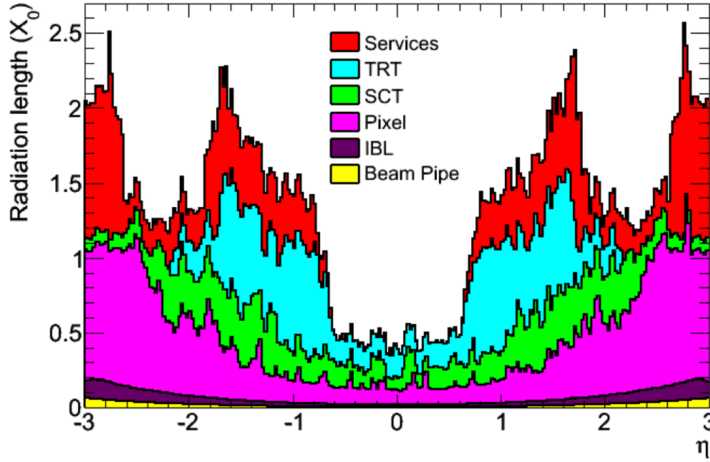


Figure 24: The integrated radiation lengths traversed by a straight track at the exit of the ID envelope, including the services and thermal enclosures. The distribution is shown as a function of $|\eta|$ and averaged over ϕ . The breakdown indicates the contributions of individual sub-detectors, including services in their active volume.

As the closest system to the interaction point, it is crucial for the inner detector to use as little material as possible to avoid scattering of charged particles or photon conversions before they reach the remaining subdetectors. The various components, including the readout electronics, cooling infrastructure, gas volumes, and support structures, were designed to accommodate this need for minimal components. Even with these optimizations, the combination of stringent performance requirements and the harsh radiation environment in the inner detector requires a significant amount of material. This material causes many electrons to lose most of their energy before reaching the electromagnetic calorimeter and approximately 40% of photons convert into an electron-positron pair while traversing the inner detector. Figure 24 shows the integrated radiation lengths traversed by a straight track in the inner detector as a function of η , grouped by subdetector. There is a large increase in the amount of material for support structures around $|\eta| = 1.7$, where the inner detector transitions from barrel to endcap.

The inner detector is designed to work as a cohesive unit to provide complete tracking information for charged particulars, and the subdetectors are complementary. Table 5 summarizes the parameters of each of the subdetectors as well as the parameters of the combined inner detector. Table 6 summarizes the expected performance that can be achieved by the inner detector as a whole.

5.3.1 PIXEL DETECTOR

The Pixel detector is the closest detector to the interaction point and therefore is designed to provide extremely high granularity while simultaneously handling a very large dose of radiation from collisions. It consists of four layers of silicon pixel modules, each of which provides a precision measurement on the trajectory

Parameter	Inner Detector	Pixel	SCT	TRT
Inner Radius	3.1 cm	3.1 cm	30 cm	56 cm
$ \eta $ Coverage	-	2.5	2.5	2.0
Cell Width	-	50 μm	80 μm	4 mm
Cell Length	-	400 μm	12 cm	70 cm
Material at $ \eta = 0.0$	0.3 X/X_0			
Material at $ \eta = 1.7$	1.2 X/X_0			
Material at $ \eta = 2.5$	0.5 X/X_0			
Number of Hits	48	4	8	36
Channels	99 M	92 M	6.3 M	350 k

Table 5: A summary of the parameters of the inner detector and each of the subdetectors [12].

of any charged particle. In the barrel region, the four layers are located at radial distances of 31 mm, 51 mm, 89 mm, and 123 mm. The three outer layers also include endcap elements, illustrated in Figure 21, which are located at 495 mm, 580 mm, and 650 mm away from the interaction point.

The pixel sensor technology uses a p-n junction of n-type bulk that contains both p⁺ and n⁺ impurities. This combination is crucial in maintaining performance after a significant radiation dose, as the n⁺ implants allow the sensor to continue function after the n-type bulk has been converted to a p-type bulk by the accumulation of radiation. In either configuration, when a charged particle passes through the bulk, it ionizes thousands of electron-hole pairs. The electrons and holes are pulled in opposite directions by the electric field established between the anode and cathode of the junction, which then produces a current that can be measured and recorded by readout electronics.

The size of the pixels in the original three layers are 50 μm x 400 μm in the $r - \phi$ and z directions, respectively. Those pixels are bump-bonded to front-end readout chips, the FE-I3, which contains a total of 2880 pixels per chip. In the three original pixel layers, the chips are grouped into modules composed of 16 chips each with 46,080 pixels per module and a total size of 20 mm x 60 mm x 250 μm . The modules are further arranged into long rectangular structures that run parallel to the beamline called staves. By tiling several staves with an offset of 20°, the stave geometry provides full azimuthal coverage in the barrel region while accommodating the readout and cable systems. The endcap regions are instead arranged into petals and then into wheels. This arrangement can be seen in Figure 25 which shows a computer-generated, cut-away image of the outer three layers of the pixel detector. Together these three layers contain 1744 modules between the barrel and two endcap sections.

The innermost layer, the IBL, was added during the long shutdown before Run 2, and provides the fourth track measurement. It was inserted directly into the existing pixel detector by removing the existing beam pipe and replacing it with a significantly smaller version. This insertion can be seen in action in Figure 26,

Parameter	Particle	Value
Reconstruction Efficiency	Muon, $p_T = 1 \text{ GeV}$	96.8%
	Pion, $p_T = 1 \text{ GeV}$	84.0%
	Electron, $p_T = 5 \text{ GeV}$	90.0%
Momentum Resolution	$p_T = 1 \text{ GeV}, \eta \approx 0$	1.3%
	$p_T = 1 \text{ GeV}, \eta \approx 2.5$	2.0%
	$p_T = 100 \text{ GeV}, \eta \approx 0$	3.8%
	$p_T = 100 \text{ GeV}, \eta \approx 2.5$	11%
Transverse IP Resolution	$p_T = 1 \text{ GeV}, \eta \approx 0$	$75 \mu\text{m}$
	$p_T = 1 \text{ GeV}, \eta \approx 2.5$	$200 \mu\text{m}$
	$p_T = 1000 \text{ GeV}, \eta \approx 0$	$11 \mu\text{m}$
	$p_T = 1000 \text{ GeV}, \eta \approx 2.5$	$11 \mu\text{m}$
Longitudinal IP Resolution	$p_T = 1 \text{ GeV}, \eta \approx 0$	$150 \mu\text{m}$
	$p_T = 1 \text{ GeV}, \eta \approx 2.5$	$900 \mu\text{m}$
	$p_T = 1000 \text{ GeV}, \eta \approx 0$	$90 \mu\text{m}$
	$p_T = 1000 \text{ GeV}, \eta \approx 2.5$	$190 \mu\text{m}$

Table 6: A summary of the expected performance of the combined inner detector [16]. Included are the reconstruction efficiencies for multiple particle types as well as the momentum and IP resolution for various momenta.

which emphasizes the extreme precision required to place the the 70 cm long layer with only 2 mm of clearance. The IBL was commissioned to provide continued tracking robustness and high precision in the higher luminosity environment of Run 2 [17]. The proximity of this layer to the collisions necessitated an even higher granularity and better radiation hardness than the other pixel layers. And the strict space requirements to add an active sensing layer so close to the interaction point required a sensor chip with a much higher active area and a larger overall area per chip. These requirements led to the development of a new chip type, the FE-I4 (compared to the FE-I3 chips used in the original pixel detector) with improved radiation hardness and a larger active footprint of 90%. The IBL is comprised of 448 of these individual chips arranged in 14 staves, with 26,880 pixels per chip and a chip size of 18.5 mm x 41.3 mm x 200 μm . The staves, like in the other layers of the pixel detector, are offset by 14° to provide full azimuthal coverage. This arrangement can be seen in Figure 27, which shows two computer-generated images of the IBL geometry and includes the some of the remaining pixel layers.

5.3.2 SEMICONDUCTOR TRACKER

The SCT, the subdetector which immediately surrounds the Pixel detector, provides additional discrete measurements of the trajectory of a charged particle. Because the SCT is further away from the interaction point, the spatial resolution

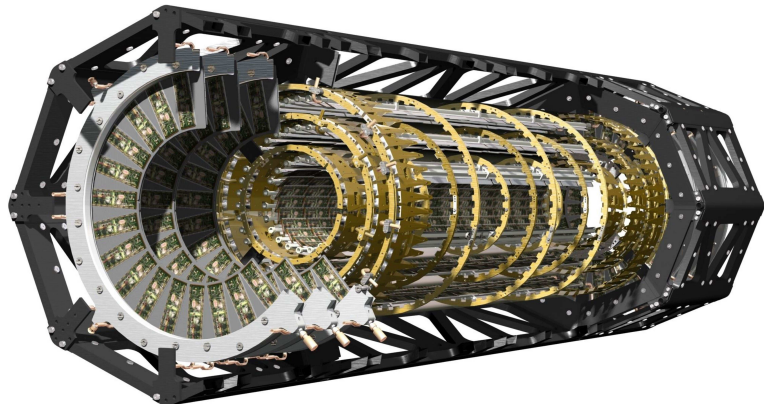


Figure 25: A cut away image of the outer three layers of the pixel detector.

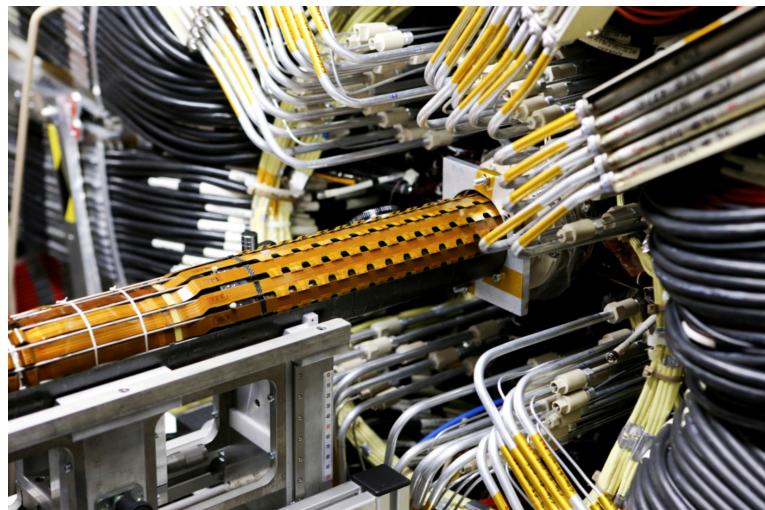


Figure 26: An image of the insertion of the IBL into the current pixel detector.

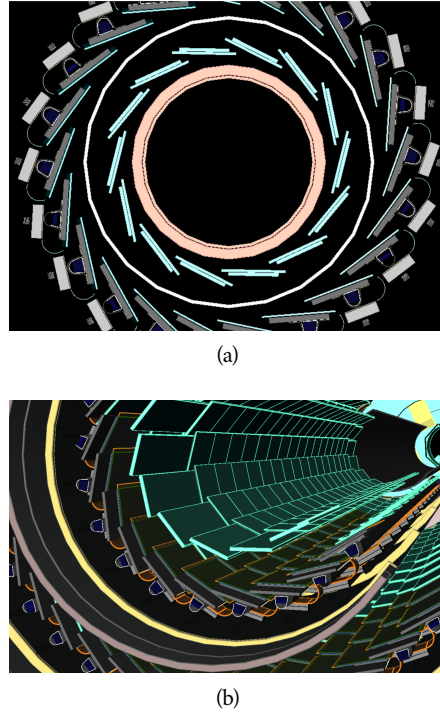


Figure 27: A three-dimensional computer-generated image of the geometry of the **IBL** with a view (a) mostly transverse to the beam pipe (b) mostly parallel to the beam pipe.

does not need to be as high as in the pixel detector, and so the **SCT** uses micro-strips instead of pixels. Although pixels provide a more accurate measurement, the number of pixels and readout channels required to cover the cylindrical area at the radius of the **SCT** layers would be prohibitively complicated and expensive.

Each individual silicon strip sensor contains 768 individual readout strips with a total area of $6.36 \text{ cm} \times 6.40 \text{ cm}$ and a pitch of $80 \mu\text{m}$. Pairs of these sensors are then bonded together to form a combined strip with a length of 12.8 cm. Two of these combined strips are then placed back to back with a relative tilt of 40 mrad. This geometry is illustrated in an expanded view in Figure 28. The purpose of angular offset of the consecutive layers is to allow the strip sensor areas to more accurately measure the position of a particle by comparing the overlap of the two strips which were traversed by a track.

Four of these double layers are placed in the barrel region, with radii of 284 mm, 355 mm, 427 mm, and 498 mm. Together these layers provide eight additional measurements for each track that traverses the central $|\eta|$ region. In the endcap region, the layers are arranged in wheels, with the double layers similarly offset to provide improved resolution. With these configurations, the **SCT** achieves a spatial resolution of $17 \mu\text{m}$ in the $r - \phi$ direction and $580 \mu\text{m}$ in the z direction.

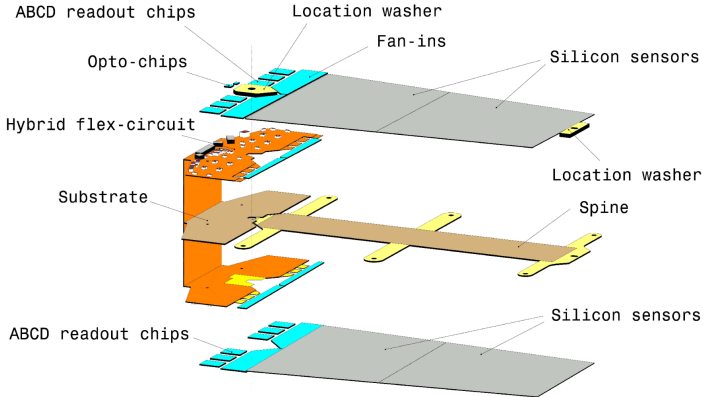


Figure 28: An expanded view of the geometry of the **SCT** double layers in the barrel region.

1710 5.3.3 TRANSITION RADIATION TRACKER

1711 The final component of the inner detector, the **TRT**, provides continuous track-
 1712 ing using straw drift tubes. The tubes are made of Kapton and aluminum with
 1713 a diameter of 4 mm and are filled with a gas mixture of 70% Xe, 27% CO₂, and
 1714 3% O₂. At the center of each tube is a gold-plated anode tungsten wire 30 μm in
 1715 diameter. When a charged particle passes through these tubes, it ionizes the gas
 1716 within. The ions produced drift in the electric field established between the wire
 1717 and the tube wall, and the large electric field near the wire produces avalanche
 1718 multiplication and results in an electric current on the wire that is read out by
 1719 the electronics and provides a track measurement. The time it takes the ioniza-
 1720 tion to drift to the wire can be used to estimate the distance from the wire that
 1721 the particle passed through the tube; this gives a resolution on the distance of ap-
 1722 proximately 130 μm . Combining several such measurements between consecu-
 1723 tive hits in the **TRT** tubes allows the trajectory of the particle to be reconstructed
 1724 with much better resolution than is available in each individual tube.

1725 In addition to the continuous tracking, the detector can use transition radia-
 1726 tion produced when a particle passes between the layers to distinguish between
 1727 electrons and heavier charged particles. The space between the tubes is filled
 1728 with CO₂, and so has a different dielectric constant than the gas within the tubes
 1729 which contains Xe. At the transition between those media, a relativistic par-
 1730 ticle emits radiation proportional to γ , so inversely proportional to mass at a
 1731 fixed momentum. The photons produced in this transition then produce an
 1732 ionization cascade which is significantly larger than the signal for the minimally-
 1733 ionizing charged particles. To distinguish between these two cases, the **TRT** de-
 1734 fines two signal thresholds, a low threshold for the typical signal produced by a
 1735 minimally ionizing particle (**MIP**) and a high threshold for the the signal produced
 1736 by transition radiation. A high momentum electron is expected to produce ap-
 1737 proximately 7 to 10 high threshold hits as it traverses the **TRT**, and thus these hits
 1738 provide a way to distinguish electrons from other charged particles.

1739 The [TRT](#) contains 351,000 tubes in total, divided between the barrel and end-
 1740 cap regions. In the barrel region, the tubes are 144 cm long and arranged in 73
 1741 layers parallel to the beampipe. In the endcap region, the tubes are 37 cm long
 1742 and arranged in 160 layers transverse to the beampipe. These configurations
 1743 can be seen in [Figure 22](#) and [Figure 23](#). With this geometry the [TRT](#) achieves a
 1744 resolution of 130 μm in the $r - \phi$ direction.

1745 5.4 CALORIMETRY

1746 The combination of calorimeter systems used in [ATLAS](#) can measure the energy
 1747 of electrons, photons, hadrons, and hadronic jets with complete coverage up to
 1748 $|\eta| < 4.9$ and across ϕ . Unlike the inner detector, the calorimeters are capable
 1749 of measuring neutral particles. To accomplish precision measurements of these
 1750 particle types, the [ATLAS](#) calorimeter system uses four individual calorimeters,
 1751 a [LAr](#) electromagnetic calorimeter in the barrel region, a tile hadronic calorime-
 1752 ter in the barrel region, a [LAr](#) hadronic endcap calorimeter, and a [LAr](#) forward
 1753 calorimeter. Together these provide hermetic coverage for the [ATLAS](#) detector.
 1754 The configuration of these calorimeters is illustrated in [Figure 29](#). **Note: I could
 1755 make this section much longer. It might be nice to include a more com-
 1756 plete description of showers for example. I will extend this section if there
 1757 is space at the end.**

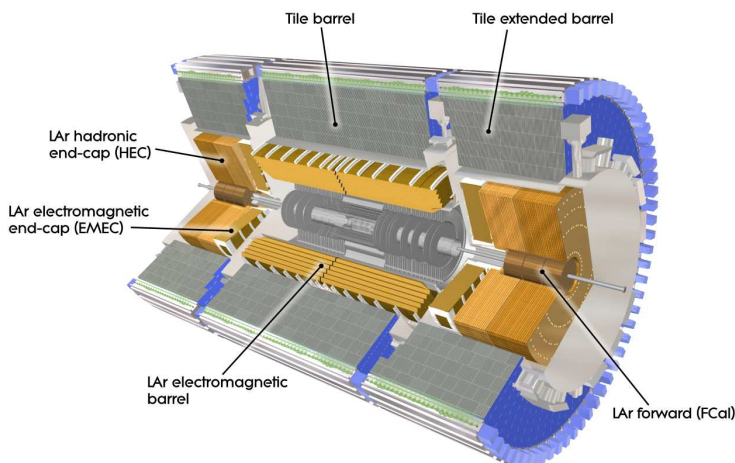


Figure 29

1758 The calorimeters are designed to absorb and measure the energy carried by
 1759 a particle, and completely stop the particle's propagation in the process. This
 1760 requires a significant amount of material to provide interactions. These interac-
 1761 tions then produce secondary particles, which can produce secondary particles
 1762 in turn, and thus form a cascade of particles called an electromagnetic ([EM](#)) or
 1763 hadronic shower, depending on the governing mechanism. Electromagnetic and
 1764 hadronic showers have very different properties and require different technolo-
 1765 gies to measure them accurately. All of the calorimeters in the [ATLAS](#) calorimeter
 1766 system are sampling calorimeters: they use alternating layers of absorbing and

active material. The dense absorbing layers initiate the showers while the active layers measure the energy of the produced particles. A fraction of the energy is lost in the inactive layers, so the energy measurement from the active layers has to be corrected to estimate the actual energy of the particle.

The EM calorimeter provides around 20 radiation lengths (X_0) while the hadronic calorimeter provides around 10 interaction lengths (λ_0). As mentioned previously, radiation lengths measure the distance over which an electromagnetically interacting particle loses a characteristic fraction of its energy. Interaction lengths, on the other hand, measure the mean distance traveled by a hadronic particle before undergoing a nuclear interaction [5]. Figure 30 show the radiation lengths in the layers of the EM calorimeter in the barrel region as well as the interaction lengths for all calorimeters.

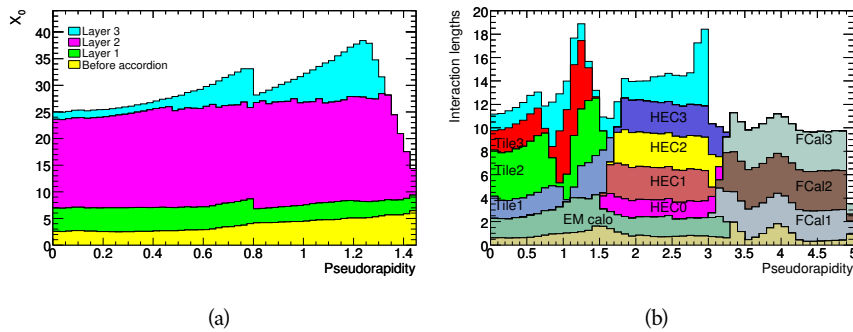


Figure 30: The depth of (a) the electromagnetic barrel calorimeter in radiation lengths and (b) all calorimeters in interaction lengths as a function of pseudorapidity.

5.4.1 ELECTROMAGNETIC CALORIMETER

The electromagnetic calorimeters use alternating layers of liquid argon and lead in an accordion shape. The accordion shape provides complete coverage in the ϕ direction while also providing many alternating layers for the a particle to pass through. The configuration is detailed in Figure 31. When an electron or photon passes through the lead, it produces an electromagnetic shower. The particles produced in those showers then pass into and ionize the liquid argon; the ions produced can then be collected by an electrode in the liquid argon layer to provide the actual energy measurement.

The barrel region is covered by a presampler and three separate sampling layers with decreasing segmentation. The presampler is a thin layer of liquid argon which measures the energy of any electromagnetic showers which are initiated before the particle reaches the calorimeter due to interactions with the detector material. The first layer is the strip layer, which has fine segmentation in η to enhance the identification of shower shapes and to provide a precise η measurement for reconstructing photons and electrons. The strip layer has only 4 radiation lengths worth of material, and has a segmentation of $\Delta\eta = 0.003$ and $\Delta\phi = 0.1$. The second layer is also finely segmented, with a segmentation of $\Delta\eta = 0.025$ and $\Delta\phi = 0.025$, and a thickness of 16 X_0 . This layer is designed

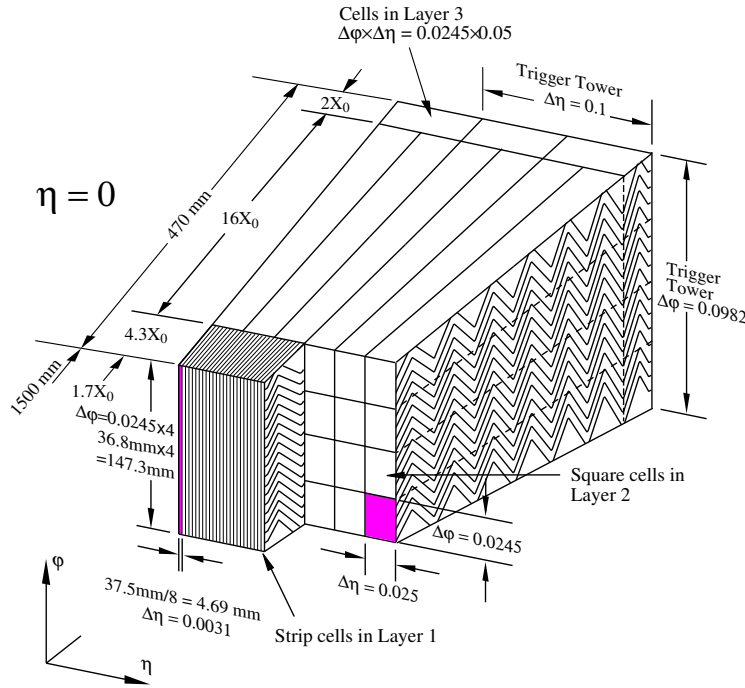


Figure 31: A schematic of the LAr calorimeter in the barrel region, highlighting the accordion structure.

1798 to contain an electromagnetic shower and to measure the majority of the energy
 1799 for photons and electrons. The third layer is only $2 X_0$ thick and measures the
 1800 energy of electromagnetic showers which leak out of the second layer, and helps
 1801 to separate electromagnetic showers from hadronic showers. The structure of
 1802 the LAr endcap calorimeter is similar except that the layers are arranged parallel
 1803 to the beampipe to measure energy deposits from high η particles.

1804 5.4.2 HADRONIC CALORIMETERS

1805 The hadronic calorimeters use a few different technologies to satisfy the resolu-
 1806 tion demands in the different areas of the detector, and together they cover the
 1807 region $|\eta| < 2.7$. In the barrel region, for $|\eta| < 1.7$, the hadronic calorimeters
 1808 are constructed of alternating tiles of steel and plastic scintillator. Like in the
 1809 electromagnetic calorimeter, the dense layer initiates a shower (in this case the
 1810 dense layer is the steel and the shower is hadronic) of particles which pass into
 1811 and ionize the following layer. The ionization in the plastic scintillator instead
 1812 produces a light signal proportional to the amount of ionization produced by the
 1813 shower, and this signal is measured using photomultipliers and provides the ac-
 1814 tual energy measurement. The construction of a tile in the calorimeter is shown
 1815 Figure 32, which highlights the alternating layers of steel and scintillator.

1816 This tile calorimeter, as well as the remaining hadronic calorimeters, have a
 1817 much coarser granularity than the electromagnetic calorimeters. The high gran-
 1818 ularity is not needed for an accurate energy measurement, and the hadronic
 1819 calorimeters are not designed to distinguish particle types like the electromag-

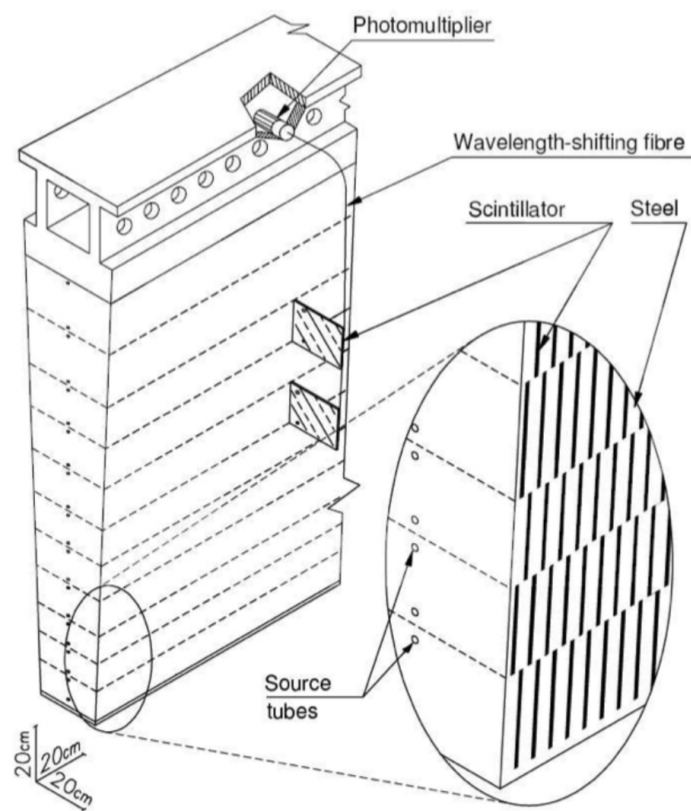


Figure 32: A schematic of a hadronic tile module which shows the alternating layers of steel and plastic scintillator.

netic calorimeters. The tile granularity is approximately $\Delta\eta = 0.1$ and $\Delta\phi = 0.1$, and the segmentation in depth and η is shown in Figure 33.

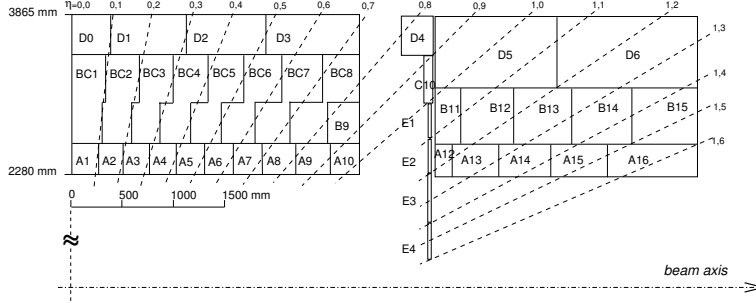


Figure 33: The segmentation in depth and η of the tile-calorimeter modules in the central (left) and extended (right) barrels.

The remaining hadronic calorimeters all use the same alternating sampling structure but with different active and inactive materials. The hadronic endcap calorimeter covers the range of $1.5 < |\eta| < 3.2$ and uses an inactive layer of copper and an active layer of liquid argon. The forward calorimeter covers the range of $3.1 < |\eta| < 4.9$ and uses a dense matrix of copper and tungsten filled with liquid argon.

5.5 MUON SPECTROMETER

Among SM particles, only muons and neutrinos consistently pass through the calorimeters. Because the neutrinos are also electrically neutral, there is no feasible option to measure them directly in ATLAS. The muons, on the other hand, are charged and are thus already measured as a track in the inner detector. The muon spectrometer provides a way to consistently identify muon tracks and also a way to provide an additional measurement of their momentum.

The muon spectrometer contains four subdetectors that cover the barrel and endcap regions. In the barrel region, the muon spectrometer uses a combination of Resistive Plate Chambers (RPCs) and MDTs to provide both a coarse, fast measurement for triggering and a precise momentum measurement for offline event reconstruction. Similarly, in the endcap region, the TGCs, MDTs, and CSCs allow for both triggering and precise measurements. The CSCs are used only in the innermost layer of the endcap region between $2.0 < |\eta| < 2.7$ where the particle flux is too large for the MDTs to provide accurate measurements. The overall layout of the muon systems are shown in the cut-away diagram in Figure 34, and Figure 35 shows a precise schematic of the layout of each of the detecting elements. The geometric arrangement shown provides consistent coverage for muons produced up to $|\eta| < 2.7$, and takes full advantage of the bending of the muons in the toroidal magnetic field, described in Section 5.2, to measure their momentum. Figure 36 shows a cross-section of the arrangement of the muon spectrometer in the barrel; the layers are divided into eight small and eight large chambers that are overlapped to provide complete coverage in ϕ .

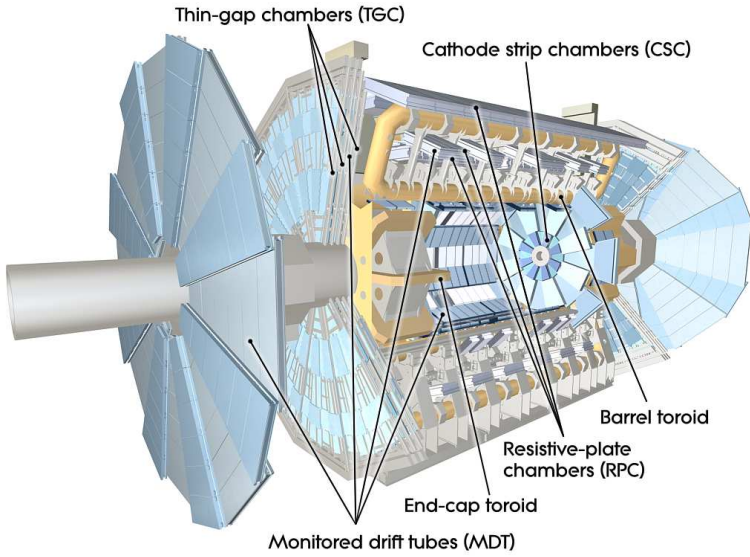


Figure 34: A cut-away diagram of the muon systems on [ATLAS](#).

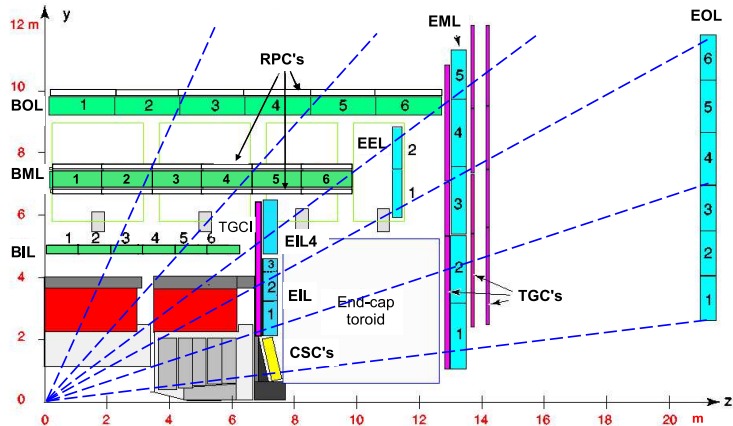


Figure 35: A quarter view of the muon spectrometer which highlights the layout of each of the detecting elements. The BOL, BML, BIL, EOL, EML, and EIL are all [MDT](#) elements, where the acronyms encode their positions.

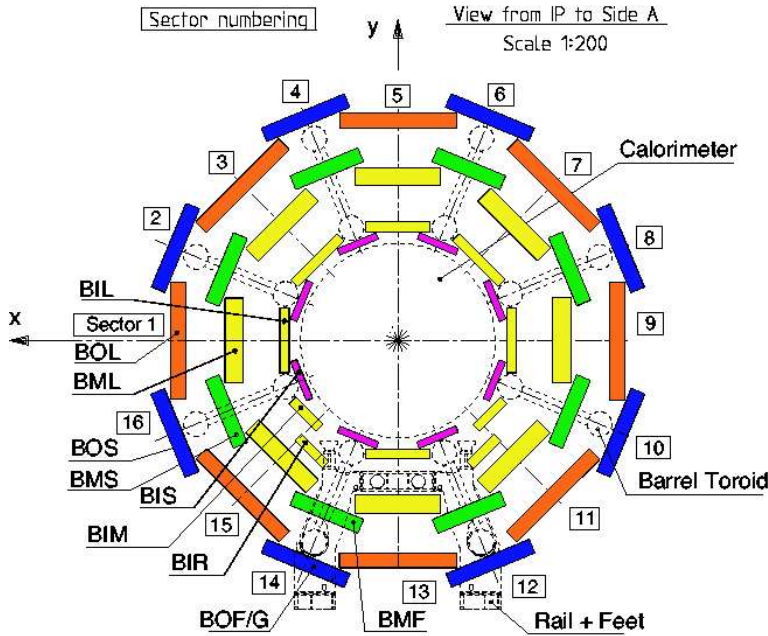


Figure 36: A schematic of the cross-section of the muon spectrometer in the barrel region.

1851 5.5.1 MONITORED DRIFT TUBE

1852 The momentum measurements in the barrel region are provided by three consecutive layers of MDT elements, located at approximately 5 m, 7 m, and 9 m from
 1853 the interaction point. Each of these layers is a composite of two multilayers of
 1854 drift tubes: two layers of three to four layers of tubes, as shown in Figure 37.
 1855 These aluminum tubes are 3 cm in diameter, with lengths between 0.9 and 6.2 m,
 1856 and are filled with a mixture of ArCO₂ kept at 3 bar absolute pressure. A central
 1857 tungsten-rhenium wire with a diameter of 50 μm runs along the length of the
 1858 tube, and is kept at a potential of 3080 V.
 1859

1860 A muon traversing these tubes ionizes the gas, and the ionization electrons
 1861 then drift in the electric field toward the central wire. Close to the wire, the
 1862 electric field is strong enough to cause the original ionization electrons to ionize
 1863 additional electrons, producing an avalanche that can be measured as a current
 1864 along the wire. The time of arrival of that current depends on how far the muon
 1865 entered from the wire, and can be used to achieve a position resolution of 80 μm
 1866 in an individual tube. The combination of the measurements in the consecutive
 1867 layers of tubes improves this position resolution to 35 μm transverse to the tubes,
 1868 with a resolution of 1 m along the tube direction.

1869 To achieve a good resolution over the entire length of a muon track, the rel-
 1870 ative positions of the tubes of the muon spectrometer must be known to an ac-
 1871 curacy of 30 μm . This is achieved by an optical laser alignment system placed in
 1872 each of the individual chambers and throughout the cavern. These monitor any
 1873 changes in position or alignment due to effects like gravitational sag, tempera-
 1874 ture shifts, and the magnetic field. The configuration of the alignment system
 1875 within an individual chamber is also shown in Figure 36.

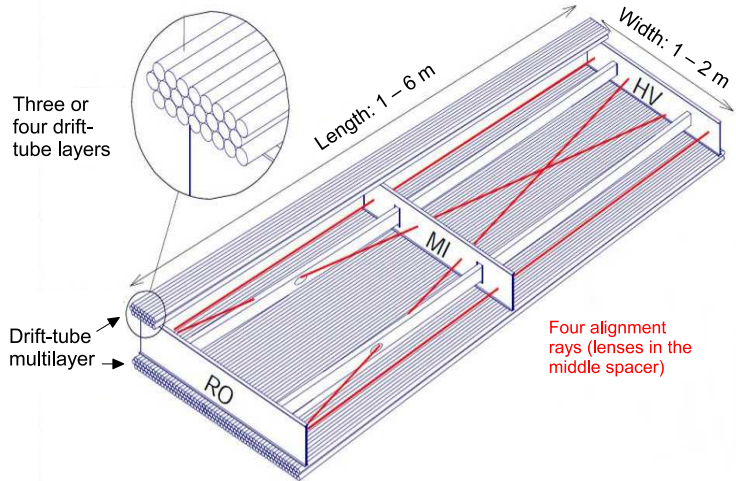


Figure 37: A schematic of a single **MDT** chamber, which shows the multilayers of drift tubes as well as the alignment system.

1876 5.5.2 RESISTIVE PLATE CHAMBER

1877 The **RPC** is the outermost detecting layer in the muon spectrometer in the barrel
 1878 region, and provides a fast measurement of the ϕ position of muons for triggering.
 1879 The speed of the measurement, with a time resolution of just a few tens of
 1880 nanoseconds, requires a poor spatial resolution of approximately 1 cm. There
 1881 are three **RPCs** layers in the muon spectrometer, two located on either side of
 1882 the central **MDT** layer and one located outside the final **MDT** layer, as shown in
 1883 Figure 35. The **RPCs** consist of two layers of parallel plates filled with a gas mix-
 1884 ture of $C_2H_2F_4$. A muon passing through these systems ionizes the gas, like in
 1885 the **MDT**, which causes an avalanche of ionization electrons in the electric field
 1886 maintained between the plates. Metal strips on the outside of the chamber ca-
 1887 pacitively couple to the accumulated charge, and are read out to measure the η
 1888 and ϕ positions of the muon track.

1889 5.5.3 CATHODE STRIP CHAMBER

1890 The majority of the momentum measurements in the endcap region are provided
 1891 by the **MDTs**. In the most forward region of the muon spectrometer, between
 1892 $2.0 < \eta < 2.7$, the particle flux is very high due to contributions from low energy
 1893 photons and neutrons. The **MDT** can only sustain a hit rate of approximately 150
 1894 Hz/cm² because of limitations in the drift times of the gas and the capacity of
 1895 the readout electronics. The **CSCs** were designed to handle higher hit rates, up to
 1896 1000 Hz/cm², and provide the necessary coverage in that high flux region.

1897 The **CSC** consists of several multiwire proportional chambers, where the wires
 1898 are oriented in the radial direction out from the beampipe. There are eight large
 1899 and eight small chambers, arranged to partially overlap in the ϕ direction, as
 1900 shown in Figure 38. Like in the **MDT**, a muon traversing the system produces
 1901 ionization in the gas; here, however, the ionization is collected on a number of

wires. These wires couple to cathodes on the chambers which are segmented into strips in two directions. The relative amount of charge on each of the neighboring strips can be used to interpolate to the position of the muon in both η and ϕ .

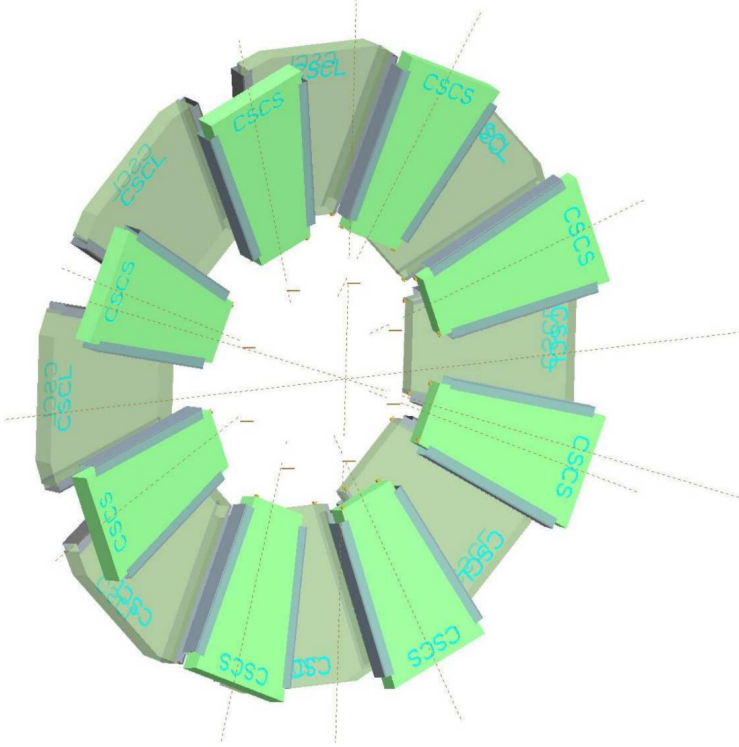


Figure 38: A schematic of the [CSC](#) endcap, showing the overlapping arrangement of the eight large and eight small chambers.

5.5.4 THIN GAP CHAMBER

Like in the barrel region, a separate, fast detector is required to provide position measurements of muons for trigger in the endcap region. This is provided by the [TGC](#) which consists of seven layers in the middle station of the endcap, two doublet layers and one triplet layer, and a single doublet layer in the inner endcap station. Figure 39 shows the arrangement of the triple and doublet layers of the [TGCs](#).

Like the [CSCss](#), the [TGCs](#) are multiwire proportional chambers with a wire-to-cathode distance of 1.4 mm and a wire-to-wire distance of 1.8 mm. Readout strips on the outside of the chambers run perpendicular to the wires, and couple to the charge collected on the wires to provide a position measurement in the η direction. The current induced on the wires is also readout to provide a position measurement in the ϕ direction. The high electric field and small wire-to-wire distance give it the required good time resolution to be used for triggering events.

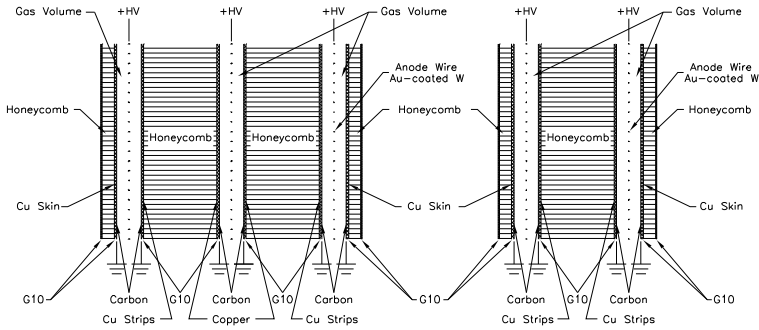


Figure 39: A schematic of the TGC doublet and triplet layers.

1920 5.6 TRIGGER

1921 It is not possible for the detector and the associated computing systems to record
 1922 the terabytes of data that the 40 MHz event rate produces every second. Instead,
 1923 a small fraction of these events are selected by the trigger system to be recorded
 1924 and later analyzed. Selecting interesting events at such a high rate poses a sig-
 1925 nificant challenge for the both the detector design and the implementation of a
 1926 trigger decision and data acquisition system. The trigger must balance the time
 1927 needed to decide to keep an event, to avoid losing information, with the filtering
 1928 accuracy to consistently select a full menu of physics events that can be used for
 1929 the wide array of searches and measurements targeted by [ATLAS](#).

1930 The [ATLAS](#) trigger system, as of Run 2, consists of two levels of decision mak-
 1931 ing. The first level, referred to as L1, is hardware based and uses inputs from
 1932 a subset of the detector elements to narrow the considered event rate from the
 1933 original 40 MHz down to 100 kHz. The 100 kHz rate is the maximal rate that the
 1934 event information can be transferred from the detector. The second, software-
 1935 based level, referred to as the [HLT](#), makes the final decisions on which events to
 1936 keep for analysis and selects a rate of around 1 kHz. The collection of selection
 1937 criteria used to make the L1 decisions feed into subsequent selection criteria in
 1938 the [HLT](#), and the set of these combinations of L1 and [HLT](#) criteria from the trig-
 1939 ger menu which defines exactly what events are recorded on [ATLAS](#). The trigger
 1940 menu used for 2015 data collection is shown in Table 7, which summarizes the
 1941 selection requirements at both levels and additionally shows the peak measured
 1942 rates contributed by each.

1943 At L1, the trigger system uses information primarily from the calorimeters
 1944 and muon spectrometer to select high p_T jets, electrons, photons, and muons.
 1945 The electromagnetic calorimeter uses reduced granularity energy measurements
 1946 as well as isolation requirements to select electrons and photons. The hadronic
 1947 calorimeter also uses a combination of reduced granularity energy measurements
 1948 and isolation to select high momentum jets and hadronically decaying tau lep-
 1949 tons.

1950 The calorimeters are also used to provide triggers based on missing energy:
 1951 the coarse granularity energy measurements are used to calculate a directional
 1952 sum of energies and to trigger on a significant imbalance. Only the [RPCs](#) and

Trigger	Typical offline selection	Trigger Selection		Level-1 Peak Rate (kHz)	HLT Peak Rate (Hz) $L = 5 \times 10^{33} \text{ cm}^{-2}\text{s}^{-1}$
		Level-1 (GeV)	HLT (GeV)		
Single leptons	Single iso μ , $p_T > 21$ GeV	15	20	7	130
	Single e , $p_T > 25$ GeV	20	24	18	139
	Single μ , $p_T > 42$ GeV	20	40	5	33
	Single τ , $p_T > 90$ GeV	60	80	2	41
Two leptons	Two μ 's, each $p_T > 11$ GeV	2×10	2×10	0.8	19
	Two μ 's, $p_T > 19, 10$ GeV	15	18, 8	7	18
	Two loose e 's, each $p_T > 15$ GeV	2×10	2×12	10	5
	One e & one μ , $p_T > 10, 26$ GeV	20 (μ)	7, 24	5	1
	One loose e & one μ , $p_T > 19, 15$ GeV	15, 10	17, 14	0.4	2
	Two τ 's, $p_T > 40, 30$ GeV	20, 12	35, 25	2	22
	One τ , one μ , $p_T > 30, 15$ GeV	12, 10 (+jets)	25, 14	0.5	10
Three leptons	One τ , one e , $p_T > 30, 19$ GeV	12, 15 (+jets)	25, 17	1	3.9
	Three loose e 's, $p_T > 19, 11, 11$ GeV	15, 2×7	17, 2×9	3	< 0.1
	Three μ 's, each $p_T > 8$ GeV	3×6	3×6	< 0.1	4
	Three μ 's, $p_T > 19, 2 \times 6$ GeV	15	18, 2×4	7	2
	Two μ 's & one e , $p_T > 2 \times 11, 14$ GeV	2×10 (μ 's)	$2 \times 10, 12$	0.8	0.2
	Two loose e 's & one μ , $p_T > 2 \times 11, 11$ GeV	$2 \times 8, 10$	$2 \times 12, 10$	0.3	< 0.1
	One photon	one γ , $p_T > 125$ GeV	22	120	8
Two photons	Two loose γ 's, $p_T > 40, 30$ GeV	2×15	35, 25	1.5	12
	Two tight γ 's, $p_T > 25, 25$ GeV	2×15	2×20	1.5	7
Single jet	Jet ($R = 0.4$), $p_T > 400$ GeV	100	360	0.9	18
	Jet ($R = 1.0$), $p_T > 400$ GeV	100	360	0.9	23
E_T^{miss}	$E_T^{\text{miss}} > 180$ GeV	50	70	0.7	55
Multi-jets	Four jets, each $p_T > 95$ GeV	3×40	4×85	0.3	20
	Five jets, each $p_T > 70$ GeV	4×20	5×60	0.4	15
	Six jets, each $p_T > 55$ GeV	4×15	6×45	1.0	12
b -jets	One loose b , $p_T > 235$ GeV	100	225	0.9	35
	Two medium b 's, $p_T > 160, 60$ GeV	100	150, 50	0.9	9
	One b & three jets, each $p_T > 75$ GeV	3×25	4×65	0.9	11
	Two b & two jets, each $p_T > 45$ GeV	3×25	4×35	0.9	9
b -physics	Two μ 's, $p_T > 6, 4$ GeV plus dedicated b -physics selections	6, 4	6, 4	8	52
Total				70	1400

Table 7: The trigger menu for the 2015 data collection with $L = 5 \times 10^{33} \text{ cm}^{-2}\text{s}^{-1}$. Both the L1 and HLT selection requirements and their trigger rates are shown measured at the specified luminosity are shown. The typical offline selections represent a typical set of offline requirements imposed after the trigger in an analysis.

1953 **TGCs** muon subdetectors contribute to the decision at L1, and are used to identify
 1954 high momentum muons. The contributions to the triggering rate of the various
 1955 types of L1 triggers are shown in Figure 40. The total rate is indicated in black
 1956 and is lower than the sum of individual rates because their is significant overlap
 1957 between different trigger channels. The majority of the rate comes from lepton
 1958 and photon triggers.

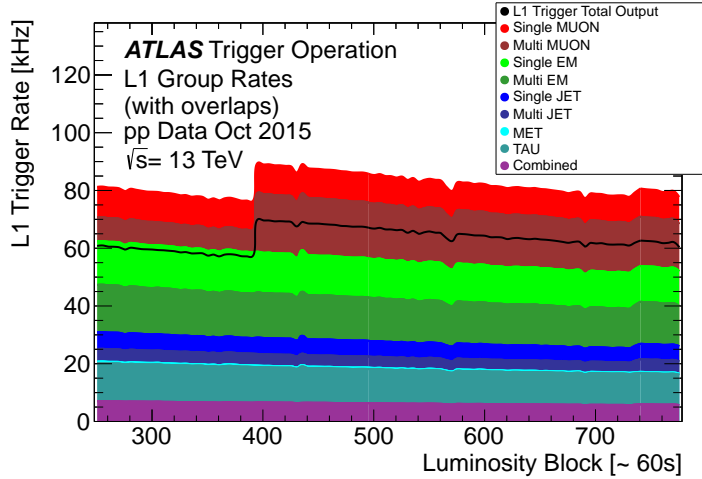


Figure 40: The L1 Trigger rate broken down into the types of triggers as a function of the luminosity block for the 2015 data collection period.

1959 After an event is chosen by the L1 trigger, the detector measurements from the
 1960 bunch crossing which fired the trigger is read out from the front-end electronics
 1961 and stored on read-out boards. This inclusive information is necessary to make
 1962 more the more precise event selections than is possible with the reduced infor-
 1963 mation at L1. The **HLT** then uses this information with software algorithms to
 1964 decide whether or not to permanently record the event. The L1 trigger also for-
 1965 wards which decision was made and Region of Interests (**Rois**) to the **HLT**, which
 1966 allows the **HLT** to focus on particular algorithms and particular sections of the
 1967 detector to greatly improve the algorithmic selection speed. The additional in-
 1968 formation available to the **HLT** allows it to implement additional trigger targets,
 1969 such as identified jets from the decays of b-hadrons. The contributions to the
 1970 triggering rate of the various types of **HLT** triggers are shown in Figure 41.

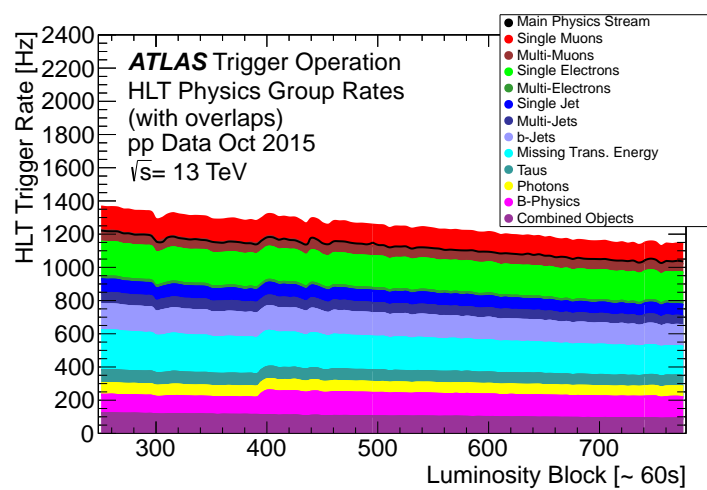


Figure 41: The HLT Trigger rate broken down into the types of triggers as a function of the luminosity block for the 2015 data collection period.

1971

1972 EVENT RECONSTRUCTION

1973 The ATLAS experiment combines measurements in the subdetectors to form a
 1974 cohesive picture of each physics event. The majority of particles that traverse
 1975 the detector leave behind some combination of ionization hits in the tracking
 1976 detectors or energy deposits in the calorimeters, and these measurements can
 1977 be used to reconstruct physical quantities like the particle's energy, momentum,
 1978 or trajectory. Even the type of the particle can be distinguished by comparing
 1979 the various ways that different species of stable particles interact with the sub-
 1980 detectors. Reconstruction is the series of algorithms which take the electronic
 1981 outputs of the detector and assigns them into individual physics objects. The
 1982 physics objects summarize the properties of particles produced by the collision
 1983 or subsequent decays, either for individual isolated particles like leptons, or for
 1984 a collection of the cascade of products produced in the decay of an energetic
 1985 hadron, called a jet. These are the objects and quantities most often used in anal-
 1986 ysis to make measurements of SM processes or to search for new physics.

1987 6.1 CHARGED PARTICLES

1988 As described in Section 5.3, charged particles that traverse the inner detector
 1989 leave behind hits in the subdetectors. Each of these hits translates into a position
 1990 measurement along the trajectory of that particle, with position resolutions de-
 1991 pending on the subdetector that provided the measurement. Track reconstruc-
 1992 tion uses these position measurements to collect hits in consecutive layers of
 1993 the detector into a trajectory consistent with a particle curving in a magnetic
 1994 field [18, 19]. This reconstructed trajectory is called a track. The number of hits
 1995 in the inner detector for each event makes a combinatorial method completely
 1996 infeasible: the algorithms that form tracks must be significantly more intelligent
 1997 so that event reconstruction does not exhaust computing resources.

1998 The first and primary algorithm employed in track reconstruction is called
 1999 the inside-out method, which begins with the assumption that the track orig-
 2000 inated from the interaction point. Its purpose is to identify primary particles,
 2001 those which originate in the proton-proton collisions and with a lifetime long
 2002 enough to reach the inner detector. Combinations of three hits are considered
 2003 from measurements in the Pixel detector and the SCT, and form the seed for a
 2004 track. Specifically, the seeding algorithm looks for a seed using three pixel hits,
 2005 two pixel hits and one SCT hit, or three SCT hits. The seed is then extrapolated
 2006 forwards and backwards into the Pixel and SCT detectors depending on the seed
 2007 location, and hits in each layer are considered to be added to the track using a
 2008 combinatorial Kalman filter [19]. After all of the silicon layers have been consid-
 2009 ered, tracks are filtered to reduce ambiguities from other nearby tracks or from
 2010 combinatorial coincidences. Then the tracks are extended outwards into the TRT

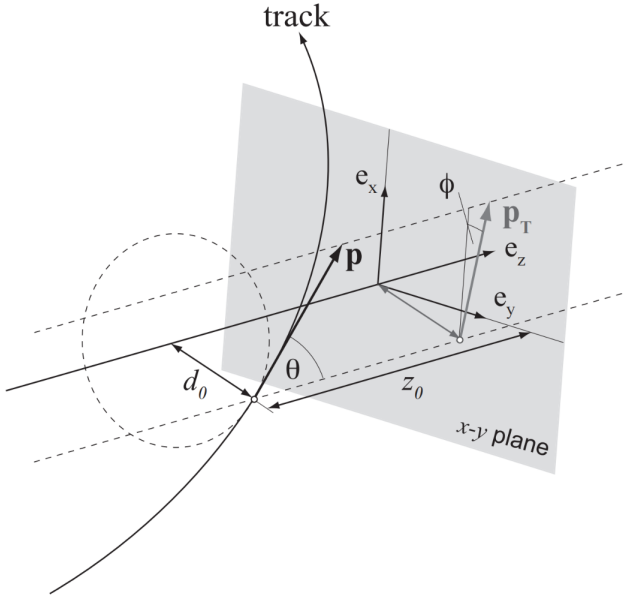


Figure 42: An illustration of the perigee representation of track parameters for an example track. The charge is not directly shown, but is indicated by the direction of curvature of the track [20].

in the same way. This algorithm is how the hits are chosen to be incorporated into a single track. Once the hits are collected, a fitting algorithm calculates the track parameters which best model the locations of the hits and their resolutions. The fitting uses five parameters, $(d_0, z_0, \phi, \theta, q/p)$, to specify a track in a perigee representation: d_0 and z_0 are the transverse and longitudinal impact parameters at the closest approach to the nominal beam axis, ϕ and θ are the usual angular coordinates, and q/p is the charge divided by the momentum. These parameters are illustrated in Figure 42. Those parameters directly determine the direction and momentum of the particle which produced the track.

This inside-out algorithm is complemented by an outside-in algorithm, which is used to find tracks from secondary particles, those produced in the decays or interactions of the primary particles inside the detector. As the name indicates, the outside-in algorithm begins by seeding tracks in the outermost layers of the inner detector, in the TRT. The seed in this case is formed by a segment in the TRT, and the track is propagated backwards into the SCT before being refitted to use all the included points. Some tracks are found with TRT segments only, which can result from interactions with the detector following the SCT. Figure 43 shows an example of the geometry of tracks formed by both algorithms, where the hits belonging to tracks found using the inside-out algorithm are highlighted in red, and the hits belonging to the tracks found using the outside-in algorithm are circled in black. The figure highlights the presence of a large number of both primary and secondary tracks in a single event, as well as the overall large number of hits present in the inner detector.

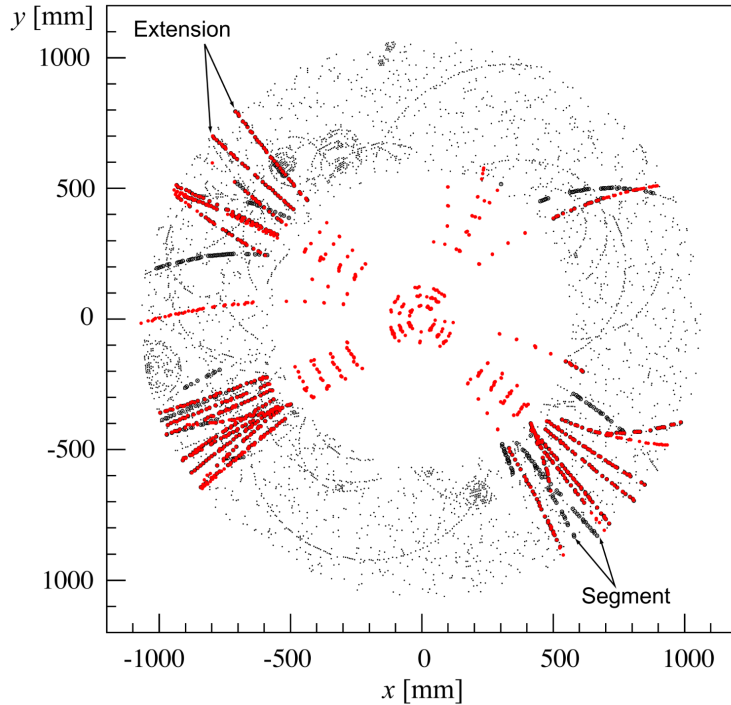


Figure 43: The x and y locations of the hits generated in a simulated $t\bar{t}$ event in the inner detector. The hits which belong to tracks formed using the inside-out algorithm are highlighted in red, while the hits which belong to tracks formed using the outside-in algorithm are circled in black.

2034 The tracks resulting from these algorithms can be contaminated by nearby
 2035 particles confusing the tracking algorithm in a high luminosity environment.
 2036 For example, enough hits present in the inner detector can lead to fake tracks
 2037 from combinations of hits from multiple individual tracks. Therefore, after the
 2038 tracks are formed and fitted, additional quality requirements are imposed in
 2039 order to reduce such backgrounds. Most tracking applications require at least
 2040 seven silicon hits, that is, seven hits between the Pixel detector and **SCT**. Then the
 2041 tracks are required to have at most two holes in the Pixel detector, where holes
 2042 are non-existing but expected measurements in a layer of the subdetector. If the
 2043 missing hit corresponds to an inactive module, however, it is not counted as a
 2044 hole but instead as a hit for tracking as the lack of a measurement is expected in
 2045 that case.

2046 6.1.1 PIXEL NEURAL NETWORK

2047 The hits in the Pixel detector are not typically confined to a single pixel, but
 2048 rather the charge is spread over several pixels per layer which are grouped to-
 2049 gether into clusters. The clustering of these pixels for isolated tracks is relatively
 2050 straightforward, but complications can arise in the high occupancy environment
 2051 where hits from multiple particles can overlap in a single cluster. Figure 44
 2052 shows examples of clusters generated by a single isolated particle, two nearly
 2053 overlapping particles, and a particle which emits a δ -ray. A δ -ray is a secondary

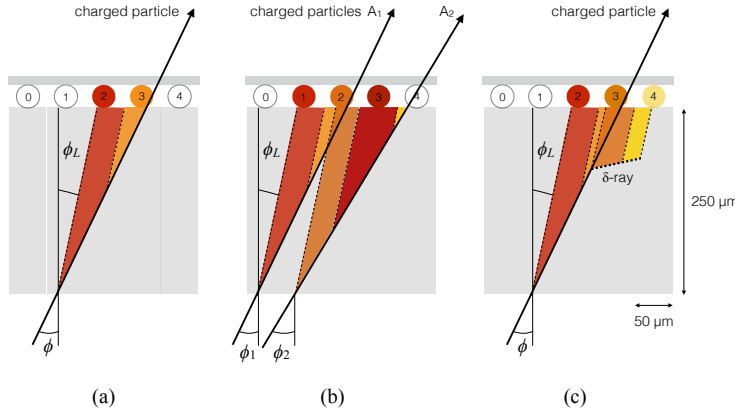


Figure 44: Examples of the clusters formed in a single layer of the pixel detector for (a) a single isolated particle, (b) two nearly-overlapping particles, and (c) a particle which emits a δ -ray [21].

2054 electron which is generated with enough energy to escape a significant distance
2055 away from the original particle and to generate additional ionization.

2056 A series of neural-networks analyzes the shape of the clusters to determine
2057 how many particles produced the cluster and to estimate the positions of each
2058 of the particles within the cluster. These allow for an identification of clusters
2059 caused by more than one particle or by a particle that emits a δ -ray. In a high-
2060 density tracking environment, the multiple position outputs can be used as the
2061 locations of individual hits to allow reconstruction of tracks which almost over-
2062 lap and with a much better separation than is possible without the splitting of
2063 individual clusters.

2064 6.1.2 PIXEL DE/DX

2065 A hit in the Pixel detector corresponds to the voltage generated from ionization
2066 current rising above a threshold value that is tuned to consistently record the
2067 passing of MIPs. A larger amount of charge deposited results in a larger voltage,
2068 and a larger signal remains above the threshold for a longer period of time. The
2069 time over threshold (ToT) is read out of the Pixel detector, and can be used to
2070 provide a measurement of the charge deposited in each pixel. The charge mea-
2071 surements from each of the pixels included in a pixel cluster are summed to form
2072 one charge measurement per layer of the pixel detector. That charge measure-
2073 ment, combined with the angle of incidence of the track and the known sizes of
2074 each detector element, can be converted into a measurement of dE/dx , the ion-
2075 ization energy deposited per unit distance, measured in $\text{MeVg}^{-1}\text{cm}^2$. The IBL
2076 only has sixteen available values (4 bits) of ToT to readout, compared to the 256
2077 available values (8 bits) in the remaining pixel layers. To help alleviate this lack
2078 of range, the IBL also records if it is in overflow: when the ionization is sufficient
2079 to generate a ToT above the largest value that can be recorded in the 4 bits.

2080 The measurements across multiple layers are combined to form an average
 2081 value of dE/dx for the track as a whole. Depending on where a charge particle
 2082 is produced, it will traverse four Pixel layers and create four clusters on average.
 2083 It can produce as few as two clusters in the Pixel detector if it passes through in-
 2084 active modules, and as many as five if it is in a region of the detector where multiple
 2085 modules overlap. To reduce the influence of the typical long Landau tails of the
 2086 distribution of dE/dx deposits [5], the average is calculated as a truncated mean
 2087 of these clusters. The value measured in the IBL is removed if it is in overflow, as
 2088 the measured value is not reliable in that case. If a track has five measurements
 2089 in the pixel detector, the two highest cluster values are removed. If a track has
 2090 two, three, or four measurements in the pixel detector, only the single highest
 2091 cluster value is removed. The remaining values are averaged to form the pixel
 2092 dE/dx .

2093 6.1.3 VERTEX RECONSTRUCTION

2094 A vertex represents the intersection of multiple tracks and corresponds to the
 2095 location of an interaction. If at least two charged particles result from the in-
 2096 teraction, the intersection of their resulting tracks reveals its position with high
 2097 precision. Vertices are divided into two groups, primary vertices which corre-
 2098 spond to the actual proton-proton collisions, and secondary vertices which cor-
 2099 respond to decays of short-lived particles or interactions with the detector. Pri-
 2100 mary vertices are particularly important, as they can provide a precise location
 2101 for the interaction which generated the observed particles. Understanding that
 2102 location is crucial in understanding the geometry of the event.

2103 Primary vertices are reconstructed by iteratively identifying seeds from recon-
 2104 structed tracks [22]. Each track's extrapolated z position at the beamline forms a
 2105 seed, and nearby tracks are fitted using that position as a point along their trajec-
 2106 tory. The goodness of fit with that vertex is considered for each track, measured
 2107 in χ^2 . The final position of the vertex is determined by a fit to all of the con-
 2108 sidered tracks, where the contribution from each track is weighted according to
 2109 the χ^2 compatibility with that vertex. Any tracks from this procedure that are
 2110 displaced by more than 7σ from that vertex are removed from the fit and used
 2111 to seed a new vertex. This procedure is iterated until no additional vertices can
 2112 be found.

2113 This procedure is typically performed twice. The first set of vertices is used
 2114 to fit a profile for the beamspot, which indicates the position of the intersec-
 2115 tion of beams in that particular bunch crossing. The fitted beamspot then provides
 2116 a constraint for the second attempt to locate primary vertices, where both the
 2117 track fitting and seeding of vertices are required to be consistent with interac-
 2118 tions occurring within the beamspot.

2119 6.2 ELECTRONS AND PHOTONS

2120 Electrons are measured as both a charged particle track and energy deposits in
 2121 the electromagnetic calorimeter. Photons, on the other hand, leave energy de-

2122 posits in the electromagnetic calorimeter but do not produce a corresponding
 2123 track. Because the electromagnetic interactions with the calorimeter of both
 2124 photons and electrons produces more photons and electrons, the behavior in the
 2125 calorimeter is very similar and there is significant overlap in the reconstruction
 2126 techniques for each.

2127 The reconstruction of a photon or an electron in the calorimeter is based on
 2128 clustering algorithms which identify groups of energy deposits [23–25]. For this
 2129 purpose, the entire electromagnetic calorimeter is subdivided into a grid of 200
 2130 by 256 towers in the η and ϕ directions, respectively, where the individual grid
 2131 units have a size of $\Delta\eta = 0.025$ and $\Delta\phi = 0.025$. These towers correspond to
 2132 individual cells in the middle, coarsest layer of the EM calorimeter, and in the re-
 2133 maining layers the cells are grouped together cover the same area in $\eta - \phi$ space.
 2134 The clustering begins by finding seeds with a sliding-window algorithm based
 2135 on the towers: a window of 3 by 5 towers is formed and translated until the sum
 2136 of the energy within the window is maximized. If that energy is above 2.5 GeV,
 2137 then that region becomes a seed. The choice of 2.5 GeV was chosen to com-
 2138 promise between maximizing reconstruction efficiency while minimizing fake
 2139 electron seeds from electronic noise or soft hadrons from additional interactions.
 2140 The seeds are rejected if the energy measured in the hadronic calorimeter behind
 2141 the seed is large, as this typically indicates a hadron rather than an electron or
 2142 photon.

2143 Next, the inner detector tracks within a cone of $\Delta R = 0.3$ are compared to
 2144 the location and energy of the seed. Tracks are matched to the cluster if the ex-
 2145 trapolation of the track to the energy-weighted center in the middle layer of the
 2146 EM calorimeter falls within $\Delta\phi < 0.2$ in the direction of the curvature of the
 2147 track or $\Delta\phi < 0.05$ in the direction opposite of the curvature of the track. If the
 2148 seed matches with a track that originated from a primary vertex, the combina-
 2149 tion of track and electromagnetic cluster is reconstructed as an electron. If the
 2150 seed matches with a track that did not originate from a primary vertex, then the
 2151 electromagnetic cluster is reconstructed as a converted photon. And if there is
 2152 no corresponding track in the inner detector, then the cluster is reconstructed
 2153 as a photon.

2154 After classification, the final clustering of the energy in the EM calorimeter
 2155 calorimeter is performed. The classification must be done first, as the expected
 2156 size of the energy deposits in the calorimeter are different for electrons and pho-
 2157 tons. In the barrel region, the final clusters for electrons are formed in rectangles
 2158 of 3 towers in the η -direction and 7 towers in the ϕ -direction. This asymmetric
 2159 window accounts for the curving of the produced charged particles only in the
 2160 ϕ direction. For photons, the size of the rectangle is 3 towers by 5 towers. In the
 2161 endcap region, all object types are clustered in rectangles of 5 towers by 5 tow-
 2162 ers, as the effect of the magnetic field curvature is less pronounced in this region.
 2163 The sum of the energies in these clusters provide the final energy measurement
 2164 for the electron or photon.

2165 6.2.1 PHOTON IDENTIFICATION

2166 The original requirement for constructing a photon cluster, a significant energy
 2167 deposit in the electromagnetic calorimeter without a corresponding track or en-
 2168 ergy deposits in the hadronic calorimeter, is already effective in identifying pho-
 2169 tons. However, there is a significant background for prompt photon production
 2170 from the decays of pions, $\pi^0 \rightarrow \gamma\gamma$. These can be identified using the shape of
 2171 the cluster in the narrow η granularity in the first layer of the EM calorimeter.

2172 6.2.2 ELECTRON IDENTIFICATION

2173 Prompt electrons have a number of backgrounds, such as secondary electrons
 2174 from hadron decays or misidentified hadronic jets, that can be rejected using ad-
 2175 dditional information from the EM calorimeter and the inner detector. The most
 2176 basic level of electron identification, referred to as Loose, makes requirements
 2177 on the shower shapes in the high granularity first layer of the EM calorimeter
 2178 as well as the quality of the inner detector track. It also requires a good match
 2179 between the track and the calorimeter energy deposits and a small fraction of
 2180 energy in the hadronic calorimeter behind the electromagnetic cluster. ATLAS
 2181 defines several additional working points, including Medium and Tight, which
 2182 provide progressively lower background rates for electrons by imposing addi-
 2183 tionally strict requirements on the above variables as well as new requirements
 2184 like the impact parameter of the inner detector track or the comparison of the
 2185 cluster energy to the momentum in the inner detector.

2186 6.3 MUONS

2187 Muons produced in ATLAS first traverse the inner detector and leave behind a
 2188 track as described in Section 6.1. The muon then passes through the calorimeter,
 2189 leaving behind a small, characteristic amount of energy, and then passes through
 2190 the muon spectrometer where it produces hits in the MDTs or CSCs. Muon tracks
 2191 are formed from local segments of hits in each layer of the MDTs or CSCs, and
 2192 then the final muon spectrometer track is formed by combining the two local
 2193 segments [26]. When a track is reconstructed in both the inner detector and
 2194 the muon spectrometer, the track is refitted to include the hits in both the inner
 2195 detector and the muon spectrometer, and forms a combined muon.

2196 In a few regions of the detector, a muon may fail to leave behind both a com-
 2197 plete inner detector and muon system track. For a very small fraction of the
 2198 acceptance of the muon system, there is only one layer of muon chambers and a
 2199 global muon system track is not formed. In this case, as long as the track in the
 2200 inner detector exists and geometrically matches to a segment, a segment-tagged
 2201 muon is formed using momentum measurements from the inner detector. In
 2202 the region where the muon system has coverage but the inner detector does not,
 2203 $2.5 < |\eta| < 2.7$, a stand-alone muon is formed which uses only information
 2204 from the muon system. And for muons produced within one of the few holes in
 2205 the muon system, including $|\eta| < 0.1$, the characteristic energy deposits in the

2206 calorimeter can be used to tag an inner detector track as a calo-tag muon. These
 2207 additional categories are used to achieve high efficiency over a larger range of
 2208 acceptance, but the combined muons are the most reliable.

2209 6.3.1 MUON IDENTIFICATION

2210 The various types of muons are incorporated into three working points: Loose,
 2211 Medium, and Tight, which reflect the increasing muon purity for each of the
 2212 selections definitions. Tight muons include only combined muons with a good
 2213 track fit quality and momentum resolution and at least two hits in a precision
 2214 muon system layer. Medium muons include those in tight as well as combined
 2215 muons with one precision hit and one precision hole, where hole is defined in
 2216 the same way as in Section 6.1. The medium working point also includes stand-
 2217 alone muons with $|\eta| > 2.5$ and at least two hits in precision layers. And finally
 2218 the loose working point includes both medium and tight muons, but additional
 2219 includes segment-tagged and calo-tagged muons in the region $|\eta| < 0.1$.

2220 6.4 JETS

2221 A jet does not directly correspond to a physical particle, unlike all of the recon-
 2222 structed objects described above, but instead tries to capture the conical cascade
 2223 of particles produced in the hadronization of a quark or gluon from the proton-
 2224 proton collision. The hadronization process creates a very large number of col-
 2225 limated particles, with a high enough density that individually reconstructing all
 2226 of the produced particles in the calorimeter is not possible within ATLAS. How-
 2227 ever most analyses are interested only in the kinematics of the particle which
 2228 produced the cascade, rather than the individual products. Therefore, jets are
 2229 a useful tool to measure the combined energy and direction of the ensemble of
 2230 products and thus represents the kinematics of the original. Jet algorithms are
 2231 very generic and can be used to group together a number of types of objects to
 2232 form aggregate representations. For example, truth particles in simulation can
 2233 be grouped in truth jets, or tracks from the inner detector can be grouped to-
 2234 gether to form track jets. This section, however, will focus on calorimeter jets
 2235 which take topoclusters of energy deposits in the calorimeter as inputs and pro-
 2236 duce a combined object which represents the energy measured by the calorime-
 2237 ter and the location where it was deposited.

2238 6.4.1 TOPOLOGICAL CLUSTERING

2239 Hadrons often deposit their energy into multiple individual cells in both the elec-
 2240 tromagnetic and hadronic calorimeters. The purpose of topological clustering is
 2241 to group cells in all three dimensions into clusters that represent a single energy
 2242 deposit. The procedure must be robust enough to reject noise fluctuations in
 2243 the cell energy measurements that can come from both electronic noise and ad-
 2244 dditional low energy particles produced in pileup activity. The background level

of calorimeter noise is called σ_{noise} , and is an important component of the topological clustering.

The topological clusters are formed in a three step process called the 4-2-0 threshold scheme, which uses three energy thresholds to build up a cluster from cells [27]. First, any cells with a measured energy above $4\sigma_{\text{noise}}$ are identified as seed cells. The cells adjacent to the seed cells with a measured energy above $2\sigma_{\text{noise}}$ are called secondary cells. All of the cells which are adjacent to a secondary cell with $E_{\text{cell}} > 2\sigma_{\text{noise}}$ are also labeled secondary cells. Tertiary cells are those immediately adjacent to a seed or secondary cell with a measured energy above zero. Adjacency in this sense is defined in three dimensions, cells are adjacent if they are neighbors within a layer but also if they have the same $\eta - \phi$ coordinates but are in adjacent layers or even in an adjacent layer in another calorimeter.

From these definitions, clusters are built by resolving the seeds in order of significance, the ratio $E_{\text{cell}}/\sigma_{\text{noise}}$. All adjacent secondary cells to the highest significance seed are added to that seed's topocluster, and any of those cells which would also have qualified as seeds are removed from the list of seeds. Once all of the secondary cells have been added, the tertiary cells are then added to that cluster as well. This procedure is then iterated until no seeds remain, forming the first round of topoclusters.

It is also useful to split topoclusters into multiples if local maxima are present within the topocluster, as clusters produced by multiple nearby particles can merge. The splitting process begins by finding local maxima cells in the middle layer of the calorimeters with a minimum energy of 500 MeV and at least four neighboring secondary cells. These requirements reduce the likelihood to split a cluster due to random fluctuations, as the middle layers provide the most reliable energy measurements. Cells between two local maxima can then be shared between two clusters to account for overlapping contributions from two particles. The energy sharing is weighted by the energy of each cluster as well as the distance of the cell to the centroid of that cluster.

The energies of all the cells in the cluster are then summed together to form the energy of that cluster. The energy needs to be corrected for the various losses expected in the calorimeter, as described in Section 5.4. The simplest correction, scaling the measured energy by the sampling fraction, brings the cluster energies to the EM scale. It is called the EM scale because it accurately describes the energy of electromagnetic showers.

Another scale is defined to improve accuracy for hadronic processes, the local cluster weighted (LCW) scale, that helps to correct for the expected variations in hadronic energy deposits. The LCW correction first determines if the shower is hadronic or electromagnetic, based on the depth of the shower and the cluster energy density. For hadronic showers, the energy is corrected for calorimeter non-compensation, an effect which reduces the measured energy of hadronic showers because some of the energy goes into invisible processes like the break up of nuclei. All clusters are then corrected for energy that may be deposited in uninstrumented regions in that cluster's location in the calorimeter, and they are

2290 also corrected with an estimate of how much energy falls outside the extent of
 2291 the cluster based on its shape and the deposit type.

2292 6.4.2 JET ALGORITHMS

2293 Using the topological clusters as inputs, a jet algorithm groups them together
 2294 into a collection of adjacent energy deposits that is intended to correspond to
 2295 a single process [28]. Jet algorithms need a few key characteristics to be usable
 2296 for physics analysis. First, the jets produced by the algorithm should have little
 2297 dependence on the addition of soft particles to the event (infrared safety), as a
 2298 negligible addition of energy should not significantly modify the event topology.
 2299 Similarly, the jets produced by the algorithm should also not significantly depend
 2300 on mostly collinear splitting of an input particle (collinear safety); that is, a single
 2301 quark replaced by two, parallel quarks with half the original's momentum should
 2302 not change the resulting jets, which are intended to capture only the properties
 2303 of the aggregate and not those of individual particles. And finally the algorithm
 2304 needs to be sufficiently simple and fast to be used for the large rate of collected
 2305 proton-proton collisions on [ATLAS](#).

2306 The most commonly used algorithm on [ATLAS](#) that satisfies these requirements
 2307 is called the anti- k_t algorithm, and is discussed in further detail in Reference [29].
 2308 The anti- k_t , in brief, relies on iteratively combining the input objects that are
 2309 closest together, where closest is defined by a particular distance metric, $d_{i,j}$,
 2310 where the index i represents the combination constructed so far and j is an ad-
 2311 ditional object being considered. The combinations stop when the closest re-
 2312 maining object is the beam itself, where the distance to the beam is called $d_{i,B}$.
 2313 An entire class of algorithms follows this procedure with the following distance
 2314 metrics

$$d_{i,j} = \min(k_{ti}^{2p}, k_{tj}^{2p}) \frac{\Delta_{ij}^2}{R^2} \quad (18)$$

$$d_{i,B} = k_{ti}^{2p} \quad (19)$$

2315 where $\Delta_{ij} = (y_i - y_j)^2 + (\phi_i - \phi_j)^2$, k_{ti} is the transverse momentum of the
 2316 object, y is the rapidity, and p is a parameter of the algorithm. Anti- k_t is the
 2317 particular case where $p = -1$, and is a choice that results in an algorithm that is
 2318 both infrared and collinear safe.

2319 The algorithm is repeated until there are no input objects remaining, which
 2320 results in a series of jets. Each jet has a complete four momentum from the com-
 2321 bination of its input clusters, where the combinations assume a mass of zero.
 2322 The jet energies then need to be calibrated to attempt to match the energy of the
 2323 object which produced the jet.

2324 6.4.3 JET ENERGY SCALE

2325 Though the [LCW](#) scheme attempts to correct the topoclusters to reflect the true
 2326 deposited energy, the correction does not fully account for energy lost within

2327 the calorimeters. Because of these effects, the original reconstructed jet energy
 2328 does not reflect the true energy of the particle which initiated the jet. Therefore
 2329 it is necessary to additionally correct the reconstructed jet itself, in addition to
 2330 the corrections on the inputs. This correction is referred to as the **JES**, which
 2331 combines several individual steps of calibration [30].

2332 The first calibration step corrections the direction of the jet to ensure that it
 2333 points back to the primary vertex. Next, the energy of the jet is corrected for
 2334 pileup by subtracting the expected contribution from pileup based on the mo-
 2335 mentum, η , and area of the jet as well as the number of reconstructed vertices
 2336 and expected number of interactions per crossing. The largest single correction
 2337 is the absolute η and scale correction, where the jet energy and pseudorapidity
 2338 is corrected to attempt to match the energy and pseudorapidity of the parton
 2339 which produced it. This correction is measured in simulation by comparing the
 2340 reconstructed jet energies to the energy of the truth particle which produced it.
 2341 However the simulation is not relied on alone to estimate this correction, and an
 2342 additional step applies an additional energy correction based on in-situ measure-
 2343 ments in data. These corrections come from various techniques which measure
 2344 jet energies indirectly by balancing them with other, well-measured objects. In
 2345 the central region ($|\eta| < 1.2$), jets are balanced against photons and the leptonic
 2346 decays of Z bosons and high momentum jets ($p_T > 210$ GeV) are also balanced
 2347 against multiple smaller jets in multijet events. Jets at larger pseudorapidities,
 2348 above $|\eta| = 1.2$, are calibrated by balancing with lower pseudorapidity jets.

2349 These steps introduce a number of systematic uncertainties, referred to as
 2350 the **JES** uncertainty. The largest of these comes from the in-situ measurements,
 2351 which are statistically limited in measuring high momentum and high pseudora-
 2352 pidity jets. The total, fractional **JES** uncertainty is shown as a function of p_T in
 2353 Figure 45. The uncertainty falls to a minimum value of just over 1.0% around a
 2354 few hundred GeV, and rises again at high momentum because of the difficulty of
 2355 measuring jet balance in data above 2-3 TeV. The uncertainty is also minimized
 2356 at low $|\eta|$, and grows at large $|\eta|$ again where making in-situ measurements is
 2357 difficult. This technique does not actually provide a measurement of the uncer-
 2358 tainty for the highest energy jets, above 3 TeV, because there are not enough
 2359 measured data events to provide them. An alternative method for deriving the
 2360 **JES** and **JES** uncertainty that can be used even for very high p_T jets will be dis-
 2361 cussed in Chapter 8.

2362 6.5 MISSING TRANSVERSE ENERGY

2363 Among stable **SM** particles, only the neutrino cannot be directly measured in the
 2364 **ATLAS** detector. Because the neutrino carries neither electric nor color charge, it
 2365 is very unlikely to interact with the tracking detectors or the calorimeters, and in-
 2366 stead passes through the detector completely unobserved. Some particles which
 2367 have been conjectured to exist, like the **LSP** in many **SUSY** models, would also
 2368 have the same behavior. Therefore, it is important for **ATLAS** to provide some
 2369 way to assess the momentum carried away by a neutral, colorless particle. This
 2370 can be accomplished through a measurement of missing energy in the transverse

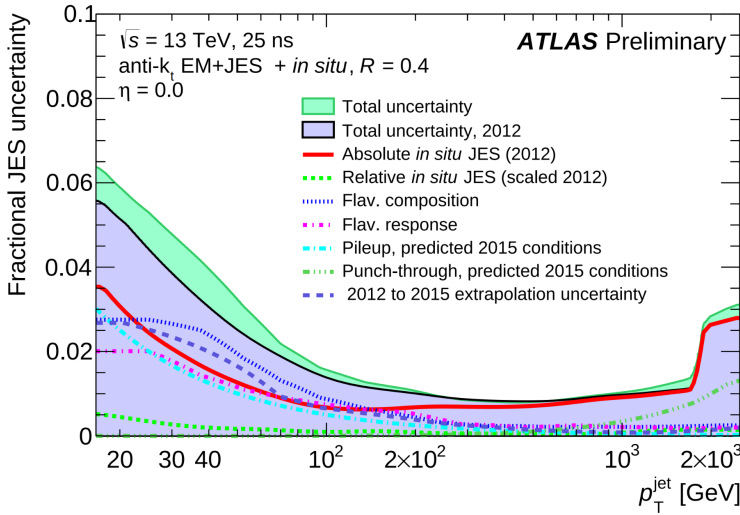


Figure 45: The total, fractional JES uncertainties estimated for 2015 data as a function of jet p_T .

direction, or E_T^{miss} , which quantifies the momentum imbalance of the observed particles. From the conservation of momentum and the lack of the initial momentum in the transverse plane in the proton-proton collisions, any imbalance of momentum can be inferred to be carried away by an unmeasured particle.

E_T^{miss} is more precisely defined as the magnitude of the vector sum of the (p_x, p_y) components of each observed object's momentum. The definition is simple, but there can be significant complexity in defining the inputs. As of Run 2, ATLAS uses a common algorithmic approach to carefully calculate missing energy, but each analysis is free to define its own inputs. For the analysis discussed throughout this thesis, the missing energy inputs consist of the electrons, photons, muons, and jets discussed in the previous sections, in addition to a track-based soft term.

To produce the most precise measurement of E_T^{miss} , it is important to use the best representation of the momentum of each of the input objects, which can often be reconstructed as multiple different types in a single event. For example, an electron can be reconstructed separately as an electron (Section 6.2) and a jet (Section 6.4), but the electron representation has the highest precision for reconstructing the true electron momentum. To ensure no duplications in the E_T^{miss} definition, the inputs are collectively considered for overlap removal. Only the most precise object type is kept for objects that fall within a cone of $\Delta R < 0.2$ for pairs of electrons and jets and a cone of $\Delta R < 0.4$ for other pair types.

The fully reconstructed objects do not include all of the energy within the events, as some clusters do not enter into a jet and some tracks are not classified as electrons or muons. These momentum carried by these objects is accounted for in a soft-term, which tallies all of the energy carried by the particles too soft to form separate objects. The track soft term uses only tracking information to estimate the contribution of soft objects, and does so by vectorially summing the momentum of all well-reconstructed tracks with momentum above 400 MeV.

2399 All of these contributions together give a single E_T^{miss} value for a given event.
2400 The direction of that missing energy is taken as opposite the vector sum of all the
2401 constituents, to correspond to the momentum an invisible particle would have to
2402 have to make the event balanced. Depending on the context, this missing energy
2403 can be considered the energy of a neutrino or an LSP, with a large missing energy
2404 being a common signal criteria for searches for new physics.

2405

PART IV

2406

CALORIMETER RESPONSE

2407

You can put some informational part preamble text here.

2408

2409 RESPONSE MEASUREMENT WITH SINGLE HADRONS

2410 As discussed in Section 6.4, colored particles produced in collisions hadronize
2411 into jets of multiple hadrons. One approach to understanding jet energy mea-
2412 surements in the ATLAS calorimeters is to evaluate the calorimeter response to
2413 those individual hadrons; measurements of individual hadrons can be used to
2414 build up an understanding of the jets that they form. The redundancy of the
2415 momentum provided by the tracking system and the energy provided by the
2416 calorimeter provides an opportunity to study calorimeter response using real
2417 collisions, as described further in Section 7.2.

2418 Calorimeter response includes a number of physical effects that can be ex-
2419 tracted to provide insight into many aspects of jet modeling. First, many charged
2420 hadrons interact with the material of the detector prior to reaching the calorime-
2421 ters and thus do not deposit any energy. Comparing this effect in data and sim-
2422 ulation is a powerful tool in validating the interactions of particles with the mate-
2423 rial of the detector and the model of the detector geometry in simulation, see Sec-
2424 tion 7.2.2. The particles which do reach the calorimeter deposit their energy into
2425 several adjacent cells, which are then clustered together. The energy of the clus-
2426 ter is then the total energy deposited by that particle. Comparing the response of
2427 hadrons in data to that of simulated hadrons provides a direct evaluation of the
2428 showering of hadronic particles and the energy deposited by particles in matter
2429 (Section 7.2.4).

2430 The above studies all use an inclusive selection of charged particles, which are
2431 comprised predominantly of pions, kaons, and (anti)protons. It is also possible to
2432 measure the response to various identified particle types separately to evaluate
2433 the simulated interactions of each particle, particularly at low energies where
2434 differences between species are very relevant. Pions and (anti)protons can be
2435 identified through decays of long-lived particles, in particular Λ , $\bar{\Lambda}$, and K_S^0 , and
2436 then used to measure response as described above. This is discussed in detail in
2437 Section 7.3.

2438 The results in this chapter use data collected at 7 and 8 TeV collected in 2010
2439 and 2012, respectively. Both are included as the calorimeter was repaired and
2440 recalibrated between those two data-taking periods. Both sets of data are com-
2441 compared to an updated simulation that includes new physics models provided by
2442 Geant4 [31] and improvements in the detector description [32, 33]. The present
2443 results are published in European Physical Journal C (EPJC) [34] and can be com-
2444 compared to a similar measurement performed in 2009 and 2010 [35], which used
2445 the previous version of the simulation framework [36].

2446 7.1 DATASET AND SIMULATION

2447 7.1.1 DATA SAMPLES

2448 The two datasets used in this chapter are taken from dedicated low-pileup runs
 2449 where the fraction of events with multiple interactions was negligible. These
 2450 datasets are used rather than those containing full-pileup events to facilitate mea-
 2451 surement of isolated hadrons. The 2012 dataset at $\sqrt{s} = 8$ TeV contains 8 mil-
 2452 lion events and corresponds to an integrated luminosity of 0.1 nb^{-1} . The 2010
 2453 dataset at $\sqrt{s} = 7$ TeV contains 3 million events and corresponds to an inte-
 2454 grated luminosity of 3.2 nb^{-1} . The latter dataset was also used for the 2010 re-
 2455 sults [35], but it has since been reanalyzed with an updated reconstruction in-
 2456 cluding the final, best understanding of the detector description for the material
 2457 and alignment from Run 1.

2458 7.1.2 SIMULATED SAMPLES

2459 The two datasets above are compared to simulated single-, double-, and non-
 2460 diffractive events generated with Pythia8 [37] using the A2 configuration of
 2461 hadronization [38] and the MSTW 2008 parton-distribution function set [39,
 2462 40]. The admixture of the single-, double-, and non-diffractive events uses the
 2463 default relative contributions from Pythia8. The conditions and energies for
 2464 the two simulations are chosen so that they match those of the corresponding
 2465 dataset.

2466 To evaluate the interaction of hadrons with detector material, the simulation
 2467 uses two different collections of hadronic physics models, called physics lists, in
 2468 Geant4 9.4 [41]. The first, QGSP_BERT, combines the Bertini intra-nuclear
 2469 cascade [42–44] below 9.9 GeV, a parametrized proton inelastic model from 9.5
 2470 to 25 GeV [45], and a quark-gluon string model above 12 GeV [46–50]. The
 2471 second, FTFP_BERT, combines the Bertini intra-nuclear cascade [42–44] below
 2472 5 GeV and the Fritiof model [51–54] above 4 GeV. In either list, Geant4 en-
 2473 forces a smooth transition between models where multiple models overlap.

2474 7.1.3 EVENT SELECTION

2475 The event selection for this study is minimal, as the only requirement is selecting
 2476 good-quality events with an isolated track. Such events are triggered by requir-
 2477 ing at least two hits in the minimum-bias trigger scintillators. After trigger, each
 2478 event is required to have exactly one reconstructed vertex, and that vertex is re-
 2479 quired to have four or more associated tracks.

2480 The particles which are selected for the response measurements are first iden-
 2481 tified as tracks in the inner detector. The tracks are required to have at least 500
 2482 MeV of transverse momentum. To ensure a reliable momentum measurement,
 2483 these tracks are required to have at least one hit in the pixel detector, six hits in
 2484 the SCT, and small longitudinal and transverse impact parameters with respect
 2485 to the primary vertex [35]. For the majority of the measurements in this chapter,

2486 the track is additionally required to have 20 hits in the TRT, which significantly
 2487 reduces the contribution from tracks which undergo nuclear interactions. This
 2488 requirement and its effect is discussed in more detail in Section 7.2.5. In addition,
 2489 tracks are rejected if there is any other reconstructed track which extrapolates
 2490 to the calorimeter within a cone of $\Delta R = \sqrt{(\Delta\phi)^2 + (\Delta\eta)^2} < 0.4$. This require-
 2491 ment guarantees that the contamination of energy from nearby charged particles
 2492 is negligible [35].

2493 7.2 INCLUSIVE HADRON RESPONSE

2494 The calorimeter response is more precisely defined as the ratio of the measured
 2495 calorimeter energy to the true energy carried by the particle, although this true
 2496 energy is unknown. For charged particles, however, the inner detector provides
 2497 a very precise measurement of momentum (with uncertainty less than 1%) that
 2498 can be used as a proxy for true energy. The ratio of the energy deposited by
 2499 the charged particle in the calorimeter, E , to its momentum measured in the
 2500 inner detector p , forms the calorimeter response measure called E/p . Though
 2501 the distribution of E/p contains a number of physical features, this study focuses
 2502 on the trends in two aggregated quantities: $\langle E/p \rangle$, the average of E/p for the
 2503 selected tracks, and the zero fraction, the fraction of tracks with no associated
 2504 energy in the calorimeter for those tracks.

2505 The calorimeter energy assigned to a track is defined using clusters. The clus-
 2506 ters are formed using a 4–2–0 algorithm [55] that begins with seeds requiring
 2507 at least 4 times the average calorimeter cell noise. The neighboring cells with
 2508 at least twice that noise threshold are then added to the cluster, and all bound-
 2509 ing cells are then added with no requirement. This algorithm minimizes noise
 2510 contributions through its seeding process, and including the bounding cells im-
 2511 proves the energy resolution [56]. The clusters are associated to a given track
 2512 if they fall within a cone of $\Delta R = 0.2$ of the extrapolated position of the track,
 2513 which includes about 90% of the energy on average [35].

2514 7.2.1 E/P DISTRIBUTION

2515 The E/p distributions measured in both data and simulation are shown in Fig-
 2516 ure 46 for two example bins of track momentum and for tracks in the central
 2517 region of the detector. These distributions show several important features of
 2518 the E/p observable. The large content in the bin at $E = 0$ comes from tracks that
 2519 have no associated cluster, which occurs due to interactions with detector mate-
 2520 rial prior to reaching the calorimeter or the energy deposit being insufficiently
 2521 large to generate a seed, and are discussed in Section 7.2.2. The small negative
 2522 tail also comes from tracks that do not deposit any energy in the calorimeter but
 2523 are randomly associated to a cluster with an energy below the noise threshold.
 2524 The long positive tail above 1.0 comes from the contribution of neutral parti-
 2525 cles. Nearby neutral particles deposit (sometimes large) additional energy in the
 2526 calorimeter but do not produce tracks in the inner detector, so they cannot be
 2527 rejected by the track isolation requirement. Additionally the peak and mean of

2528 the distribution falls below 1.0 because of the loss of energy not found within
 2529 the cone as well as the non-compensation of the calorimeter.

2530 The data and simulation share the same features, but the high and low tails
 2531 are significantly different. The simulated events tend to overestimate the con-
 2532 tribution of neutral particles to the long tail, an effect which can be isolated and
 2533 removed as discussed in Section 7.2.3. Additionally, the simulated clusters have
 2534 less noise on average, although this is a small effect on the overall response.

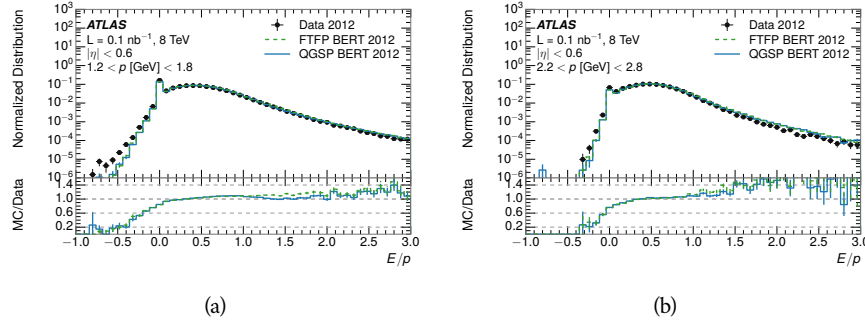


Figure 46: The E/p distribution and ratio of simulation to data for isolated tracks with
 (a) $|\eta| < 0.6$ and $1.2 < p/\text{GeV} < 1.8$ and (b) $|\eta| < 0.6$ and $2.2 < p/\text{GeV} < 2.8$.

2535 7.2.2 ZERO FRACTION

2536 The fraction of particles with no associated clusters, or similarly those with $E \leq$
 2537 0, reflects the modeling of both the detector geometry and hadronic interactions.
 2538 The zero fraction is expected to rise as the amount of material a particle traverses
 2539 increases, while it is expected to decrease as the particle energy increases. This
 2540 dependence can be seen in Figure 47, where the zero fraction in data and simula-
 2541 tion is shown as a function of momentum and the amount of material measured
 2542 in interaction lengths. The trends are similar between 2010 and 2012 and for
 2543 positively and negatively charged particles. The zero fraction decreases with
 2544 energy as expected. The absolute discrepancy in zero fraction between data and
 2545 simulation decreases with momentum from 5% to less than 1%, but this becomes
 2546 more pronounced in the ratio as the zero fraction shrinks quickly with increas-
 2547 ing momentum. The amount of material in the detector increases with η , which
 2548 is used to obtain results for interaction lengths ranging between 0.1 and 0.65 λ .
 2549 As the data and simulation have significant disagreement in the zero fraction
 2550 over a number of interaction lengths, the difference must be primarily from the
 2551 modeling of hadronic interactions with detector material and not just the detec-
 2552 tor geometry. Although two different hadronic interaction models are shown
 2553 in the figure, they have very similar discrepancies to data because both use the
 2554 same description (the BERT model) at low momentum.

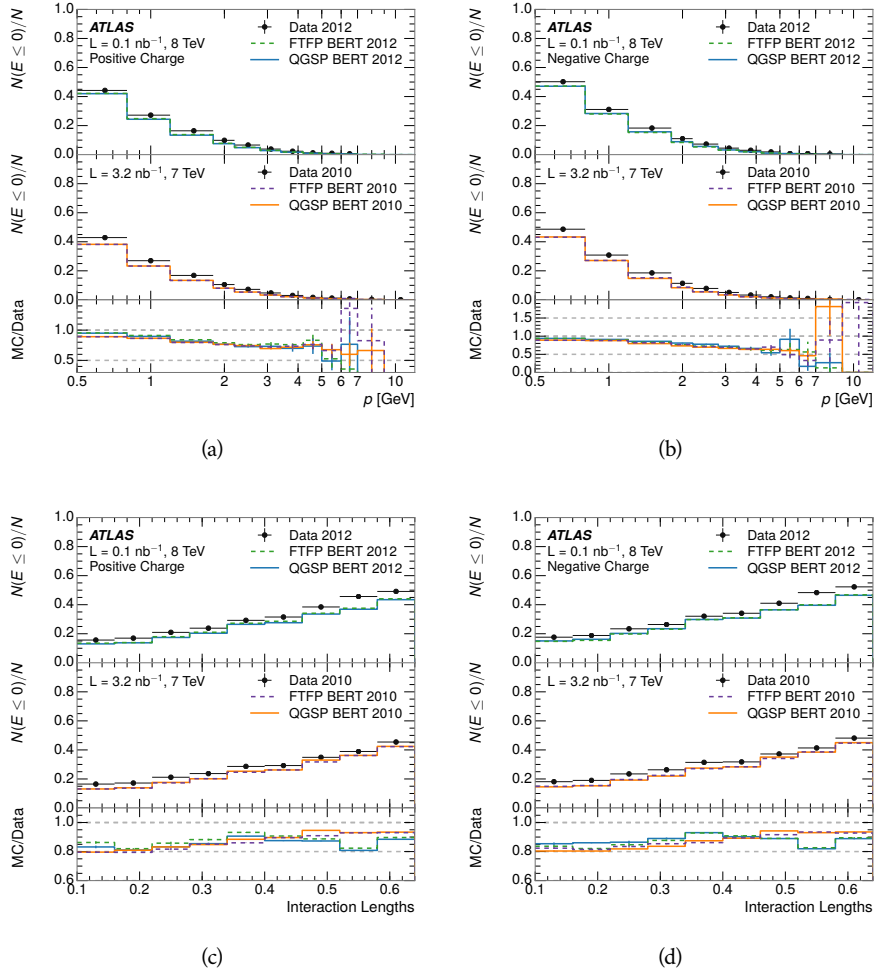


Figure 47: The fraction of tracks as a function (a, b) of momentum, (c, d) of interaction lengths with $E \leq 0$ for tracks with positive (on the left) and negative (on the right) charge.

2555 7.2.3 NEUTRAL BACKGROUND SUBTRACTION

2556 The isolation requirement on hadrons is only effective in removing an energy
 2557 contribution from nearby charged particles. Nearby neutral particles, predomi-
 2558 nantly photons from π^0 decays, also add their energy to the calorimeter clusters,
 2559 but mostly in the electromagnetic calorimeter. The arrangement of energy de-
 2560 posits is shown in Figure 48, which illustrates both energy deposits from the
 2561 hadronic particle and additional deposits from neutral particles. It is possible to
 2562 measure this contribution, on average, using late-showering hadrons that min-
 2563 imally ionize in the electromagnetic calorimeter. Such particles are selected by
 2564 requiring that they deposit less than 1.1 GeV in the EM calorimeter within a
 2565 cone of $\Delta R < 0.1$ around the track. To ensure that these particles are well mea-
 2566 sured, they are additionally required to deposit between 40% and 90% of their
 2567 energy in the hadronic calorimeter within the same cone.

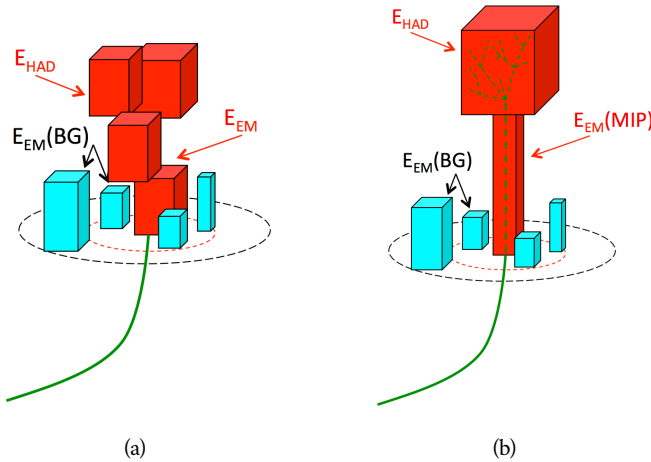


Figure 48: An illustration (a) of the geometry of energy deposits in the calorimeter. The red energy deposits come from the charged particle targeted for measurement, while the blue energy deposits are from nearby neutral particles and must be subtracted. The same diagram (b) for the neutral-background selec-
 tion, described in Section 7.2.3.

2568 These particles provide a clean sample to measure the nearby neutral back-
 2569 ground because they do not deposit energy in the area immediately surround-
 2570 ing them in the EM calorimeter, as shown in Figure 48. So, the energy deposits in the
 2571 region $0.1 < \Delta R < 0.2$ can be attributed to neutral particles alone. To estimate
 2572 the contribution to the whole cone considered for the response measurement,
 2573 that energy is scaled by a geometric factor of $4/3$. This quantity, $\langle E/p \rangle_{BG}$, mea-
 2574 sured in aggregate over a number of particles, gives the contribution to $\langle E/p \rangle$
 2575 from neutral particles in the EM calorimeter. Similar techniques were used in
 2576 the individual layers of the hadronic calorimeters to show that the background
 2577 from neutrals is negligible in those layers [35].

2578 The distribution of this background estimate is shown in Figure 49 for data
 2579 and simulation with the two different physics lists. The contribution from neu-

tral particles falls from 0.1 at low momentum to around 0.03 for particles above 7 GeV. Although the simulation captures the overall trend, it significantly overestimates the neutral contribution for tracks with momentum between 2 and 8 GeV. This effect was also seen in the tails of the E/p distributions in Figure 46. This difference is likely due to modeling of coherent neutral particle radiation in Pythia8 that overestimates the production of π^0 near the production of the charged particles. The discrepancy does not depend on η and thus is unlikely to be a mismodeling of the detector. This difference can be subtracted to form a corrected average of E/p .

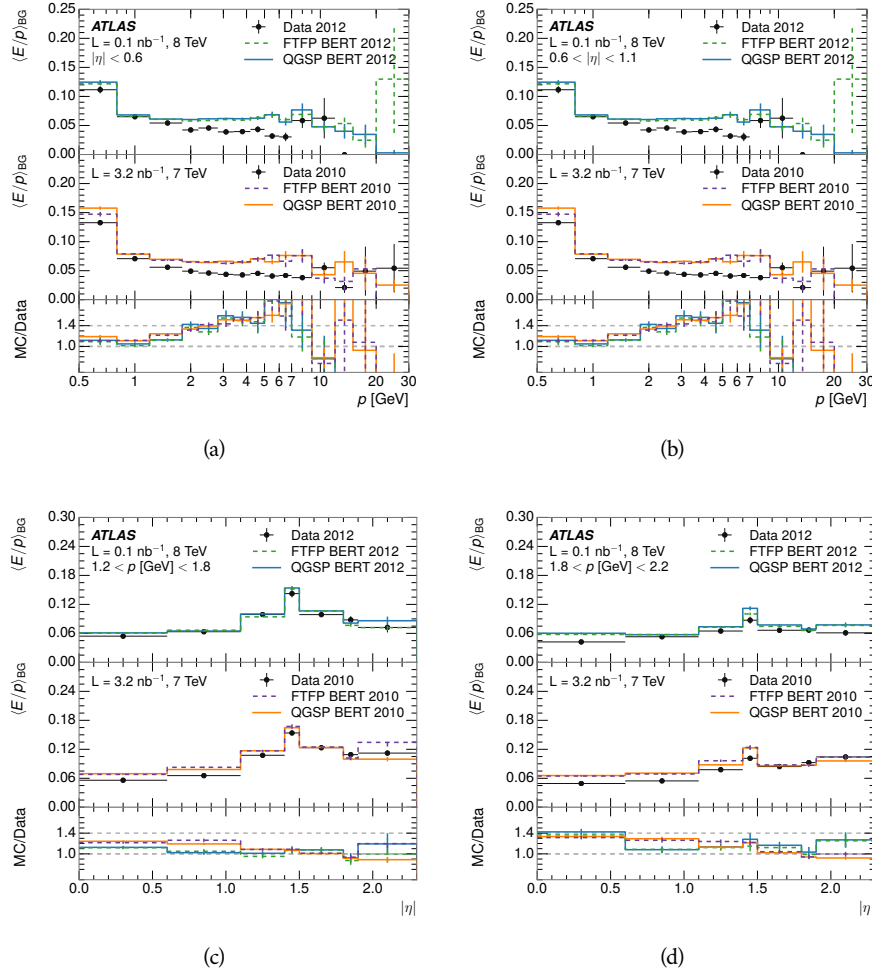


Figure 49: $\langle E/p \rangle_{BG}$ as a function of the track momentum for tracks with (a) $|\eta| < 0.6$, (b) $0.6 < |\eta| < 1.1$, and as a function of the track pseudorapidity for tracks with (c) $1.2 < p/\text{GeV} < 1.8$, (d) $1.8 < p/\text{GeV} < 2.2$.

7.2.4 CORRECTED RESPONSE

Figure 50 shows $\langle E/p \rangle_{COR}$ as a function of momentum for several bins of pseudorapidity. This corrected $\langle E/p \rangle_{COR} \equiv \langle E/p \rangle - \langle E/p \rangle_{BG}$ measures the average calorimeter response without the contamination of neutral particles. It is the

most direct measurement of calorimeter response in that it is the energy measured for fully isolated hadrons. The correction is performed separately in data and simulation, so that the mismodeling of the neutral background in simulation is removed from the comparison of response. The simulation overestimates the response at low momentum by about 5%, an effect that can be mostly attributed to the underestimation of the zero fraction mentioned previously. For $|\eta| < 0.6$, the data-simulation agreement has a larger discrepancy by about 5% for 2010 than 2012, although this is not reproduced in at higher pseudorapidity.

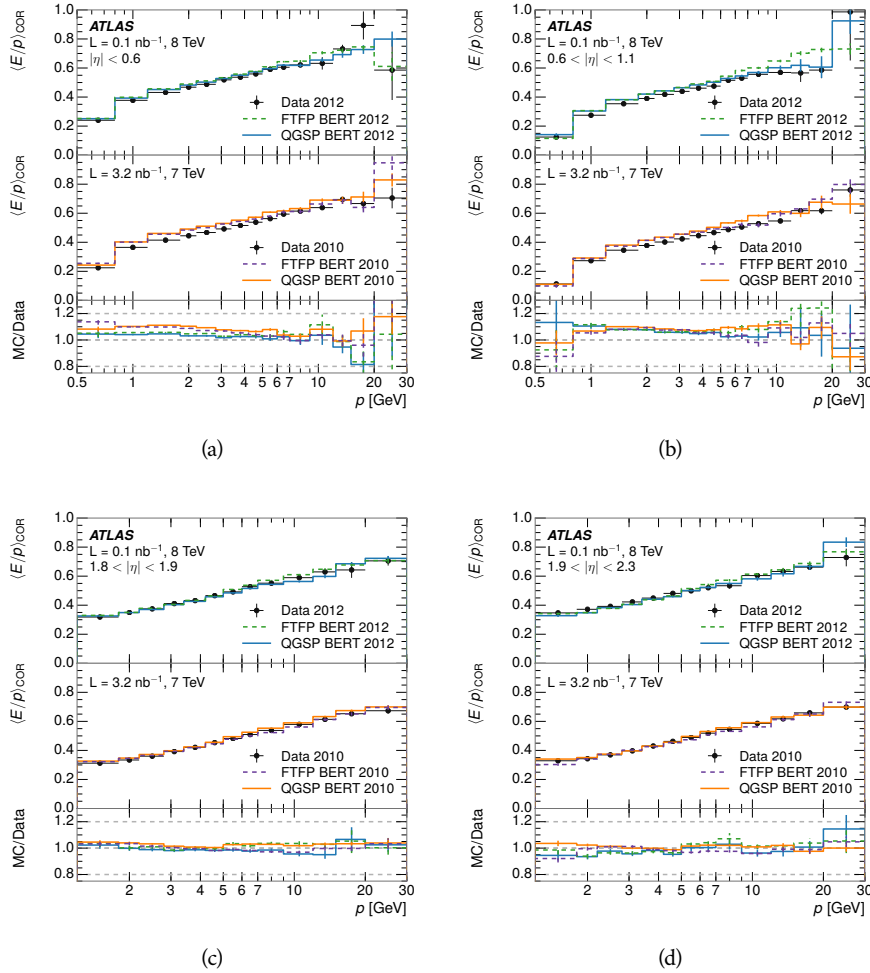


Figure 50: $\langle E/p \rangle_{\text{COR}}$ as a function of track momentum, for tracks with (a) $|\eta| < 0.6$, (b) $0.6 < |\eta| < 1.1$, (c) $1.8 < |\eta| < 1.9$, and (d) $1.9 < |\eta| < 2.3$.

The response measurement above used topological clustering at the EM scale, that is clusters were formed to measure energy but no corrections were applied to correct for expected effects like energy lost outside of the cluster or in uninstrumented material. It is also interesting to measure $\langle E/p \rangle_{\text{COR}}$ using LCW energies, which accounts for those effects by calibrating the energy based on the properties of the cluster such as energy density and depth in the calorimeter. Figure 51 shows these distributions for tracks with zero or more clusters and separately for tracks with one or more clusters. The calibration moves the mean

2609 value of $\langle E/p \rangle_{\text{COR}}$ significantly closer to 1.0 as desired, but the discrepancy be-
 2610 between data and simulation remains in the comparison that includes tracks with
 2611 zero associated clusters. The agreement between data and simulation improves
 2612 noticeably when at least one cluster is required, as this removes the contribution
 2613 from the mismodeling of the zero fraction.

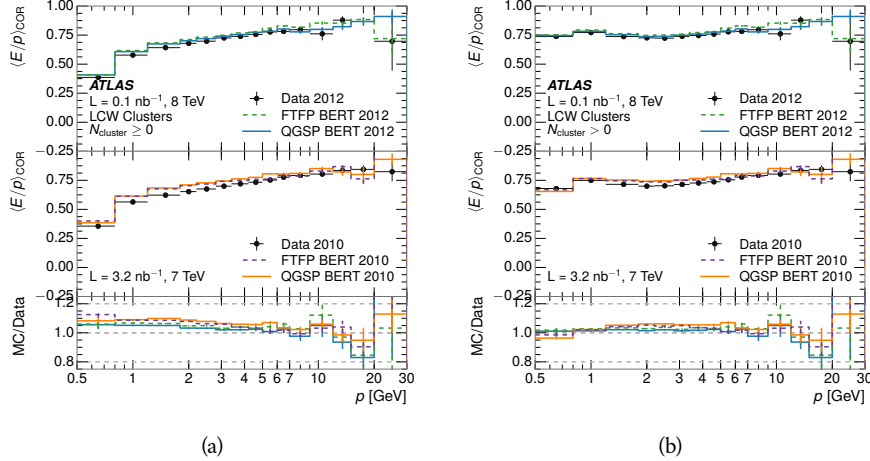


Figure 51: $\langle E/p \rangle_{\text{COR}}$ calculated using LCW-calibrated topological clusters as a function of track momentum for tracks with (a) zero or more associated topological clusters or (b) one or more associated topological clusters.

2614 7.2.5 ADDITIONAL STUDIES

2615 As has been seen in several measurements in previous sections, the simulation
 2616 does not correctly model the chance of a low momentum hadron to reach the
 2617 calorimeter. Because of the consistent discrepancy across pseudorapidity and
 2618 interaction lengths, this can be best explained by incomplete understanding of
 2619 hadronic interactions with the detector [34]. For example, a hadron that scat-
 2620 ters off of a nucleus in the inner detector can be deflected through a significant
 2621 angle and not reach the expected location in the calorimeter. In addition, these
 2622 interactions can produce secondary particles that are difficult to model.

2623 The requirement used throughout the previous sections on the number of
 2624 hits in the TRT reduces these effects by preferentially selecting tracks that do
 2625 not undergo nuclear interactions. It is interesting to check how well the simula-
 2626 tion models tracks with low numbers of TRT hits, which selects tracks that are
 2627 more likely to have undergone a hadronic interaction. Figure 52 compares the
 2628 distributions with $N_{\text{TRT}} < 20$ to $N_{\text{TRT}} > 20$ for real and simulated particles¹.
 2629 As expected, the tracks with fewer hits are poorly modeled in the simulation as
 2630 $\langle E/p \rangle_{\text{COR}}$ differs by as much as 25% at low momentum. They also have signifi-
 2631 cantly lower $\langle E/p \rangle_{\text{COR}}$ on average, because they are much less likely to have an
 2632 associated cluster.

¹The distribution with $N_{\text{TRT}} > 20$ is the same as shown in Figure 50 (a) and is included again here for the comparison.

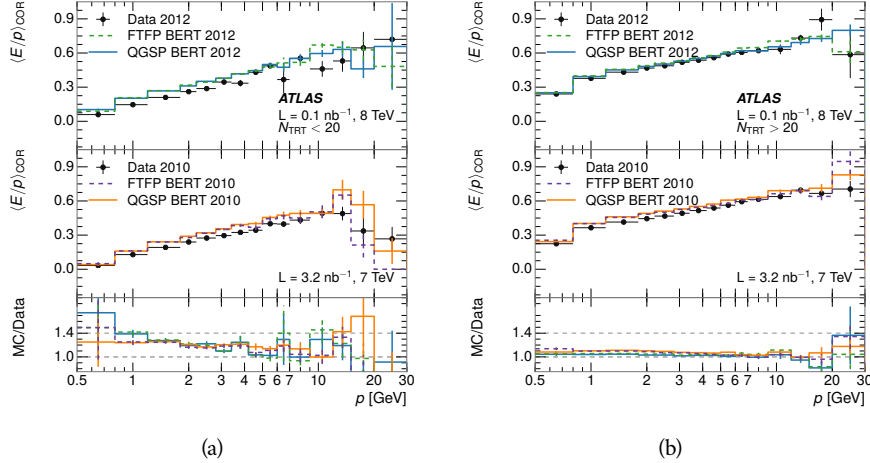


Figure 52: Comparison of the $\langle E/p \rangle_{\text{COR}}$ for tracks with (a) less than and (b) greater than 20 hits in the TRT.

Another interesting aspect of the simulation is the description of antiprotons at low momentum, where QGSP_BERT and FTFP_BERT have significant differences. This can be seen to have an effect in the inclusive response measurement when separated into positive and negative charge. The $\langle E/p \rangle_{\text{COR}}$ distributions for positive and negative particles are shown in Figure 53, where a small difference between QGSP_BERT and FTFP_BERT can be seen in the distribution for negative tracks. The figure also includes data, and the simulation overestimates $\langle E/p \rangle_{\text{COR}}$ mostly due to an underestimation in zero fraction. There is an approximately 5% difference between the 2010 and 2012 simulated events. The difference between positive and negative particles is demonstrated more clearly in Figure 54, which shows the E/p distribution in the two simulations separated by charge. There is a small difference around $E/p > 1.0$, which can be explained by the additional energy deposited by the annihilation of the antiproton in the calorimeter that is modeled well only in FTFP_BERT. This is also explored with data using identified antiprotons in Section 7.3.

The $\langle E/p \rangle$ results in previous sections have considered the electromagnetic and hadronic calorimeters together as a single energy measurement, to emphasize the total energy deposited for a given particle. However, the deposits in each calorimeter are measured separately and $\langle E/p \rangle$ can be constructed for each layer separately. As the layers are composed of different materials and are modeled separately in the detector geometry, confirmation that the simulation matches the data well in each layer adds confidence in both the description of hadronic interactions with the two different materials and also the geometric description of each.

The technique discussed in Section 7.2.3 for selecting MIPs in the electromagnetic calorimeter is also useful in studying deposits in the hadronic calorimeter. The tracks selected with the MIP requirements deposit almost all of their energy exclusively in the hadronic calorimeter. Figure 55 shows $\langle E/p \rangle_{\text{Had}}^{\text{RAW}}$, where RAW indicates that no correction has been applied for neutral backgrounds and

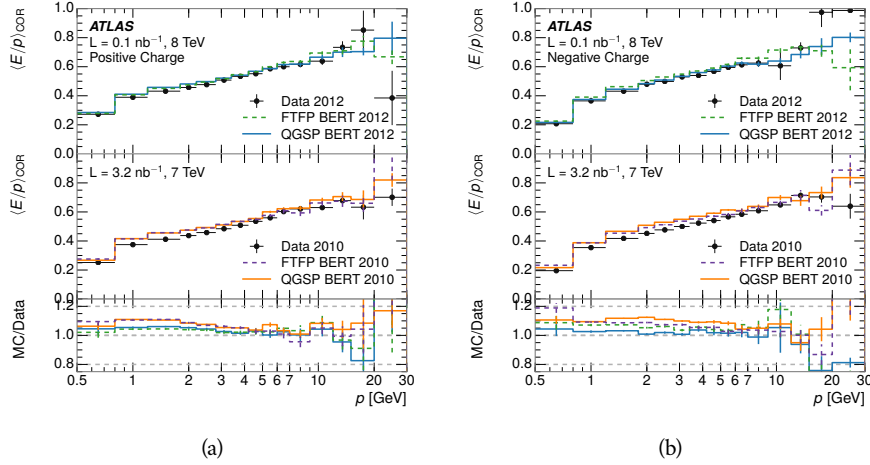


Figure 53: Comparison of the $\langle E/p \rangle_{\text{COR}}$ for (a) positive and (b) negative tracks as a function of track momentum for tracks with $|\eta| < 0.6$.

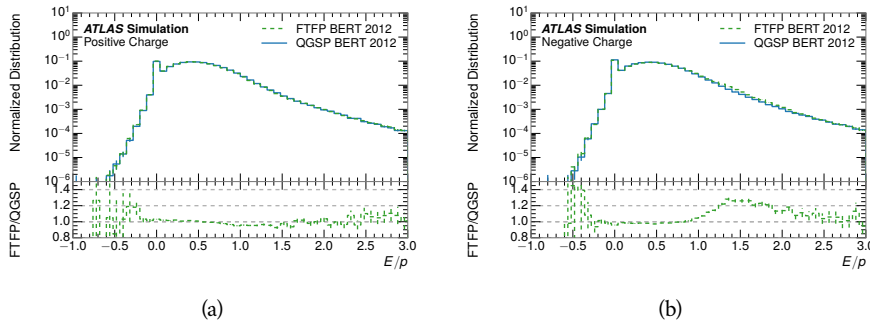


Figure 54: Comparison of the E/p distributions for (a) positive and (b) negative tracks with $0.8 < p/\text{GeV} < 1.2$ and $|\eta| < 0.6$, in simulation with the FTFP_BERT and QGSP_BERT physics lists.

Had indicates that only clusters for the hadronic calorimeter are included². The distributions are shown both for the original EM scale calibration and after LCW calibration. The data and simulation agree very well in this comparison, except in the lowest momentum bin where there is a 5% discrepancy that has already been seen in the measurements in Section 7.2.4.

A similar comparison can be made in the electromagnetic calorimeter by selecting particles which have no associated energy in the hadronic calorimeter. These results are measured in terms of $\langle E/p \rangle_{\text{COR}}^{\text{EM}}$, where EM designates that only clusters in the electromagnetic calorimeter are included and COR designates that the neutral background is subtracted as the neutral background is present in this case. Figure 56 shows the analogous comparisons to Figure 55 in the electromagnetic calorimeter. The $\langle E/p \rangle_{\text{COR}}$ values are lower on average in the EM calorimeter than in the hadronic calorimeter, which is an expected conse-

² The RAW and COR versions of $\langle E/p \rangle$ in this case are the same, as the neutral background is negligible in that calorimeter layer.

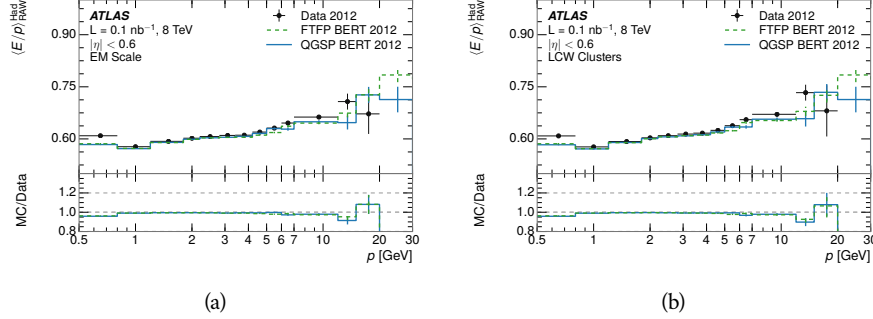


Figure 55: Comparison of the response of the hadronic calorimeter as a function of track momentum (a) at the EM-scale and (b) after the LCW calibration.

quence of their different material types (discussed in Section 5.4). In this case the disagreement between data and simulation is more pronounced, with discrepancies as high as 5% over a larger range of momenta. This level of discrepancy indicates that the description of the electromagnetic calorimeter is actually the dominant source of discrepancy in the combined distributions in Section 7.2.4.

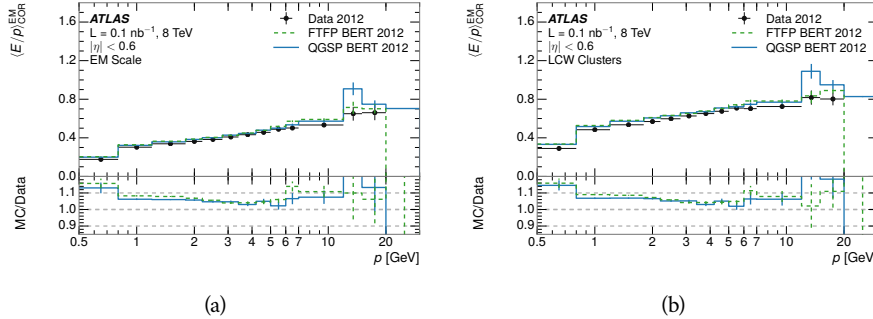


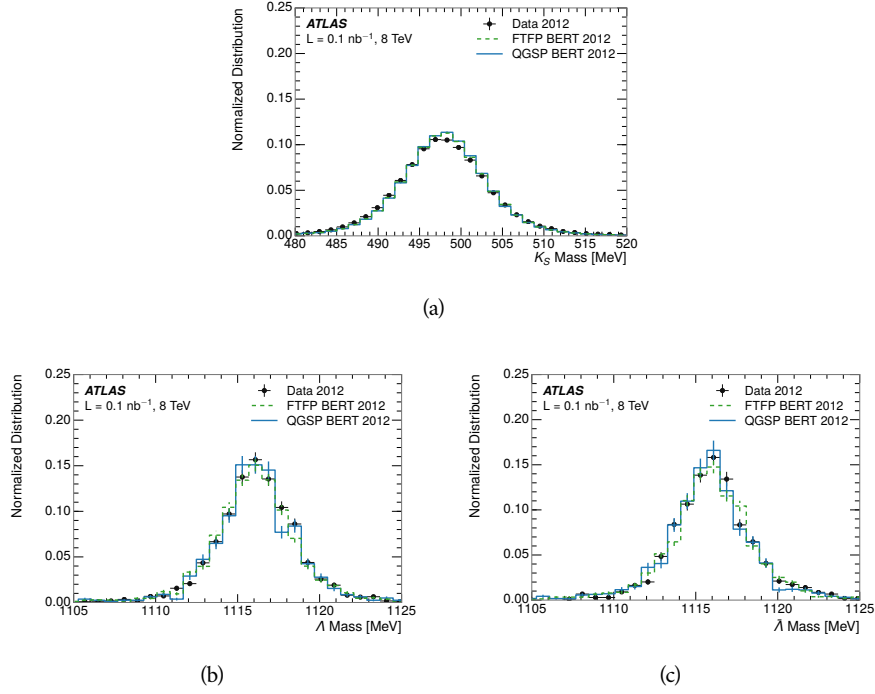
Figure 56: Comparison of the response of the EM calorimeter as a function of track momentum (a) at the EM-scale and (b) with the LCW calibration.

7.3 IDENTIFIED PARTICLE RESPONSE

The inclusive response measurement for hadrons can be augmented by measuring the response for specific particle species. The simulation models each particle type separately, and understanding the properties of each is important in constraining the uncertainty on jets. In order to select and measure specific hadrons, this section relies on the displaced decays of long-lived particles. Such decays can be identified by reconstructing secondary vertices with a requirement on mass. In particular, Λ , $\bar{\Lambda}$, and K_S^0 can be used to select a pure sample of protons, antiprotons, and pions, respectively.

2689 7.31 DECAY RECONSTRUCTION

2690 The measurement of the response for identified particles uses the same selection
 2691 as for inclusive particles (Section 7.1.3) with a few additions. Each event used is
 2692 required to have at least one secondary vertex, as described in Section 6.1.3, and
 2693 the tracks are required to match to that vertex rather than the primary vertex.
 2694 Pions are selected from decays of $K_S^0 \rightarrow \pi^+ \pi^-$, which is the dominant decay for
 2695 K_S^0 to charged particles. Protons are selected from decays of $\Lambda \rightarrow \pi^- p$ and an-
 2696 tiprotons from $\bar{\Lambda} \rightarrow \pi^+ \bar{p}$, which are similarly the dominant decays of Λ and $\bar{\Lambda}$
 2697 to charged particles. The species of parent hadron in these decays is determined
 2698 by reconstructing the mass of the tracks associated to the secondary vertex. The
 2699 sign of the higher momentum decay particle can distinguish between Λ and $\bar{\Lambda}$,
 2700 which of course have the same mass, as the proton or antiproton is kinemati-
 2701 cally favored to have higher momentum. The proton or antiproton will carry
 2702 the higher momentum above 95% of the time. Examples of the reconstructed
 2703 masses used to select these decays are shown in Figure 57. The mass peaks in
 2704 data and both simulation models are very similar.



2705 Figure 57: The reconstructed mass peaks of (a) K_S^0 , (b) Λ , and (c) $\bar{\Lambda}$ candidates.
 2706
 2707
 2708
 2709
 2710
 2711

The dominant backgrounds for the identified particle decays are nuclear interactions and combinatoric sources. These are suppressed by the kinematic requirements on the tracks as well as an additional veto which removes candidates that are consistent with both a Λ or $\bar{\Lambda}$ and a K_S^0 hypothesis, which is possible because of the different assumptions on particle mass in each case [35]. After these requirements, the backgrounds are found to be negligible compared to the statistical errors on these measurements.

2712 7.3.2 IDENTIFIED RESPONSE

2713 With these techniques the E/p distributions are extracted in data and simulation
 2714 for each particle species and shown in Figure 58. These distributions are shown
 2715 for a particular bin of E_a ($2.2 < E_a/\text{GeV} < 2.8$), rather than p . E_a is the energy
 2716 available to be deposited in the calorimeter: for pions $E_a = \sqrt{p^2 + m_\pi^2}$, for pro-
 2717 tons $E_a = \sqrt{p^2 + m_p^2} - m_p$, and for antiprotons $E_a = \sqrt{p^2 + m_p^2} + m_p$. In the
 2718 pion case, the entire energy of the pion is deposited in the calorimeter, so E_a is
 2719 just the usual energy. For protons, the proton remains after depositing its energy
 2720 in the calorimeter, so its mass is not available and must be subtracted from E_a .
 2721 And for antiprotons, the antiproton constituents annihilate with the quarks in
 2722 the protons and neutrons of the calorimeter material, so it deposits its entire en-
 2723 ergy as well as an the additional energy from the annihilation; this extra energy
 2724 is equal to the mass of the antiproton and is added to the available energy. The
 2725 features of the E/p distributions are similar to the inclusive case, with a peak
 2726 around 0.5 at low momentum. The zero fraction is not as pronounced as in the
 2727 inclusive case. There is a small negative tail from noise and a large fraction of
 2728 tracks with zero energy from particles which do not reach the calorimeter. The
 2729 long positive tail is noticeably more pronounced for antiprotons because of the
 2730 additional energy generated by the annihilation of the antiproton with the mate-
 2731 rial of the detector, and the peak of the distribution is also increased for the same
 2732 reason. The simulation correctly captures these features, and the agreement be-
 2733 tween data and simulation is good to within the available statistical limitations.

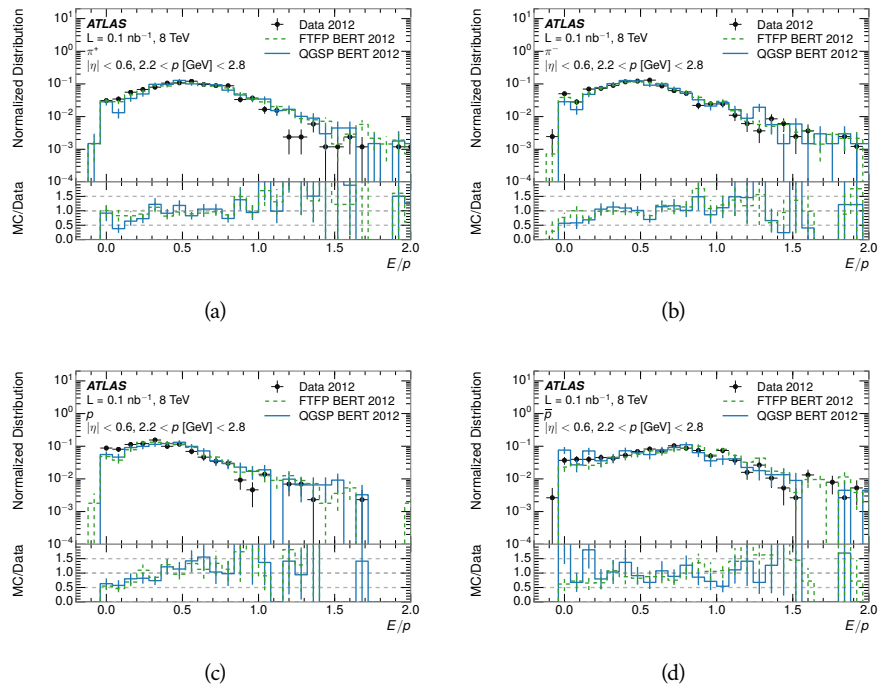


Figure 58: The E/p distribution for isolated (a) π^+ , (b) π^- , (c) proton, and (d) anti-proton tracks.

The zero fraction is further explored in Figure 59 for pions and protons in data and simulation. The simulation consistently underestimates the zero fraction independent of particle species, which implies that this discrepancy is not caused by the model of a particular species but rather a feature common to all. The zero fraction is larger for π^- than π^+ , which is evident in both data and simulation. However there is some suggestion that this increase in zero fraction leads to an even larger discrepancy in the modeling of π^- in simulation.

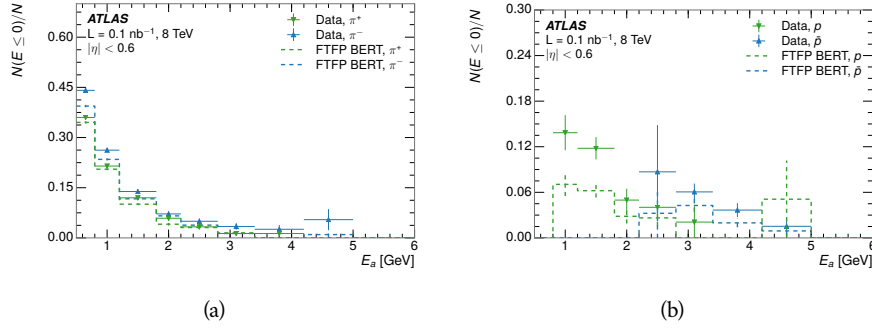


Figure 59: The fraction of tracks with $E \leq 0$ for identified (a) π^+ and π^- , and (b) proton and anti-proton tracks

It is also interesting to compare the response between the different particle species. One approach to do this is to measure the difference in $\langle E/p \rangle$ between two types, which has the advantage of removing the neutral background. These differences are shown in various combinations in Figure 60. The response for π^+ is greater on average than the response to π^- because of a charge-exchange effect which causes the production of additional neutral pions in the showers of π^+ [57]. This effect becomes less significant as the $\langle E/p \rangle$ increases, and the difference approaches zero. Both version of the simulation correctly model this trend. The response for π^+ is also greater on average than the response to p , because a large fraction of the energy of π^+ hadrons is converted to an electromagnetic shower [58, 59]. This effect is again reproduced by both simulations. The \bar{p} response, however, is significantly higher than the response to π^- because of the annihilation of the antiproton, but the difference decreases at higher energies where the additional energy has less relative importance. FTFP_BERT models this effect more accurately than QGSP_BERT because of their different descriptions of \bar{p} interactions with material.

It is also possible to remove the neutral background from these response distributions using the same technique as in Section 7.2.3. The technique is largely independent of the particle species and so can be directly applied to $\langle E/p \rangle$ for pions. The $\langle E/p \rangle_{\text{COR}}$ distributions for pions are shown in Figure 61, which are very similar to the inclusive results. The inclusive hadrons are comprised mostly of pions, so this similarity is not surprising. It is also possible to see the small differences between π^+ and π^- response here, where $\langle E/p \rangle_{\text{COR}}$ is higher on average for π^+ . The agreement between data and simulation is significantly worse for the π^- distributions than for the π^+ , with a discrepancy greater than 10% below 2-3 GeV.

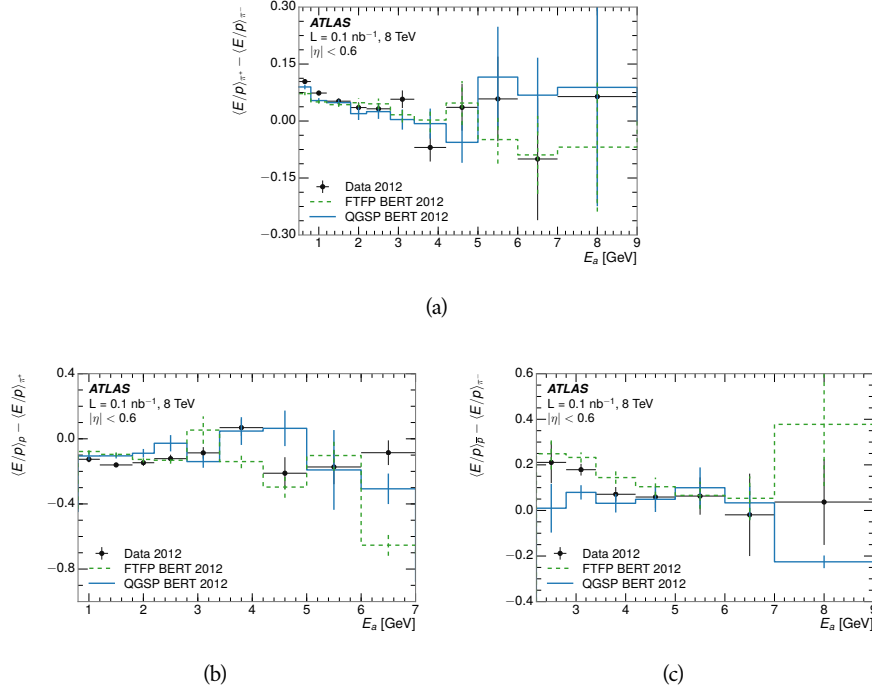


Figure 60: The difference in $\langle E/p \rangle$ between (a) π^+ and π^- (b) p and π^+ , and (c) \bar{p} and π^- .

2767 7.3.3 ADDITIONAL SPECIES IN SIMULATION

2768 The techniques above provide a method to measure the response separately for
 2769 only pions and protons. However the hadrons which forms jets include a number
 2770 of additional species such as kaons and neutrons. The charged kaons are an im-
 2771 portant component of the inclusive charged hadron distribution, which is com-
 2772 prised of roughly 60-70% pions, 15-20% kaons, and 5-15% protons [34]. These
 2773 fractions vary depending on the production mechanism, and the ranges are in-
 2774 dicative of the variations between different events. These are difficult to measure
 2775 in data at the ATLAS detector, as the particles which decay to kaons such as ϕ and
 2776 D mesons have shorter lifetimes and are comparatively rare. These properties
 2777 make it impractical to identify a sufficient number of decays to make statistically
 2778 meaningful measurements. The simulation of these particles includes noticeable
 2779 differences in response between species at low energies, which are shown in Fig-
 2780 ure 62 for FTFP_BERT. The significant differences in response between protons
 2781 and antiprotons below 1 GeV are accounted for above in the definitions of E_a .

2782 7.4 SUMMARY

2783 These various measurements of calorimeter response shown above for data and
 2784 simulation illuminate the accuracy of the simulation of hadronic interactions at
 2785 the ATLAS detector. The results were obtained using 2010 and 2012 data at 7
 2786 and 8 TeV, but reflect the most current understanding of the detector alignment

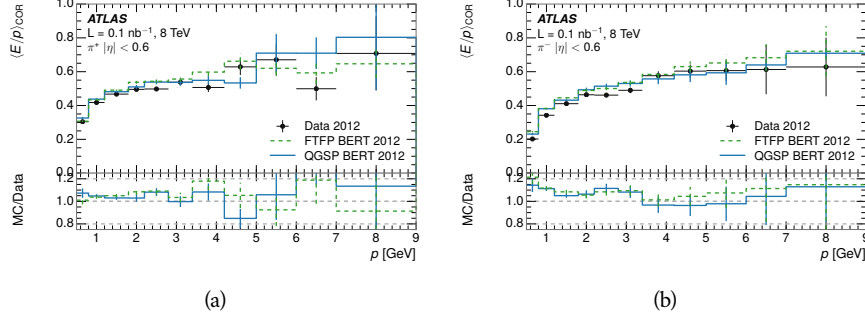


Figure 61: $\langle E/p \rangle_{\text{COR}}$ as a function of track momentum for (a) π^+ tracks and (b) π^- tracks.

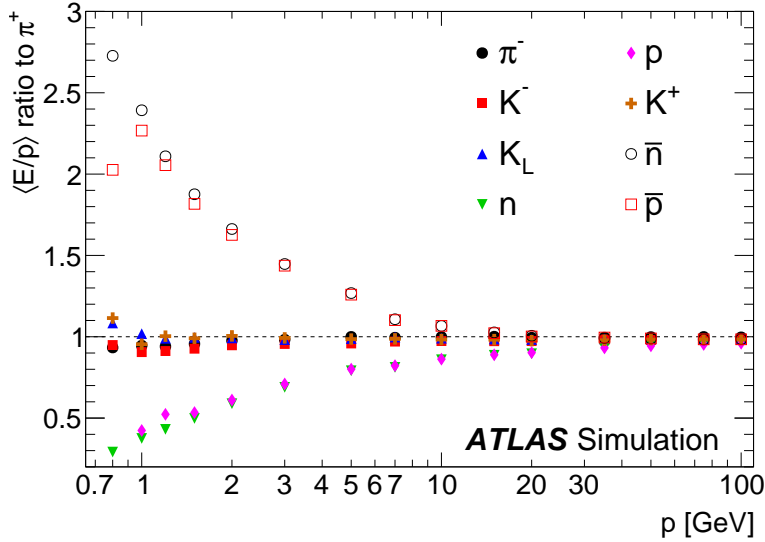


Figure 62: The ratio of the calorimeter response to single particles of various species to the calorimeter response to π^+ with the physics list FTFP_BERT.

and geometry. A number of measurements focusing on a comparison between protons and antiprotons suggest that FTFP_BERT models those interaction more accurately than QGSP_BERT. These measurements, among others, were the motivation to switch the default Geant4 simulation from QGSP_BERT to FTFP_BERT for all ATLAS samples.

Even with these updates, there are a number of approximately 5% discrepancies in response between the data and simulation. The differences result mostly from a difference in the modeling of the zero fraction, which is most significant at low energies. The difference in response without the zero fraction are primarily in the electromagnetic calorimeter, while the modeling of the hadronic calorimeter is accurate. At higher momenta the simulation of hadronic interactions is very consistent with data. Chapter 8 discusses how to use these observed differences to constrain the jet energy scale and its associated uncertainties.

2800

2801 JET ENERGY RESPONSE AND UNCERTAINTY

2802 8.1 MOTIVATION

2803 As jets form a major component of many physics analyses at ATLAS, it is crucial
 2804 to carefully calibrate the measurement of jet energies and to derive an uncer-
 2805 tainty on that measurement. These uncertainties are often the dominant sys-
 2806 tematic uncertainty in high-energy analyses at the LHC. Jet balance techniques,
 2807 as discussed in Section 6.4.3, provide a method to constrain the JES and its uncer-
 2808 tainty in data, and provide the default values used for ATLAS jet measurements at
 2809 most energies [60]. These techniques are limited by their reliance on measuring
 2810 jets in data, so they are statistically limited in estimating the jet energy scale at the
 2811 highest jet energies. This chapter presents another method for estimating the jet
 2812 energy scale and its uncertainty which builds up a jet from its constituents and
 2813 thus can be naturally extended to high jet momentum. Throughout this chapter
 2814 the jets studied are simulated using Pythia8 with the CT10 parton distribution
 2815 set [61] and the AU2 tune [38], and corrections are taken from the studies includ-
 2816 ing data and simulation in Chapter 7.

2817 As described in Section 6.4, jets are formed from topological clusters of energy
 2818 in the calorimeters using the anti- k_t algorithm. These clusters originate from a
 2819 diverse spectrum of particles, in terms of both species and momentum, leading to
 2820 significantly varied jet properties and response between jets of similar produced
 2821 momentum. Figure 63 shows the momentum and particle distributions of sim-
 2822 ultated particles within jets at a few examples energies. Each bin for each distri-
 2823 bution shows the fraction of jet constituents of that particle type and that truth
 2824 energy for a jet of the specified energy. These show that majority of particles in
 2825 jets are charged pions and photons, and the charged pions constituent carry the
 2826 highest energies on average. The figure also demonstrates that the majority of
 2827 the particles in a jet have much lower momentum than the jet itself; for example
 2828 in 90-100 GeV jets less than 1% of particles have energies above 20 GeV. The
 2829 E/p measurements provide a thorough understanding of the dominant particle
 2830 content of jets, the charged hadrons.

2831 8.2 UNCERTAINTY ESTIMATE

2832 A correct modeling of jets in the data by simulation requires that both the parti-
 2833 cle production inside jets as well as the response of the calorimeter to particles
 2834 are correctly modeled. Chapter 7 showed that the simulation does not perfectly
 2835 model the calorimeter response, and provided measurements that can be used
 2836 to correct for discrepancies. To determine the corrections appropriate for jets,
 2837 that is to evaluate a jet energy response, the simulated jet energies are compared

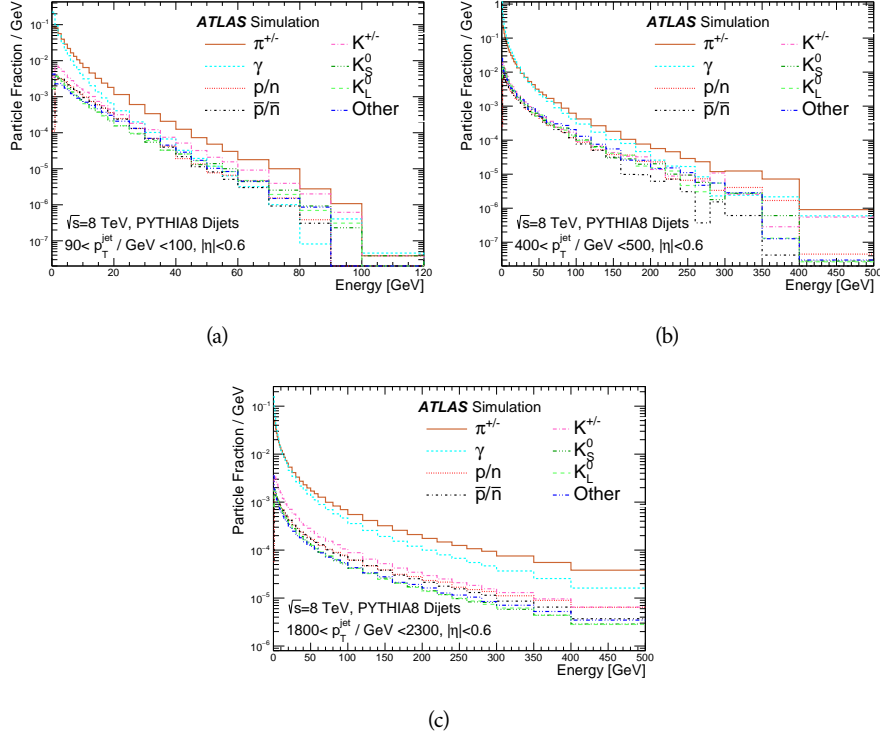


Figure 63: The spectra of true particles inside anti- k_t , $R = 0.4$ jets with (a) $90 < p_T/\text{GeV} < 100$, (b) $400 < p_T/\text{GeV} < 500$, and (c) $1800 < p_T/\text{GeV} < 2300$.

to a corrected jet built up at the particle level. Each cluster in a jet is associated to the truth particle which deposited it, and the energy in that cluster is then corrected for a number of effects based on measurements in data. The primary corrections come from the single hadron response measurements in addition to response measured using the combined test beam which covers higher momentum particles [62]. These corrections include both a shift (Δ), in order to make the simulation match the average response in data, and an uncertainty (σ) associated with the ability to constrain the difference between data and simulation. Some of the dominant sources of uncertainty are itemized in Table 8 with typical values, and the full list considered is described in detail in the associated paper [34]. These uncertainties cover differences between the data and simulation in the modeling of calorimeter response to a given particle. The typical values are listed as ranges to show the variation over momentum and pseudorapidity. For the in situ E/p term, for example, Δ corresponds to the difference between data and simulation for $\langle E/p \rangle_{\text{COR}}$ at the LCW scale (shown in Figure 51 (b)) and σ is the uncertainty on that difference including the statistical uncertainties of both the data and simulated events. No uncertainties are added for the difference between particle composition of jets in data and simulation, as this method focuses on providing a response correction for discrepancies of particle interactions rather than differences in particle composition.

From these terms, the jet energy scale and uncertainty is built up from individual energy deposits in simulation. Each uncertainty term is treated inde-

Abbrev.	Description	Δ (%)	σ (%)
In situ E/p	The comparison of $\langle E/p \rangle_{\text{COR}}$, at the LCW scale, as described in Chapter 7 with statistical uncertainties from 500 MeV to 20 GeV.	0-3	1-5
CTB	The main $\langle E/p \rangle$ comparison uncertainties, binned in p and $ \eta $, as derived from the combined test beam results, from 20 to 350 GeV [62].	0-3	1-5
E/p Zero Fraction	The difference in the zero-fraction between data and MC simulation from 500 MeV to 20 GeV.	5-25	1-5
E/p Threshold	The uncertainty in the EM calorimeter response from the potential mismodeling of threshold effects in topological clustering.	0	0-10
Neutral	The uncertainty in the calorimeter response to neutral hadrons based on studies of physics model variations.	0	5-10
K_L	An additional uncertainty in the response to neutral K_L in the calorimeter based on studies of physics model variations.	0	20
E/p Misalignment	The uncertainty in the p measurement from misalignment of the ID.	0	1
Hadrons, $p > 350$ GeV	An energy independent uncertainty for all particles above the energy range or outside the longitudinal range probed with the combined test beam.	0	10

Table 8: The dominant sources of corrections and systematic uncertainties in the [JES](#) estimation technique, including typical values for the correcting shift (Δ) and the associated uncertainty (σ).

pendently, and is taken to be gaussian distributed. The resulting scale and uncertainty is shown in Figure 64, where the mean response is measured relative to the calibrated energy reported by simulation. The mean response is slightly below one, indicating that the simulation slightly overestimates the calorimeter response on average, and this response is relatively constant as a function of the jet p_T . The dominant uncertainties come from the statistical uncertainties on the E/p measurements at lower energies and the additional uncertainty for out of range measurements at higher energies. Combined the resulting uncertainty ranges from between 1.5% at low momentum and pseudorapidity to as much as 4% at higher momentum and pseudorapidity. The total uncertainty from this method at intermediate jet energies is comparable to other simulation-based methods [63] and is about twice as large as in-situ methods using data [60]. This method is the only one which provides an estimation above 1.8 TeV, however, and so is still a crucial technique in analyses that search for very energetic jets.

These techniques can also be used to measure the correlation between bins of average reconstructed jet momentum across a range of p_T and $|\eta|$, where correlations are expected because of a similarity in particle composition at similar energies. Figure 65 shows these correlations, where the uncertainties on jets in neighboring bins are typically between 30% and 60% correlated. The uncertainty on all jets becomes significantly correlated at high energies and larger pseudorapidities, when the uncertainty becomes dominated by the single term reflecting out of range particles.

8.3 SUMMARY

The technique described above provides a jet energy scale and uncertainty by building up jet corrections from the energy deposits of constituent particles. The E/p measurements are crucial in providing corrections for the majority of particles in the jets. The uncertainty derived this way is between 2 and 5% and is about twice as large at corresponding momentum than jet balance methods. However this is the only uncertainty available for very energetic jets using 2012 data and simulation, and repeating this method with Run 2 data and simulation will be important in providing an uncertainty for the most energetic jets in 13 TeV collisions.

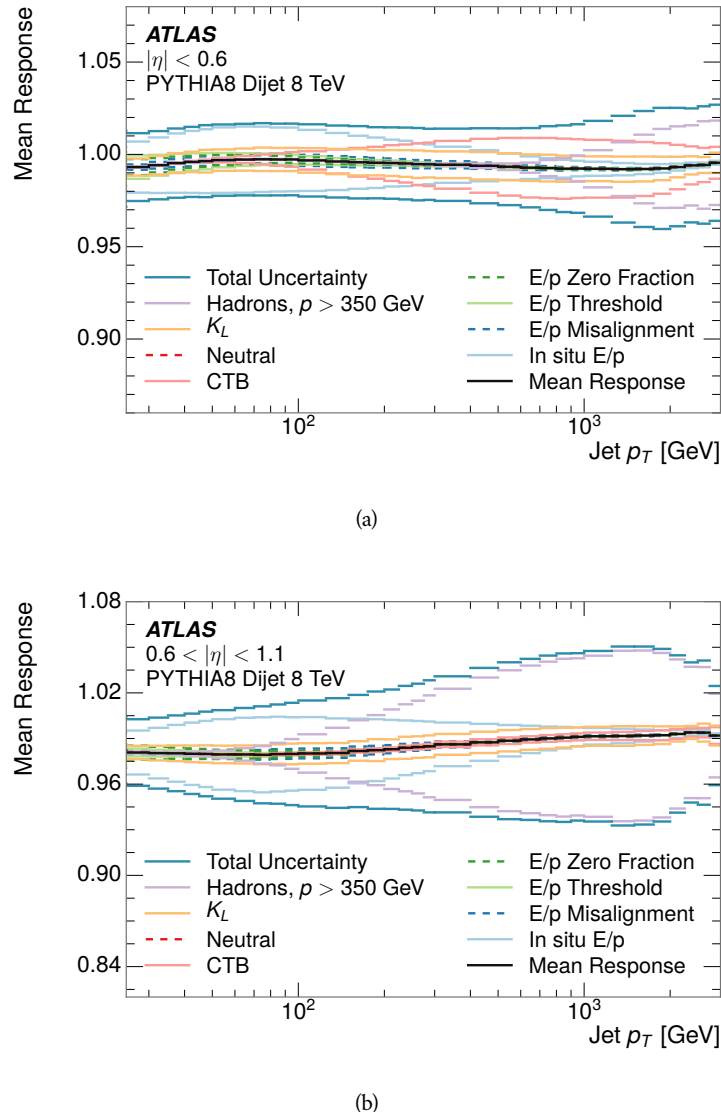


Figure 64: The JES response uncertainty contributions, as well as the total JES uncertainty, as a function of jet p_T for (a) $|\eta| < 0.6$ and (b) $0.6 < |\eta| < 1.1$.

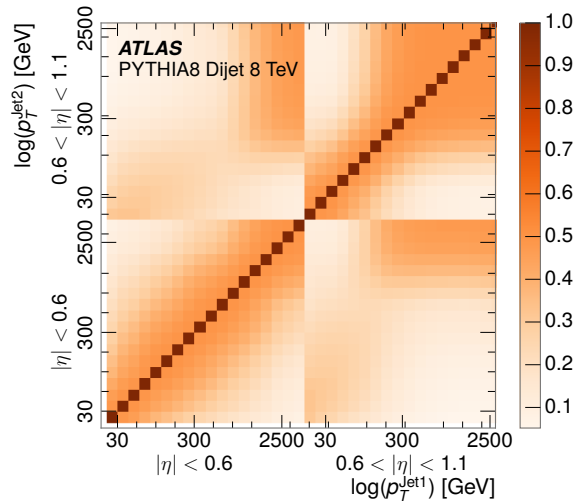


Figure 65: The correlations between bins of average reconstructed jet momentum as a function of jet p_T and $|\eta|$ for jets in the central region of the detector.

2893

PART V

2894

SEARCH FOR LONG-LIVED PARTICLES

2895

You can put some informational part preamble text here.

2898 As discussed in Section 2.6, various limitations in the SM suggest a need for new
 2899 particles at the TeV scale. A wide range of extensions to the Standard Model
 2900 predict that these new particles can have lifetimes greater than approximately
 2901 one-hundredth of a nanosecond. These include theories with universal extra-
 2902 dimensions [64, 65], with new fermions [66], and with leptoquarks [67]. As dis-
 2903 cussed in Section 3.3, many SUSY theories also produce these LLPs, in both R-
 2904 Parity violating [68–70] and R-Parity conserving [71–74] formulations. Split su-
 2905 persymmetry [7, 8], for example, predicts long-lived gluinos with O(TeV) masses.
 2906 This search focuses specifically on the SUSY case, but many of the results are
 2907 generic to any model with LLPs.

2908 Long-lived gluinos or squarks carry color-charge and will thus hadronize into
 2909 color neutral bound states called R-Hadrons. These are composit particles like
 2910 the usual hadrons but with one supersymmetric constituent, for example $\tilde{g}q\bar{q}$
 2911 and $\tilde{q}\bar{q}$. Through this hadronization process, the neutral gluino can acquire a
 2912 charge. Gluino pair production, $pp \rightarrow \tilde{g}\tilde{g}$ has the largest cross sectional increase
 2913 with the increase in energy to 13 TeV, and so this search focuses on gluino R-
 2914 Hadrons. Planned future updates will extend the case to explicitly include squark
 2915 and chargino models, but the method covers any long-lived, charged, massive
 2916 particle.

2917 9.1 EVENT TOPOLOGY

2918 The majority of SUSY models predict that gluinos will be produced in pairs at
 2919 the LHC, through processes like $pp \rightarrow q\bar{q} \rightarrow \tilde{g}\tilde{g}$ and $pp \rightarrow gg \rightarrow \tilde{g}\tilde{g}$, where the
 2920 gluon mode dominates for the collision energy and gluino masses considered
 2921 for this search. During their production, the long-lived gluinos hadronize into
 2922 color singlet bound states including $\tilde{g}q\bar{q}$, $\tilde{g}qq\bar{q}$, and even $\tilde{g}g$ [75]. The probability
 2923 to form the gluon-only bound states is a free parameter usually taken to be 0.1,
 2924 while the meson states are favored among the R-Hadrons [76]. The charged and
 2925 neutral states are approximately equally likely for mesons, so the R-Hadrons will
 2926 be charged roughly 50% of the time.

2927 These channels produce R-Hadrons with large p_T , comparable to their mass,
 2928 so that they typically propagate with $0.2 < \beta < 0.9$ [76]. The fragmentation that
 2929 produces that hadrons is very hard, so the jet structure around the R-Hadron
 2930 is minimal, with less than 5 GeV of summed particle momentum expected in a
 2931 cone of $\Delta R < 0.25$ around the R-Hadron [76]. After hadronization, depending
 2932 on the gluino lifetime, the R-Hadrons then decay into hadrons and a LSP [75].

2933 In summary, the expected event for pair-produced long-lived gluinos is very
 2934 simple: two isolated, high-momentum R-Hadrons that propagate through the
 2935 detector before decaying to jets. The observable features of such events depend

2936 strongly on the interaction of the R-Hadron with the material of the detector
 2937 and also its lifetime. Section 9.1.1 describes the interactions of R-Hadrons which
 2938 reach the various detector elements in ATLAS and Section 9.1.2 provides a sum-
 2939 mary of the observable event descriptions for R-Hadrons of various lifetimes.

2940 9.1.1 DETECTOR INTERACTIONS

2941 After approximately 0.2 ns, the R-Hadron reaches the pixel detector. If charged,
 2942 it deposits energy into the material through repeated single collisions that result
 2943 in ionization of the silicon substrate [5]. Because of its comparatively low β , the
 2944 ionization energy can be significantly greater than expected for SM particles be-
 2945 cause the most-probable energy loss grows significantly as β decreases [5]. This
 2946 large ionization can be measured through the ToT read out from the pixel detec-
 2947 tor as described in Section 6.1.2. Large ionization in the inner detector is one of
 2948 the major characteristic features of LLPs.

2949 Throughout the next few nanoseconds, the R-Hadron propagates through the
 2950 remainder of the inner detector. A charged R-Hadron will provide hits in each
 2951 of these systems as would any other charged particle, and can be reconstructed
 2952 as a track. The track reconstruction provides a measurement of its trajectory
 2953 and thus its momentum as described in Section 6.1. The large momentum is
 2954 another characteristic feature of massive particles produced at the LHC. **Note: At**
 2955 **this point I am failing to mention that the TRT provides a possible dE/dx**
 2956 **measurement, because no one uses it as far as I know.**

2957 As of roughly 20 ns, the R-Hadron enters the calorimeter where it interacts
 2958 hadronically with the material. Because of its large mass and momentum, the
 2959 R-Hadron does not typically stop in the calorimeter, but rather deposits a small
 2960 fraction of its energy through repeated interactions with nucleons. The proba-
 2961 bility of interaction between the gluino itself and a nucleon is low because the
 2962 cross section drops off with the inverse square of its mass, so the interactions are
 2963 primarily governed by the light constituents [77]. Each of these interactions can
 2964 potentially change that quark content and thus change the sign of the R-Hadron,
 2965 so that the charge at exit is typically uncorrelated with the charge at entry [76].
 2966 The total energy deposited in the calorimeters during the propagation is small
 2967 compared to the kinetic energy of the R-Hadron, around 20-40 GeV, so that
 2968 E/p is typically less than 0.1 [76].

2969 Then, 30 ns after the collision, it reaches the muon system, where it again
 2970 ionizes in the material if charged and can be reconstructed as a muon track. Be-
 2971 cause of the charge-flipping interactions in the calorimeter, this track may have
 2972 the opposite sign of the track reconstructed in the inner detector, or there may
 2973 be a track present when there was none in the inner detector and vice-versa. The
 2974 propagation time at the typically lower β results in a significant delay compared
 2975 to muons, and that delay can be assessed in terms of a time-of-flight measure-
 2976 ment. Because of the probability of charge-flip and late arrival, there is a signif-
 2977 icant chance that an R-Hadron which was produced with a charge will not be
 2978 identified as a muon. The long time-of-flight is another characteristic feature of
 2979 R-Hadrons which are reconstructed as muons.

2980 91.2 LIFETIME DEPENDENCE

2981 The above description assumed a lifetime long enough for the R-Hadron to exit
 2982 the detector, which through this search is referred to as “stable”, even though
 2983 the particle may decay after exiting the detector. There are several unique sig-
 2984 natures at shorter lifetimes where the R-Hadron decays in various parts of the
 2985 inner detector; these lifetimes are referred to as “metastable”.

2986 The shortest case where the R-Hadron is considered metastable is for life-
 2987 times around 0.01 ns, where the particle decays before reaching any of the de-
 2988 tector elements. Although the R-Hadrons are produced opposite each other in
 2989 the transverse plane, each R-Hadron decays to a jet and an LSP. The LSPs are not
 2990 measured, so the produced jets can be significantly imbalanced in the transverse
 2991 plane which results in large missing energy. That missing energy can be used
 2992 to trigger candidate events, and provides the most efficient trigger option for
 2993 shorter lifetimes. Additionally, the precision of the tracking system allows the
 2994 displaced vertex of the R-Hadron decay to be reconstructed from the charged
 2995 particles in the jet. The distance of that vertex from the interaction point can
 2996 be used to distinguish R-Hadron decays from other processes. Figure 66 shows
 2997 a schematic diagram of an example R-Hadron event with such a lifetime. The
 2998 diagram is not to scale, but instead illustrates the detector interactions in the
 2999 pixel detector, calorimeters, and muon system. It includes a representation of
 3000 the charged R-Hadron and the neutral R-Hadron, as well as the LSPs and jets
 3001 (shown as charged hadrons) produced in the decay. Neutral hadrons may also
 3002 be produced in the decay but are not depicted. Previous searches on ATLAS have
 3003 used the displaced vertex to target LLP decays [78].

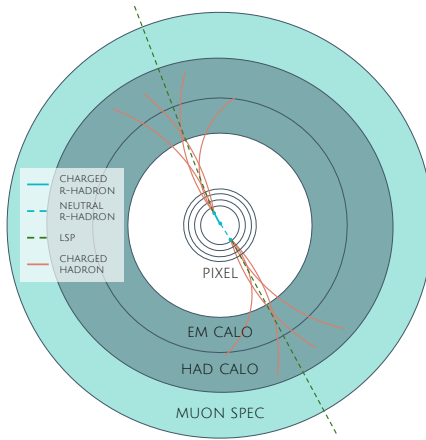


Figure 66: A schematic diagram of an R-Hadron event with a lifetime around 0.01 ns.

The diagram includes one charged R-Hadron (solid blue), one neutral R-Hadron (dashed blue), LSPs (dashed green) and charged hadrons (solid orange). The pixel detector, calorimeters, and muon system are illustrated but not to scale.

3004 The next distinguishable case occurs at lifetimes greater than 0.1 ns, where
 3005 the R-Hadron forms a partial track in the inner detector. If the decay products
 3006 are sufficiently soft, they may not be reconstructed, and this forms a unique sig-

3007 nature of a disappearing track. An example of such an event is illustrated in
 3008 Figure 67, which shows the short track in the inner detector and the undetected
 3009 soft charged hadron and LSP that are produced. A dedicated search on ATLAS used
 3010 the disappearing track signature to search for LLP in Run 1 [79]. ***zNote: might***
 3011 ***not be worth mentioning the disappearing track here since it is actually a***
 3012 ***chargino search, the soft pion is pretty unique to charginos.***

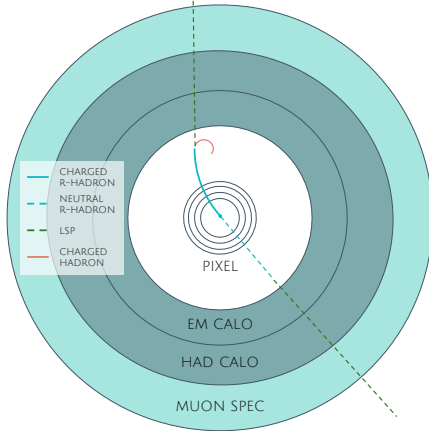


Figure 67: A schematic diagram of an R-Hadron event with a lifetime around 4 ns. The diagram includes one charged R-Hadron (solid blue), one neutral R-Hadron (dashed blue), LSPs (dashed green) and a charged hadron (solid orange). The pixel detector, calorimeters, and muon system are illustrated but not to scale.

3013 If the decay products are not soft, the R-Hadron daughters form jets, resulting
 3014 in an event-level signature of up to two high-momentum tracks, jets, and signif-
 3015 icant missing energy. The missing energy has the same origin as in the case of
 3016 0.01 ns lifetimes, from the decay to unmeasured particles, and again can be large.
 3017 The high-momentum tracks will also have the characteristically high-ionization
 3018 of massive, long-lived particles in the inner detector. Figure 68 illustrates an ex-
 3019 ample event with one charged R-Hadron which decays after approximately 10 ns,
 3020 and shows how the jets from the decay can still be reconstructed in the calorime-
 3021 ter. Several previous searches on ATLAS from Run 1 have used this signature to
 3022 search for R-Hadrons [80, 81], including a dedicated search for metastable parti-
 3023 cles [82].

3024 If the lifetime is longer than several nanoseconds, in the range of 15-30 ns,
 3025 the R-Hadron decay can occur in or after the calorimeters, but prior to reaching
 3026 the muon system. This case is similar to the above, although the jets may not be
 3027 reconstructed, and is covered by many of the same search strategies. The events
 3028 still often have large missing energy, although it is generated through different
 3029 mechanisms. The R-Hadrons do not deposit much energy in the calorimeters, so
 3030 a neutral R-Hadron will not enter into the missing energy calculation. A charged
 3031 R-Hadron opposite a neutral R-Hadron will thus generate significant missing en-
 3032 ergy, and close to 50% of pair-produced R-Hadron events fall into this category.
 3033 If both R-Hadrons are neutral then the missing energy will be low because nei-
 3034 ther is detected. Two charged R-Hadrons will also result in low missing energy
 3035 because both are reconstructed as tracks and will balance each other in the trans-

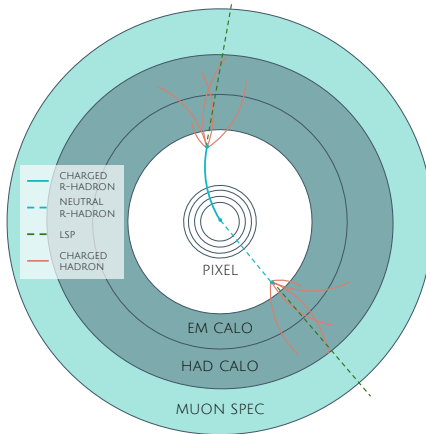


Figure 68: A schematic diagram of an R-Hadron event with a lifetime around 5 ns. The diagram includes one charged R-Hadron (solid blue), one neutral R-Hadron (dashed blue), LSPs (dashed green) and charged hadrons (solid orange). The pixel detector, calorimeters, and muon system are illustrated but not to scale.

3036 verse plane. A small fraction of the time, one of the charged R-Hadron tracks may
 3037 fail quality requirements and thus be excluded from the missing energy calcula-
 3038 tion and again result in significant missing energy. Figure 69 illustrates another
 3039 example event with one charged R-Hadron which decays after approximately 20
 3040 ns, and shows how the jets from the decay might not be reconstructed.

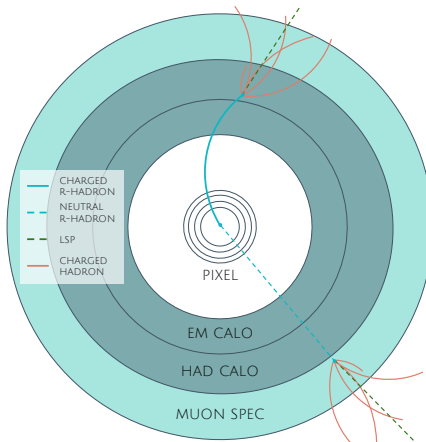


Figure 69: A schematic diagram of an R-Hadron event with a lifetime around 20 ns. The diagram includes one charged R-Hadron (solid blue), one neutral R-Hadron (dashed blue), LSPs (dashed green) and charged hadrons (solid orange). The pixel detector, calorimeters, and muon system are illustrated but not to scale.

3041 The longest lifetimes, the stable case, has all of the features of the 30-50 ns case
 3042 but with the addition of muon tracks for any R-Hadrons that exit the calorimeter
 3043 with a charge. That muon track can provide additional information from time-
 3044 of-flight measurements to help identify LLPs. An example of the event topology
 3045 for one charged and one neutral stable R-Hadron is shown in Figure 70. Some
 3046 searches on ATLAS have included this information to improve the search reach
 3047 for stable particles [81, 83].

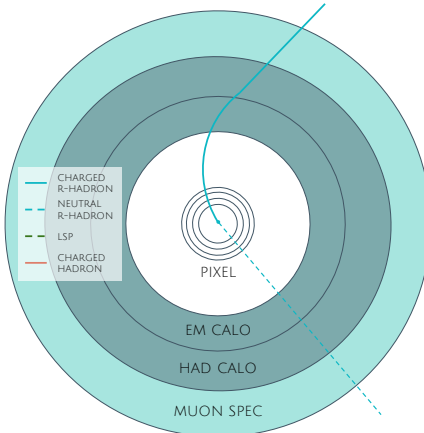


Figure 70: A schematic diagram of an R-Hadron event with a lifetime around 20 ns. The diagram includes one charged R-Hadron (solid blue) and one neutral R-Hadron (dashed blue). The pixel detector, calorimeters, and muon system are illustrated but not to scale.

3048 9.2 SIMULATION

3049 All of the event topologies discussed above are explored by simulations of R-
 3050 Hadron events in the [ATLAS](#) detector. A large number of such samples are gen-
 3051 erated to determine signal efficiencies, to measure expected yields, and to esti-
 3052 mate uncertainties. The primary interaction, pair production of gluinos with
 3053 masses between 400 and 3000 GeV, is simulated using [Pythia 6.4.27](#) [84]
 3054 with the AUET2B [85] set of tuned parameters for the underlying event and the
 3055 CTEQ6L1 [61] PDF set. The simulated interactions include a modeling of pileup
 3056 by adding secondary, minimum bias interactions from both the same (in-time
 3057 pileup) and nearby (out-of-time pileup) bunch crossings. This event generation
 3058 is then augmented with a dedicated hadronization routine to hadronize the long-
 3059 lived gluinos into final states with R-Hadrons [86], with the probability to form
 3060 a gluon-gluino bound set at 10% [87].

3061 The cross sections used for these processes are calculated at next-to-leading
 3062 order ([NLO](#)) in the strong coupling constant with a resummation of soft-gluon
 3063 emmission at next-to-leading logarithmic ([NLL](#)) [88–92]. The nominal predic-
 3064 tions and the uncertainties for each mass point are taken from an envelope of
 3065 cross-section predictions using different PDF sets and factorization and renor-
 3066 malization scales [93].

3067 The R-Hadrons then undergo a full detector simulation [], where the interac-
 3068 tions of the R-Hadrons with the material of the detector are described by dedi-
 3069 cated [Geant4](#) [31] routines. These routines model the interactions described in
 3070 Section 9.1.1, including the ionizing interactions in the silicon modules of the
 3071 inner detector and the R-Hadron-nucleon interactions in the calorimeters [94,
 3072 95]. The specific routine chosen to describe the interactions of the R-Hadrons
 3073 with nucleons, the “generic model”, uses a pragmatic approach where the scatter-
 3074 ing cross section is taken to be a constant 12 mb per light quark. In this model

3075 the gluino itself does not interact at all except through its role as a reservoir of
3076 kinetic energy.

3077 The lifetimes of these R-Hadrons are then simulated at several working points,
3078 $\tau = 0.1, 1.0, 3.0, 10, 30, 50$ and detector stable, where the particle is required to
3079 decay after propagating for a time compatible with its lifetime. Only one decay
3080 mode is simulated for these samples, $\tilde{g} \rightarrow q\bar{q}\tilde{\chi}_1^0$ with the neutralino mass set to
3081 100 GeV, which is chosen because it has the highest sensitivity among all of the
3082 modes studied in previous searches [82]. Heavier neutralinos have similar results
3083 but generate less missing energy which reduces the efficiency of triggering.

3084 All of the simulated events are then reconstructed using the same software
3085 used for collision data. The fully reconstructed events are then reweighted to
3086 match the distribution of initial state radiation in an alternative sample of events,
3087 generated with MG5_aMC@NLO [96], which has a more accurate description of ra-
3088 diate effects than Pythia6. This reweighting provides a more accurate descrip-
3089 tion of the momentum of the gluino-gluino system and is important in modeling
3090 the efficiency of triggering and offline event selection.

3091

3092 EVENT SELECTION

3093 The **LLPs** targeted by this search differ in their interactions with the detector from
 3094 **SM** particles primarily because of their large mass. When produced at the ener-
 3095 gies available at the **LHC**, that large mass results in a low β (typically $0.2 < \beta <$
 3096 0.9). Such slow-moving particles heavily ionize in detector material. Each layer
 3097 of the pixel detector provides a measurement of that ionization, through **ToT**, as
 3098 discussed in Section 6.1.2. The ionization in the pixel detector, quantified in
 3099 terms of dE/dx , provides the major focus for this search technique, along with
 3100 the momentum measured in the entire inner detector. It is effective both for its
 3101 discriminating power and its use in reconstructing a particle’s mass, and it can be
 3102 used for a wide range of masses and lifetimes as discussed in Section 9.1.2. How-
 3103 ever dE/dx needs to be augmented with a few additional selection requirements
 3104 to provide a mechanism for triggering and to further reduce backgrounds.

3105 Ionization itself is not currently accessible for triggering, so this search in-
 3106 stead relies on E_T^{miss} to trigger signal events. Although triggering on E_T^{miss} can
 3107 be inefficient, E_T^{miss} is often large for many production mechanisms of **LLPs**, as
 3108 discussed in Section 9.1.

3109 The use of ionization to reject **SM** backgrounds relies on well-measured, high-
 3110 momentum tracks, so some basic requirements on quality and kinematics are
 3111 placed on the tracks considered in this search. These quality requirements have
 3112 been significantly enhanced in Run 2 by a newly introduced tracking variable
 3113 that is very effective in removing highly-ionizing backgrounds caused by over-
 3114 lapsing tracks. A few additional requirements are placed on the tracks consid-
 3115 ered for **LLP** candidates that increase background rejection by targeting specific
 3116 types of **SM** particles. These techniques provide a significant analysis improve-
 3117 ment over previous iterations of ionization-based searches on ATLAS by provid-
 3118 ing additional background rejection with minimal loss in signal efficiency.

3119 The ionization measurement with the Pixel detector can be calibrated to pro-
 3120 vide an estimator of $\beta\gamma$. That estimate, together with the momentum measure-
 3121 ment provided by tracking, can be used to reconstruct a mass for each track
 3122 which traverses the pixel detector. That mass variable will be peaked at the **LLP**
 3123 mass for any signal, and provides an additional tool to search for an excess. In
 3124 addition to an explicit requirement on ionization, this search constructs a mass-
 3125 window for each targeted signal mass in order to evaluate any excess of events
 3126 and to set limits.

3127 The strategy discussed here is optimized for lifetimes of $O(1) - O(10)$ ns.
 3128 Pixel ionization is especially useful in this regime as particles only need to prop-
 3129 agate through the first seven layers of the inner detector, about 37 cm from the
 3130 beam axis. The search is still competitive with other searches for **LLPs** at longer
 3131 lifetimes, because the primary discriminating variables are still applicable even
 3132 for particles that do not decay within the detector [83]. Although the majority of

3133 the requirements will be the same for all lifetimes, two signal regions are defined
 3134 to optimize separately for intermediate and long lifetime particles.

3135 10.1 TRIGGER

3136 Triggering remains a significant difficulty in defining an event selection with
 3137 high signal efficiency in a search for **LLPs**. There are no triggers available in
 3138 the current ATLAS system that can fire directly from a high momentum track
 3139 with large ionization (Section 5.6). Although in some configurations a charged
 3140 **LLP** can fire muon triggers, this requirement introduces significant model depen-
 3141 dence on both the allowed lifetimes and the interactions in the calorimeter [76],
 3142 as discussed in Section 9.1.1.

3143 For a search targeting particles which may decay prior to reaching the muon
 3144 system, the most efficient available trigger is based on missing energy [76]. As
 3145 discussed in Section 9.1, signal events can produce significant E_T^{miss} by a few
 3146 mechanisms. At the trigger level however, the missing energy is only calculated
 3147 using the calorimeters (Section 5.6) where the R-Hadrons deposit little energy.
 3148 So, at short lifetimes, E_T^{miss} measured in the calorimeter is generated by an im-
 3149 balance between the jets and undetected **LSPs** produced in R-Hadron decays. At
 3150 longer lifetimes, without the decay products, missing energy is only produced in
 3151 the calorimeters when the R-Hadrons recoil against an initial state radiation (**ISR**)
 3152 jet.

3153 These features are highlighted in Figure 71, which shows the E_T^{miss} distribu-
 3154 tions for simulated short lifetime (3 ns) and stable R-Hadron events. The figure
 3155 includes both the offline E_T^{miss} , the missing energy calculated with all available
 3156 information, and Calorimeter E_T^{miss} , the missing energy calculated using only
 3157 information available at the calorimeter which approximates the missing energy
 3158 available at the trigger. The short lifetime sample has significantly greater E_T^{miss}
 3159 and Calorimeter E_T^{miss} than the stable sample as expected. For the stable sam-
 3160 ple, a small fraction of events with very large E_T^{miss} (about 5%) migrate into the
 3161 bin with very small Calorimeter E_T^{miss} because the E_T^{miss} produced by a charged
 3162 R-Hadron track opposite a neutral R-Hadron track does not contribute any miss-
 3163 ing energy in the calorimeters.

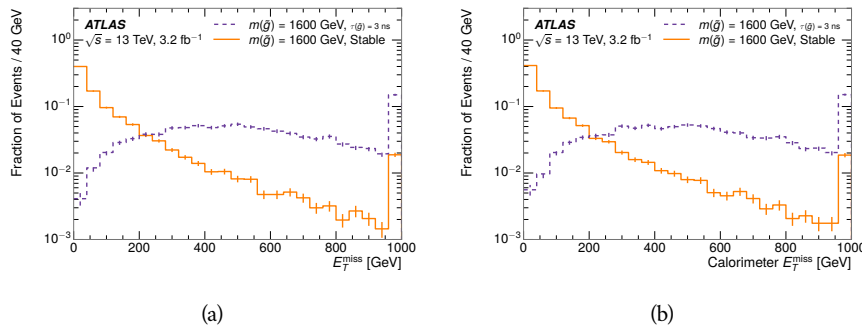


Figure 71: The distribution of (a) E_T^{miss} and (b) Calorimeter E_T^{miss} for simulated signal
 events before the trigger requirement.

3164 So, either case to some extent relies on kinematic degrees of freedom to pro-
 3165 duce missing energy, as the pair-produced LLPs tend to balance each other in
 3166 the transverse plain. That balance results in a relatively low efficiency for long-
 3167 lifetime particles, roughly 40%, and efficiencies between 65% and 95% for shorter
 3168 lifetimes depending on both the mass and the lifetime. For long lifetimes in par-
 3169 ticular, the presence of ISR is important in providing an imbalance in the trans-
 3170 verse plane, and is an important aspect of modeling the selection efficiency for
 3171 R-Hadron events.

3172 The missing energy trigger with the lowest threshold available is chosen for
 3173 this selection in order to maximize the trigger efficiency. During 2015 data col-
 3174 lection this was the HLT_xe70 trigger, which used a 50 GeV threshold on miss-
 3175 ing energy at LVL1 and a 70 GeV threshold on missing energy at the HLT. These
 3176 formation of the trigger decision for missing energy was discussed in more detail
 3177 in Section 5.6.

3178 10.2 KINEMATICS AND ISOLATION

3179 After the trigger requirement, each event is required to have a primary vertex
 3180 reconstructed from at least two well-measured tracks in the inner detector, each
 3181 with $p_T > 400$ MeV. If more than one such vertex exists, the primary vertex
 3182 is taken to be the one with the largest summed track momentum for all tracks
 3183 associated to that vertex. The offline reconstructed E_T^{miss} is required to be above
 3184 130 GeV to additionally reject SM backgrounds. The transverse missing energy
 3185 is calculated using fully reconstructed and calibrated offline objects, as described
 3186 in Section 6.5. In particular the E_T^{miss} definition in this selection uses jets recon-
 3187 structed with the anti- k_t algorithm with radius $R = 0.4$ from clusters of energy
 3188 in the calorimeter (Section 6.4) and with $p_T > 20$ GeV, as well as reconstructed
 3189 muons, electrons, and tracks not identified as another object type.

3190 The E_T^{miss} distributions are shown for data and a few simulated signals in Fig-
 3191 ure 72, after the trigger requirement. The cut placed at 130 GeV is 95% effi-
 3192 cient for metastable and 90% efficient for stable particles, after the trigger re-
 3193 quirement, because of the missing energy generating mechanisms discussed pre-
 3194 viously. The distribution of data in this figure and subsequent figures in this sec-
 3195 tion can be interpreted as the distribution of backgrounds, as any signal contam-
 3196 ination would be negligible if present at these early stages of the selection (prior
 3197 to the final requirement on ionization). The background falls rapidly with miss-
 3198 ing energy, motivating the direct requirement on E_T^{miss} for the signal region. Al-
 3199 though a tighter requirement than the specified value of 130 GeV would seem to
 3200 increase the search potential from these early distributions, other requirements
 3201 are more optimal when taken as a whole. The specific values for each require-
 3202 ment in signal region were optimized considering the increase in discovery reach
 3203 for tightening the requirement on each discriminating variable. **NOTE: If space**
 3204 **and time permit, I will add a whole section about signal region optimiza-**
 3205 **tion..**

3206 It is typically the practice for searches for new physics on ATLAS to place an
 3207 offline requirement on the triggering variable that is sufficiently tight to guar-

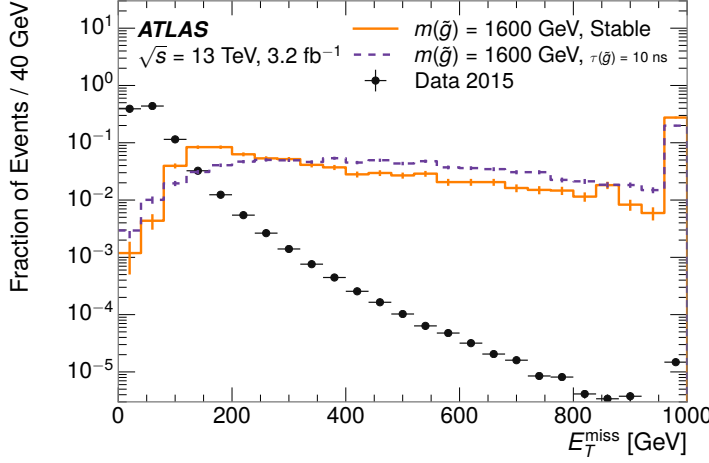


Figure 72: The distribution of E_T^{miss} for data and simulated signal events, after the trigger requirement.

3208 antee that the event would pass the trigger. Such a tight requirement makes the
 3209 uncertainty on the trigger efficiency of the simulation negligible, as modeling the
 3210 regime where the trigger is only partially efficient can be difficult. In this analy-
 3211 sis, however, because of the atypical interactions of R-Hadrons with the tracker
 3212 and the calorimeter, the offline requirement on E_T^{miss} is not sufficient to guar-
 3213 antee a 100% trigger efficiency even at large values, as can be seen in Figure 73.
 3214 This figure shows the efficiency for passing the HLT_xe70 trigger as a function
 3215 of the requirement on E_T^{miss} , which plateaus to roughly 85% even at large values.
 3216 This plateau does not reach 100% because events which have large offline miss-
 3217 ing energy from a neutral R-Hadron produced opposite of a charged R-Hadron
 3218 can have low missing energy in the calorimeters. The Calorimeter E_T^{miss} , on the
 3219 other hand, does not have this effect and reaches 100% efficiency at large values
 3220 because it is the quantity that directly corresponds to the trigger threshold. In
 3221 both cases the efficiency of triggering is greater for the short lifetime sample be-
 3222 cause the late decays to hadrons and LSPs produce an imbalance in the calorime-
 3223 ters even though they may not be reconstructed offline as tracks or jets. For this
 3224 reason, the requirement on E_T^{miss} is determined by optimizing the background
 3225 rejection even though it corresponds to a value of trigger efficiency significantly
 3226 below 1.0.

3227 Potential signal events are then required to have at least one candidate LLP
 3228 track. Although the LLPs are produced in pairs, many models do not consistently
 3229 yield two charged particles. For example, in the R-Hadron model highlighted
 3230 here, only 20% of events have two charged R-Hadrons while 47% of events have
 3231 just one. A signal region requiring two charged candidates could be a powerful
 3232 improvement in background rejection for a larger dataset, but it is not consid-
 3233 ered in this version of the analysis as it was found to be unnecessary to reject the
 3234 majority of backgrounds.

3235 For a track to be selected as a candidate, it must have $p_T > 50 \text{ GeV}$ and pass
 3236 basic quality requirements. The track must be associated to the primary vertex.

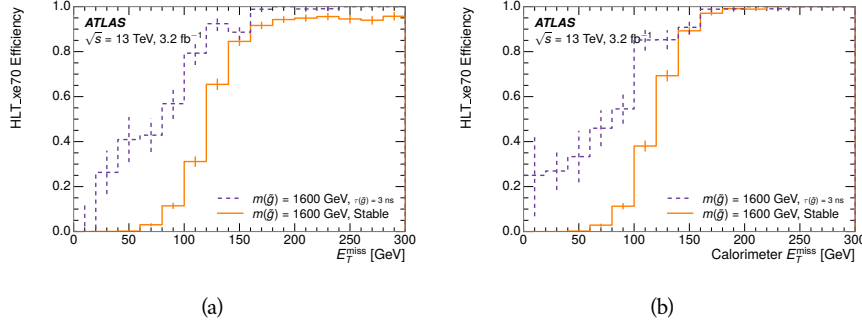


Figure 73: The trigger efficiency for the HLT_xe70 trigger requirement as a function of (a) E_T^{miss} and (b) Calorimeter E_T^{miss} for simulated signal events.

It must also have at least seven clusters in the silicon layers in the inner detector to ensure an accurate measurement of momentum. Those clusters must include one in the innermost layer if the extrapolated track is expected to pass through that layer. And to ensure a reliable measurement of ionization, the track is required to have at least two clusters in the pixel detector that provide a measurement of dE/dx .

At this point in the selection, there is a significant high-ionization background from multiple tracks that significantly overlap in the inner detector. Previous version of this analysis have rejected these overlaps by an explicit overlap rejection between pairs of fully reconstructed tracks, typically by requiring no additional tracks within a cone around the candidate. This technique, however, fails to remove the background from tracks that overlap so precisely that the tracks cannot be separately resolved, which can be produced in very collimated photon conversions or decays of pions.

A new method, added in Run 2, identifies cluster shapes that are likely formed by multiple particles based on a neural network classification algorithm. The number of clusters that are classified this way in the pixel detector for a given track is called N_{split} . As the shape of clusters requires significantly less spatial separation to identify overlaps than it does to reconstruct two fully resolved tracks, this variable is more effective at rejecting backgrounds from overlaps. Figure 74 shows the dependence of ionization on N_{split} ; as N_{split} increases the most probable value of dE/dx grows significantly up to twice the expected value when $N_{\text{split}} = 4$.

This requirement is very successful in reducing the long positive tail of the dE/dx distributions, as can be seen in Figure 75. Comparing the distribution for “baseline tracks”, tracks with only the above requirements on clusters applied and before the requirement on N_{split} , to the distribution with $N_{\text{split}} = 0$, it is clear that the fraction of tracks with large dE/dx is reduced be several orders of magnitude. The tracks without split hits are very close to the dE/dx distribution of identified muons, which are extremely well isolated on average. Figure 75 also includes the distribution of dE/dx in an example signal simulation to demonstrate how effective dE/dx is as a discriminating variable with this isolation applied. The background falls rapidly for $dE/dx > 1.8 \text{ MeVg}^{-1}\text{cm}^2$

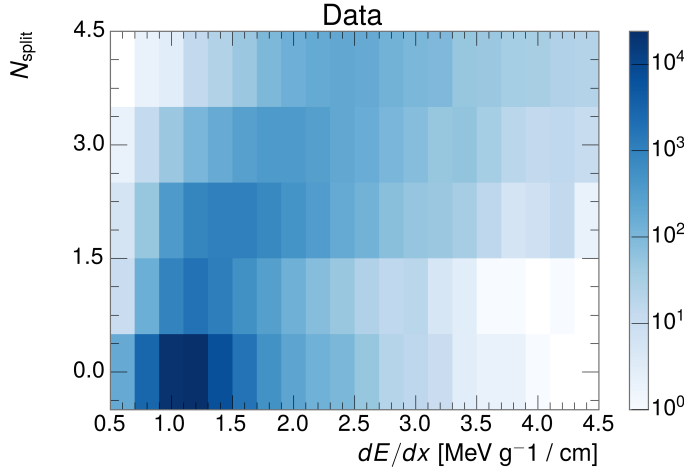


Figure 74: The dependence of dE/dx on N_{split} in data after basic track hit requirements have been applied.

3270 while the majority of the signal, approximately 90% depending on the mass, falls
 3271 above that threshold. Over 90% of LLP tracks in simulated signal events pass the
 3272 N_{split} -based isolation requirement.

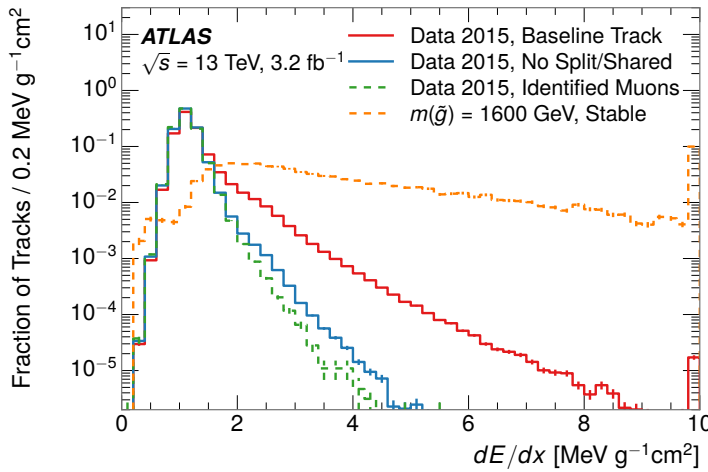


Figure 75: The distribution of dE/dx with various selections applied in data and simulated signal events.

3273 A few additional kinematic requirements are imposed to help reduce SM back-
 3274 grounds. The momentum of the candidate track must be at least 150 GeV, and
 3275 the uncertainty on that measurement must be less than 50%. The distribution of
 3276 momentum is shown in Figure 76 for tracks in data and simulated signal events
 3277 after the previously discussed requirements on clusters, transverse momentum,
 3278 and isolation have been imposed. The signal particles are much harder on aver-

age than their backgrounds because of the high energy interactions required to produce them. The transverse mass, M_T , defined as

$$M_T = \sqrt{2p_T E_T^{\text{miss}}(1 - \cos(\Delta\phi(E_T^{\text{miss}}, \text{track})))} \quad (20)$$

estimates the mass of a decay of to a single charged particle and an undetected particle and is required to be greater than 130 GeV to reject contributions from the decay of W bosons. Figure 77 shows the distribution of M_T for data and simulated signal events. The signal is distributed over a wide range of M_T , with about 90% above the threshold value of 130 GeV. The data shows a dual-peaked structure, where the first peak comes from W boson decays and the second peak is a kinematic shaping from the requirements on E_T^{miss} and the track p_T in dijet events.

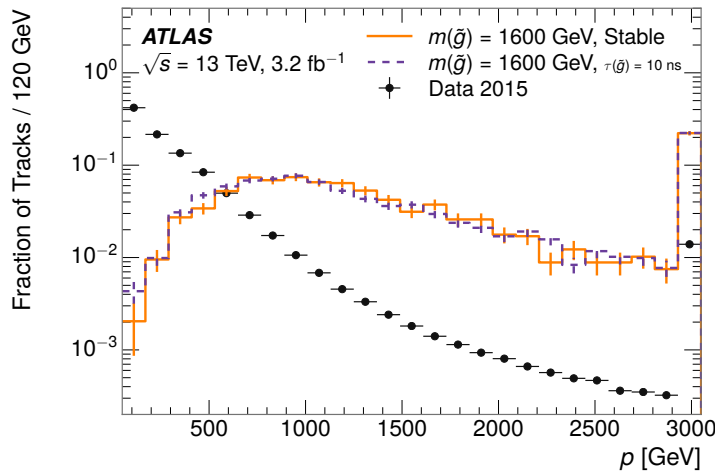


Figure 76: The distribution of track momentum for data and simulated signal events, after previous selection requirements have been applied.

10.3 PARTICLE SPECIES REJECTION

The amount of ionization deposited by particles with low mass and high momentum has a large positive tail [5], so backgrounds can be formed by a wide variety of SM processes when various charged particles have a few randomly large deposits of energy in the pixel detector. Those backgrounds can be additionally reduced by targeting other interactions with the detector where they are expected to have different behavior than R-Hadrons. The interactions with the detector depend on the types of particles produced rather than the processes which produce them, so this search forms a series of rejections to remove backgrounds from individual particle species. These rejections focus on using additional features of the event, other than the kinematics of the candidate track, as they can provide a powerful source of background rejection with very high signal efficiency. However, the lifetime of an R-Hadron can significantly change

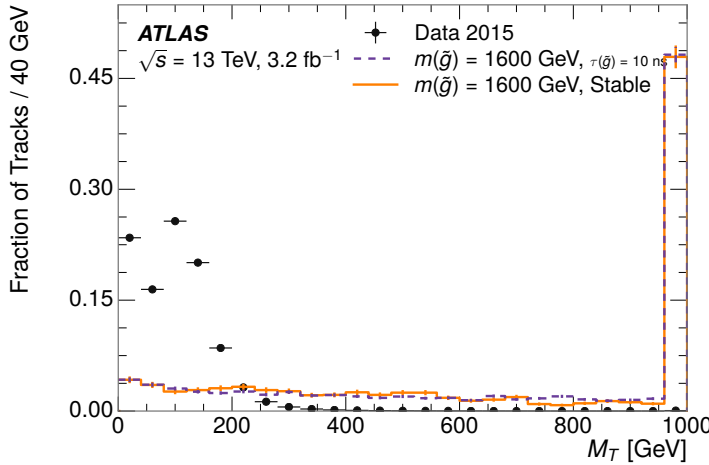


Figure 77: The distribution of M_T for data and simulated signal events, after previous selection requirements have been applied.

its detector characteristics, as discussed in Section 9.1.2. To accommodate these differences, the SM rejections defined in this section are split to form two signal regions, one for long-lifetimes particles, the stable region ($50 \leq \tau[\text{ns}] < \infty \text{ ns}$), and one for intermediate lifetime particles, the metastable region ($0.4 < \tau[\text{ns}] < 50$).

Jets can be very effectively rejected by considering the larger-scale isolation of the candidate track. In this case the isolation focuses on the production of nearby particles as a jet-veto, rather than the isolation from overlapping tracks based on N_{split} that was used to reduce high-ionization backgrounds. As explained in Section 9.1, the fragmentation process which produces an R-Hadron is very hard and thus is not expected to produce additional particles with a summed momentum of more than 5 GeV. The jet-veto uses the summed momentum of tracks with a cone of $\Delta R < 0.25$, referred to as p_T^{Cone} , which is shown in Figure 78 for data and simulated signal events. In the data this value has a peak at zero from isolated tracks such as leptons, and a long tail from jets which contains as much as 80% of the background above 20 GeV at this stage of the selection. In signal events p_T^{Cone} is strongly peaked at zero and significantly less than 1% of signal events have p_T^{Cone} above 20 GeV. This makes a requirement of $p_T^{\text{Cone}} < 20 \text{ GeV}$ a very effective method to reject background without losing signal efficiency. For the stable signal region, this cut is further tightened to $p_T^{\text{Cone}} < 5 \text{ GeV}$ as it is the most effective variable remaining to extend the search reach for long lifetimes.

Even for fully isolated particles, there are additional methods to reject each type of particle using information in the muon system and calorimeters. Muons can be identified very reliably using the tracks in the muon system, as described in Section 6.3. For intermediate lifetimes the LLPs do not survive long enough to reach the muon system, and so muons are vetoed by rejecting tracks that associate to a muon with medium muon identification requirements (Section 6.3). For longer lifetimes, this rejection is not applied because LLPs which reach the

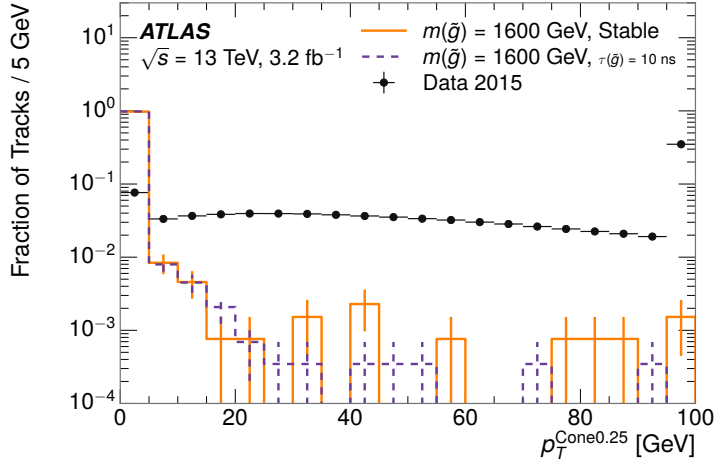


Figure 78: The distribution of summed tracked momentum within a cone of $\Delta R < 0.25$ around the candidate track for data and simulated signal events, after previous selection requirements have been applied.

muon system can be identified as muons as often as 30% of the time in simulated samples.

Calorimeter-based particle rejection relies on the expected small deposits of energy from LLPs. When the lifetime is long enough to reach the calorimeter, a LLP deposits little of its energy as it traverses the material, as discussed in Section 9.1. Even when the particle does decay before the calorimeter, the majority of its energy is carried away by the LSP and not deposited in the calorimeter. In both cases the energy is expected to be distributed across the layers of the calorimeters and not peaked in just one layer. This can be quantified in terms of E/p , the ratio of calorimeter energy of a nearby jet to the track momentum, and f_{EM} , the fraction of energy in that jet within the electromagnetic calorimeter. When no jets fall within a cone of 0.05 of the particle, E/p and f_{EM} are both defined as zero. E/p is expected to be above 1.0 for typical SM particles because of calibration and the contributions from other nearby particles, as discussed in Chapter 7. At these momenta there is no significant zero fraction due to interactions with the detector or insufficient energy deposits (see Section 7.2.2). f_{EM} is peaked close to 1.0 for electrons, and distributed between 10% and 90% for hadrons.

These trends can be seen in the two dimensional distribution for signal in Figure 79 for stable and metastable (10 ns) events. The majority of R-Hadrons in both samples fall into the bin for $E/p = 0$ and $f_{\text{EM}} = 0$ because the majority of the time there is no associated jet. In the stable sample, when there often is an associated jet, E/p is typically still below 0.1, and the f_{EM} is predominantly under 0.8. In the metastable sample, on the other hand, E/p is larger but still typically below 0.1 because of actual jets produced during the decay. The f_{EM} is much lower on average in this case, below 0.1, because the 10 ns lifetime particles rarely decay before passing through the electromagnetic calorimeter. Figure 79 also includes simulated Z decays to electrons or tau leptons. From the decays

3359 to electrons it is clear that the majority of electrons have f_{EM} above 0.9. The
 3360 tau decays include a variety of products. Muons can be seen in the bin where
 3361 $E/p = 0$ and $f_{\text{EM}} = 0$ because they do not have an associated jet. Electrons fall
 3362 into the range where $E/p > 1$ and $f_{\text{EM}} > 0.9$. Hadronic tau decays are the most
 3363 common, and fall in the range of $0.1 < f_{\text{EM}} < 0.9$ and $E/p > 1.0$.

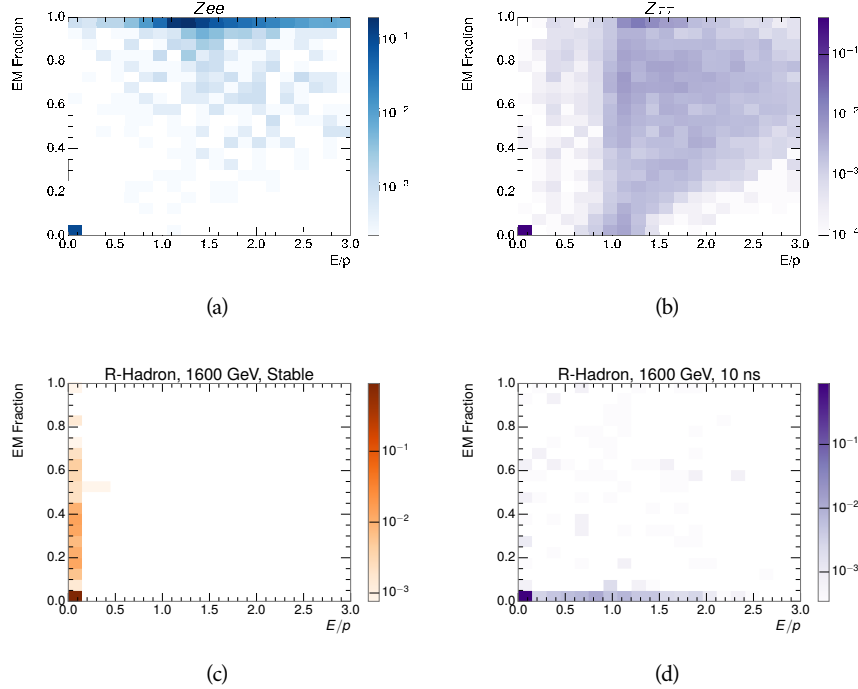


Figure 79: The normalized, two-dimensional distribution of E/p and f_{EM} for simulated
 (a) $Z \rightarrow ee$, (b) $Z \rightarrow \tau\tau$, (c) 1200 GeV Stable R-Hadron events, and (d) 1200
 GeV, 10 ns R-Hadron events.

3364 These differences motivate an electron rejection by requiring an f_{EM} below
 3365 0.9. Similarly, isolated hadrons are rejected by requiring $E/p < 1.0$. These re-
 3366 quirements combine to remove the majority of isolated electrons and hadrons
 3367 but retain over 95% of the simulated signal across a range of masses and lifetimes.

3368 10.4 IONIZATION

3369 The final requirement on the candidate track is the primary discriminating vari-
 3370 able, the ionization in the pixel detector. That ionization is measured in terms
 3371 of dE/dx , which was shown for data and simulated signal events in Figure 75.
 3372 dE/dx is dramatically greater for the high mass signal particles than the back-
 3373 grounds, which start to fall immediately after the minimally ionizing peak at 1.1
 3374 MeV g $^{-1}$ cm 2 . The dE/dx for candidate tracks must be greater than a pseudorapidity-
 3375 dependent threshold, specifically $1.80 - 0.11|\eta| + 0.17\eta^2 - 0.05|\eta|^3$ MeV g $^{-1}$ cm $^{-2}$,
 3376 in order to correct for an approximately 5% dependence of the MIP peak on η .
 3377 The requirement was chosen as part of the signal region optimization, and man-

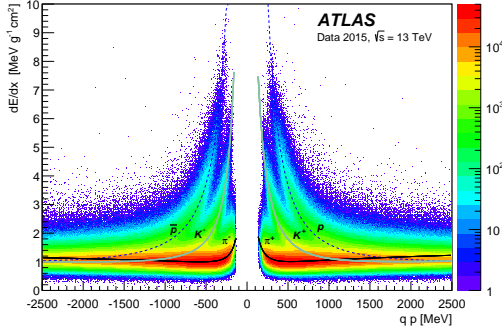


Figure 80: Two-dimensional distribution of dE/dx versus charge signed momentum (qp) for minimum-bias tracks. The fitted distributions of the most probable values for pions, kaons and protons are superimposed.

3378 ages to reduce the backgrounds by a factor of 100 while remaining 70-90% efficient
 3379 for simulated signal events depending on the mass.

3380 10.4.1 MASS ESTIMATION

3381 The mean value of ionization in silicon is governed by the Bethe equation and
 3382 the most probable value follows a Landau-Vavilov distribution [5]. Those forms
 3383 inspire a parametric description of dE/dx in terms of $\beta\gamma$,

$$(dE/dx)_{MPV}(\beta\gamma) = \frac{p_1}{\beta^{p_3}} \ln(1 + [p_2 \beta\gamma]^{p_5}) - p_4 \quad (21)$$

3384 which performs well in the range $0.3 < \beta\gamma < 1.5$. This range includes the ex-
 3385 pected range of $\beta\gamma$ for the particles targeted for this search, with $\beta\gamma \approx 2.0$ for
 3386 lower mass particles (O(100 GeV)) and up to $\beta\gamma \approx 0.5$ for higher mass par-
 3387 ticles (O(1000 GeV)). The parameters, p_i , are fit using a 2015 data sample of
 3388 low-momentum pions, kaons, and protons as described in Ref. [97]. Figure 80
 3389 shows the two-dimensional distribution of dE/dx and momentum along with
 3390 the above fitted values for $(dE/dx)_{MPV}$.

3391 The above equation (21) is then numerically inverted to estimate $\beta\gamma$ and the
 3392 mass for each candidate track. In simulated signal events, the mean of this mass
 3393 value reproduces the generated mass up to around 1800 GeV to within 3%, and
 3394 3% shift is applied to correct for this difference. The mass distributions prior to
 3395 this correction are shown for a few stable mass points in Figure 81. The large
 3396 widths of these distributions come from the high variability in energy deposits
 3397 in the pixel detector as well as the uncertainty on momentum measurements at
 3398 high momentum, but the means converge to the expected values.

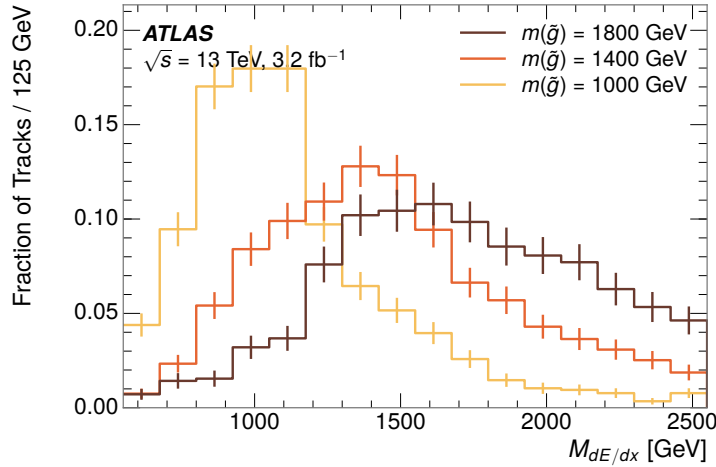


Figure 81: The distribution of mass estimated using dE/dx for simulated stable R-Hadrons with masses between 1000 and 1600 GeV.

3399 This analysis evaluates expected yields and the resulting cross sectional limits
 3400 using windows in this mass variable. The windows are formed by fitting mass
 3401 distributions in simulated signal events like those in Figure 81 to Gaussian distri-
 3402 butions and taking all events that fall within $\pm 1.4\sigma$ of the mean. As can be seen
 3403 in Figure 81, typical values for this width are $\sigma \approx 300 - 500$ GeV depending on
 3404 the generated mass.

3405 10.5 EFFICIENCY

3406 The numbers of events passing each requirement through ionization are shown
 3407 in Table 9 for the full 2015 dataset and a simulated 1600 GeV, 10 ns lifetime R-
 3408 Hadron sample. The table highlights the overall acceptance \times efficiency for sig-
 3409 nal events, which for this example is 19%. Between SM rejection and ionization,
 3410 this signal region reduces the background of tracks which pass the kinematic
 3411 requirements down by an additional factor of almost 2000.

3412 There is a strong dependence of this efficiency on lifetime and mass, with effi-
 3413 ciencies dropping to under 1% at low lifetimes. Figure 82 shows the dependence
 3414 on both mass and lifetime for all signal samples considered in this search. The
 3415 dependence on mass is relatively slight and comes predominantly from the in-
 3416 creasing fraction of R-Hadrons which pass the ionization cut with increasing
 3417 mass. The trigger and E_T^{miss} requirements are most efficient for particles that
 3418 decay before reaching the calorimeters. However, the chance of a particle to be
 3419 reconstructed as a high-quality track decreases significantly at low lifetimes as
 3420 the particle does not propagate sufficiently through the inner detector. These
 3421 effects lead to a maximum in the selection efficiency for lifetimes around 10-30
 3422 ns.

3423 The inefficiency of this signal region at short lifetimes comes almost exclu-
 3424 sively from an acceptance effect, in that the particles do not reach the necessary

Selection	Exp. Signal Events	Observed Events in 3.2 fb^{-1}
Generated	26.0 ± 0.3	
E_T^{miss} Trigger	24.8 ± 0.3 (95%)	
$E_T^{\text{miss}} > 130 \text{ GeV}$	23.9 ± 0.3 (92%)	
Track Quality and $p_T > 50$	10.7 ± 0.2 (41%)	368324
Isolation Requirement	9.0 ± 0.2 (35%)	108079
Track $p > 150 \text{ GeV}$	6.6 ± 0.2 (25%)	47463
$M_T > 130 \text{ GeV}$	5.8 ± 0.2 (22%)	18746
Electron and Hadron Veto	5.5 ± 0.2 (21%)	3612
Muon Veto	5.5 ± 0.2 (21%)	1668
Ionization Requirement	5.0 ± 0.1 (19%)	11

Table 9: The expected number of events at each level of the selection for metastable 1600 GeV , 10 ns R-Hadrons, along with the number of events observed in data, for 3.2 fb^{-1} . The simulated yields are shown with statistical uncertainties only. The total efficiency \times acceptance is also shown for the signal.

3425 layers of the SCT. This can be seen more clearly by defining a fiducial region
 3426 which includes events with at least one R-Hadron that is produced with non-
 3427 zero charge, $p_T > 50 \text{ GeV}$, $p > 150 \text{ GeV}$, $|\eta| < 2.5$, and a decay distance greater
 3428 than 37 cm in the transverse plane. At short (1 ns) lifetimes, the acceptance into
 3429 this region is as low as 4%. Once this acceptance is accounted for, the selection
 3430 efficiency ranges from 25% at lifetimes of 1 ns up to 45% at lifetimes of 10 ns.

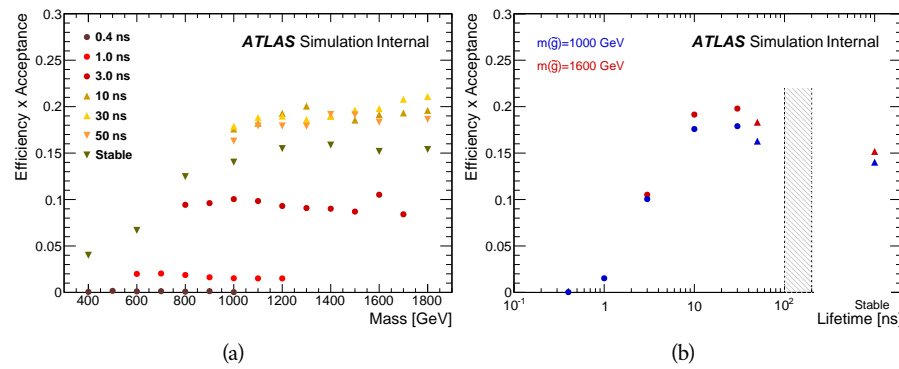


Figure 82: The acceptance \times efficiency as a function of R-Hadron (a) mass and (b) lifetime. (a) shows all of the combinations of mass and lifetime considered in this search, and (b) highlights the lifetime dependence for 1000 GeV and 1600 GeV R-Hadrons.

3431

3432 BACKGROUND ESTIMATION

3433 The event selection discussed in the previous section focuses on detector sig-
 3434 natures, emphasizing a single high-momentum, highly-ionizing track. That track
 3435 is then required to be in some way inconsistent with the expected properties
 3436 of SM particles, with various requirements designed to reject jets, hadrons, elec-
 3437 trons, and muons (Section 10.3). Therefore the background for this search comes
 3438 entirely from reducible backgrounds that are outliers of various distributions in-
 3439 cluding dE/dx , f_{EM} , and p_T^{Cone} . The simulation can be tuned in various ways to
 3440 do an excellent job of modeling the average properties of each particle type [98],
 3441 but it is not necessarily expected to accurately reproduce outliers. For this rea-
 3442 sons, the background estimation used for this search is estimated entirely using
 3443 data.

3444 11.1 BACKGROUND SOURCES

3445 SM charged particles with lifetimes long enough to form tracks in the inner de-
 3446 tector can be grouped into three major categories based on their detector inter-
 3447 actions: hadrons, electrons, and muons. Every particle that enters into the back-
 3448 ground for this search belongs to one of these types. Relatively pure samples of
 3449 tracks from each of these types can be formed in data by inverting the various
 3450 rejection techniques in Section 10.3. Specifically, muons are selected requiring
 3451 medium muon identification, electrons requiring $E/p > 1.0$ and $f_{EM} > 0.95$,
 3452 and hadrons requiring $E/p > 1.0$ and $f_{EM} < 0.95$.

3453 Figure 83 shows the distributions of momentum and dE/dx for these cate-
 3454 gories in data, after requiring the event level selection as well as the track re-
 3455 quirements on p_T , hits, and N_{split} , as discussed in Section 10.2. Simulated signal
 3456 events are included for reference. These distribution are only illustrative of the
 3457 differences between types, as the rejection requirements could alter their shape.
 3458 This is especially significant for momentum which enters directly into E/p and
 3459 can indirectly affect muon identification. However the various types show clear
 3460 differences in both distributions. The distributions of momentum are not nec-
 3461 essarily expected to match between the various types because the production
 3462 mechanisms for each type result in different kinematic distributions. dE/dx is
 3463 also different between types because of incomplete isolation; although the re-
 3464 quirement on N_{split} helps to reduce the contribution of nearby particles it does
 3465 not completely remove the effect of overlaps. Muons are better isolated because
 3466 they do not have the additional particle from hadronization present for hadrons
 3467 and they are significantly less likely to interact with the detector and produce
 3468 secondary particles compared to hadrons and electrons. Thus muons have the
 3469 smallest fraction of dE/dx above the threshold of $1.8 \text{ MeVg}^{-1}\text{cm}^2$; hadrons and
 3470 electrons have a larger fraction above this threshold.

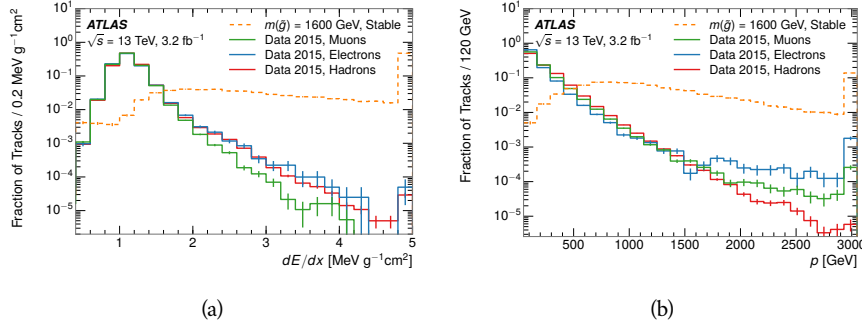


Figure 83: The distribution of (a) dE/dx and (b) momentum for tracks in data and simulated signal after requiring the event level selection and the track selection on p_T , hits, and N_{split} . Each sub-figure shows the normalized distributions for tracks classified as hadrons, electrons, and muons in data and R-Hadrons in the simulated signal.

3471 It is difficult to determine what fraction of each particle type enters into the fi-
 3472 nal signal region. The background method will not have significant dependence
 3473 on the relative contributions of each species, but it is useful to understand the
 3474 differences between each when considering the various tests of the method.

3475 11.2 PREDICTION METHOD

3476 The data-driven background estimation relies on the independence between ion-
 3477 ization and other kinematic variables in the event. For standard model particles
 3478 with momenta above 50 GeV, dE/dx is not correlated with momentum; though
 3479 there is a slight relativistic rise as momentum increases, the effect is small com-
 3480 pared to the width of the distribution of ionization energy deposits.. So, the
 3481 proposed method to estimate the mass distribution of the signal region is to use
 3482 momentum from a track with low dE/dx (below the threshold value) and to com-
 3483 bine it with a random dE/dx value from a dE/dx template. The resulting track is
 3484 just as likely as the original, so a number of such random generations provide the
 3485 expected distributions of momentum and ionization. These are then combined
 3486 using the parametrization described in Section 10.4.1 to form a distribution of
 3487 mass for the signal region.

3488 Algorithmically this method is implemented by forming two distinct Control
 3489 Regions (**CRs**). The first **CR**, CR1, is formed by applying the entire event selec-
 3490 tion from Chapter 10 up to the dE/dx and mass requirements. The dE/dx re-
 3491 quirement is instead inverted for this region. Because of the independence of
 3492 dE/dx , the tracks in this control region have the same kinematic distribution
 3493 as the tracks in the signal region, and are used to measure a two-dimensional
 3494 template of p and η . The second **CR**, CR2, is formed from the event selection
 3495 through the dE/dx requirement, but with an inverted E_T^{miss} requirement. The
 3496 tracks in this control region are expected to have similar dE/dx distributions to
 3497 the signal region before the ionization requirement, and so this region is used to
 3498 measure a two-dimensional template of dE/dx and η .

3499 The contribution of any signal to the control regions is minimized by the in-
 3500 verted selection requirements. Only less than 10% of simulated signal events
 3501 have either dE/dx or E_T^{miss} below the threshold values in the original signal re-
 3502 gion, while the backgrounds are significantly enhanced by inverting those re-
 3503 quirements. The signal contamination is less than 1% in both control regions
 3504 for all of the simulated masses and lifetimes considered in this analysis.

3505 With those measured templates, the shape of the mass estimation is generated
 3506 by first selecting a random (p , η) combination from CR1. This momentum
 3507 value is combined with a dE/dx value taken from the appropriate distribution
 3508 of dE/dx for the selected η from CR2. The use of η in both random samplings
 3509 controls for any correlation between p , dE/dx , and η . Those values are then
 3510 used to calculate a mass in the same way that is done for regular tracks in data,
 3511 see Section 10.4.1. As this procedure includes all dE/dx values, the cut at 1.8
 3512 MeVg $^{-1}$ cm 2 is then enforced to fully model the signal region. The generated
 3513 mass distribution is then normalized by scaling the background estimate to the
 3514 data in the region $M < 160$ GeV, where signals of this type have already been
 3515 excluded [82]. This normalization uses the distributions of mass generated with-
 3516 out the ionization requirement.

3517 The statistical uncertainties on these background distributions are calculated
 3518 by independently fluctuating each bin of the input templates according to their
 3519 Poisson uncertainties. These fluctuations are repeated a large number of times,
 3520 and the uncertainty on the resulting distribution is taken as the root mean square
 3521 (RMS) deviation of the fluctuations from the average. As the procedure uses one
 3522 million random combinations to generate the distributions, The statistical un-
 3523 certainty from the actual random generations is negligible compared to the un-
 3524 certainty from measuring the templates.

3525 11.3 VALIDATION

3526 The validity of the background estimation technique can be evaluated in both
 3527 data and simulation. The underlying assumption that random combinations of
 3528 dE/dx and momentum can predict a mass distribution in an orthogonal region
 3529 can be tested using simulated samples where concerns like multiple particle types
 3530 can be controlled. Using the same technique in another set of signal-depleted
 3531 regions in data then extends this confidence to the more complicated case where
 3532 several particle species are inherently included.

3533 11.3.1 CLOSURE IN SIMULATION

3534 The first test of the procedure is done using a simulated sample of $W \rightarrow \mu\nu$
 3535 decays. These types of events provide the ingredients required to test the back-
 3536 ground estimate, E_T^{miss} and isolated tracks, with high statistics. In this example
 3537 there is no signal, so simulated events in the orthogonal CRs are used to estimate
 3538 the shape of the mass distribution of the simulated events in the signal region. To
 3539 reflect the different topology for W boson decays, the CRs use slightly modified
 3540 definitions. In all CRs, the requirement of $p > 150$ GeV and the SM rejection

3541 requirements are removed. Additionally, for the signal region the requirement
3542 on E_T^{miss} is relaxed to 30 GeV and the corresponding inverted requirement on
3543 CR2 is also set at 30 GeV.

With these modified selections, the simulated and randomly generated distributions of $M_{dE/dx}$ are shown in Figure 84. This figure includes the mass distributions before and after the requirement on dE/dx , which significantly shapes the distributions. In both cases the background estimation technique reproduces the shape of $M_{dE/dx}$ in the signal region. There is a small difference in the positive tail of the mass distribution prior to the ionization cut, where the random events underestimate the fraction of tracks with mass above 150 GeV by about 20%. After the ionization requirement, however, this discrepancy is not present and the two distributions agree to within statistical uncertainties.

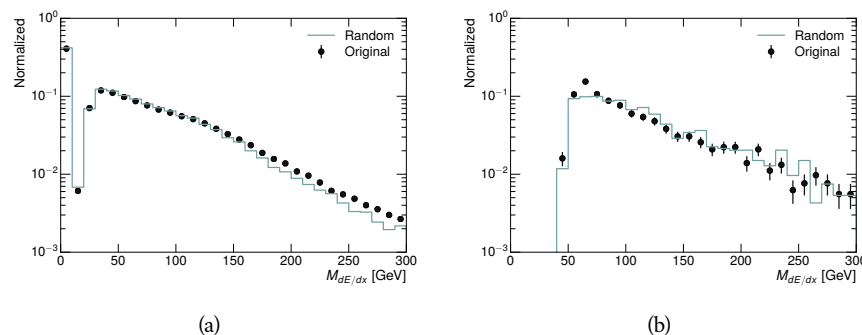


Figure 84: The distribution of $M_{dE/dx}$ (a) before and (b) after the ionization requirement for tracks in simulated W boson decays and for the randomly generated background estimate.

This ability to reproduce the shape of the mass distribution in simulated events shows that the technique works as expected. No significant biases are acquired in using low dE/dx events to select kinematic templates or in using low E_T^{miss} events to select ionization templates, as either would result in a mismodeling of the shape of the mass distribution. The simulated events contain only one particle type, however, so this test only establishes that the technique works well when the the CRs are populated by exactly the same species.

3560 11.3.2 VALIDATION REGION IN DATA

The second test of the background estimate is performed using data in an orthogonal validation region. The validation region, and the corresponding CRs, are formed using the same selection requirements as in the nominal method but with a modified requirement on momentum, $50 < p[\text{GeV}] < 150$. This allows the technique to be checked in a region with very similar properties but where the signal is depleted, as the majority of the signal has momentum above 150 GeV while the backgrounds are enhanced below that threshold. Any biases on the particle composition of the CRs for the signal region will be reflected in the CRs used to estimate the mass distribution in the validation region.

Figure 85 shows the measured and randomly generated mass distributions for data before and after the ionization requirement. The background estimate does an excellent job of modeling the actual background before the ionization requirement, with good agreement to within the statistical uncertainties out to the limit of the mass distribution. There are very few events in the validation region after the ionization requirement, but the few observed events are consistent with the background prediction. The good agreement in this validation region provides a confirmation that the technique works even in the full-complexity case with multiple particle types entering the distributions. Any bias from changes in particle composition between regions is small compared to statistical uncertainties.

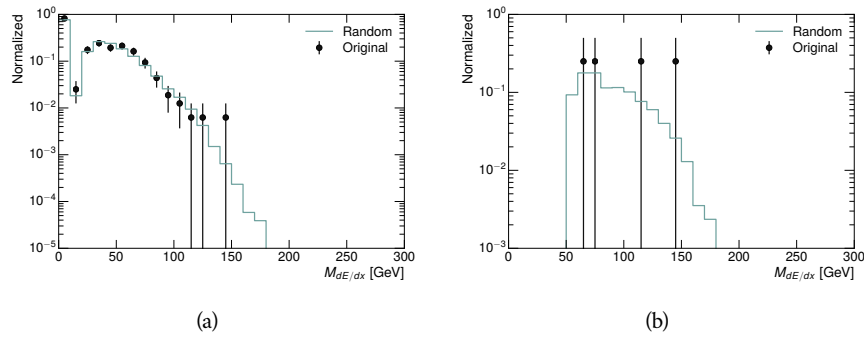


Figure 85: The distribution of $M_{dE/dx}$ (a) before and (b) after the ionization requirement for tracks in the validation region and for the randomly generated background estimate.

12

3580

3581 SYSTEMATIC UNCERTAINTIES AND RESULTS

3582

3583 SYSTEMATIC UNCERTAINTIES AND RESULTS

3584 13.1 SYSTEMATIC UNCERTAINTIES

3585 A number of systematic uncertainties affect the interpretation of the results of
 3586 the search. These uncertainties can broken down into two major categories,
 3587 those which affect the estimate of the background using data and those which
 3588 affect the measurement of the signal yield estimated with simulated events. The
 3589 total measured systematic uncertainties are 7% for the background estimation
 3590 and approximately 32% for the signal yield depending on lifetime. These system-
 3591atic uncertainties are expected to be small compared to the statistical fluctuations
 3592 of the measured yields so that measured cross-sectional limits will be dominated
 3593 by statistical uncertainties. The following sections describe each source of sys-
 3594 tematic uncertainty for each of the two types.

3595 13.1.1 BACKGROUND ESTIMATE

3596 The systematic uncertainties on the background estimate come primarily from
 3597 considering alternative methods for generating the background distributions.
 3598 These uncertainties are small compared to the statistical uncertainties on the
 3599 background estimate which come from the limited statistics in measuring the
 3600 template distributions, as described in Section 11.2. They are summarized in
 3601 Table 10.

Source of Uncertainty:	Value [%]
Analytic Description of dE/dx	4.0
Muon Fraction (Stable Region only)	3.0
IBL Ionization Correction	3.8
Normalization	3.0
Total (Metastable Region):	6.3
Total (Stable Region):	7.0

Table 10: A summary of the sources of systematic uncertainty for the data-driven back-
 ground in the signal region. If the uncertainty depends on the mass, the maxi-
 mum values are reported.

3602 13.1.1.1 ANALYTIC DESCRIPTION OF DE/DX

3603 The background estimate uses a binned template distribution to estimate the
 3604 dE/dx of tracks in the signal region, as described in Section 11.2. It is also possi-

ble to fit that measured distribution to a functional form to help smooth the distribution in the tails of dE/dx where the template is driven by a small number of tracks. Both Landau convolved with a Gaussian and Crystal Ball functions are considered as the functional form and used to re-estimate the background distribution. The deviations compared to the nominal method are found to be 4%, and this is taken as a systematic uncertainty to cover the inability carefully predict the contribution from the long tail of dE/dx where there are few measurements available in data.

3613 13.1.1.2 MUON FRACTION

3614 The stable region of the analysis explicitly includes tracks identified as muons,
 3615 which have a known difference in their dE/dx distributions compared to non-
 3616 muon tracks (Section 11.1). To account for a difference in muon fraction be-
 3617 tween the background region and the signal region for this selection, the dE/dx
 3618 templates for muons and non-muons are measured separately and then the rel-
 3619 ative fraction of each is varied in the random generation. The muon fraction
 3620 is varied by its statistical uncertainty and the resulting difference of 3% in back-
 3621 ground yield is taken as the systematic uncertainty.

3622 13.1.1.3 IBL CORRECTIONS

3623 The **IBL**, described in Section 5.3.1, received a significant dose of radiation during
 3624 the data collection in 2015. The irradiation can cause a drift in the frontend
 3625 electronics and thus alter the dE/dx measurement which includes the **ToT** output
 3626 by the **IBL**. These effects are corrected for in the nominal analysis by scaling the
 3627 dE/dx measurements by a constant factor derived for each run to match the
 3628 average dE/dx value to a reference run where the **IBL** was known to be stable
 3629 to this effect. However, this corrective factor does not account for inter-run
 3630 variations. To account for this potential drift of dE/dx , the correction procedure
 3631 is repeated by varying the corrections up and down by the maximal run-to-run
 3632 variation from the full data-taking period, which results in an uncertainty of
 3633 3.8%.

3634 13.1.1.4 NORMALIZATION

3635 As described in Section 11.2, the generated distribution of masses is normalized
 3636 in a shoulder region ($M < 160$ GeV) where signals have been excluded by pre-
 3637 vious analyses. That normalization factor is varied by its statistical uncertainty
 3638 and the resulting fluctuation in the mass distribution of 3% is taken as a system-
 3639 atic uncertainty on the background estimate.

3640 13.1.2 SIGNAL YIELD

3641 The systematic uncertainties on the signal yield can be divided into three cate-
 3642 gories; those on the simulation process, those on the modeling of the detector
 3643 efficiency or calibration, and those affecting the overall signal yield. They are
 3644 summarized in Table 10. The largest uncertainty comes from the uncertainty

3645 on the production cross section for gluinos, which is the dominant systematic
 3646 uncertainty in this analysis.

Source of Uncertainty	-[%]	+[%]
ISR Modeling (Metastable Region)	1.5	1.5
ISR Modeling (Stable Region)	14	14
Pile-up Reweighting	1.1	1.1
Trigger Efficiency Reweighting	0.9	0.9
E_T^{miss} Scale	1.1	2.2
Ionization Parametrization	7.1	0
Momentum Parametrization	0.3	0.0
Electron Rejection	0.0	0.0
Hadron Rejection	0.0	0.0
μ Identification	4.3	4.3
Luminosity	5	5
Signal size uncertainty	28	28
Total (Metastable Region)	30	29
Total (Stable Region)	33	32

Table 11: A summary of the sources of systematic uncertainty for the simulated signal yield. The uncertainty depends on the mass and lifetime, and the maximum negative and positive values are reported in the table.

3647 13.1.2.1 ISR MODELING

3648 As discussed in Section 9.2, MadGraph is expected to reproduce the distribution
 3649 of ISR in signal events more accurately than the nominal Pythia samples. The
 3650 analysis reweights the distribution of ISR in the simulated signal events to match
 3651 the distribution found in generated MadGraph samples. This has an effect on the
 3652 selection efficiency in the signal samples, where ISR contributes to the generation
 3653 of E_T^{miss} . To account for the potential inaccuracy on the simulation of ISR at high
 3654 energies, half of the difference between the signal efficiency with the reweighted
 3655 distribution and the original distribution is taken as a systematic uncertainty.

3656 13.1.2.2 PILEUP REWEIGHTING

3657 The simulated events were generated prior to data collection with an estimate of
 3658 the average number of interactions per bunch crossing. This estimate does not
 3659 match the value of pileup during actual data collection, but a large fraction of the
 3660 simulated events would be discarded in order to match the distribution in data.
 3661 Therefore the simulated signal events are not reweighted for pileup by default
 3662 in the analysis. The effect of the pileup on signal efficiency is not expected to
 3663 depend on the mass or lifetime of the generated signal events, which allows all

of the generated signal events to be used together to assess the pileup dependence. To account for the potential effect of the difference in the number of interactions per bunch crossing between data and simulation, the difference in yield between the nominal signal events and the reweighted events averaged over all masses and lifetimes is taken as a systematic uncertainty on the yield for each mass and lifetime (1.1%).

13.1.2.3 TRIGGER EFFICIENCY REWEIGHTING

As described in Section 10.2, the selection for this analysis does not require a sufficiently large value of E_T^{miss} to be above the plateau of trigger efficiency. Therefore, some signal events which would otherwise pass the event selection can be excluded because of the trigger requirement. These effects can be difficult to estimate in simulation, and thus are constrained by comparing data and simulated events in an alternative W boson region which uses decays to muons to find a relatively pure sample of events with missing energy. The trigger efficiency for data and simulated W events are shown in Figure 86. The comparison between data and MC in this region constrains the simulation of the trigger efficiency. The simulated signal events are reweighted by the ratio of data to simulation in the W boson decays, while the difference between the data and simulation in those decays is taken as a systematic uncertainty. This results in an uncertainty of only 0.9% as the majority of events are well above the plateau and the disagreement between data and simulation is small even below that plateau.

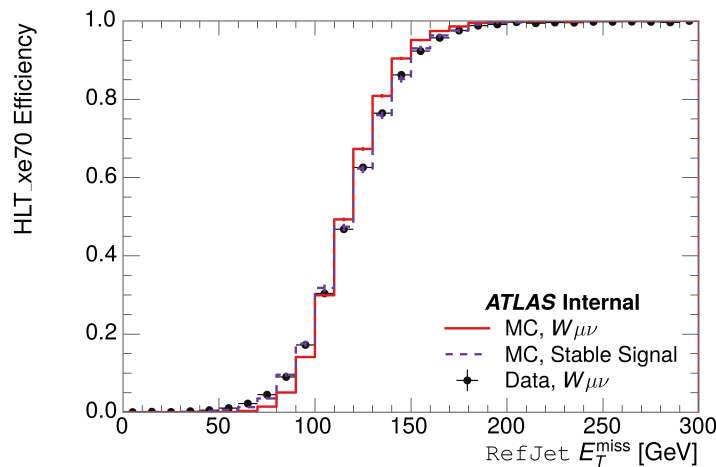


Figure 86: The trigger efficiency for the HLT_xe70 trigger requirement as a function of Calorimeter E_T^{miss} for simulated data events with a W boson selection. Simulated signal events and simulated W boson events are also included.

13.1.2.4 MISSING TRANSVERSE MOMENTUM SCALE

The ATLAS Combined Performance (CP) group provides a default recommendation for systematic variations of jets and missing energy (**note: I'm not quite sure what to cite for this - I don't see any papers from the jet/met group**

Systematic Variation	-[%]	+[%]
JET_GroupedNP_1	-0.7	1.3
JET_GroupedNP_2	-0.7	1.2
JET_GroupedNP_3	-0.5	1.3

Table 12: Example of the contributing systematic variations to the total systematic for the E_T^{miss} Scale, as measured in a 1200 GeV, Stable R-Hadron signal sample.

3689 **after this was implemented).** These variations enter into this analysis only in
 3690 the requirement on E_T^{miss} . The effect of the measured scale of E_T^{miss} is evaluated
 3691 by varying the E_T^{miss} scale according to the one sigma variations provided by all
 3692 **CP** recommendations on objects affecting event kinematics in simulated signal
 3693 events. Missing energy is reconstructed from fully reconstructed objects so any
 3694 systematic uncertainties affecting jets, muons, electrons, or the E_T^{miss} soft terms
 3695 are included. The only non-negligible contributions found using this method are
 3696 itemized in Table 12 for an example signal sample (1200 GeV, Stable R-Hadron),
 3697 where the systematic is measured as the relative difference in the final signal ef-
 3698 ficiency after applying the associated variation through the CP tools. The only
 3699 variations that are significant are the grouped jet systematic variations, which
 3700 combine recommended jet systematic uncertainties into linearly independent
 3701 variations.

3702 As the peak of the reconstructed E_T^{miss} distribution in the signal is significantly
 3703 above the current threshold for events which pass the trigger requirement, the
 3704 effect of scale variation is expected to be small, which is consistent with the mea-
 3705 sured systematic of approximately 2%. Events which do not pass the trigger re-
 3706 quirement usually fail because there are no ISR jets in the event to balance the
 3707 R -hadrons' transverse momentum, so the reconstructed E_T^{miss} is low and there-
 3708 fore also expected to be not very sensitive to scale changes.

3709 13.1.2.5 MOMENTUM PARAMETRIZATION

3710 The uncertainty on the signal efficiency from track momentum is calculated us-
 3711 ing the **CP** group recommendations for tracks. In particular, only one recom-
 3712 mended systematic variation affects track momentum, the sagitta bias for q/P .
 3713 This uncertainty is propagated to the final selection efficiency by varying the
 3714 track momentum by the recommended one sigma variation, and the associated
 3715 uncertainty is found to be negligible (0.3%).

3716 13.1.2.6 IONIZATION REQUIREMENT

3717 The dE/dx distributions in data and simulated events have different most prob-
 3718 able values, which is due in part to radiation effects in the detector that are not
 3719 fully accounted for in the simulation. The difference does not affect the mass
 3720 measurement used in this analysis, as independent calibrations are done in sim-
 3721 ulation and in data. However, it does affect the efficiency of the high dE/dx
 3722 selection requirement. To calculate the size of the effect on the signal efficiency,

3723 the dE/dx distribution in signal simulation is scaled by a scale factor obtained
 3724 from comparing the dE/dx distribution of inclusive tracks in data and in sim-
 3725 ulation. The difference in efficiency for this sample with a scaled dE/dx dis-
 3726 tribution, relative to the nominal case, is taken as a systematic uncertainty on
 3727 signal efficiency. The uncertainty is as large as 7% for low masses and falls to a
 3728 negligible effect for large masses.

3729 13.1.2.7 ELECTRON AND JET REJECTION

3730 The systematic uncertainty on the electron rejection is measured by varying the
 3731 EM fraction requirement significantly, from 0.95 to 0.9. This is found to have
 3732 a less than 0.04% effect on signal acceptance, on average, and so is completely
 3733 negligible. Similarly, the uncertainty on jet rejection is measured by tightening
 3734 the E/p requirement from 0.5 to 0.4. This is found to have no effect on signal
 3735 acceptance, so again the systematic is again negligible.

3736 13.1.2.8 MUON VETO

3737 The metastable signal region requires that the candidate tracks are not identi-
 3738 fied as medium muons because the majority of R-Hadrons in the lifetime range
 3739 included in that region do not reach the muon spectrometers before they de-
 3740 cay. However, the exponential tail of the R-Hadron lifetime distribution results
 3741 in some R-Hadrons traversing the muon spectrometer. These can still fail the
 3742 muon medium identification because they can fail on the requirement on the
 3743 number of precision hits required to pass the loose selection because they ar-
 3744 rive late to the muon spectrometer. This can be seen in Figure 87, which shows
 3745 the efficiency of the muon veto as a function of $1/\beta$, for two simulated stable
 3746 R-Hadron samples.

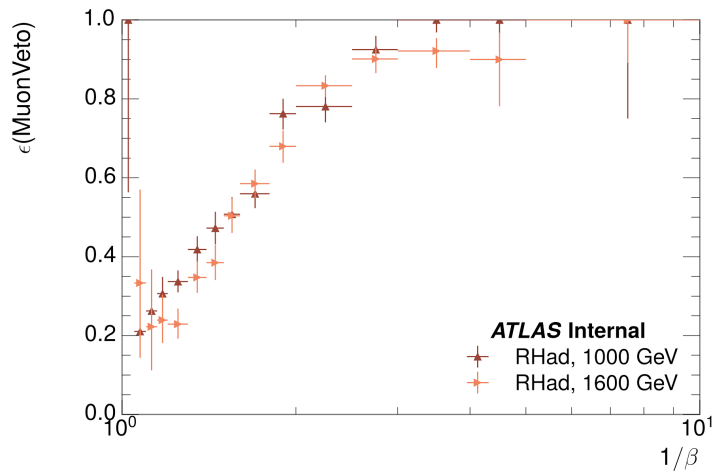


Figure 87: The efficiency of the muon veto for R -hadrons of two different masses, as a function of $\frac{1}{\beta}$ for simulated R-Hadron tracks.

3747 Thus, the efficiency of the muon veto depends on the timing resolution of
 3748 the spectrometer, so an uncertainty is applied to the signal efficiency to cover

3749 differences in timing resolution between data and simulation. First, a sample of
 3750 $Z \rightarrow \mu\mu$ events is selected in data in which one of the muons has a late arrival
 3751 time measured in the MDT. Then the reconstructed β distribution is compared
 3752 to the distribution in simulated $Z \rightarrow \mu\mu$ events; the difference between these
 3753 two distributions reflects the difference in timing resolution between data and
 3754 simulation. To emulate this difference in simulated signal events, the magnitude
 3755 of the difference is used to scale and shift the true β distribution of R-Hadrons in
 3756 simulation. Signal events are then reweighted based on this varied β distribution,
 3757 and the difference in the efficiency of the muon veto selection is compared with
 3758 the nominal and reweighted true β distributions. The difference in muon veto
 3759 efficiency is taken as a systematic uncertainty of the muon veto.

3760 The comparison of reconstructed β between data and simulation is performed
 3761 separately in the barrel, transition, and endcap regions of the spectrometer, and
 3762 the reweighting of the true β distribution in signal is done per region. The com-
 3763 parison of average reconstructed MDT β between data and simulation for the
 3764 barrel region is shown in Figure 88 for $Z \rightarrow \mu\mu$ events. As expected, The uncer-
 3765 tainty is found to be negligible for R -hadrons with short lifetimes, and is only
 3766 significant for lifetimes above 30 ns.

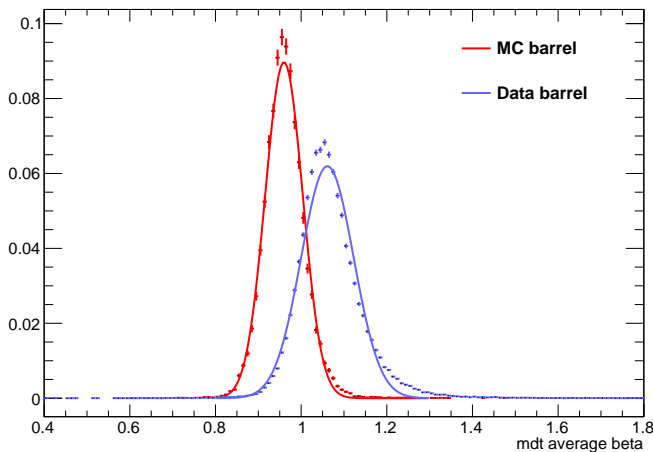


Figure 88: The average reconstructed MDT β distribution for $Z \rightarrow \mu\mu$ events in which
 one of the muons is reconstructed as a slow muon, for both data and simula-
 tion. A gaussian fit is superimposed.

3767 13.1.2.9 LUMINOSITY

3768 The luminosity uncertainty is provided by a luminosity measurement on ATLAS
 3769 and was measured to be 5% at the time of the publication of this analysis.

3770 13.1.2.10 SIGNAL SIZE

3771 As discussed in Section 9.2, the signal cross sections are calculated at NLO in the
 3772 strong coupling constant with a resummation of soft-gluon emission at NLL. The
 3773 uncertainties on those cross sections are between 14% to 28% for the R-Hadrons

Selection Region	Expected Background	Data
Stable	$17.2 \pm 2.6 \pm 1.2$	16
Metastable	$11.1 \pm 1.7 \pm 0.7$	11

Table 13: The estimated number of background events and the number of observed events in data for the specified selection regions prior to the requirement on mass. The background estimates show statistical and systematic uncertainties.

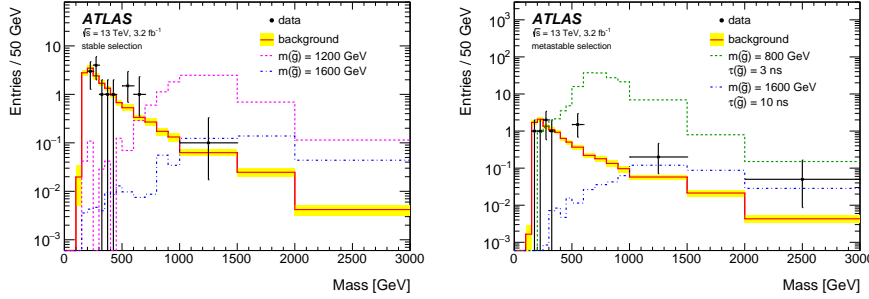


Figure 89: The observed mass distribution of events in data and the generated background distribution in (a) the stable and (b) the metastable signal region. A few example simulated signal distributions are superimposed.

3774 in the range of 400 to 1800 GeV [94, 95], where the uncertainty increases with
3775 the mass.

3776 13.2 FINAL YIELDS

3777 This full analysis was performed using the 3.2 fb^{-1} from the 2015 data-taking.
3778 Using the selections discussed in Chapter 10, sixteen events were observed in
3779 the stable signal region and eleven events were observed in the metastable signal
3780 region, prior to requirements on the candidate track mass. The background esti-
3781 mate discussed in Chapter 11 predicts $17 \pm 2.6(\text{stat}) \pm 1.2(\text{syst})$ events for the
3782 stable region and $11.1 \pm 1.7(\text{stat}) \pm 0.7(\text{syst})$ events for the metastable region.
3783 These counts are summarized in Table 13.

3784 The mass estimated using dE/dx (Section 10.4.1) provides the final discrimi-
3785 nating variable, where the signal would be expected as an excess in the falling ex-
3786 ponential tail of the expected background. The observed distribution of masses
3787 is shown in Figure 89, along with the predicted distribution from the background
3788 estimate for each signal region. Both include a few example simulated signal dis-
3789 tributions, which show the scale of an excess were the R-Hadron signals present.
3790 Their is no statistically significant evidence of an excess in the data over the back-
3791 ground estimation. From this distribution it is clearly possible to rule out signals
3792 with lower masses, around 1200 GeV, which have larger cross sections.

3793 13.3 CROSS SECTIONAL LIMITS

3794 Because there is no observed significant excess of events in the signal region, this
 3795 analysis sets upper limits on the allowed cross section for R-Hadron production.
 3796 These limits are set for each mass point by counting the observed events in data,
 3797 along with the expected background and simulated signal events, in windows of
 3798 mass. The mass windows are formed by fitting the distribution of signal events to
 3799 a Gaussian distribution, and the window is then $\pm 1.4\sigma$ around the center of that
 3800 Gaussian. Two examples of the windows formed by this procedure are shown
 3801 in Tables 14-15, for the stable and 10 ns working points. The corresponding
 3802 counts of observed data, expected background, and simulated signal for those
 3803 same working points are shown in Tables 16-17. Appendix B includes the mass
 3804 windows and counts for all of the considered signal points.

$m(\tilde{g})$ [GeV]	Left Extremum [GeV]	Right Extremum [GeV]
1000	655	1349
1100	734	1455
1200	712	1631
1300	792	1737
1400	717	1926
1500	815	2117
1600	824	2122
1700	900	2274
1800	919	2344

Table 14: The left and right extremum of the mass window for each generated mass point with a 10 ns lifetime.

$m(\tilde{g})$ [GeV]	Left Extremum [GeV]	Right Extremum [GeV]
800	627	1053
1000	726	1277
1200	857	1584
1400	924	1937
1600	993	2308
1800	1004	2554

Table 15: The left and right extremum of the mass window used for each generated stable mass point.

3805 The 95% confidence level upper limits on the cross sections for a large grid of
 3806 masses (between 800 and 1800 GeV) and lifetimes (between 0.4 and stable) are
 3807 extracted from these counts with the CL_S method using the profile likelihood

$m(\tilde{g})$ [GeV]	Expected Signal	Expected Background	Observed Data
800	462.83 ± 14.86	1.764 ± 0.080	2.0
1000	108.73 ± 3.38	1.458 ± 0.070	1.0
1200	31.74 ± 0.95	1.137 ± 0.060	1.0
1400	10.22 ± 0.29	1.058 ± 0.058	1.0
1600	3.07 ± 0.09	0.947 ± 0.054	1.0
1800	1.08 ± 0.05	0.940 ± 0.054	1.0

Table 16: The expected number of signal events, the expected number of background events, and the observed number of events in data with their respective statistical errors within the respective mass window for each generated stable mass point

$m(\tilde{g})$ [GeV]	Expected Signal	Expected Background	Observed Data
1000	144.48 ± 5.14	1.499 ± 0.069	2.0
1100	73.19 ± 2.61	1.260 ± 0.060	2.0
1200	41.54 ± 1.41	1.456 ± 0.067	2.0
1300	22.58 ± 0.77	1.201 ± 0.058	2.0
1400	12.70 ± 0.42	1.558 ± 0.071	2.0
1500	6.73 ± 0.24	1.237 ± 0.060	2.0
1600	3.90 ± 0.13	1.201 ± 0.058	2.0
1700	2.27 ± 0.07	1.027 ± 0.052	2.0
1800	1.34 ± 0.04	1.019 ± 0.052	2.0

Table 17: The expected number of signal events, the expected number of background events, and the observed number of events in data with their respective statistical errors within the respective mass window for each generated mass point with a lifetime of 10 ns.

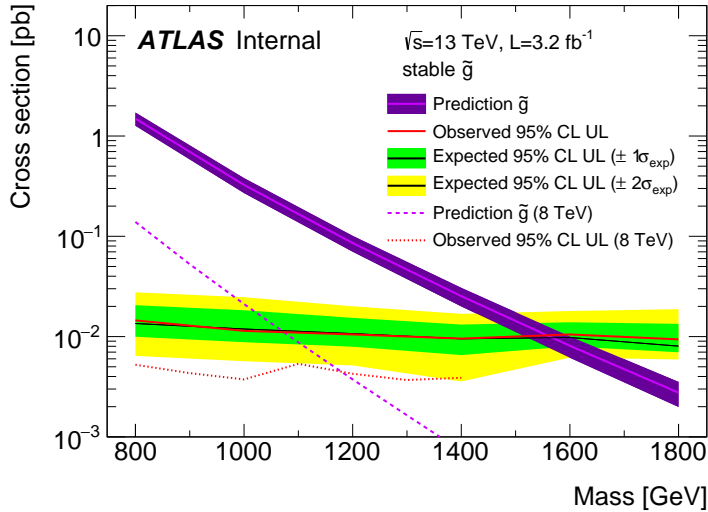


Figure 90: The observed and expected cross section limits as a function of mass for the stable simulated signal. The predicted cross section values for the corresponding signals are included.

ratio as a test statistic [99]. For this procedure, the systematic uncertainties estimated for the signal and background yields are treated as Gaussian-distributed nuisance parameters. The uncertainty on the normalization of the expected background distribution is included in the expected background events. At this point the expected cross section limit is calculated for both the metastable and stable signal region for each lifetime point, and the region with the best expected limit is selected for each lifetime. Using that procedure, the metastable region is used for lifetimes up to and including 30 ns, and the stable region for lifetimes above it.

The resulting cross-sectional upper limits are shown as a function of mass in Figure 90 and Figure 91 for each lifetime considered. The limits are interpolated linearly between each mass point, and the dependence of the limit on the mass is small as the efficiency is relatively constant for large R-Hadron masses. There is however a strong dependence on lifetime, as discussed in Section 10.5, where the probability to form a fully reconstructed track and the kinematic freedom to produce E_T^{miss} result in a local maximum in the limit at 10–30 ns. The figures also include the expected cross section for pair-produced gluino R-Hadrons for reference. For the 10 ns and stable cross section limits, both the observed limit and expected cross section for the Run 1, 8 TeV version of this analysis are included. There the cross sectional limits are lower because of the increased available luminosity, while the signal cross sections were also much lower because of the lower collision energy.

3830 13.4 MASS LIMITS

3831 The cross-sectional limits can then be used to derive a lower mass limit for gluino
 3832 R-Hadrons by comparing them to the theoretically predicted production cross

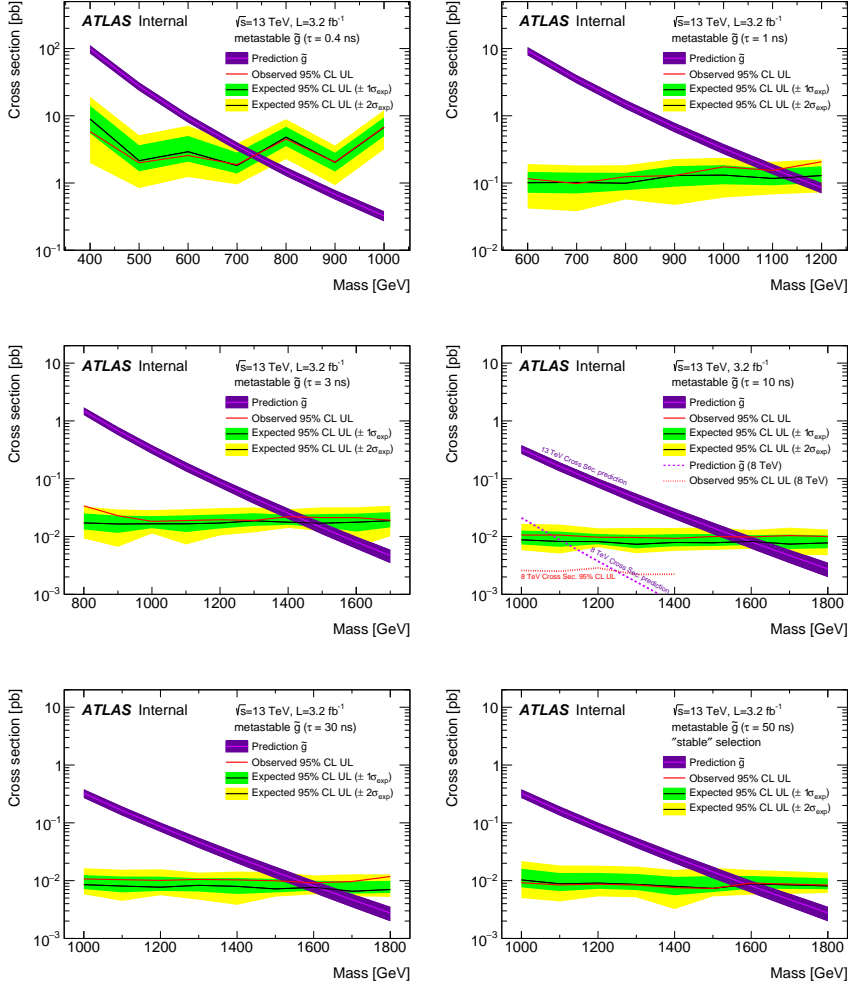


Figure 91: The observed and expected cross section limits as a function of mass for each generated lifetime. The predicted cross section values for the corresponding signals are included.

sections. These mass limits range from only 740 GeV at the lowest lifetimes considered, where the selection efficiency is very low, to up to 1580 GeV at 30 ns where the selection efficiency is maximized. The observed and expected mass limits for each lifetime point are detailed in Table 18, which also lists which selection region was used for each lifetime. These excluded range of masses as a function of lifetime is also shown in Figure 92. The Run 1 limits are included for comparison; the limits have increased by about 200 GeV on average. The search has also improved since the previous incarnation from Run 1 in optimizing the region between 30 GeV and detector-stable lifetimes by introducing the second signal region. The definition of the stable region prevents the significant drop in mass limit that occurred above 30 GeV in the Run 1 analysis.

Selection	τ [ns]	$M_{\text{obs}} > [\text{GeV}]$	$M_{\text{exp}} > [\text{GeV}]$
Metastable	0.4	740	730
"	1.0	1110	1150
"	3.0	1430	1470
"	10	1570	1600
"	30	1580	1620
Stable	50	1590	1590
"	stable	1570	1580

Table 18: The observed and expected 95% CL lower limit on mass for gluino R-Hadrons for each considered lifetime.

13.5 CONTEXT FOR LONG-LIVED SEARCHES

This search plays an important role in the current, combined [ATLAS](#) search for long lived particles. The mass limits provided by various [ATLAS](#) searches for long-lived gluino R-Hadrons can be seen in Figure 93. This search provides the most competitive limit for lifetimes between 3 ns up through very long lifetimes, where it is still competitive with dedicated searches for stable particles. The limits placed on gluino production are very similar to the limits on promptly decaying models.

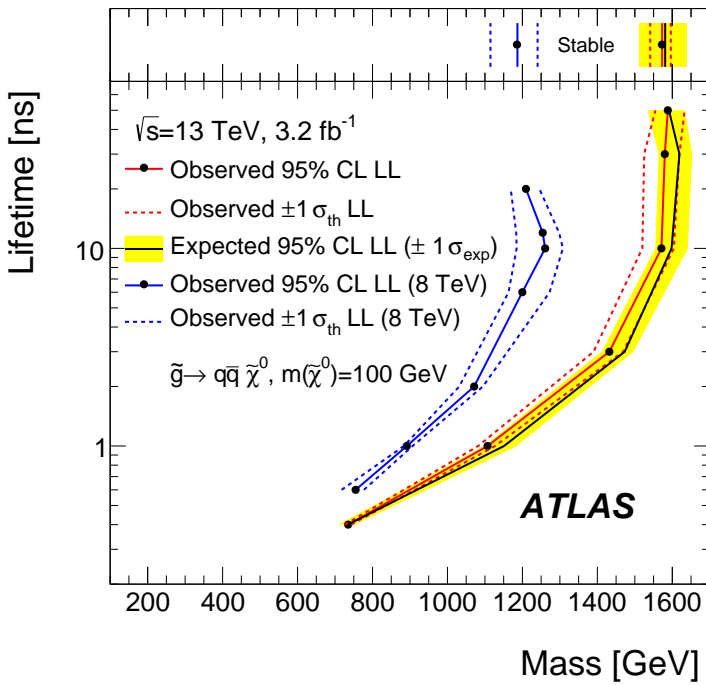


Figure 92: The excluded range of masses as a function of gluino lifetime. The expected lower limit (LL), with its experimental $\pm 1\sigma$ band, is given with respect to the nominal theoretical cross-section. The observed 95% LL obtained at $\sqrt{s} = 8 \text{ TeV}$ [82] is also shown for comparison.

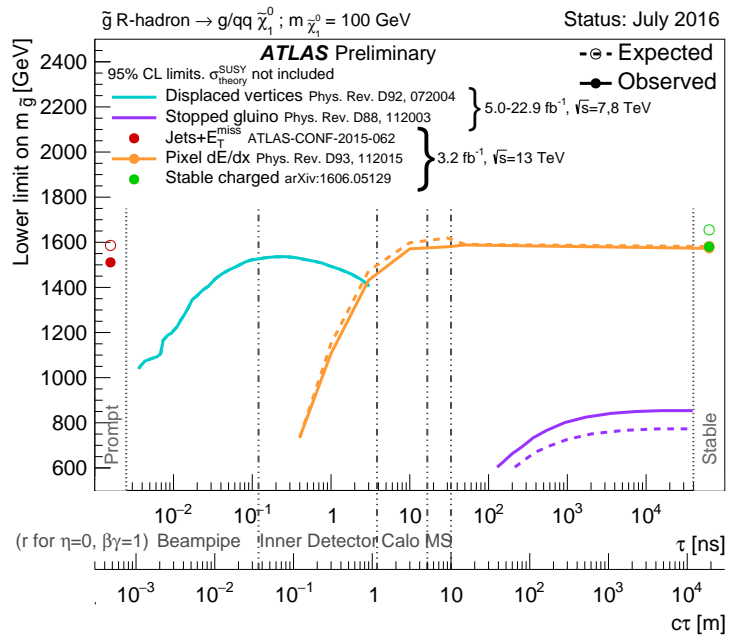


Figure 93: The constraints on the gluino mass as a function of lifetime for a split-supersymmetry model with the gluino R-Hadrons decaying into a gluon or light quarks and a neutralino with mass of 100 GeV. The solid lines indicate the observed limits, while the dashed lines indicate the expected limits. The area below the curves is excluded. The dots represent results for which the particle is assumed to be prompt or stable.

3852

PART VI

3853

CONCLUSIONS

3854

You can put some informational part preamble text here.

14

3855

3856 SUMMARY AND OUTLOOK

3857 14.1 SUMMARY

3858 14.2 OUTLOOK

3859

PART VII

3860

APPENDIX

3861

A

3862

3863 INELASTIC CROSS SECTION

$m(\tilde{g})$ [GeV]	Left Extremum [GeV]	Right Extremum [GeV]
1000	682	1387
1100	763	1478
1200	801	1606
1300	809	1841
1400	861	2011
1500	920	2032
1600	952	2173
1800	1017	2422

Table 19: The left and right extremum of the mass window for each generated mass point with a 50 ns lifetime.

$m(\tilde{g})$ [GeV]	Left Extremum [GeV]	Right Extremum [GeV]
1000	689	1321
1100	746	1513
1200	788	1670
1300	860	1734
1400	833	1925
1500	852	2048
1600	833	2283
1700	946	2379
1800	869	2505

Table 20: The left and right extremum of the mass window for each generated mass point with a 30 ns lifetime.

$m(\tilde{g})$ [GeV]	Left Extremum [GeV]	Right Extremum [GeV]
1000	655	1349
1100	734	1455
1200	712	1631
1300	792	1737
1400	717	1926
1500	815	2117
1600	824	2122
1700	900	2274
1800	919	2344

Table 21: The left and right extremum of the mass window for each generated mass point with a 10 ns lifetime.

$m(\tilde{g})$ [GeV]	Left Extremum [GeV]	Right Extremum [GeV]
800	531	1065
900	576	1165
1000	610	1345
1100	635	1432
1200	663	1563
1300	620	1667
1400	742	1727
1500	761	1937
1600	573	2000
1700	621	2182

Table 22: The left and right extremum of the mass window used for each generated mass point with a lifetime of 3 ns.

$m(\tilde{g})$ [GeV]	Left Extremum [GeV]	Right Extremum [GeV]
600	411	758
700	385	876
800	486	970
900	406	987
1000	408	1136
1100	555	1196
1200	516	1378

Table 23: The left and right extremum of the mass window used for each mass point with a lifetime of 1 ns.

$m(\tilde{g})$ [GeV]	Left Extremum [GeV]	Right Extremum [GeV]
400	204	510
500	295	639
600	288	702
700	323	701
800	190	771
900	277	677
1000	249	688

Table 24: The left and right extremum of the mass window for each generated mass point with a lifetime of 0.4 ns.

$m(\tilde{g})$ [GeV]	Left Extremum [GeV]	Right Extremum [GeV]
800	627	1053
1000	726	1277
1200	857	1584
1400	924	1937
1600	993	2308
1800	1004	2554

Table 25: The left and right extremum of the mass window used for each generated stable mass point.

$m(\tilde{g})$ [GeV]	Expected Signal	Expected Background	Observed Data
1000	131.18 ± 6.35	1.803 ± 0.081	1.0 ± 1.0
1100	71.11 ± 3.35	1.409 ± 0.069	1.0 ± 1.0
1200	37.18 ± 1.75	1.310 ± 0.066	1.0 ± 1.0
1300	20.76 ± 0.95	1.431 ± 0.069	1.0 ± 1.0
1400	12.63 ± 0.57	1.273 ± 0.065	1.0 ± 1.0
1500	6.57 ± 0.29	1.115 ± 0.059	1.0 ± 1.0
1600	3.56 ± 0.16	1.041 ± 0.057	1.0 ± 1.0
1800	1.27 ± 0.05	0.918 ± 0.053	1.0 ± 1.0

Table 26: The expected number of signal events, the expected number of background events, and the observed number of events in data with their respective statistical errors within the respective mass window for each generated mass point with a lifetime of 50 ns.

$m(\tilde{g})$ [GeV]	Expected Signal	Expected Background	Observed Data
1000	144.65 ± 6.34	1.328 ± 0.063	2.0 ± 1.4
1100	75.28 ± 3.27	1.255 ± 0.060	2.0 ± 1.4
1200	40.51 ± 1.75	1.193 ± 0.058	2.0 ± 1.4
1300	20.91 ± 0.93	0.997 ± 0.051	2.0 ± 1.4
1400	11.97 ± 0.51	1.131 ± 0.056	2.0 ± 1.4
1500	6.81 ± 0.28	1.111 ± 0.055	2.0 ± 1.4
1600	4.19 ± 0.16	1.193 ± 0.058	2.0 ± 1.4
1700	2.42 ± 0.09	0.963 ± 0.050	2.0 ± 1.4
1800	1.46 ± 0.05	1.138 ± 0.056	3.0 ± 1.7

Table 27: The expected number of signal events, the expected number of background events, and the observed number of events in data with their respective statistical errors within the respective mass window for each generated mass point with a lifetime of 30 ns.

$m(\tilde{g})$ [GeV]	Expected Signal	Expected Background	Observed Data
1000	144.48 ± 5.14	1.499 ± 0.069	2.0 ± 1.4
1100	73.19 ± 2.61	1.260 ± 0.060	2.0 ± 1.4
1200	41.54 ± 1.41	1.456 ± 0.067	2.0 ± 1.4
1300	22.58 ± 0.77	1.201 ± 0.058	2.0 ± 1.4
1400	12.70 ± 0.42	1.558 ± 0.071	2.0 ± 1.4
1500	6.73 ± 0.24	1.237 ± 0.060	2.0 ± 1.4
1600	3.90 ± 0.13	1.201 ± 0.058	2.0 ± 1.4
1700	2.27 ± 0.07	1.027 ± 0.052	2.0 ± 1.4
1800	1.34 ± 0.04	1.019 ± 0.052	2.0 ± 1.4

Table 28: The expected number of signal events, the expected number of background events, and the observed number of events in data with their respective statistical errors within the respective mass window for each generated mass point with a lifetime of 10 ns.

$m(\tilde{g})$ [GeV]	Expected Signal	Expected Background	Observed Data
800	362.97 ± 14.68	1.841 ± 0.080	5.0 ± 2.2
900	169.20 ± 6.69	1.710 ± 0.076	3.0 ± 1.7
1000	84.78 ± 3.23	1.727 ± 0.076	2.0 ± 1.4
1100	40.06 ± 1.60	1.679 ± 0.075	2.0 ± 1.4
1200	20.06 ± 0.81	1.598 ± 0.072	2.0 ± 1.4
1300	10.76 ± 0.43	1.851 ± 0.080	2.0 ± 1.4
1400	5.52 ± 0.22	1.374 ± 0.064	2.0 ± 1.4
1500	3.16 ± 0.13	1.355 ± 0.064	2.0 ± 1.4
1600	2.13 ± 0.11	2.235 ± 0.093	3.0 ± 1.7
1700	1.10 ± 0.06	1.995 ± 0.085	2.0 ± 1.4

Table 29: The expected number of signal events, the expected number of background events, and the observed number of events in data with their respective statistical errors within the respective mass window for each generated mass point with a lifetime of 3 ns.

$m(\tilde{g})$ [GeV]	Expected Signal	Expected Background	Observed Data
600	431.80 ± 36.60	2.418 ± 0.099	3.0 ± 1.7
700	192.77 ± 15.28	3.267 ± 0.126	3.0 ± 1.7
800	69.63 ± 5.90	2.125 ± 0.089	3.0 ± 1.7
900	28.91 ± 2.59	3.114 ± 0.121	3.0 ± 1.7
1000	13.64 ± 1.22	3.359 ± 0.129	5.0 ± 2.2
1100	6.13 ± 0.57	1.879 ± 0.081	3.0 ± 1.7
1200	3.24 ± 0.30	2.387 ± 0.098	5.0 ± 2.2

Table 30: The expected number of signal events, the expected number of background events, and the observed number of events in data with their respective statistical errors within the respective mass window for each generated mass point with a lifetime of 1 ns.

$m(\tilde{g})$ [GeV]	Expected Signal	Expected Background	Observed Data
400	181.71 ± 75.59	6.780 ± 0.238	4.0 ± 2.0
500	103.88 ± 30.05	4.310 ± 0.160	4.0 ± 2.0
600	28.34 ± 9.34	4.868 ± 0.177	4.0 ± 2.0
700	13.62 ± 4.00	3.908 ± 0.147	4.0 ± 2.0
800	2.75 ± 1.15	9.001 ± 0.308	8.0 ± 2.8
900	2.25 ± 0.71	5.045 ± 0.183	5.0 ± 2.2
1000	0.34 ± 0.19	6.026 ± 0.214	6.0 ± 2.4

Table 31: The expected number of signal events, the expected number of background events, and the observed number of events in data with their respective statistical errors within the respective mass window for each generated mass point with a lifetime of $p4$ ns.

$m(\tilde{g})$ [GeV]	Expected Signal	Expected Background	Observed Data
800	462.83 ± 14.86	1.764 ± 0.080	2.0 ± 1.4
1000	108.73 ± 3.38	1.458 ± 0.070	1.0 ± 1.0
1200	31.74 ± 0.95	1.137 ± 0.060	1.0 ± 1.0
1400	10.22 ± 0.29	1.058 ± 0.058	1.0 ± 1.0
1600	3.07 ± 0.09	0.947 ± 0.054	1.0 ± 1.0
1800	1.08 ± 0.05	0.940 ± 0.054	1.0 ± 1.0

Table 32: The expected number of signal events, the expected number of background events, and the observed number of events in data with their respective statistical errors within the respective mass window for each generated stable mass point

- 3867 [1] A. D. Martin, W. J. Stirling, R. S. Thorne, and G. Watt. “Parton distributions
3868 for the LHC”. In: *Eur. Phys. J.* C63 (2009), pp. 189–285. doi: [10.1140/epjc/s10052-009-1072-5](https://doi.org/10.1140/epjc/s10052-009-1072-5). arXiv: [0901.0002](https://arxiv.org/abs/0901.0002) [hep-ph].
- 3870 [2] Prajwal Raj Kafle, Sanjib Sharma, Geraint F. Lewis, and Joss Bland-Hawthorn.
3871 “On the Shoulders of Giants: Properties of the Stellar Halo and the Milky
3872 Way Mass Distribution”. In: *Astrophys. J.* 794.1 (2014), p. 59. doi: [10.1088/0004-637X/794/1/59](https://doi.org/10.1088/0004-637X/794/1/59). arXiv: [1408.1787](https://arxiv.org/abs/1408.1787) [astro-ph.GA].
- 3874 [3] Savas Dimopoulos and Howard Georgi. “Softly broken supersymmetry
3875 and SU(5)”. In: *Nuclear Physics B* 193.1 (1981), pp. 150 – 162. ISSN: 0550-
3876 3213. doi: [http://dx.doi.org/10.1016/0550-3213\(81\)90522-8](https://dx.doi.org/10.1016/0550-3213(81)90522-8).
- 3878 [4] A. Djouadi et al. “The Minimal supersymmetric standard model: Group
3879 summary report”. In: *GDR (Groupement De Recherche) - Supersymetrie Mont-
3880 pellier, France, April 15-17, 1998*. 1998. arXiv: [hep-ph/9901246](https://arxiv.org/abs/hep-ph/9901246) [hep-ph].
3881 URL: https://inspirehep.net/record/481987/files/arXiv:hep-ph_9901246.pdf.
- 3883 [5] K. A. Olive et al. “Review of Particle Physics”. In: *Chin. Phys.* C38 (2014),
3884 p. 090001. doi: [10.1088/1674-1137/38/9/090001](https://doi.org/10.1088/1674-1137/38/9/090001).
- 3885 [6] Lawrence J. Hall, Yasunori Nomura, and Satoshi Shirai. “Spread Super-
3886 symmetry with Wino LSP: Gluino and Dark Matter Signals”. In: *JHEP* 01
3887 (2013), p. 036. doi: [10.1007/JHEP01\(2013\)036](https://doi.org/10.1007/JHEP01(2013)036). arXiv: [1210.2395](https://arxiv.org/abs/1210.2395)
3888 [hep-ph].
- 3889 [7] G. F. Giudice and A. Romanino. “Split supersymmetry”. In: *Nucl. Phys. B*
3890 699 (2004), p. 65. doi: [10.1016/j.nuclphysb.2004.11.048](https://doi.org/10.1016/j.nuclphysb.2004.11.048). arXiv:
3891 [hep-ph/0406088](https://arxiv.org/abs/hep-ph/0406088).
- 3892 [8] N. Arkani-Hamed, S. Dimopoulos, G. F. Giudice, and A. Romanino. “As-
3893 pects of split supersymmetry”. In: *Nucl. Phys. B* 709 (2005), p. 3. doi: [10.1016/j.nuclphysb.2004.12.026](https://doi.org/10.1016/j.nuclphysb.2004.12.026). arXiv: [hep-ph/0409232](https://arxiv.org/abs/hep-ph/0409232).
- 3895 [9] Lyndon Evans and Philip Bryant. “LHC Machine”. In: *JINST* 3 (2008), S08001.
3896 doi: [10.1088/1748-0221/3/08/S08001](https://doi.org/10.1088/1748-0221/3/08/S08001).
- 3897 [10] C Lefevre. “LHC: the guide (English version). Guide du LHC (version anglaise)”.
3898 2009. URL: <https://cds.cern.ch/record/1165534>.
- 3899 [11] “LEP Design Report Vol.1”. In: (1983).
- 3900 [12] ATLAS Collaboration. “The ATLAS Experiment at the CERN Large Hadron
3901 Collider”. In: *JINST* 3 (2008), S08003. doi: [10.1088/1748-0221/3/08/S08003](https://doi.org/10.1088/1748-0221/3/08/S08003).
- 3903 [13] S. Chatrchyan et al. “The CMS experiment at the CERN LHC”. In: *JINST*
3904 3 (2008), S08004. doi: [10.1088/1748-0221/3/08/S08004](https://doi.org/10.1088/1748-0221/3/08/S08004).

- 3905 [14] A. Augusto Alves Jr. et al. "The LHCb Detector at the LHC". In: *JINST* 3
 3906 (2008), S08005. doi: [10.1088/1748-0221/3/08/S08005](https://doi.org/10.1088/1748-0221/3/08/S08005).
- 3907 [15] K. Aamodt et al. "The ALICE experiment at the CERN LHC". In: *JINST* 3
 3908 (2008), S08002. doi: [10.1088/1748-0221/3/08/S08002](https://doi.org/10.1088/1748-0221/3/08/S08002).
- 3909 [16] Daniel Froidevaux and Paris Sphicas. "General-Purpose Detectors for the
 3910 Large Hadron Collider". In: *Annual Review of Nuclear and Particle Science*
 3911 56.1 (2006), pp. 375–440. doi: [10.1146/annurev.nucl.54.070103.181209](https://doi.org/10.1146/annurev.nucl.54.070103.181209). URL: <http://dx.doi.org/10.1146/annurev.nucl.54.070103.181209>.
- 3912 [17] M Capeans, G Darbo, K Einsweiller, M Elsing, T Flick, M Garcia-Sciveres,
 3913 C Gemme, H Pernegger, O Rohne, and R Vuillermet. *ATLAS Insertable B-*
 3914 *Layer Technical Design Report*. Tech. rep. CERN-LHCC-2010-013. ATLAS-
 3915 TDR-19. 2010. URL: <https://cds.cern.ch/record/1291633>.
- 3916 [18] T. Cornelissen, M. Elsing, S. Fleischmann, W. Liebig, and E. Moyse. "Con-
 3917 cepts, Design and Implementation of the ATLAS New Tracking (NEWT)".
 3918 In: (2007). Ed. by A. Salzburger.
- 3919 [19] "Performance of the ATLAS Inner Detector Track and Vertex Reconstruc-
 3920 tion in the High Pile-Up LHC Environment". In: (2012).
- 3921 [20] A. Salzburger. "The ATLAS Track Extrapolation Package". In: (2007).
- 3922 [21] ATLAS Collaboration. "A neural network clustering algorithm for the AT-
 3923 LAS silicon pixel detector". In: *JINST* 9 (2014), P09009. doi: [10.1088/1748-0221/9/09/P09009](https://doi.org/10.1088/1748-0221/9/09/P09009). arXiv: [1406.7690 \[hep-ex\]](https://arxiv.org/abs/1406.7690).
- 3924 [22] ATLAS Collaboration. *Performance of primary vertex reconstruction in proton-*
 3925 *proton collisions at $\sqrt{s} = 7$ TeV in the ATLAS experiment*. ATLAS-CONF-
 3926 2010-069. 2010. URL: <https://cds.cern.ch/record/1281344>.
- 3927 [23] ATLAS Collaboration. "Electron reconstruction and identification efficiency
 3928 measurements with the ATLAS detector using the 2011 LHC proton–proton
 3929 collision data". In: *Eur. Phys. J. C* 74 (2014), p. 2941. doi: [10.1140/epjc/s10052-014-2941-0](https://doi.org/10.1140/epjc/s10052-014-2941-0). arXiv: [1404.2240 \[hep-ex\]](https://arxiv.org/abs/1404.2240). PERF-2013-03.
- 3930 [24] ATLAS Collaboration. *Electron efficiency measurements with the ATLAS de-*
 3931 *tector using the 2012 LHC proton–proton collision data*. ATLAS-CONF-2014-
 3932 032. 2014. URL: <https://cds.cern.ch/record/1706245>.
- 3933 [25] ATLAS Collaboration. *Measurements of the photon identification efficiency*
 3934 *with the ATLAS detector using 4.9 fb^{-1} of pp collision data collected in 2011*.
 3935 ATLAS-CONF-2012-123. 2012. URL: <https://cds.cern.ch/record/1473426>.
- 3936 [26] ATLAS Collaboration. "Muon reconstruction performance of the ATLAS
 3937 detector in proton–proton collision data at $\sqrt{s} = 13$ TeV". In: (2016).
 3938 arXiv: [1603.05598 \[hep-ex\]](https://arxiv.org/abs/1603.05598). PERF-2015-10.
- 3939 [27] ATLAS Collaboration. "Topological cell clustering in the ATLAS calorime-
 3940 ters and its performance in LHC Run 1". In: (2016). arXiv: [1603.02934](https://arxiv.org/abs/1603.02934)
 3941 [hep-ex]. PERF-2014-07.

- 3947 [28] ATLAS Collaboration. *Properties of jets and inputs to jet reconstruction and*
 3948 *calibration with the ATLAS detector using proton–proton collisions at $\sqrt{s} =$*
 3949 *13 TeV.* ATL-PHYS-PUB-2015-036. 2015. URL: <https://cds.cern.ch/record/2044564>.
- 3951 [29] Matteo Cacciari, Gavin P. Salam, and Gregory Soyez. “The anti- k_t jet clus-
 3952 tering algorithm”. In: *JHEP* 04 (2008), p. 063. doi: [10.1088/1126-6708/2008/04/063](https://doi.org/10.1088/1126-6708/2008/04/063). arXiv: [0802.1189 \[hep-ph\]](https://arxiv.org/abs/0802.1189).
- 3954 [30] ATLAS Collaboration. *Jet global sequential corrections with the ATLAS detec-*
 3955 *tor in proton–proton collisions at $\sqrt{s} = 8$ TeV.* ATLAS-CONF-2015-002.
 3956 2015. URL: <https://cds.cern.ch/record/2001682>.
- 3957 [31] S. Agostinelli et al. “GEANT4: A simulation toolkit”. In: *Nucl. Instrum. Meth.*
 3958 *A* 506 (2003), pp. 250–303. doi: [10.1016/S0168-9002\(03\)01368-8](https://doi.org/10.1016/S0168-9002(03)01368-8).
- 3959 [32] ATLAS Collaboration. “A study of the material in the ATLAS inner de-
 3960 *tector using secondary hadronic interactions*. In: *JINST* 7 (2012), P01013.
 3961 doi: [10.1088/1748-0221/7/01/P01013](https://doi.org/10.1088/1748-0221/7/01/P01013). arXiv: [1110.6191 \[hep-ex\]](https://arxiv.org/abs/1110.6191).
 3962 PERF-2011-08.
- 3963 [33] ATLAS Collaboration. “Electron and photon energy calibration with the
 3964 ATLAS detector using LHC Run 1 data”. In: *Eur. Phys. J. C* 74 (2014), p. 3071.
 3965 doi: [10.1140/epjc/s10052-014-3071-4](https://doi.org/10.1140/epjc/s10052-014-3071-4). arXiv: [1407.5063 \[hep-ex\]](https://arxiv.org/abs/1407.5063). PERF-2013-05.
- 3967 [34] ATLAS Collaboration. “A measurement of the calorimeter response to sin-
 3968 *gle hadrons and determination of the jet energy scale uncertainty using*
 3969 *LHC Run-1 pp -collision data with the ATLAS detector*. In: (2016). arXiv:
 3970 [1607.08842 \[hep-ex\]](https://arxiv.org/abs/1607.08842). PERF-2015-05.
- 3971 [35] ATLAS Collaboration. “Single hadron response measurement and calorime-
 3972 *ter jet energy scale uncertainty with the ATLAS detector at the LHC*. In:
 3973 *Eur. Phys. J. C* 73 (2013), p. 2305. doi: [10.1140/epjc/s10052-013-2305-1](https://doi.org/10.1140/epjc/s10052-013-2305-1). arXiv: [1203.1302 \[hep-ex\]](https://arxiv.org/abs/1203.1302). PERF-2011-05.
- 3975 [36] ATLAS Collaboration. “The ATLAS Simulation Infrastructure”. In: *Eur.*
 3976 *Phys. J. C* 70 (2010), p. 823. doi: [10.1140/epjc/s10052-010-1429-9](https://doi.org/10.1140/epjc/s10052-010-1429-9).
 3977 arXiv: [1005.4568 \[hep-ex\]](https://arxiv.org/abs/1005.4568). SOFT-2010-01.
- 3978 [37] T. Sjöstrand, S. Mrenna, and P. Skands. “A Brief Introduction to PYTHIA
 3979 8.1”. In: *Comput. Phys. Commun.* 178 (2008), pp. 852–867. doi: [10.1016/j.cpc.2008.01.036](https://doi.org/10.1016/j.cpc.2008.01.036). arXiv: [0710.3820](https://arxiv.org/abs/0710.3820).
- 3981 [38] ATLAS Collaboration. *Summary of ATLAS Pythia 8 tunes.* ATL-PHYS-PUB-
 3982 2012-003. 2012. URL: [http://cds.cern.ch/record/1474107](https://cds.cern.ch/record/1474107).
- 3983 [39] A.D. Martin, W.J. Stirling, R.S. Thorne, and G. Watt. “Parton distributions
 3984 for the LHC”. In: *Eur. Phys. J. C* 63 (2009). Figures from the **MSTW Website**,
 3985 pp. 189–285. doi: [10.1140/epjc/s10052-009-1072-5](https://doi.org/10.1140/epjc/s10052-009-1072-5). arXiv: [0901.0002](https://arxiv.org/abs/0901.0002).
- 3987 [40] A. Sherstnev and R.S. Thorne. “Parton Distributions for LO Generators”.
 3988 In: *Eur. Phys. J. C* 55 (2008), pp. 553–575. doi: [10.1140/epjc/s10052-008-0610-x](https://doi.org/10.1140/epjc/s10052-008-0610-x). arXiv: [0711.2473](https://arxiv.org/abs/0711.2473).

- 3990 [41] A. Ribon et al. *Status of Geant4 hadronic physics for the simulation of LHC*
 3991 *experiments at the start of LHC physics program.* CERN-LCGAPP-2010-02.
 3992 2010. URL: <http://lcgapp.cern.ch/project/docs/noteStatusHadronic2010.pdf>.
- 3993
- 3994 [42] M. P. Guthrie, R. G. Alsmiller, and H. W. Bertini. "Calculation of the cap-
 3995 ture of negative pions in light elements and comparison with experiments
 3996 pertaining to cancer radiotherapy". In: *Nucl. Instrum. Meth.* 66 (1968), pp. 29–
 3997 36. doi: [10.1016/0029-554X\(68\)90054-2](https://doi.org/10.1016/0029-554X(68)90054-2).
- 3998 [43] H. W. Bertini and P. Guthrie. "News item results from medium-energy
 3999 intranuclear-cascade calculation". In: *Nucl. Instr. and Meth. A* 169 (1971),
 4000 p. 670. doi: [10.1016/0375-9474\(71\)90710-X](https://doi.org/10.1016/0375-9474(71)90710-X).
- 4001 [44] V.A. Karmanov. "Light Front Wave Function of Relativistic Composite
 4002 System in Explicitly Solvable Model". In: *Nucl. Phys. B* 166 (1980), p. 378.
 4003 doi: [10.1016/0550-3213\(80\)90204-7](https://doi.org/10.1016/0550-3213(80)90204-7).
- 4004 [45] H. S. Fesefeldt. *GHEISHA program.* Pitha-85-02, Aachen. 1985.
- 4005 [46] G. Folger and J.P. Wellisch. "String parton models in Geant4". In: (2003).
 4006 arXiv: [nucl-th/0306007](https://arxiv.org/abs/nucl-th/0306007).
- 4007 [47] N. S. Amelin et al. "Transverse flow and collectivity in ultrarelativistic
 4008 heavy-ion collisions". In: *Phys. Rev. Lett.* 67 (1991), p. 1523. doi: [10.1103/PhysRevLett.67.1523](https://doi.org/10.1103/PhysRevLett.67.1523).
- 4010 [48] N. S. Amelin et al. "Collectivity in ultrarelativistic heavy ion collisions". In:
 4011 *Nucl. Phys. A* 544 (1992), p. 463. doi: [10.1016/0375-9474\(92\)90598-E](https://doi.org/10.1016/0375-9474(92)90598-E).
- 4013 [49] L. V. Bravina et al. "Fluid dynamics and Quark Gluon string model - What
 4014 we can expect for Au+Au collisions at 11.6 AGeV/c". In: *Nucl. Phys. A* 566
 4015 (1994), p. 461. doi: [10.1016/0375-9474\(94\)90669-6](https://doi.org/10.1016/0375-9474(94)90669-6).
- 4016 [50] L. V. Bravin et al. "Scaling violation of transverse flow in heavy ion col-
 4017 lisions at AGS energies". In: *Phys. Lett. B* 344 (1995), p. 49. doi: [10.1016/0370-2693\(94\)01560-Y](https://doi.org/10.1016/0370-2693(94)01560-Y).
- 4019 [51] B. Andersson et al. "A model for low-pT hadronic reactions with general-
 4020 izations to hadron-nucleus and nucleus-nucleus collisions". In: *Nucl. Phys.*
 4021 *B* 281 (1987), p. 289. doi: [10.1016/0550-3213\(87\)90257-4](https://doi.org/10.1016/0550-3213(87)90257-4).
- 4022 [52] B. Andersson, A. Tai, and B.-H. Sa. "Final state interactions in the (nuclear)
 4023 FRITIOF string interaction scenario". In: *Z. Phys. C* 70 (1996), pp. 499–
 4024 506. doi: [10.1007/s002880050127](https://doi.org/10.1007/s002880050127).
- 4025 [53] B. Nilsson-Almqvist and E. Stenlund. "Interactions Between Hadrons and
 4026 Nuclei: The Lund Monte Carlo, Fritiof Version 1.6". In: *Comput. Phys. Com-*
 4027 *mun.* 43 (1987), p. 387. doi: [10.1016/0010-4655\(87\)90056-7](https://doi.org/10.1016/0010-4655(87)90056-7).
- 4028 [54] B. Ganhuyag and V. Uzhinsky. "Modified FRITIOF code: Negative charged
 4029 particle production in high energy nucleus nucleus interactions". In: *Czech.*
 4030 *J. Phys.* 47 (1997), pp. 913–918. doi: [10.1023/A:1021296114786](https://doi.org/10.1023/A:1021296114786).

- 4031 [55] ATLAS Collaboration. “Topological cell clustering in the ATLAS calorimeters and its performance in LHC Run 1”. In: (2016). arXiv: [1603.02934](https://arxiv.org/abs/1603.02934) [hep-ex].
- 4032
- 4033
- 4034 [56] Peter Speckmayer. “Energy Measurement of Hadrons with the CERN ATLAS Calorimeter”. Presented on 18 Jun 2008. PhD thesis. Vienna: Vienna, Tech. U., 2008. URL: <http://cds.cern.ch/record/1112036>.
- 4035
- 4036
- 4037 [57] CMS Collaboration. “The CMS barrel calorimeter response to particle beams from 2 to 350 GeV/c”. In: *Eur. Phys. J. C* 60.3 (2009). doi: [10.1140/epjc/s10052-009-0959-5](https://doi.org/10.1140/epjc/s10052-009-0959-5).
- 4038
- 4039
- 4040 [58] J. Beringer et al. (Particle Data Group). “Review of Particle Physics”. In: *Chin. Phys. C* 38 (2014), p. 090001. URL: <http://pdg.lbl.gov>.
- 4041
- 4042 [59] P. Adragna et al. “Measurement of Pion and Proton Response and Longitudinal Shower Profiles up to 20 Nuclear Interaction Lengths with the ATLAS Tile Calorimeter”. In: *Nucl. Instrum. Meth. A* 615 (2010), pp. 158–181. doi: [10.1016/j.nima.2010.01.037](https://doi.org/10.1016/j.nima.2010.01.037).
- 4043
- 4044
- 4045
- 4046 [60] ATLAS Collaboration. “Jet energy measurement and its systematic uncertainty in proton–proton collisions at $\sqrt{s} = 7$ TeV with the ATLAS detector”. In: *Eur. Phys. J. C* 75 (2015), p. 17. doi: [10.1140/epjc/s10052-014-3190-y](https://doi.org/10.1140/epjc/s10052-014-3190-y). arXiv: [1406.0076](https://arxiv.org/abs/1406.0076) [hep-ex]. PERF-2012-01.
- 4047
- 4048
- 4049
- 4050 [61] Hung-Liang Lai, Marco Guzzi, Joey Huston, Zhao Li, Pavel M. Nadolsky, et al. “New parton distributions for collider physics”. In: *Phys. Rev. D* 82 (2010), p. 074024. doi: [10.1103/PhysRevD.82.074024](https://doi.org/10.1103/PhysRevD.82.074024). arXiv: [1007.2241](https://arxiv.org/abs/1007.2241) [hep-ph].
- 4051
- 4052
- 4053
- 4054 [62] E. Abat et al. “Study of energy response and resolution of the ATLAS barrel calorimeter to hadrons of energies from 20 to 350 GeV”. In: *Nucl. Instrum. Meth. A* 621.1-3 (2010), pp. 134 – 150. doi: <http://dx.doi.org/10.1016/j.nima.2010.04.054>.
- 4055
- 4056
- 4057
- 4058 [63] ATLAS Collaboration. “Jet energy measurement with the ATLAS detector in proton–proton collisions at $\sqrt{s} = 7$ TeV”. In: *Eur. Phys. J. C* 73 (2013), p. 2304. doi: [10.1140/epjc/s10052-013-2304-2](https://doi.org/10.1140/epjc/s10052-013-2304-2). arXiv: [1112.6426](https://arxiv.org/abs/1112.6426) [hep-ex]. PERF-2011-03.
- 4059
- 4060
- 4061
- 4062 [64] Nausheen R. Shah and Carlos E. M. Wagner. “Gravitons and dark matter in universal extra dimensions”. In: *Phys. Rev. D* 74 (2006), p. 104008. doi: [10.1103/PhysRevD.74.104008](https://doi.org/10.1103/PhysRevD.74.104008). arXiv: [hep-ph/0608140](https://arxiv.org/abs/hep-ph/0608140) [hep-ph].
- 4063
- 4064
- 4065 [65] Jonathan L. Feng, Arvind Rajaraman, and Fumihiro Takayama. “Graviton cosmology in universal extra dimensions”. In: *Phys. Rev. D* 68 (2003), p. 085018. doi: [10.1103/PhysRevD.68.085018](https://doi.org/10.1103/PhysRevD.68.085018). arXiv: [hep-ph/0307375](https://arxiv.org/abs/hep-ph/0307375) [hep-ph].
- 4066
- 4067
- 4068
- 4069 [66] Paul H. Frampton and Pham Quang Hung. “Long-lived quarks?” In: *Phys. Rev. D* 58 (5 1998), p. 057704. doi: [10.1103/PhysRevD.58.057704](https://doi.org/10.1103/PhysRevD.58.057704). URL: <http://link.aps.org/doi/10.1103/PhysRevD.58.057704>.
- 4070
- 4071
- 4072
- 4073

- 4073 [67] C. Friberg, E. Norrbin, and T. Sjostrand. “QCD aspects of leptoquark pro-
 4074 duction at HERA”. In: *Phys. Lett.* B403 (1997), pp. 329–334. doi: [10.1016/S0370-2693\(97\)00543-1](https://doi.org/10.1016/S0370-2693(97)00543-1). arXiv: [hep-ph/9704214](https://arxiv.org/abs/hep-ph/9704214) [hep-ph].
- 4076 [68] Herbert K. Dreiner. “An introduction to explicit R-parity violation”. In:
 4077 (1997). arXiv: [hep-ph/9707435](https://arxiv.org/abs/hep-ph/9707435).
- 4078 [69] Edmond L. Berger and Zack Sullivan. “Lower limits on R-parity-violating
 4079 couplings in supersymmetry”. In: *Phys. Rev. Lett.* 92 (2004), p. 201801. doi:
 4080 [10.1103/PhysRevLett.92.201801](https://doi.org/10.1103/PhysRevLett.92.201801). arXiv: [hep-ph/0310001](https://arxiv.org/abs/hep-ph/0310001).
- 4081 [70] R. Barbieri, C. Berat, M. Besancon, M. Chemtob, A. Deandrea, et al. “R-
 4082 parity violating supersymmetry”. In: *Phys. Rept.* 420 (2005), p. 1. doi: [10.1016/j.physrep.2005.08.006](https://doi.org/10.1016/j.physrep.2005.08.006). arXiv: [hep-ph/0406039](https://arxiv.org/abs/hep-ph/0406039).
- 4084 [71] M. Fairbairn et al. “Stable massive particles at colliders”. In: *Phys. Rept.* 438
 4085 (2007), p. 1. doi: [10.1016/j.physrep.2006.10.002](https://doi.org/10.1016/j.physrep.2006.10.002). arXiv: [hep-ph/0611040](https://arxiv.org/abs/hep-ph/0611040).
- 4087 [72] Christopher F. Kolda. “Gauge-mediated supersymmetry breaking: Intro-
 4088 duction, review and update”. In: *Nucl. Phys. Proc. Suppl.* 62 (1998), p. 266.
 4089 doi: [10.1016/S0920-5632\(97\)00667-1](https://doi.org/10.1016/S0920-5632(97)00667-1). arXiv: [hep-ph/9707450](https://arxiv.org/abs/hep-ph/9707450).
- 4090 [73] Howard Baer, Kingman Cheung, and John F. Gunion. “A Heavy gluino as
 4091 the lightest supersymmetric particle”. In: *Phys. Rev. D* 59 (1999), p. 075002.
 4092 doi: [10.1103/PhysRevD.59.075002](https://doi.org/10.1103/PhysRevD.59.075002). arXiv: [hep-ph/9806361](https://arxiv.org/abs/hep-ph/9806361).
- 4093 [74] S. James Gates Jr. and Oleg Lebedev. “Searching for supersymmetry in
 4094 hadrons”. In: *Phys. Lett. B* 477 (2000), p. 216. doi: [10.1016/S0370-2693\(00\)00172-6](https://doi.org/10.1016/S0370-2693(00)00172-6). arXiv: [hep-ph/9912362](https://arxiv.org/abs/hep-ph/9912362).
- 4096 [75] Glennys R. Farrar and Pierre Fayet. “Phenomenology of the Production,
 4097 Decay, and Detection of New Hadronic States Associated with Supersym-
 4098 metry”. In: *Phys. Lett.* B76 (1978), pp. 575–579. doi: [10.1016/0370-2693\(78\)90858-4](https://doi.org/10.1016/0370-2693(78)90858-4).
- 4100 [76] A. C. Kraan, J. B. Hansen, and P. Nevski. “Discovery potential of R-hadrons
 4101 with the ATLAS detector”. In: *Eur. Phys. J.* C49 (2007), pp. 623–640. doi:
 4102 [10.1140/epjc/s10052-006-0162-x](https://doi.org/10.1140/epjc/s10052-006-0162-x). arXiv: [hep-ex/0511014](https://arxiv.org/abs/hep-ex/0511014)
 4103 [hep-ex].
- 4104 [77] Rasmus Mackeprang and David Milstead. “An Updated Description of
 4105 Heavy-Hadron Interactions in GEANT-4”. In: *Eur. Phys. J.* C66 (2010), pp. 493–
 4106 501. doi: [10.1140/epjc/s10052-010-1262-1](https://doi.org/10.1140/epjc/s10052-010-1262-1). arXiv: [0908.1868](https://arxiv.org/abs/0908.1868)
 4107 [hep-ph].
- 4108 [78] ATLAS Collaboration. “Search for massive, long-lived particles using mul-
 4109 titrack displaced vertices or displaced lepton pairs in pp collisions at $\sqrt{s} =$
 4110 8 TeV with the ATLAS detector”. In: *Phys. Rev. D* 92 (2015), p. 072004.
 4111 doi: [10.1103/PhysRevD.92.072004](https://doi.org/10.1103/PhysRevD.92.072004). arXiv: [1504.05162](https://arxiv.org/abs/1504.05162) [hep-ex].
 4112 SUSY-2014-02.

- 4113 [79] ATLAS Collaboration. “Search for charginos nearly mass degenerate with
 4114 the lightest neutralino based on a disappearing-track signature in pp col-
 4115 lisions at $\sqrt{s} = 8$ TeV with the ATLAS detector”. In: *Phys. Rev. D* 88 (2013),
 4116 p. 112006. doi: [10.1103/PhysRevD.88.112006](https://doi.org/10.1103/PhysRevD.88.112006). arXiv: [1310.3675](https://arxiv.org/abs/1310.3675)
 4117 [[hep-ex](#)]. SUSY-2013-01.
- 4118 [80] ATLAS Collaboration. “Searches for heavy long-lived sleptons and R-Hadrons
 4119 with the ATLAS detector in pp collisions at $\sqrt{s} = 7$ TeV”. In: *Phys. Lett. B*
 4120 720 (2013), p. 277. doi: [10.1016/j.physletb.2013.02.015](https://doi.org/10.1016/j.physletb.2013.02.015). arXiv:
 4121 [1211.1597](https://arxiv.org/abs/1211.1597) [[hep-ex](#)]. SUSY-2012-01.
- 4122 [81] ATLAS Collaboration. “Searches for heavy long-lived charged particles
 4123 with the ATLAS detector in proton–proton collisions at $\sqrt{s} = 8$ TeV”. In: *JHEP* 01 (2015), p. 068. doi: [10.1007/JHEP01\(2015\)068](https://doi.org/10.1007/JHEP01(2015)068). arXiv:
 4124 [1411.6795](https://arxiv.org/abs/1411.6795) [[hep-ex](#)]. SUSY-2013-22.
- 4126 [82] ATLAS Collaboration. “Search for metastable heavy charged particles with
 4127 large ionisation energy loss in pp collisions at $\sqrt{s} = 8$ TeV using the AT-
 4128 LAS experiment”. In: *Eur. Phys. J. C* 75 (2015), p. 407. doi: [10.1140/epjc/s10052-015-3609-0](https://doi.org/10.1140/epjc/s10052-015-3609-0). arXiv: [1506.05332](https://arxiv.org/abs/1506.05332) [[hep-ex](#)]. SUSY-
 4129 2014-09.
- 4131 [83] ATLAS Collaboration. “Search for heavy long-lived charged R -hadrons
 4132 with the ATLAS detector in 3.2 fb^{-1} of proton–proton collision data at
 4133 $\sqrt{s} = 13$ TeV”. In: *Phys. Lett. B* 760 (2016), pp. 647–665. doi: [10.1016/j.physletb.2016.07.042](https://doi.org/10.1016/j.physletb.2016.07.042). arXiv: [1606.05129](https://arxiv.org/abs/1606.05129) [[hep-ex](#)].
- 4135 [84] Torbjorn Sjöstrand, Stephen Mrenna, and Peter Skands. “PYTHIA 6.4 Physics
 4136 and Manual”. In: *JHEP* 0605 (2006), p. 026. doi: [10.1088/1126-6708/2006/05/026](https://doi.org/10.1088/1126-6708/2006/05/026). arXiv: [hep-ph/0603175](https://arxiv.org/abs/hep-ph/0603175).
- 4138 [85] ATLAS Collaboration. *Further ATLAS tunes of PYTHIA 6 and Pythia 8*. ATL-
 4139 PHYS-PUB-2011-014. 2011. url: <https://cds.cern.ch/record/1400677>.
- 4141 [86] Aafke Christine Kraan. “Interactions of heavy stable hadronizing parti-
 4142 cles”. In: *Eur. Phys. J. C* 37 (2004), pp. 91–104. doi: [10.1140/epjc/s2004-01946-6](https://doi.org/10.1140/epjc/s2004-01946-6). arXiv: [hep-ex/0404001](https://arxiv.org/abs/hep-ex/0404001) [[hep-ex](#)].
- 4144 [87] M. Fairbairn et al. “Stable massive particles at colliders”. In: *Phys. Rept.* 438
 4145 (2007), p. 1. doi: [10.1016/j.physrep.2006.10.002](https://doi.org/10.1016/j.physrep.2006.10.002). arXiv: [hep-ph/0611040](https://arxiv.org/abs/hep-ph/0611040).
- 4147 [88] W. Beenakker, R. Hopker, M. Spira, and P. M. Zerwas. “Squark and gluino
 4148 production at hadron colliders”. In: *Nucl. Phys. B* 492 (1997), p. 51. doi:
 4149 [10.1016/S0550-3213\(97\)00084-9](https://doi.org/10.1016/S0550-3213(97)00084-9). arXiv: [hep-ph/9610490](https://arxiv.org/abs/hep-ph/9610490).
- 4150 [89] A. Kulesza and L. Motyka. “Threshold resummation for squark-antisquark
 4151 and gluino-pair production at the LHC”. In: *Phys. Rev. Lett.* 102 (2009),
 4152 p. 111802. doi: [10.1103/PhysRevLett.102.111802](https://doi.org/10.1103/PhysRevLett.102.111802). arXiv: [0807.2405](https://arxiv.org/abs/0807.2405) [[hep-ph](#)].

- 4154 [90] A. Kulesza and L. Motyka. “Soft gluon resummation for the production
 4155 of gluino-gluino and squark-antisquark pairs at the LHC”. In: *Phys. Rev.*
 4156 *D* 80 (2009), p. 095004. doi: [10.1103/PhysRevD.80.095004](https://doi.org/10.1103/PhysRevD.80.095004). arXiv:
 4157 [0905.4749 \[hep-ph\]](https://arxiv.org/abs/0905.4749).
- 4158 [91] Wim Beenakker, Silja Bremsing, Michael Kramer, Anna Kulesza, Eric Lae-
 4159 nen, et al. “Soft-gluon resummation for squark and gluino hadroproduction”. In: *JHEP* 0912 (2009), p. 041. doi: [10.1088/1126-6708/2009/12/041](https://doi.org/10.1088/1126-6708/2009/12/041). arXiv: [0909.4418 \[hep-ph\]](https://arxiv.org/abs/0909.4418).
- 4162 [92] W. Beenakker, S. Bremsing, M.n Kramer, A. Kulesza, E. Laenen, et al. “Squark
 4163 and Gluino Hadroproduction”. In: *Int. J. Mod. Phys. A* 26 (2011), p. 2637.
 4164 doi: [10.1142/S0217751X11053560](https://doi.org/10.1142/S0217751X11053560). arXiv: [1105.1110 \[hep-ph\]](https://arxiv.org/abs/1105.1110).
- 4165 [93] Michael Krämer et al. *Supersymmetry production cross sections in pp collisions*
 4166 at $\sqrt{s} = 7 \text{ TeV}$. 2012. arXiv: [1206.2892 \[hep-ph\]](https://arxiv.org/abs/1206.2892).
- 4167 [94] Rasmus Mackeprang and Andrea Rizzi. “Interactions of Coloured Heavy
 4168 Stable Particles in Matter”. In: *Eur. Phys. J.* C50 (2007), pp. 353–362. doi:
 4169 [10.1140/epjc/s10052-007-0252-4](https://doi.org/10.1140/epjc/s10052-007-0252-4). arXiv: [hep-ph/0612161](https://arxiv.org/abs/hep-ph/0612161)
 4170 [hep-ph].
- 4171 [95] Rasmus Mackeprang and David Milstead. “An Updated Description of
 4172 Heavy-Hadron Interactions in GEANT-4”. In: *Eur. Phys. J.* C66 (2010), pp. 493–
 4173 501. doi: [10.1140/epjc/s10052-010-1262-1](https://doi.org/10.1140/epjc/s10052-010-1262-1). arXiv: [0908.1868](https://arxiv.org/abs/0908.1868)
 4174 [hep-ph].
- 4175 [96] J. Alwall, R. Frederix, S. Frixione, V. Hirschi, F. Maltoni, O. Mattelaer, H. S.
 4176 Shao, T. Stelzer, P. Torrielli, and M. Zaro. “The automated computation of
 4177 tree-level and next-to-leading order differential cross sections, and their
 4178 matching to parton shower simulations”. In: *JHEP* 07 (2014), p. 079. doi:
 4179 [10.1007/JHEP07\(2014\)079](https://doi.org/10.1007/JHEP07(2014)079). arXiv: [1405.0301 \[hep-ph\]](https://arxiv.org/abs/1405.0301).
- 4180 [97] “dE/dx measurement in the ATLAS Pixel Detector and its use for particle
 4181 identification”. In: (2011).
- 4182 [98] ATLAS Collaboration. “The ATLAS Simulation Infrastructure”. In: *Eur.*
 4183 *Phys. J.* C70 (2010), pp. 823–874. doi: [10.1140/epjc/s10052-010-1429-9](https://doi.org/10.1140/epjc/s10052-010-1429-9). arXiv: [1005.4568 \[physics.ins-det\]](https://arxiv.org/abs/1005.4568).
- 4185 [99] Alexander L. Read. “Presentation of search results: The CL(s) technique”.
 4186 In: *J. Phys.* G28 (2002). [,11(2002)], pp. 2693–2704. doi: [10.1088/0954-3899/28/10/313](https://doi.org/10.1088/0954-3899/28/10/313).

4188 DECLARATION

4189 Put your declaration here.

4190 *Berkeley, CA, September 2016*

4191

Bradley Axen

4192

4193 COLOPHON

4194 Not sure that this is necessary.